

Experimental and Theoretical Investigations of Mechanical Properties of Randomly-Oriented Strand (ROS) Composites

Marina Selezneva
March, 2015

Department of Mechanical Engineering
McGill University, Montreal

A thesis submitted to McGill University
in partial fulfillment of the requirements for the degree of
Doctor of Philosophy

©Copyright
2015, M. Selezneva



M. Selezneva
(the student)

L. Lessard
(the supervisor)

Photo taken during the banquet at the 19th International
Conference on Composite Materials (ICCM – 19) in
Montreal 2013

Abstract

There is an emerging interest in the aerospace industry to manufacture components with intricate geometries using composites. A candidate material system is termed Randomly-Oriented Strand (ROS) bulk moulding compound and consists of strands of unidirectional carbon/poly-ether-ether-ketone (PEEK) prepreg. This material shows great potential for industrial applications but requires thorough characterization before it can be certified for general aviation. The objective of this thesis is to investigate mechanical properties of ROS composites.

Tensile, compressive and shear properties of ROS composites were measured and recommendations regarding the test protocols were proposed. It was found that properties of ROS composites are influenced by the strand size and that these materials are heterogeneous on the global scale, which is understandable since the strand size is of the same order of magnitude as the prospective part size. Interestingly, tensile, compressive and shear strength had similar magnitudes and exhibited the same failure mechanisms (strand failure or debonding). Hence, the aim of the subsequent modelling efforts was to estimate tensile properties and to explain the governing load transfer and failure mechanisms that are inherent to ROS composites.

Two stochastic modelling techniques were proposed. These models are 2D simplifications of the microstructure that aim to represent the random strand placement in the in-plane or the through-the-thickness orientations. The in-plane model utilizes the classical laminate theory (CLT), Hashin's failure criteria and fracture energies to represent the strand behaviour, and to predict damage evolution in a tensile specimen. Similarly, the through-the-thickness model relies on the CLT and Hashin's criteria to predict strand failure, but also considers the interlaminar strength and fracture toughness to account for strand debonding. Both models capture the heterogeneous nature of the material, and demonstrate that failure is matrix-dominated and follows the "weakest-link" principle. By considering the interlaminar properties it was possible to capture the effect of strand size and to show that thermoplastic ROS composites are superior to their thermoset counterparts. Work performed in this thesis fulfilled its objectives in characterizing mechanical properties and describing the failure mechanisms pertaining to the ROS composites.

Résumé

L'industrie aérospatiale démontre un intérêt grandissant pour les matériaux composites, particulièrement pour la fabrication des pièces à géométrie complexe. Un des candidats les plus prometteur est un matériau constitué de bandes de pré-imprégné orientés aléatoirement (BOA); celles-ci sont composées de fibres de carbones unidirectionnelles pré-imprégnés d'une matrice Polyétherétherkétone (PEEK). Ce matériau démontre un grand potentiel pour des applications industrielles mais nécessite une meilleure caractérisation avant de pouvoir être certifié pour une utilisation dans le domaine aérospatiale. L'objectif de cette thèse est d'examiner les propriétés mécaniques des composites BOA.

Les propriétés en tension, compression et cisaillement des composites BOA ont été mesurées et des recommandations concernant les protocoles d'expérimentation ont été apportés. Il est apparu que les composites BOA sont des matériaux hétérogènes dont les propriétés sont influencées par la taille des bandes. Il est intéressant de noter que les propriétés en tension, compression et cisaillement ont des ordre de grandeur similaires et présentent les mêmes mécanismes de défaillance (rupture des bandes et délamination). Ainsi, le but de la modélisation qui a suivie a été d'estimer les propriétés en traction et d'expliquer les mécanismes régissant le transfert de charge et la rupture intrinsèques aux composites BOA.

Deux techniques de modélisation stochastique ont été proposées. Ces modèles sont des simplifications en 2D de la microstructure et représentent le placement aléatoire des lamelles pour des orientations dans le plan et à travers l'épaisseur. Le modèle dans le plan se base sur la théorie classique des stratifiés (CLT: "the classical laminate theory" en anglais), le critère de rupture de Hashin et les énergies de fracture pour représenter le comportement des bandes et prévoir l'évolution de l'endommagement lors d'un essai en tension. De la même façon, le modèle à travers l'épaisseur repose sur la CLT et le critère de Hashin pour prédire la fracture des lamelles, mais il prend également en considération la force inter-laminaire et la ténacité à la rupture, soit les phénomènes régissant le délaminage des lamelles. Les deux modèles décrivent la nature hétérogène du matériau et démontrent que la rupture est initiée dans la matrice et suit le

principe du "maillon le plus faible". Surtout, en considérant les propriétés inter-laminaires, il a été possible de tenir compte de l'influence de la taille des lamelles pour montrer que les composites BOA à matrice thermoplastique sont de meilleures qualités que leurs équivalents thermodurcissables (époxy).

Dans l'ensemble, le travail effectué dans cette thèse a rempli les objectifs fixés en caractérisant les propriétés mécaniques des composites ROS et en décrivant leurs mécanismes fondamentaux de rupture.

Acknowledgements

My thesis would have not been possible without the support of many people and organizations for which I am very grateful. I am immensely thankful to my supervisor prof. Larry Lessard for providing me with guidance, support, encouragement and kilos of chocolate from the initial to the final stages of my thesis. I would like to extend my acknowledgements to all of my indirect supervisors who provided me with priceless advice and helped to define the course of my research: prof. Pascal Hubert from McGill University and Steven Roy, Ali Yousefpour, Rick Cole, Lolei Khoun and David Boucher from the National Research Council (NRC).

I would also like to express my deepest gratitude to all the technical officers at NRC: Hugo Laurin, François Ferland, Patrick Turnblom, Patrick Gagnon, Chantal Coulombe and Manon Plourde, whose knowledge and assistance were vital to the successful completion of my thesis.

I would like to extend a special thank you to my colleagues on the COMP 412 project: Gilles-Philippe Picher-Martel, Benoit Landry, Dominic LeBlanc and Arthur Levy for all the fruitful discussions that we had. I also want to acknowledge the help of all the undergraduate students that worked with me: Quentin Fabien, Sean Meldrum, Marion Isaaz and Nicholas Gilbert. And of course, I want to thank everyone from Structures and Composite Materials Laboratory at McGill University.

I am also very thankful to the Natural Sciences and Engineering Research Council of Canada (NSERC), Consortium for Research and Innovation in Aerospace in Quebec (CRIAQ), Pratt & Whitney Canada, Bell Helicopter Textron Canada Limited, Bombardier Inc, Hutchinson Aerospace & Industry Ltd., Delastek Inc. and Avior Integrated Products Inc. for financial support. I am greatly appreciative of Zonta International for awarding me with the Amelia Earhart Fellowship.

Most importantly, I wish to express gratitude to my parents, Lioudmila Selezneva and Andrei Seleznev for their much needed motivation, emotional support and endless love.

Table of Contents

ABSTRACT	III
RÉSUMÉ	IV
ACKNOWLEDGEMENTS	VI
TABLE OF CONTENTS	VII
LIST OF FIGURES	XII
LIST OF TABLES.....	XIX
LIST OF ABBREVIATIONS.....	XX
LIST OF SYMBOLS	XXI
CHAPTER 1	1
INTRODUCTION	1
1.1 THERMOSETS VS. THERMOPLASTICS	2
1.2 CONTINUOUS VS. DISCONTINUOUS FIBRES.....	3
1.3 COMPRESSION MOULDING.....	5
1.4 RESEARCH OBJECTIVES AND SCOPE.....	6
1.5 STRUCTURE OF THE THESIS	7
CHAPTER 2	8
LITERATURE REVIEW	8
2.1 EXPERIMENTAL WORK.....	8
2.1.1 <i>Mechanical properties</i>	8
2.1.2 <i>Material heterogeneity</i>	11
2.1.3 <i>Hybridization</i>	16
2.1.4 <i>Design of actual ROS parts</i>	16
2.1.5 <i>Summary of main findings</i>	18
2.2 BASIC ANALYTICAL MODELS FOR DISCONTINUOUS REINFORCEMENT	19
2.2.1 <i>Size effects</i>	19
2.2.1.1 Ellipsoidal inclusions.....	19

2.2.1.2 Cylindrical inclusions	21
2.2.2 <i>Orientation averaging</i>	25
2.2.2.1 Direct averaging	25
2.2.2.2 Pseudo-grain method	26
2.2.3 <i>Evaluation of the basic models</i>	28
2.2.4 <i>Additional considerations</i>	29
2.2.5 <i>Summary of analytical models</i>	34
2.3 FINITE ELEMENT MODELS.....	34
2.3.1 <i>2D models</i>	35
2.3.2 <i>3D models</i>	38
2.3.3 <i>Summary of the FE models</i>	39
2.4 CONCLUDING REMARKS AND THESIS OUTLINE	39
CHAPTER 3	41
MANUFACTURING PROCESS.....	41
3.1 OVERVIEW OF THE MANUFACTURING PROCESS.....	41
3.2 SELECTION OF THE PROCESSING PARAMETERS	42
3.2.1 <i>Panel defects</i>	43
3.2.2 <i>Cause of the problem</i>	46
3.2.3 <i>Reduction of the temperature gradient</i>	48
3.3 WARPAGE	49
3.4 VARIABILITY OF CTE	51
3.5 CONCLUDING REMARKS.....	53
CHAPTER 4	55
TENSILE PROPERTIES	55
4.1 PRELIMINARY TESTS.....	55
4.1.1 <i>Effect of specimen width</i>	56
4.1.2 <i>Effect of strand length and panel thickness</i>	57
4.2 FULL SCALE TESTS.....	59
4.2.1 <i>Procedure</i>	59
4.2.2 <i>Validation</i>	60
4.2.3 <i>Modulus</i>	62
4.2.4 <i>Strength</i>	65

4.2.5 Failure	68
4.2.6 Summary	72
4.3 ADDITIONAL EXPERIMENTS.....	73
4.3.1 Experimental procedure	73
4.3.2 Results and discussion.....	75
4.3.3 Summary.....	79
4.4 CONCLUDING REMARKS.....	79
CHAPTER 5	80
COMPRESSIVE PROPERTIES	80
5.1 EXPERIMENTAL PROCEDURE	80
5.2 EXPERIMENTAL RESULTS	82
5.2.1 Effect of test fixture	82
5.2.2 Checking for buckling	85
5.2.3 Failure modes.....	89
5.2.4 Strength and modulus.....	91
5.3 CONCLUDING REMARKS.....	91
CHAPTER 6	93
SHEAR PROPERTIES	93
6.1 SELECTION OF TEST METHODS.....	93
6.2 IN-PLANE SHEAR	97
6.2.1 Experimental procedure	97
6.2.2 Experimental results	99
6.3 OUT-OF-PLANE SHEAR	104
6.3.1 Preliminary tests	104
6.3.2 Full scale tests	105
6.4 CONCLUDING REMARKS.....	108
CHAPTER 7	110
IN-PLANE MODEL	110
7.1 MODELLING OVERVIEW	110
7.1.1 Steps 1 and 2 Generate random strand layup and partition the specimen	114
7.1.1.1 Assumptions	114

7.1.1.2	Procedure	115
7.1.1.3	Equivalent elastic properties	117
7.1.2	<i>Step 3 – Build a finite element model</i>	119
7.1.2.1	Mesh and partition size	120
7.1.2.2	Failure criteria and damage propagation	122
7.2	RESULTS AND DISCUSSION.....	126
7.2.1	<i>Analytical model (elastic properties)</i>	126
7.2.2	<i>FE model (elastic properties)</i>	129
7.2.3	<i>FE model (failure properties)</i>	131
7.3	CONCLUDING REMARKS AND FUTURE WORK	134
CHAPTER 8	135
THROUGH-THE-THICKNESS MODEL	135
8.1	MODELLING OVERVIEW	135
8.2	STEP 1 - GENERATE MICROSTRUCTURE	137
8.2.1	<i>Assumptions</i>	137
8.2.2	<i>Procedure</i>	139
8.3	STEP 2 - GENERATE PATHS.....	140
8.3.1	<i>Strand failure</i>	140
8.3.2	<i>Strand debonding</i>	144
8.3.2.1	Criterion 1: strength-based	145
8.3.2.2	Criterion 2: toughness-based	147
8.4	STEP 3 - FIND THE SHORTEST PATH	149
8.5	MATERIAL PROPERTIES.....	151
8.5.1	<i>Strength plateau - carbon/PEEK</i>	151
8.5.2	<i>Strength plateau - carbon/epoxy</i>	152
8.6	RESULTS AND DISCUSSION.....	153
8.7	CONCLUDING REMARKS AND FUTURE WORK	159
CHAPTER 9	161
CONCLUSIONS, RECOMMENDATIONS AND FUTURE WORK	161
9.1	CONCLUSIONS: INVESTIGATION OF MECHANICAL PROPERTIES.....	161
9.2	CONCLUSIONS: MODELLING EFFORTS.....	162
9.3	PRACTICAL RECOMMENDATIONS	163

9.4 FUTURE WORK	164
APPENDIX A	166
DIGITAL IMAGE CORRELATION	166
APPENDIX B	171
EXAMPLE OF THE THROUGH-THE-THICKNESS STRENGTH MODEL	171
REFERENCES	175

List of Figures

FIGURE 1-1 – THE USE OF COMPOSITES IN BOEING 787 DREAMLINER AIRFRAME [1].....	2
FIGURE 1-2 – EXAMPLES OF CARBON FIBRE/THERMOPLASTIC PARTS IN AIRBUS A350 XWB [5]	3
FIGURE 1-3 – PROCESSING AND PERFORMANCE OF VARIOUS COMPOSITE MATERIAL SYSTEMS (ADAPTED FROM [11]).....	3
FIGURE 1-4 – SCHEMATIC OF DIFFERENT LONG DISCONTINUOUS FIBRE MATERIAL PREFORMS: A) ALIGNED FIBRES, B) ALIGNED STRANDS, C) RANDOMLY ORIENTED FIBRES AND D) RANDOMLY ORIENTED STRANDS OR FIBRE BUNDLES OF UD TAPE	4
FIGURE 1-5 – COMPLEX NET-SHAPE ROS PARTS MANUFACTURED AT THE STRUCTURES AND COMPOSITE MATERIALS LABORATORY AT MCGILL UNIVERSITY [13].....	4
FIGURE 1-6 – COMPRESSION MOULDING OF A) ROS PART AND B) CF PART WITH DEFECTS [14]	5
FIGURE 1-7 – COMPLEX NET-MOULDED INDUSTRIAL ROS PARTS: A) HINGE MADE BY EGUEMANN [8], B) BRACKET MADE BY GREENE, TWEED [15, 25] AND C) BRACKET MADE BY TENCATE [26]	6
FIGURE 2-1 – TYPICAL MORPHOLOGY ASSOCIATED WITH TENSILE FAILURE: A) PHOTOS OF THE SPECIMEN SURFACE AND EDGE AND B) MICROGRAPHS OF THE EDGE [27].....	9
FIGURE 2-2 – SUMMARY OF TENSILE, COMPRESSIVE AND FLEXURAL A) STRENGTH AND B) MODULUS OF ROS CARBON/EPOXY COMPOSITES [27]. DASHED LINE REPRESENTS TENSILE PROPERTIES OF QI CF LAMINATE	10
FIGURE 2-3 – COMPARISON BETWEEN CARBON/EPOXY AND CARBON/PEEK TENSILE A) MODULUS AND B) STRENGTH [35].....	10
FIGURE 2-4 – C-SCANS AND MICROGRAPHS THAT SHOW DEFECTS, SUCH AS: A) STRAND SWIRLS, B) RESIN RICH AREA AND C) LARGE VOIDS [28]. COLOUR BAR INDICATES THE VARIATION OF THE C-SCAN SIGNAL INTENSITY MEASURED AT THAT CROSS-SECTION; COLOUR BLUE INDICATES PRESENCE OF A POTENTIAL DEFECT	11
FIGURE 2-5 – EVOLUTION OF C-SCANS TAKEN AT DIFFERENT STAGES OF AN INTERRUPTED TENSION TEST. SUBSEQUENT IMAGES CORRESPOND TO A HIGHER LOAD LEVEL REACHED DURING THE TEST AND TRACK THE EVOLUTION OF DAMAGE [28]	12
FIGURE 2-6 – A) TENSILE SPECIMEN EQUIPPED WITH STRAIN GAUGES OF DIFFERENT SIZES AND B) STRAIN CONTOURS VISUALIZED WITH DIC [29]	13
FIGURE 2-7 – STRAIN FIELD ON THE TWO SURFACES OF A DCFT SPECIMEN VISUALIZED WITH DIC [36]	14
FIGURE 2-8 – STRAIN FIELDS THAT DEVELOP IN A) CF AND B) ROS OPEN HOLE SPECIMENS VISUALIZED WITH DIC [37]	15
FIGURE 2-9 – FAILURE OF ROS OPEN HOLE SPECIMENS: EVOLUTION OF A) THE STRAIN FIELD VISUALIZED WITH DIC AND [37] AND B) THE C-SCANS WITH INCREASING LOADING [28]	15
FIGURE 2-10 - SUSPENSION CONTROL ARMS ON LAMBORGHINI <i>SESTO ELEMENTO</i> : A) METAL AND B) COMPOSITE PARTS [7]	17
FIGURE 2-11 – DOOR HINGE FROM EUROCOPTER GERMANY [12] AND ULTIMATE LOADS CARRIED BY HINGES MADE OF DIFFERENT COMPOSITE MATERIAL SYSTEMS [8]	18
FIGURE 2-12 – ESHELBY’S PROBLEM OF AN ELLIPTICAL INCLUSION [45]	20

FIGURE 2-13 – APPROXIMATION OF VARIOUS INCLUSIONS WITH AN ELLIPSOIDAL GEOMETRY [45].....	21
FIGURE 2-14 – STRESSES ACTING ON A DIFFERENTIAL ELEMENT OF A FIBRE [51]	22
FIGURE 2-15 – DISTRIBUTION OF THE MATRIX SHEAR STRESS AND FIBRE AXIAL STRESS ALONG THE FIBRE PREDICTED BY A) KELLY-TYSON AND B) COX [51].....	22
FIGURE 2-16 – THE EFFECT OF FIBRE LENGTH ON A) STRESS DISTRIBUTION ALONG THE FIBRE BASED ON THE KELLY-TYSON MODEL AND B) THE COMPOSITE STRENGTH [51]	23
FIGURE 2-17 – APPLICATION OF THE PSEUDO-GRAIN CONCEPT AND CLT TO RANDOMLY-ORIENTED FIBRES [6, 62].....	27
FIGURE 2-18 – DIRECTIONAL VECTOR P USED IN THE TENSORIAL APPROACH FOR ORIENTATION AVERAGING [45].....	27
FIGURE 2-19 – COMPARISON BETWEEN THE CALCULATED AND THE MEASURED A) STRENGTH AND B) MODULUS AS A FUNCTION OF STRAND LENGTH. EXPERIMENTAL DATA FROM [35]	29
FIGURE 2-20 – THE EFFECT OF DIFFERENT FIBRE ARRANGEMENTS ON THE STRESS PROFILE IN A FIBRE [ADAPTED FROM [65]]	30
FIGURE 2-21 – FAILURE PLANE INTERSECTING FIBRES AT A DIFFERENT LOCATION FROM THEIR ENDS [53]. DISTANCE BETWEEN THE FIBRE END AND THE FAILURE PLANE DETERMINES THE FAILURE MODE BEING FIBRE PULL-OUT OR BREAKAGE	30
FIGURE 2-22 – A) UNIT CELL USED BY PIMENTA TO REPRESENT DISCONTINUOUS STAGGERED INCLUSIONS AND B) THE EFFECT OF OVERLAP LENGTH ON THE COMPOSITE’S STRENGTH, AS DETERMINED BY THE STRENGTH AND TOUGHNESS-BASED CRITERIA [64].....	31
FIGURE 2-23 – A) GEOMETRY OF A SINGLE-LAP JOINT AND B) THE CONCEPT OF STRENGTH PLATEAU FOR JOINT STRENGTH [70]	32
FIGURE 2-24 – MICROSTRUCTURE OF UD LAMINATES WITH SLITS A) VIRGIN STATE AND B) BROKEN STATE [71].....	33
FIGURE 2-25 – PROPAGATION OF DELAMINATION IN A LAMINATE OF COLUMNS [72]	33
FIGURE 2-26 – A) MODEL OF AN ROS COMPOSITES PROPOSED BY [31] IN WHICH A SPECIMEN IS SUBDIVIDED INTO REGIONS WITH DIFFERENT PROPERTIES (SHOWN WITH DIFFERENT COLOURS) AND B) THE RESULTANT STRAIN-FIELD UNDER LOADING (COLOUR MAP CORRESPONDS TO STRAIN VARIABILITY).....	35
FIGURE 2-27 – 2D FE MODEL FOR IN-PLANE PROPERTIES OF DCFP: A) MESH OF THE MATRIX WITH EMBEDDED 1D BEAM ELEMENTS THAT REPRESENT FIBRES, B) APPLICATION OF THE BOUNDARY CONDITIONS USING A HOMOGENEOUS MATERIAL AND C) VON-MISES STRESS CONTOUR PLOTS FOR AN RVE [75, 77].....	36
FIGURE 2-28 – A) MICROGRAPH OF NACRE THAT DEPICTS THE STAGGERED ARRANGEMENT OF REINFORCING PLATELETS AND B) MICROSTRUCTURE CAPTURED BY THE FE MODEL PROPOSED BY [78].....	37
FIGURE 2-29 – DISPLACEMENT CONTOUR PLOT OBTAINED WITH THE NACRE MODEL [78]. THE BLACK LINE SHOWS THE LOCATION OF FINAL FAILURE.....	37
FIGURE 2-30 – RVEs GENERATED USING A) STRAIGHT FIBRES ($V_f = 13.5\%$) AND B) CURVED FIBRES ($V_f = 35\%$) [42].....	38
FIGURE 2-31 - COMBINED MICROMECHANICAL AND STRUCTURAL FRAMEWORK [25, 79].....	39
FIGURE 3-1 - MANUFACTURING PROCESS OF FLAT ROS PANELS.....	42
FIGURE 3-2 – CORRELATION BETWEEN SURFACE DEFECTS AND ULTRASONIC C-SCANS OF ROS PANELS WITH 25 x 6 MM STRANDS	45
FIGURE 3-3 – EFFECT OF PROCESSING CONDITIONS ON TENSILE STRENGTH OF ROS PANELS WITH 25 x 12 MM STRANDS	46

FIGURE 3-4 – A) TEMPERATURE PROFILE MEASURED AT DIFFERENT LOCATIONS IN A PANEL AND B) SCHEMATIC INDICATING TC LOCATIONS	47
FIGURE 3-5 – TEMPERATURE GRADIENT THAT DEVELOPS IN THE COOLING SYSTEM AND IN THE PANEL DURING FAST COOLING.....	47
FIGURE 3-6 – GAP BETWEEN THE MOULD AND THE COLD SIDE OF THE PANEL DUE TO NON-UNIFORM SHRINKAGE	48
FIGURE 3-7 – TEMPERATURE PROFILE IN A PANEL MANUFACTURED WITH THE USE OF PASSIVE DEVICES TO IMPROVE TEMPERATURE UNIFORMITY.....	49
FIGURE 3-8 – SCHEMATIC DEFINITION OF THE D-VALUE USED TO QUANTIFY WARPAGE.....	49
FIGURE 3-9 – WARPED SHAPES OF ROS PANELS WITH 25 x 6 MM STRANDS. PANELS HAVE D-VALUES OF A) 9 AND B) 4	50
FIGURE 3-10 – THE EFFECT OF STRAND SIZE AND PANEL THICKNESS ON WARPAGE	51
FIGURE 3-11 – SAMPLE IN THE TMA APPARATUS.....	52
FIGURE 3-12 – THERMAL EXPANSION CURVES OF UD AND DIFFERENT ROS SAMPLES WITH 25 x 6 MM STRANDS. <i>SP</i> STANDS FOR SPECIMEN NUMBER AND <i>DIR</i> STANDS FOR DIRECTIONS	53
FIGURE 4-1– EFFECT OF SPECIMEN WIDTH ON TENSILE PROPERTIES OF ROS COMPOSITES MADE OF CARBON/PEEK MATERIAL A) USED ONLY FOR PRELIMINARY STUDIES AND B) USED PREDOMINANTLY FOR FULL SCALE TESTS	57
FIGURE 4-2 - THE EFFECT OF STRAND LENGTH AND PANEL THICKNESS ON A) MODULUS AND B) STRENGTH.....	58
FIGURE 4-3 – PAINTED TENSILE SPECIMEN INSTRUMENTED WITH AN EXTENSOMETER.....	60
FIGURE 4-4 – COMPARISON BETWEEN STRESS-STRAIN CURVES MEASURED USING DIC AND AN EXTENSOMETER	60
FIGURE 4-5 – COMPARISON BETWEEN THE DIC FULL-FIELD STRAIN MAPS OF A) QI CF AND B) ROS (6 x 3 MM STRAND) COMPOSITE	62
FIGURE 4-6 - EVOLUTION OF THE STRAIN HISTOGRAMS WITH INCREASING LOADING, WHICH CORRESPOND TO A) ROS AND B) CF SPECIMENS.....	63
FIGURE 4-7 – EFFECT OF STRAND SIZE ON TENSILE MODULUS	63
FIGURE 4-8 – MICROSTRUCTURE OF ROS COMPOSITES WITH A) LONG AND B) SHORT STRANDS	64
FIGURE 4-9 – EFFECT OF STRAND SIZE ON POISSON’S RATIO (NORMALIZED TO QI CF VALUE)	65
FIGURE 4-10 - EFFECT OF STRAND SIZE ON TENSILE STRENGTH.....	66
FIGURE 4-11 – EFFECT OF STRAND SIZE ON DESIGN STRENGTH (ALLOWABLES)	67
FIGURE 4-12 - COMPARISON BETWEEN THE STRESS-STRAIN CURVES OF CF AND ROS SPECIMENS.....	68
FIGURE 4-13 – CRACK PROPAGATION MECHANISM IN ROS COMPOSITES	69
FIGURE 4-14 - FAILURE REGION OF ROS COMPOSITES WITH A) LONG AND B) SHORT STRANDS.....	70
FIGURE 4-15 – EVOLUTION OF THE FULL-FIELD STRAIN WITH LOADING, CORRESPONDING TO ROS COMPOSITES WITH A) SHORT AND B) LONG STRANDS	71
FIGURE 4-16 – STRAIN-FIELD IN A UD SPECIMEN WITH 20 MM OVERLAP	76
FIGURE 4-17 – STRAIN-FIELD IN A UD SPECIMEN WITH 20 MM OVERLAP	76
FIGURE 5-1 – COMPARISON BETWEEN A) COMBINED LOADING AND B) SHEAR LOADING METHODS FOR COMPRESSION TESTING.....	81

FIGURE 5-2 – A) SPECIMEN WITH SG PLACED IN THE COMBINED LOADING FIXTURE AND B) SIGNS OF DAMAGE IN A GRIPPED SECTION AFTER TESTING	83
FIGURE 5-3 – A) SPECIMEN PLACED IN THE HYDRAULIC GRIPS AND B) TWISTING OF THE SPECIMEN DURING LOADING.....	84
FIGURE 5-4 – A) SPECIMEN PLACED IN THE SHEAR LOADING FIXTURE AND B) SPECIMEN WITH BONDED END TABS.....	85
FIGURE 5-5 – A) STRESS-STRAIN CURVES MEASURED BY SG AND DIC AND B) STRAIN-FIELD CAPTURED WITH DIC CORRESPONDING TO A QI CF SPECIMEN	86
FIGURE 5-6 – A) STRESS-STRAIN CURVES MEASURED BY SG AND DIC AND B) STRAIN-FIELD CAPTURED WITH DIC CORRESPONDING TO A SHORT-STRAND ROS SPECIMEN	87
FIGURE 5-7 – A) STRESS-STRAIN CURVES MEASURED BY SG AND DIC WHILE USING A SMALLER GAUGE SECTION AND B) STRAIN-FIELD CAPTURED WITH DIC CORRESPONDING TO A SHORT-STRAND ROS SPECIMEN	87
FIGURE 5-8 – A) STRESS-STRAIN CURVES MEASURED BY SG AND DIC AND B) STRAIN-FIELD CAPTURED WITH DIC CORRESPONDING TO A LONG-STRAND ROS SPECIMEN.....	88
FIGURE 5-9 – OUT-OF-PLANE DISPLACEMENT OF AN ROS SPECIMEN WITH A A) 12 MM AND B) 25 MM GAUGE SECTION CAPTURED WITH DIC.....	89
FIGURE 5-10 – FAILURE MODES OF THIN AND THICK ROS COMPOSITES. GAUGE SECTION IS IDENTIFIED WITH A RED RECTANGLE.....	90
FIGURE 5-11 – EFFECT OF STRAND SIZE ON COMPRESSIVE A) MODULUS AND B) STRENGTH OF ROS PANELS	92
FIGURE 6-1 – A) MATERIAL COORDINATE PLANE AND DEFINITION OF SHEAR STRESSES, AND B) IN-PLANE STRESSES AND C) OUT-OF-PLANE STRESSES IN ROS COMPOSITES.....	94
FIGURE 6-2 – TEST METHODS FOR IN-PLANE SHEAR PROPERTIES: A) 2-RAIL AND 3-RAIL, AND B) V-NOTCH AND V-NOTCH RAIL	95
FIGURE 6-3 – TEST METHODS FOR OUT-OF-PLANE SHEAR PROPERTIES: A) V-NOTCH, B) SHORT BEAM AND C) DOUBLE-NOTCH.....	95
FIGURE 6-4 – FAILURE MODE OF SBS ROS SPECIMENS.....	97
FIGURE 6-5 – V-NOTCH RAIL: A) PAINTED SPECIMEN AND B) CLAMPED SPECIMEN IN THE FIXTURE.....	98
FIGURE 6-6 – SHEAR STRAIN FIELD AND FAILURE REGION OF A) UD CF, B) QI CF AND C) ROS SPECIMENS.....	100
FIGURE 6-7 – EFFECT OF STRAND SIZE ON IN-PLANE SHEAR A) MODULUS AND B) STRENGTH OF ROS PANELS	101
FIGURE 6-8 – COMPARISON BETWEEN THE STRESS-STRAIN CURVES OF CF AND ROS SPECIMENS.....	102
FIGURE 6-9 – EFFECT OF STRAND SIZE ON TENSILE, COMPRESSION AND SHEAR PROPERTIES OF ROS COMPOSITES.....	103
FIGURE 6-10 – DNS SPECIMEN WITH A SUPPORT JIG	104
FIGURE 6-11 – COMPARISON BETWEEN FAILURE MODES OF DNS SPECIMENS WITH 6 MM AND 12 MM DISTANCES BETWEEN THE NOTCHES	105
FIGURE 6-12 – EFFECT OF STRAND SIZE ON OUT-OF-PLANE STRENGTH OF ROS PANELS	106
FIGURE 6-13 – FAILURE MODES OF DNS UD AND ROS SPECIMENS WITH 6, 25 AND 50 MM LONG STRANDS	107
FIGURE 6-14 – COMPARISON BETWEEN OUT-OF-PLANE STRENGTH MEASURED WITH SBS AND DNS METHODS	108
FIGURE 6-15 – A) PART WITH A RIB FEATURE, B) T-SHAPE COMPONENT TEST FIXTURE AND C) MICROSTRUCTURE OF THE RIB ROOT [13]	109

FIGURE 7-1 - MODEL OF AN ROS COMPOSITE PROPOSED BY FERABOLI IN WHICH A SPECIMEN IS SUBDIVIDED INTO REGIONS WITH DIFFERENT PROPERTIES (SHOWN WITH DIFFERENT COLOURS) AND THE RESULTANT STRAIN-FIELD UNDER LOADING (COLOUR MAP CORRESPONDS TO STRAIN VARIABILITY). THESE IMAGES WERE ADAPTED FROM [31]	111
FIGURE 7-2 – METHOD FOR DETERMINING SPATIAL DENSITY VARIABILITY IN AN OSB PANEL (ADAPTED FROM [89])	112
FIGURE 7-3 - OVERVIEW OF THE MODELLING STRUCTURE	113
FIGURE 7-4 – MICROSTRUCTURE OF A) SHORT AND B) LONG STRAND ROS SPECIMENS	115
FIGURE 7-5 - STRAND GENERATION ALGORITHM.....	116
FIGURE 7-6 - VARIABILITY IN THE NUMBER OF LAYERS AMONG PARTITIONS IN 2.5 MM THICK SIMULATED ROS COMPOSITE.....	117
FIGURE 7-7 - BOUNDARY CONDITIONS IMPOSED ON THE SIMULATED TENSILE SPECIMEN. X AND Y REFER TO LONGITUDINAL AND TRANSVERSE DIRECTIONS, AND U REPRESENTS DISPLACEMENT	120
FIGURE 7-8 – DAMAGE STATE OF SIMULATED TENSILE SPECIMENS AT THE TIME OF FAILURE.....	121
FIGURE 7-9 – EFFECT OF PARTITION SIZE ON PREDICTED STRENGTH	121
FIGURE 7-10 – STRESS-DISPLACEMENT RELATIONSHIP FOR EACH DAMAGE MODE.....	124
FIGURE 7-11 – EFFECT OF FRACTURE ENERGY ON THE STRESS-STRAIN CURVE OF $[0/\pm 60]_{3S}$ LAMINATE. STRESS VALUES ARE NORMALIZED WITH RESPECT TO THE FAILURE LOAD OBTAINED EXPERIMENTALLY.	125
FIGURE 7-12 – CONVERGENCE OF THE STRESS VALUES TO FAILURE STRENGTH. STRESS VALUES ARE NORMALIZED WITH RESPECT TO THE FAILURE LOAD.....	126
FIGURE 7-13 – VARIABILITY OF THE LOCAL A) TENSILE AND B) SHEAR MODULUS IN 2.5 MM THICK DISCRETIZED SPECIMEN WITH 25 x 6 MM STRANDS. RECTANGLE IN (A) REPRESENTS SIZE OF A TENSILE SPECIMEN	127
FIGURE 7-14 – COMPARISON BETWEEN EXPERIMENTAL AND MODELLING RESULTS FOR TENSILE MODULUS OF A 2.5 MM THICK ROS PANEL WITH 25 x 6 MM STRANDS. RESULTS ARE NORMALIZED BASED ON THE STRENGTH OF QI CF LAMINATES.....	128
FIGURE 7-15 – VARIABILITY OF THE COEFFICIENT OF THERMAL EXPANSION (CTE) IN AN ROS PANEL.....	128
FIGURE 7-16 - EVOLUTION OF THE STRAIN-FIELD CAPTURED WITH A) DIC AND B) FE MODEL. STRESS VALUES ARE NORMALIZED WITH RESPECT TO THE FAILURE LOAD.....	130
FIGURE 7-17 - THE EFFECT OF STRAND LENGTH ON MODULUS. ERROR BARS SHOW THE STANDARD DEVIATION	130
FIGURE 7-18 - THE EFFECT OF STRAND LENGTH ON STRENGTH. ERROR BARS SHOW THE STANDARD DEVIATION	132
FIGURE 7-19 - PROGRESSIVE FAILURE DEPICTED BY HASHIN’S A) MATRIX TENSION AND B) FIBRE TENSION FAILURE CRITERIA, WHERE THE VALUE OF “1” SIGNIFIES FAILURE. STRESS VALUES ARE NORMALIZED WITH RESPECT TO THE FAILURE LOAD.....	133
FIGURE 8-1 – A) MICROSTRUCTURE AND B) FAILURE MECHANISM OF NACRE [96].....	136
FIGURE 8-2 – OVERVIEW OF THE MODELLING STRUCTURE	137
FIGURE 8-3 – COMPARISON BETWEEN A) ACTUAL AND B) MODELLED MICROSTRUCTURE	138
FIGURE 8-4 – DEFINITION OF THE EFFECTIVE LENGTH.....	139
FIGURE 8-5 – COMPARISON BETWEEN THE MODELLED MICROSTRUCTURE OF A) SHORT (6 x 3 MM) AND B) LONG (50 x 12 MM) STRAND ROS SPECIMENS. THESE SPECIMENS ARE 150 MM LONG AND 2.5 MM THICK.....	140

FIGURE 8-6 – EFFECT OF LAYUP VARIABILITY ON STRENGTH OF A PARTICULAR STRAND.....	143
FIGURE 8-7 – EFFECT OF ORIENTATION ON STRAND STRENGTH	143
FIGURE 8-8 – COMPARISON BETWEEN STRAND OVERLAP AND JOINT OVERLAP	144
FIGURE 8-9 – EFFECT OF THE OVERLAP LENGTH ON THE COMPOSITE’S STRENGTH, AS DETERMINED BY THE STRENGTH-BASED AND TOUGHNESS-BASED CRITERIA [64]	145
FIGURE 8-10 – EVOLUTION OF SHEAR STRESS IN A JOINT WITH INCREASING LOADING A) \rightarrow C), ASSUMING ELASTO-PLASTIC BEHAVIOUR OF THE ADHESIVE (ADAPTED FROM [70])	146
FIGURE 8-11 – EFFECT OF DEBONDING ON SHEAR STRESS DISTRIBUTION IN A LONG JOINT (ADAPTED FROM [70]).....	147
FIGURE 8-12 – A) MODELLED MICROSTRUCTURE AND B) GRAPH SCHEMATIC THAT SHOWS LINKS RELATED TO STRAND DELAMINATION ..	149
FIGURE 8-13 – A) MODELLED MICROSTRUCTURE AND B) GRAPH SCHEMATIC THAT SHOWS LINKS RELATED TO STRAND FAILURE	150
FIGURE 8-14 – VARIABILITY OF THE STRENGTH DATA. ERROR BARS ARE PLOTTED AS VERTICAL LINES WITHOUT CAPS	153
FIGURE 8-15 - COMPARISON BETWEEN EXPERIMENTAL AND MODELLED (CLT VS. TSAI-HILL) STRENGTH DATA. ABBREVIATIONS SBS AND DNS STAND FOR SHORT-BEAM SHEAR AND DOUBLE-NOTCH SHEAR TEST METHODS AND REPRESENT MATRIX SHEAR STRENGTH THAT WAS USED IN THE MODEL (100 OR 64 MPa)	154
FIGURE 8-16 - VARIABILITY OF STRENGTH OBSERVED IN A) EXPERIMENTAL AND B) MODELLED DATA OF THIN (2.5 MM) ROS COMPOSITES. ABBREVIATIONS SBS AND DNS STAND FOR SHORT-BEAM SHEAR AND DOUBLE-NOTCH SHEAR TEST METHODS AND REPRESENT MATRIX SHEAR STRENGTH THAT WAS USED IN THE MODEL (100 OR 64 MPa). ERROR BARS ARE PLOTTED AS VERTICAL LINES WITHOUT CAPS	155
FIGURE 8-17 - COMPARISON BETWEEN STRENGTH OF THIN (2.5 MM) AND THICK (6 MM) ROS COMPOSITES. ABBREVIATIONS SBS AND DNS STAND FOR SHORT-BEAM SHEAR AND DOUBLE-NOTCH SHEAR TEST METHODS AND REPRESENT MATRIX SHEAR STRENGTH THAT WAS USED IN THE MODEL (100 OR 64 MPa)	156
FIGURE 8-18 – VARIABILITY OF STRENGTH OBSERVED IN A) EXPERIMENTAL AND B) MODELLED DATA OF THICK (6 MM) ROS COMPOSITES. ABBREVIATION DNS STANDS FOR DOUBLE-NOTCH SHEAR TEST METHODS AND REPRESENT MATRIX SHEAR STRENGTH THAT WAS USED IN THE MODEL (64 MPa). ERROR BARS ARE PLOTTED AS VERTICAL LINES WITHOUT CAPS.....	156
FIGURE 8-19 – COMPARISON BETWEEN STRENGTH OF THERMOSET AND THERMOPLASTIC-BASED ROS COMPOSITES. ABBREVIATION SBS STANDS FOR SHORT-BEAM SHEAR TEST METHOD AND REPRESENT MATRIX SHEAR STRENGTH THAT WAS USED IN THE MODEL (100 MPa).....	157
FIGURE 8-20 – EXAMPLES OF DIFFERENT FAILURE MORPHOLOGIES OBTAINED WITH MODELLING AND TESTING OF ROS COMPOSITES WITH 6 X 3 MM STRANDS	158
FIGURE 8-21 – COMPARISON BETWEEN THE OLDER (BASIC) ANALYTICAL MODELS, THE CURRENTLY PROPOSED MODEL AND THE EXPERIMENTAL STRENGTH DATA FOR ROS COMPOSITES. EXPLANATION OF THE ANALYTICAL MODELS USED TO GENERATE THIS GRAPH CAN BE FOUND IN CHAPTER 2	159
FIGURE 8-22 – 3D REPRESENTATION OF THE MICROSTRUCTURE AND FAILURE PATH: A) ACTUAL AND B) MODELLED	160
FIGURE A-1 – REFERENCE IMAGE USED FOR DIC AS IT APPEARS A) ON THE SCREEN AND B) IN THE MEMORY [101, 102]	167

FIGURE A-2 - DEFORMED IMAGE USED FOR DIC AS IT APPEARS A) ON THE SCREEN AND B) IN THE MEMORY [101, 102]	167
FIGURE A-3 - DEFORMED IMAGE USED FOR DIC AS IT APPEARS A) ON THE SCREEN AND B) IN THE MEMORY. SUB-PIXEL DISPLACEMENT CREATES GREY (50) AREAS IN THE IMAGE THAT WAS ORIGINALLY BLACK (0) AND WHITE (100) [101, 102]	168
FIGURE A-4 – REFERENCE AND DEFORMED IMAGE WITH NON-SQUARE SUBSET [101]	168
FIGURE A-5 – SPECKLE PATTERN DISCRETIZED INTO SUBSETS	168
FIGURE A-6 – DIFFERENT SPECKLE PATTERNS WITH SPECKLES BEING A) THE OPTIMAL SIZE, B) SLIGHTLY BIGGER AND C) TOO SMALL [100].	169
FIGURE B-1 – A) MODELLED MICROSTRUCTURE AND B) SUMMARY OF STRAND ORIENTATIONS.....	171
FIGURE B-2 – A) LENGTHWISE VARIABILITY OF LAMINATES FORMED BY STRANDS AND B) AVERAGE STRENGTH OF EACH STRAND IN [MPa]	172
FIGURE B-3 – A) STRAND LENGTHS (WHICH ARE REPRESENTATIVE OF THEIR STRENGTHS) AND B) OVERLAP LENGTHS IN [MM].....	173
FIGURE B-4 – GRAPHICAL REPRESENTATION OF THE FAILURE NETWORK: A) DELAMINATION PATHS AND B) DELAMINATION AND STRAND FAILURE PATHS.....	174
FIGURE B-5 – FAILURE PATH OF THE MODELLED MICROSTRUCTURE	174
FIGURE B-6 – VISUALIZATION OF DIFFERENT POSSIBLE FAILURE PATHS AND THEIR RELATIVE LENGTHS (OR STRENGTHS)	174

List of Tables

TABLE 3-1 – SUMMARY OF ALL TEST CASES.....	42
TABLE 3-2 – EFFECT OF PRESSURE AND COOLING RATE ON SURFACE QUALITY OF ROS PANELS (WITH 25 X 12 MM STRANDS)	44
TABLE 4-1 – SUMMARY OF DIFFERENT OVERLAP CONFIGURATIONS THAT WERE TESTED	74
TABLE 4-2– SUMMARY OF MEASURED AND CALCULATED STRENGTH DATA AND FAILURE MORPHOLOGIES OF THE SLIT PANELS	78
TABLE 7-1 - MECHANICAL AND MATERIAL PROPERTIES OF CARBON/PEEK PLIES. MECHANICAL PROPERTIES WERE TAKEN FROM THE DATASHEET PROVIDED BY THE MANUFACTURER [83] AND THERMAL PROPERTIES WERE TAKEN FROM THE LITERATURE [80]; * OUT-OF-PLANE SHEAR MODULUS WAS CALCULATED BASED ON THE TRANSVERSE ISOTROPIC ASSUMPTION; AND ** TRANSVERSE TENSILE AND COMPRESSIVE STRENGTHS WERE ASSUMED TO BE THE SAME	125
TABLE 7-2 – FRACTURE ENERGIES USED TO MODEL FAILURE OF CARBON/PEEK.	125
TABLE 8-1 - PROPERTIES OF CARBON/PEEK AND CARBON/EPOXY LAMINATES [13, 22, 83, 98, 99]. ABBREVIATIONS SBS AND DNS STAND FOR SHORT-BEAM SHEAR AND DOUBLE-NOTCH SHEAR	151

List of Abbreviations

ASTM	American Society for Testing and Materials
CF	Continuous-fibre
CLT	Classical laminate theory
CMM	Coordinate measurement machine
CRIAQ	Consortium for Research and Innovation in Aerospace in Quebec
CTE	Coefficient of thermal expansion
DCFP	Direct carbon fibre preforming
DIC	Digital image correlation
DNS	Double-notch shear
FE	Finite element
GLARE	Glass laminate aluminium reinforced epoxy
LVDT	Linear variable displacement transducer
NRC	National Research Council
NSERC	Natural Sciences and Engineering Research Council of Canada
OSB	Oriented strandboard
PEEK	Poly-ether-ether-ketone
QI	Quasi-isotropic
ROM	Rule of mixtures
ROS	Randomly oriented strand(s)
RVE	Representative volume element
SBS	Short beam shear
SG	Strain gauges
TMA	Thermal mechanical analyzer
TC	Thermocouple
UD	Unidirectional

List of Symbols

Latin symbols

A_S	Strain-concentration factor
A, B, D	Components of laminate stiffness matrix
a, b, d	Components of laminate compliance matrix
a_n	Proportion of fibres with the off-axis orientation angle θ_n
B_i	Invariants
C, C_{ijkl}	Stiffness matrix
C_C, C_I, C_M	Stiffness matrix (composite, inclusion and matrix)
C_d	Stiffness matrix with damage
D	Diameter of the resin cylinder encapsulating a fibre
D-value	Degree of warpage
d	Fibre diameter
d_f, d_m, d_s	Damage variables (fibre, matrix and shear damage)
E_c, E_f, E_m, E_b	Tensile modulus (composite, fibre, matrix and platelet (or strand))
E_1, E_2	Tensile modulus (longitudinal and transverse)
E_{QI}	Tensile modulus of quasi-isotropic laminates
F	Constants of Hashin's failure criteria
G	Fracture energy
G_{12}, G_{23}	Shear modulus (in-plane and out-of-plane)
G_m	Shear modulus of the matrix
$G_{IIc, IL}$	Critical mode-II fracture toughness
I	Identity matrix
L	Fibre length (also strand or inclusion length)
L_{cr}	Critical length
L_{eff}	Effective length
L_{lim}	Limit length corresponding to the strength plateau

L_{short}	Length of the shortest failure path
L_o	Overlap length
M	Moment resultants
M^T	Thermal moment resultants
N	Stress resultants
N^T	Thermal stress resultants
n	Number of overlaps
\mathbf{p}	Unit directional vector
Q_{xyz}, Q_{126}	Stiffness matrix (on-axis and off-axis)
R	Strength ratio between stress in the material and its strength
R_{min}	Smallest strength ratio
S	Eshelby tensor
SE	Strain-energy of the adhesive
s	Standard deviation
T	Transformation matrix
t, t_a, t_b	Thickness (laminate, adhesive and platelet (or strand, ply or ply-block))
u	Horizontal displacement
V_f	Volume fraction of fibres
V_r	Volume fraction of each pseudo-grain
v	Vertical displacement
W	Strand width
x, y, z	Coordinates along the X, Y and Z axis

Greek symbols

$\alpha_{\text{sys}} (\alpha_x, \alpha_y, \alpha_s)$	On-axis coefficient of thermal expansion (longitudinal, transverse and shear)
$\alpha_{126} (\alpha_1, \alpha_2, \alpha_6)$	Off-axis coefficient of thermal expansion (longitudinal, transverse and shear)
β	Cox's parameter
γ	Engineering shear strain
γ_{max}	Failure shear strain
ΔT	Change in temperature

δ_{eq}	Equivalent displacement
δ_{ij}	Kronecker delta
$\epsilon_{xys}, \epsilon_{126}$	Strain components (on-axis and off-axis)
ϵ^*	Stress-free strain
$\{\epsilon_{xys}\}^T$	Stress-free thermal strain
$\{\epsilon_{126}\}_o$	Equivalent laminate thermal strains
θ	In-plane orientation angle
κ	Laminate curvature
$\lambda_{ij}, \lambda_{ijkl}$	Orientation tensors
ν_{12}, ν_{23}	Poisson's ratio (in-plane and out-of-plane)
σ	Normal stress
$\sigma_{xyz}, \sigma_{126}$	Stress components (on-axis and off-axis)
$\sigma_c, \sigma_f, \sigma_m, \sigma_s, \sigma_{ROS}$	Tensile strength (composite, fibre, matrix, strand and ROS specimen)
σ_L^T, σ_T^T	Tensile strength (longitudinal and transverse)
σ_L^C, σ_T^C	Compressive strength (longitudinal and transverse)
σ_S^L, σ_S^T	Shear strength (longitudinal and transverse)
σ_{max}	Maximum stress at the centre of the fibre
τ	Shear stress
τ_i	Interlaminar shear strength
ϕ	Out-of-plane orientation angle
\mathcal{X}_L	Length efficiency
\mathcal{X}_O	Orientation efficiency
ψ	Probability associated with angles θ and ϕ

Chapter 1

Introduction

Developments in the aerospace industry are largely driven by the demand to reduce fuel consumption and effectively lower operational costs. From the structural point of view, fuel consumption is directly related to the weight of the aircraft, and one way of reducing the weight is by using composite materials that possess high strength-to-weight properties. By definition, composite materials consist of two or more distinct materials or phases on a macroscopic level, which when combined together offer better performance than the individual constituents would. Their utilization in the aerospace industry has increased in recent years and is exemplified by the development of the Boeing 787 Dreamliner which uses composites for half of its airframe, as is shown in Figure 1-1 [1]. This design offers a 20 % weight saving in comparison to a conventional aluminum approach.

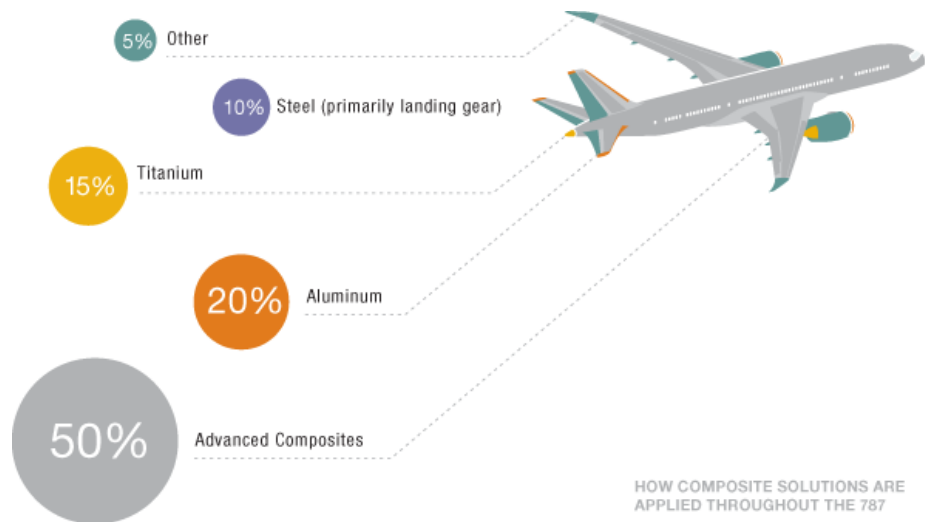


Figure 1-1 – The use of composites in Boeing 787 Dreamliner airframe [1]

1.1 Thermosets vs. thermoplastics

Aerospace grade composite materials consist of carbon fibres which act as a strong reinforcement phase and a thermosetting or thermoplastic resin which binds the fibres together. The first generation composite materials were predominantly comprised of thermosetting resins. The main distinction between the two resin systems is that the former develops permanent covalent bonds (cross-linking) during cure, whereas the latter forms links or crystals that are thermally reversible upon melting [2]. As a result, thermoplastic materials can be re-melted and re-moulded numerous times, which implies that thermoplastic components can potentially be repaired and joined by welding, and recycled at the end of their lifespan [3, 4]. Since thermoplastics do not undergo cure, their shelf life is unlimited and processing times are short, on the order of minutes vs. hours in comparison to thermosets [3]. This significantly reduces manufacturing cost and time; for instance, long and expensive autoclave cure cycles are avoided. Moreover, thermoplastic materials have higher toughness, impact strength and service temperatures than thermosetting materials [2, 4]. Overall, thermoplastic composites offer superior properties, production cost reduction and material recyclability. For these reasons, interest in thermoplastic materials had significantly increased. In fact, design of a new Airbus A350 XWB includes thousands of small thermoplastic parts, which are shown in Figure 1-2 [5].

These parts became a cost effective replacement for their metallic counterparts due to the evolution of highly efficient automated processes [5].

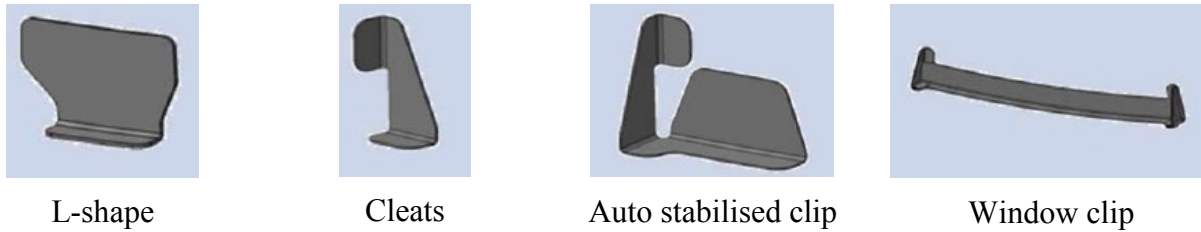


Figure 1-2 – Examples of carbon fibre/thermoplastic parts in Airbus A350 XWB [5]

1.2 Continuous vs. discontinuous fibres

Current applications of thermoplastic composites in aerospace structures are limited to simple components with minimal curvature and thickness variations. This limitation exists because continuous fibre (CF) composites, while exhibiting excellent mechanical performance, are difficult to form. Yet, there is significant interest from the aerospace industry in making more versatile and complex structural shapes. The automotive industry can produce parts with intricate features (e.g. ribs) made from flow moulding compounds, but their mechanical properties are too low for aerospace applications. A literature survey [6-10] showed that preforms with long discontinuous fibres and high fibre volume fractions ($V_f > 40\%$) are appealing for structural applications as they bridge the gap between the lack of formability of continuous fibre composites and the lack of performance of short fibre composites, as shown in Figure 1-3.

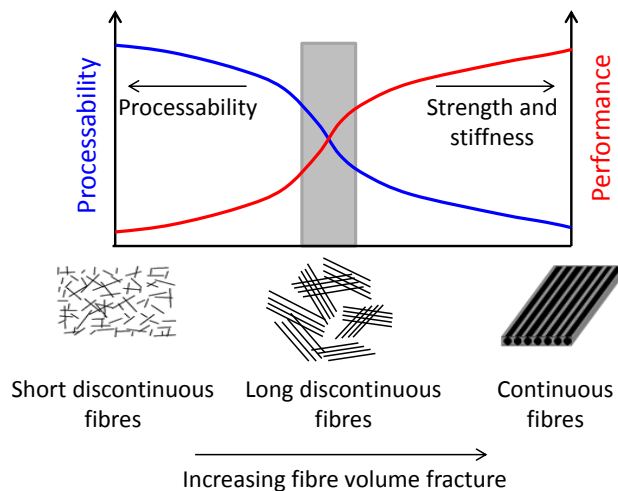


Figure 1-3 – Processing and performance of various composite material systems (adapted from [11])

Overall, different long discontinuous fibres material systems that were developed and studied over the years can be categorized based on fibre orientation (aligned vs. random) and arrangement (individual fibres vs. bundles or strands of fibres) as shown in Figure 1-4. Of particular interest is a new material system which consist of randomly oriented strands (ROS) or chips of aligned unidirectional fibres, which have V_f of 60 %. Various ROS net-shape parts with thickness gradients, ribs and moulded-in holes were manufactured by compression moulding at McGill University, as shown in Figure 1-5. ROS composites were shown to be competitive with metals for application in complex parts due to their corrosion resistance, light weight, cost-effective manufacturing methods and low waste, since parts are moulded net-shape and no post-machining is required [12].

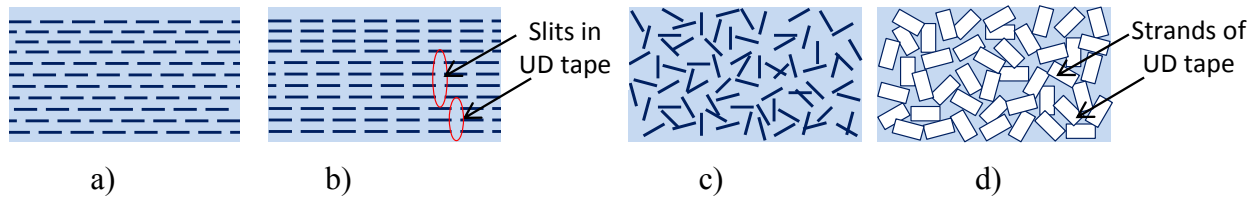


Figure 1-4 – Schematic of different long discontinuous fibre material preforms: a) aligned fibres, b) aligned strands, c) randomly oriented fibres and d) randomly oriented strands or fibre bundles of UD tape

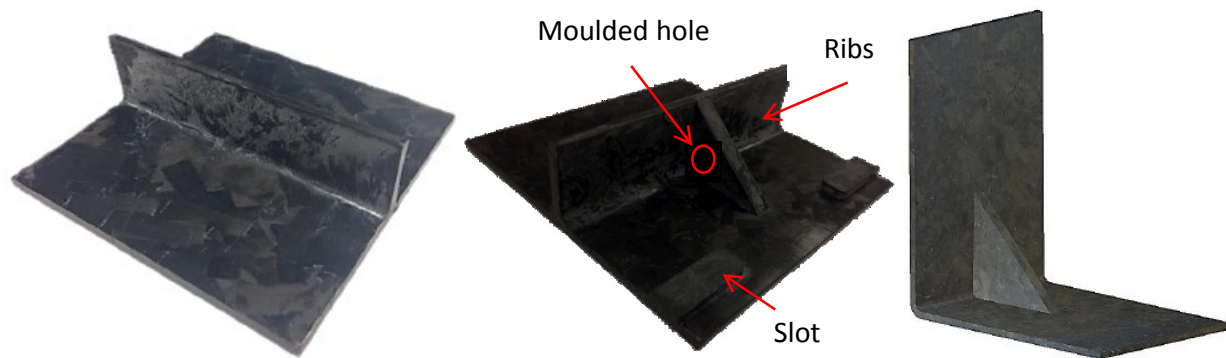


Figure 1-5 – Complex net-shape ROS parts manufactured at the Structures and Composite Materials Laboratory at McGill University [13]

1.3 Compression moulding

Compression moulding is a frequently-used technique for forming of thermoplastic composites, because required equipment is often already available in the industrial setting. For instance, presses that are used for metal forming can be easily adapted for moulding of thermoplastics. The general process involves placement of a preheated preform between two dies and closing the mould while applying temperature and pressure. Matched-die moulding involves the use of two shaped dies, which are usually made of steel, as shown in Figure 1-6. Figure 1-6 also shows finished 3D shapes made using CF and ROS preforms. Defects such as wrinkles are clearly visible in the CF part, while the ROS part is defect free. The CF part was also more time consuming to layup, whereas strands were just dropped into the mould cavity.

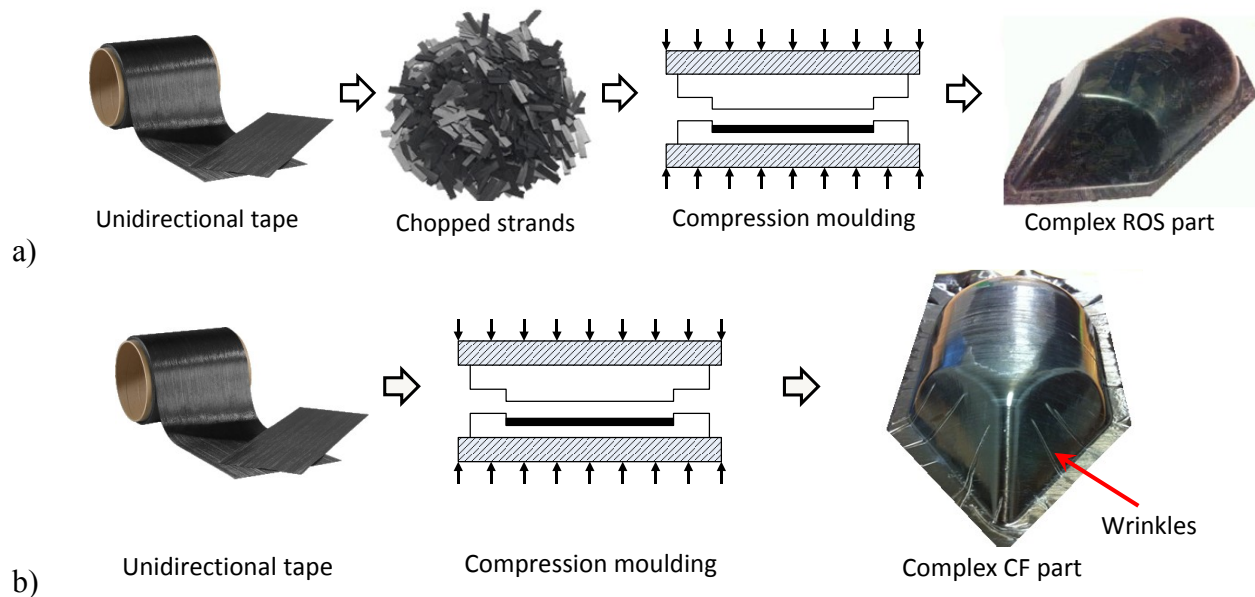


Figure 1-6 – Compression moulding of a) ROS part and b) CF part with defects [14]

Strands used to make ROS composites are available commercially as a bulk moulding compound from material suppliers, such as Hexcel (HexMCTM with thermoset matrix) and TenCate (Cetex® MC1200 with thermoplastic matrix). The feasibility of moulding complex components from ROS composites has been demonstrated by Greene, Tweed [15], Cross Composite AG [8], Feraboli [7] and TenCate [16] with examples of industrial parts shown in Figure 1-7. The general behaviour of ROS composites has been investigated and is explained in the literature, but the available data does not entail all the mechanical properties in particular for thermoplastic-based

composites. Moreover, no strength models exist for ROS composites, at least in the public domain. Further research is required to fill the gaps in the available knowledge before the use of these composites can become widespread. Research presented in this dissertation is part of multi-disciplinary and multi-partner CRIAQ (The Consortium for Research and Innovation in Aerospace in Québec) project [14, 17-24] being conducted to systematically evaluate, characterize and model the moulding process and mechanical properties of composites manufactured from carbon/polyether-ether-ketone (PEEK) ROS.



Figure 1-7 – Complex net-moulded industrial ROS parts: a) hinge made by Eguemann [8], b) bracket made by Greene, Tweed [15, 25] and c) bracket made by TenCate [26]

1.4 Research objectives and scope

The focus of this dissertation is on investigation of mechanical properties of ROS composites. The objectives of this thesis are threefold: (i) to measure and quantify properties of ROS composites, (ii) to explain the fundamental load transfer and sharing mechanisms that occur between the neighbouring strands and that govern mechanical behaviour of the material and (iii) to develop a modelling technique for calculation of strength and stiffness of these materials using the properties of unidirectional prepreg. Finally, the goal is to make practical recommendations regarding material selection, test methodologies and design considerations in relation to industrial applications of ROS composites.

1.5 Structure of the thesis

Following this introduction, a literature review on the topic of ROS composites is presented, and connections are drawn between the current state of knowledge in the open literature and the work done as a part of this thesis aiming to enrich it. The main body of this thesis covers two major components of this work, which are the experimental and the modelling contributions. First, the manufacturing process is discussed and the effect of processing conditions on part quality is touched upon (Chapter 3). Next chapters cover experimental work that was performed to characterize mechanical properties of ROS composites, which include tension (Chapter 4), compression (Chapter 5) and shear (Chapter 6). Chapter 6, being the last experimental chapter, includes a summary section that compares tensile, compressive and shear properties of ROS composites and highlights the main trends and behaviours that are typical of this material system. This section acts as a transition between the experimental and the modelling work as it defines the modelling requirements based on the test data. Two modelling approaches for calculation of strength and stiffness of ROS composites are proposed and evaluated. The development of these techniques and results obtained through them are summarized in Chapters 7 and 8. This dissertation ends with the summary of main results and contributions, as well as recommendations for future work (Chapter 9). Supplementary material is included in the Appendices.

Chapter 2

Literature review

There are a limited number of papers on the topic of mechanical properties of randomly-oriented strand (ROS) composites, even though the more general topic of discontinuous-fibre composites has been widely investigated. For this reason, the scope of the literature review was set to include papers on composites that have similar reinforcement shape (strands or platelets), fibre length ($L > 5$ mm) and fibre volume fraction ($V_f > 40\%$) as being in the category of ROS composites. This literature review is divided into two main sections: (i) experimental investigations and (ii) modelling efforts. Concluding remarks will be made at the end of this chapter to summarize knowledge that is available in the literature and explain how the work presented in this thesis will complement the existing publications.

2.1 Experimental work

2.1.1 Mechanical properties

Feraboli *et al.* [27-31] conducted a comprehensive study into the properties of carbon/epoxy ROS composites. They tested specimens cut at 0° , 45° and 90° angles with respect to the panel axis and demonstrated that ROS composites are quasi-isotropic (QI) [27]. Hence, in-plane response of ROS composites to loading is directionally independent, and analysis of their

properties can benefit from simplifications associated with isotropic materials (e.g. number of elastic constants required to describe the material is reduced). They also evaluated the effect of strand size and panel thickness on the tensile, compressive and flexural properties of the material [27]. Failure was found to be a matrix dominated event accompanied by transverse strand cracking, longitudinal strand splitting and strand debonding. Little or no fibre failure was observed. Typical failure regions are shown in Figure 2-1. Failure spread through the weakest path and was frequently redirected in the longitudinal and transverse directions. It is also noteworthy that damage propagation seemed to be unaffected by microstructural defects, such as voids and resin rich areas. Authors attributed this behaviour to complex interaction between strands [27].

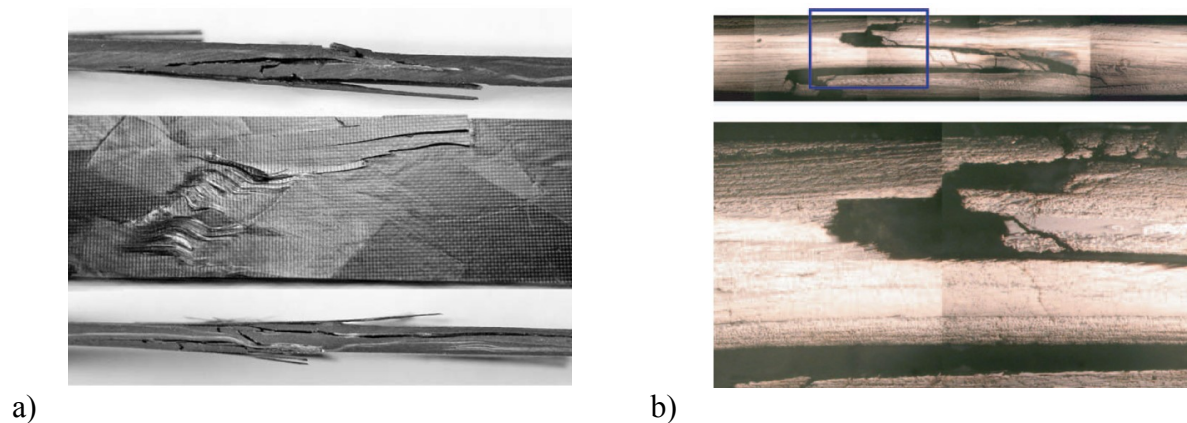
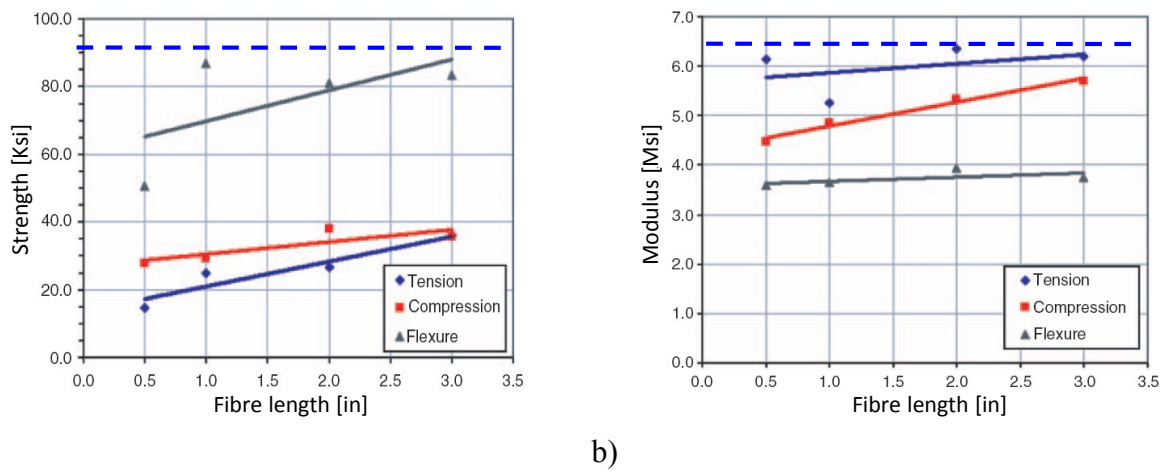


Figure 2-1 – Typical morphology associated with tensile failure: a) photos of the specimen surface and edge and b) micrographs of the edge [27]

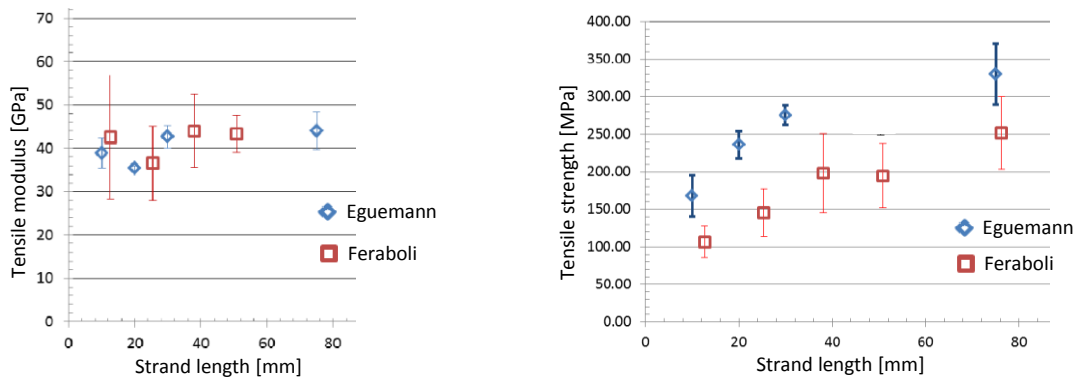
Mechanical properties measured by Feraboli *et al.* [27] are summarized in Figure 2-2. Interestingly, compressive strength of ROS composites is higher than tensile strength, while the contrary is true with continuous-fibre (CF) laminates. The same trend was reported by other authors [6, 32-34]. Overall, strength increased with longer strand length (12.5 vs. 75 mm) and larger panel thickness (2 vs. 6 mm) but was significantly lower than that of QI CF composites. Modulus showed little dependence on the aspect ratio and was essentially as high as that of QI CF laminates.

Eguémann *et al.* [35] investigated the effect of strand length on tensile properties of carbon/PEEK ROS composites and then compared their results to those published for carbon/epoxy [27]. Based on results shown in Figure 2-3, it is evident that strand length has a

definite influence on strength and a minor effect (if any) on modulus. The latter is difficult to assess with certainty due to the large scatter of the data. Figure 2-3a shows that moduli of the two material systems are similar, which is expected since matrix stiffness and fibre volume fraction in both material systems are also similar. The degree of variability between the two data sets is different, because different specimen sizes and gauge sections were used in these studies. From Figure 2-3b it is evident that PEEK-based ROS composites have superior strengths than their epoxy-based counterparts. Authors [35] noted that the most prevalent failure modes in ROS composites are transverse matrix failure and strand debonding, which are both matrix-dominated. Comparison of mechanical properties of PEEK and epoxy composites showed that shear strength and fracture toughness are higher for PEEK, which explains why PEEK-based ROS composites have superior properties [35].



a) b)
Figure 2-2 – Summary of tensile, compressive and flexural a) strength and b) modulus of ROS carbon/epoxy composites [27]. Dashed line represents tensile properties of QI CF laminate



a) b)
Figure 2-3 – Comparison between carbon/epoxy and carbon/PEEK tensile a) modulus and b) strength [35]

2.1.2 Material heterogeneity

A comprehensive study [28] was conducted to identify defects that are characteristic to this material and to relate them to quality and performance. Authors [28] noted that due to the naturally heterogeneous microstructure of ROS composites on the meso-scale, ultrasonic C-scans and thermography detect a lot of variability in the material making it difficult to differentiate true defects from noise. This inherent heterogeneity of the material is explained by the fact that characteristic length scale (e.g. strand size) of ROS composites is of the same order of magnitude as test specimens and/or the potential industrial parts. Some specimens were sectioned in the regions where signal attenuation was the greatest (i.e. hot-spots) and examined under the microscope. Manufacturing defects found at these hot-spots included macro-voids, swirls and resin-rich pockets, as is shown in Figure 2-4. However, failure did not necessarily occur in the vicinity of such hot-spots (Figure 2-5), hence making conventional non-destructive techniques and defect classification unreliable for part inspection and quality control. Overall, it is evident that other sources of “weak-spots” exist besides resin rich areas and voids, and failure is governed by complex failure mechanisms [28].

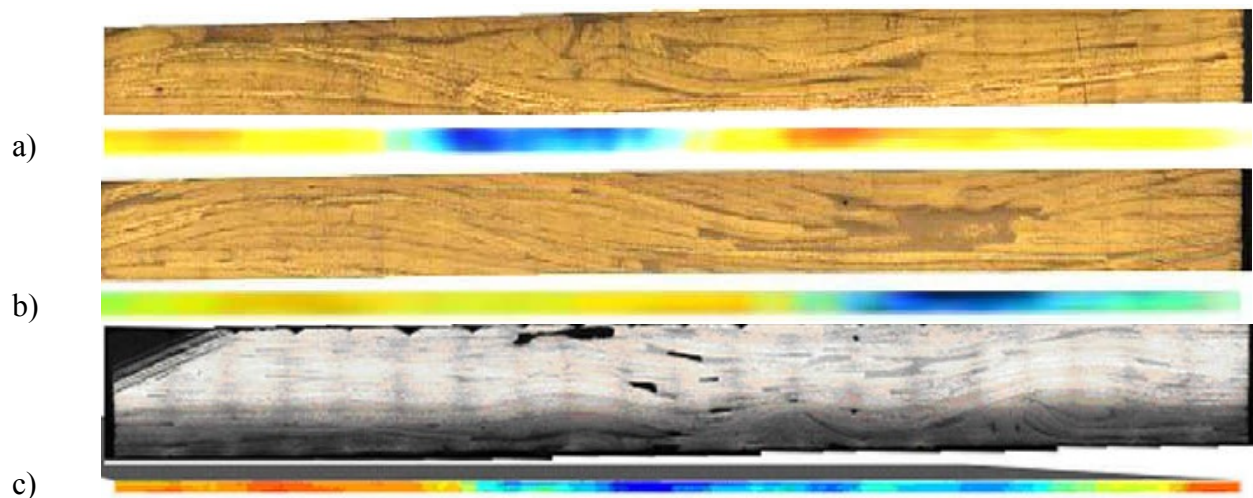


Figure 2-4 – C-scans and micrographs that show defects, such as: a) strand swirls, b) resin rich area and c) large voids [28]. Colour bar indicates the variation of the c-scan signal intensity measured at that cross-section; colour blue indicates presence of a potential defect

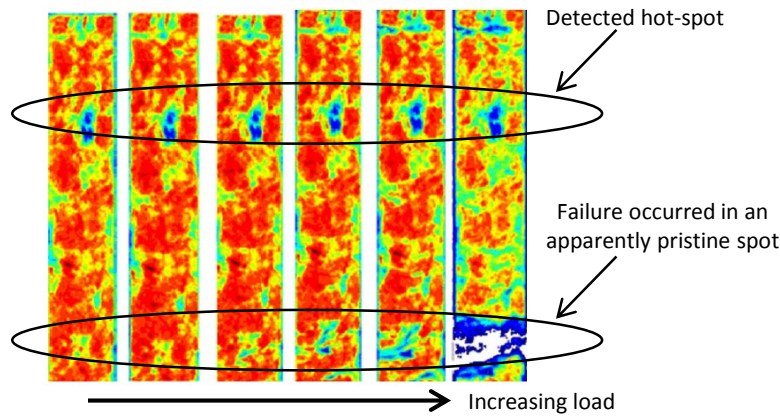


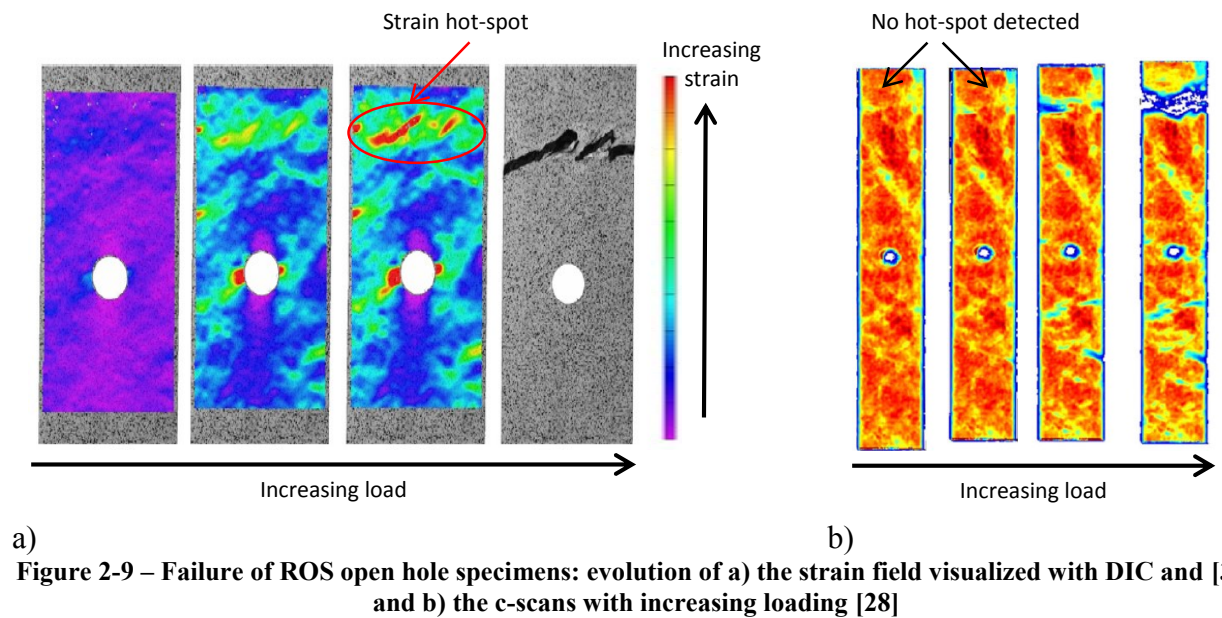
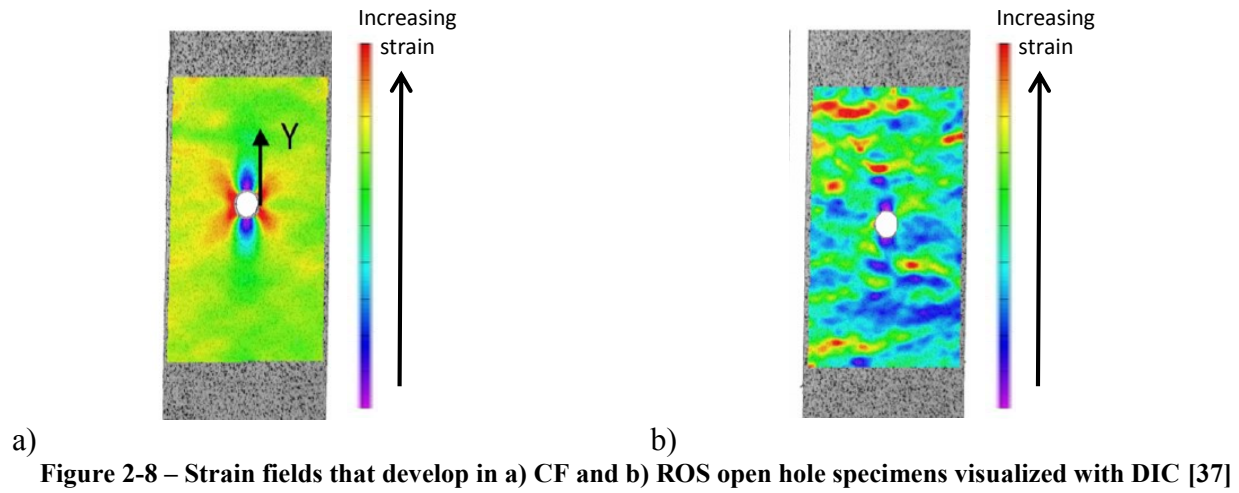
Figure 2-5 – Evolution of c-scans taken at different stages of an interrupted tension test. Subsequent images correspond to a higher load level reached during the test and track the evolution of damage [28]

Moreover, Feraboli *et al.* [29] noted that although the tensile modulus of ROS composites is essentially equivalent to that QI CF laminates, the variability in measurements obtained with strain gauges is high (19 %). To investigate the cause of this variation, authors evaluated different measurement techniques: extensometer (25.4 mm gauge length), strain gauges of various lengths (3.2 – 50.8 mm) and the digital image correlation (DIC) technique. DIC technique involves the use of a camera to capture images of the specimen during the test. Specialized correlation software is then used to analyze the images and to calculate the deformation of the specimen throughout the test. A more detailed description of this technique can be found in Appendix A. In this study, specimens were equipped with strain gauges (Figure 2-6a) and an extensometer, and subjected to tensile testing. Data obtained with the DIC technique revealed large strain variation on the surface of the specimen (Figure 2-6b) that makes extensometers and strain gauges, even large ones, inadequate for global strain measurement. Overall, the DIC technique was found to yield the most accurate and repeatable modulus measurement, since the full-field strain data can be averaged to get the global value. Authors also concluded that surface strands are not the only influence on the measured strain; instead it is a result of the whole underlying “laminates” [29].



Figure 2-7 – Strain field on the two surfaces of a DCFT specimen visualized with DIC [36]

Furthermore, Feraboli *et al.* [30] measured open-hole tensile and compressive strength of ROS composites and evaluated their sensitivity to size effects such as hole diameter and specimen size. Interestingly, open-hole tensile specimens were found to be insensitive to the presence of a small hole (3 mm diameter), and most of them failed in the gross section away from the hole. The number of net-section failures increased with larger hole diameters (6 and 9.5mm) and in the case of a 12.5 mm hole, all the specimens failed at the hole. Analogous behaviour was also exhibited by DCFP composites [37]. This phenomenon is not typical for conventional CF composites, in which case stress concentrations around the hole cause failure to occur in that region. Authors related this atypical behaviour of ROS composites to the highly heterogeneous meso-structure of the material and the inherent presence of high stress concentrations at the strand or bundle ends [30]. A clear difference between the strain-fields that develop in open-hole QI CF laminates and DCFP composites is shown in Figure 2-8 [37]. Naturally occurring material stress concentrations in ROS and DCFP composites can be larger than geometric stress concentrations and can trigger the onset of failure in a pristine area away from the notch [37]. This is demonstrated in Figure 2-9 which shows the evolution of the strain field (with DIC) and damage (with C-scan) at and away from the hole with increasing loading [28, 37]. Overall, ROS and DCFP composites can be considered as relatively notch insensitive. Nonetheless, even in the case of really small notches, specimens can fail in the net-section because its inherent weakest-point can occur in the vicinity of the notch.



Thus far, it is evident that ROS composites are heterogeneous on the meso-scale, to an extent that the material is essentially notch insensitive and measured properties are highly variable [28, 37]. Motivated by these observations, numerous authors have also investigated the effect of specimen width on measured properties [17, 30, 31, 37, 38]. Ideally, specimen size should be large enough to capture the global properties of the material; however, currently there are no test standards specifically designed for ROS composites. Overall, it is not clear what effect (if any) specimen size has on the average measured properties, but it is evident that larger specimens lead to lower scatter [17, 30, 31, 37, 38].

2.1.3 Hybridization

In light of two main issues associated with ROS composites, which are low strength and high variability, some authors explored the possibility of hybridization. For instance, Matsou *et al.* [39] optimized the design of a carbon/polypropylene hollow beam such that it met the high-stiffness and high impact-absorption characteristics of a steel beam while having only half its weight. They relied on a hybrid design of unidirectional (UD) plies and randomly oriented strands to achieve the optimal performance. UD plies were used to meet the stiffness requirements and ROS were expected to give good energy absorbing capacity to the structure.

Moreover, Han *et al.* [32] explored the effect of hybridization on in-plane and bearing properties of ROS-based composites. Hybrid specimens were manufactured from carbon/PEEK strands and satin-weave fabric. Experimental results showed that tensile and compressive strength of ROS composites is improved and shear strength is reduced by the addition of fabric layers. Overall, in-plane properties of hybrids were in-between those of ROS-only and fabric-only specimens. Interestingly, a significant improvement in bearing strength and stiffness was achieved through hybridization, even though bearing strengths of ROS-only and fabric-only specimens were lower. The repeatability of test results was also improved.

2.1.4 Design of actual ROS parts

Actual parts made of ROS-UD hybrids are already present in the automotive industry. For instance, Forged composite® technology was used to manufacture suspension control arms for Lamborghini *Sesto Elemento* [7]. Design of the control arms was driven by both strength and stiffness requirements. Authors also note that they were able to achieve higher strength and lower variability of material properties through localized hybridization with UD fibres. A total of 30 % weight reduction was achieved in comparison to the aluminum baseline. The metal and the composite parts are shown in Figure 2-10.

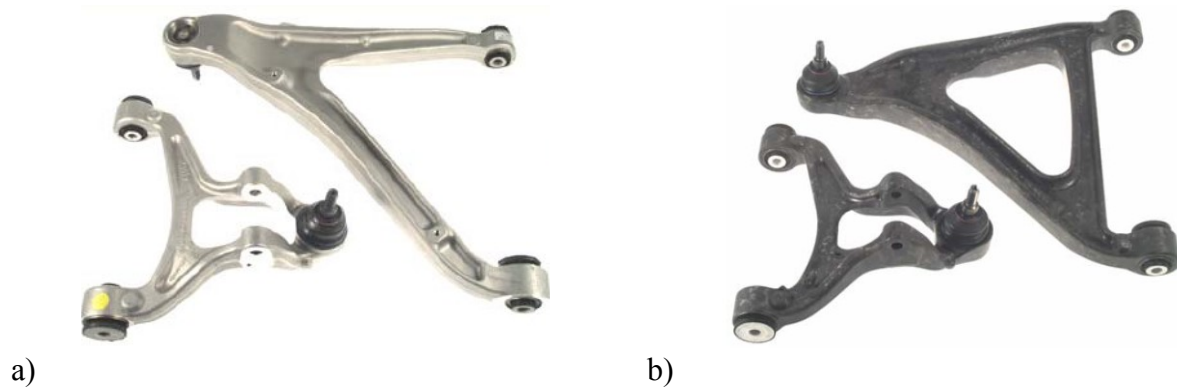


Figure 2-10 - Suspension control arms on Lamborghini Sesto Elemento: a) metal and b) composite parts [7]

To conclude the section on the experimental work, an application of ROS composites in the aerospace industry is discussed. Eguemann *et al.* [8, 12, 40] designed and manufactured a helicopter door hinge (Figure 2-11) by compression moulding of various carbon/PEEK material systems: UD tape, ROS (fibre length 10 and 20 mm), recycled fragments (< 10 mm) and moulding granules (< 1 mm). A summary of the ultimate load carried by these hinges is presented in Figure 2-11b. The best mechanical performance was achieved with UD tape hinges, but they were difficult and time consuming to manufacture. Hinges made of 20 mm long strands showed good load carrying abilities, but had a lot of variability, which resulted in unacceptably low design allowables. The use of shorter strands (10 mm) led to a lower strength but also lower scatter, which resulted in higher allowables and made this strand length a more viable design choice. This outcome demonstrated the importance of documenting the variability when characterizing properties of ROS composites. Hinges made of recycled fragments had 15 % lower strength than hinges made of the virgin material, but were nonetheless stronger than those manufactured from granules. The possibility of recycling is an attractive attribute of thermoplastic-based composites. Overall, 10 mm long strands were found to be the best candidate for this application because of the ease of manufacturing, satisfactory strength, good repeatability and weight savings of 80 % over the steel counterpart.

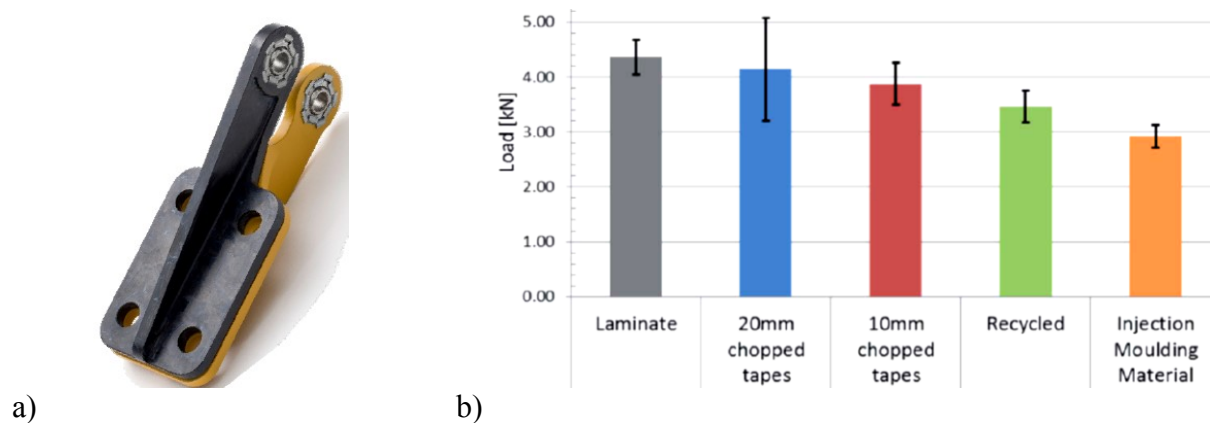


Figure 2-11 – Door hinge from Eurocopter Germany [12] and ultimate loads carried by hinges made of different composite material systems [8]

Overall, even though ROS composites have lower strength and higher variability in comparison to CF composites, they have better formability and hence can offer a competitive advantage over CF preforms for applications that are stiffness-driven. ROS composites are also competitive with metals for application in complex parts due to their corrosion resistance, light weight and cost-effective manufacturing methods. In addition, their properties can be improved through hybridization. Greater availability of experimental data, better understanding of their fundamental behavior, and improved modelling techniques will help to enhance confidence in ROS composites and increase their implementation in the field.

2.1.5 Summary of main findings

Experimental data that is currently available for ROS composites in the open literature is very limited, which is understandable since development of this material system is still in its infancy.

The main traits of ROS composites that can be drawn from the literature are:

- modulus is comparable to that of QI CF laminates
- strength is significantly lower than that of QI CF laminates
- strength is influenced by the strand size
- strength is a matrix dominated property
- material properties are highly variable on the meso-scale
- weak-spots are inherent to the material and make it essentially notch insensitive.

These material characteristics form the objectives for a modelling technique to fulfill. It is important for the model to predict the average properties and their variability, since it has a detrimental effect on design allowables. The next section will review of basic analytical models and will evaluate their applicability to ROS composites. After that a short overview of interesting finite element (FE) approaches will be presented. Finally, the general modelling approaches that were selected for further investigation in this thesis will be highlighted.

2.2 Basic analytical models for discontinuous reinforcement

A wide range of analytical models has been developed over the years to predict strength and stiffness of composites with a discontinuous reinforcement phase. A thorough review and evaluation of these models can be found in [6, 41-43]. Literature review presented in this chapter is limited to a selection of frequently referenced fundamental models, which highlight the main trends and assumptions that are prevalent to models that deal with discontinuous inclusions. In general, modelling techniques aim to capture the influence of inclusion length and orientation on the effective properties of the composite. For this reason, review of analytical models is also segregated into two sections.

2.2.1 Size effects

Analytical models that deal with size effects can be categorized based on the idealized inclusion geometry that they consider: (i) ellipsoid and (ii) cylinder.

2.2.1.1 Ellipsoidal inclusions

It is difficult to predict analytically the stress and the strain fields that develop in a composite reinforced by an arbitrary shaped inclusion. However, Eshelby [44] acknowledged that a closed-form solution can be derived for an ellipsoidal inclusion, because it develops uniform internal strains. He first addressed the following problem (Figure 2-12):

- an ellipsoidal volume is removed from an infinite solid body
- it develops a stress-free strain (ϵ^*), for instance by undergoing a phase change

- and it is inserted back into the cavity which it had previously occupied.

He solved for the stress and the strain fields in and around that ellipsoidal inclusion and found that strain inside the inclusion is dependent on the stiffness, Poisson's ratio, aspect ratio and orientation of the inclusion [43, 45]. Eshelby showed that his solution is also applicable to problems with external loading and inhomogeneous inclusions (i.e. inclusion and matrix have different properties). However, his model is meant for dilute composites with a volume fraction of about 1 % or less [43].

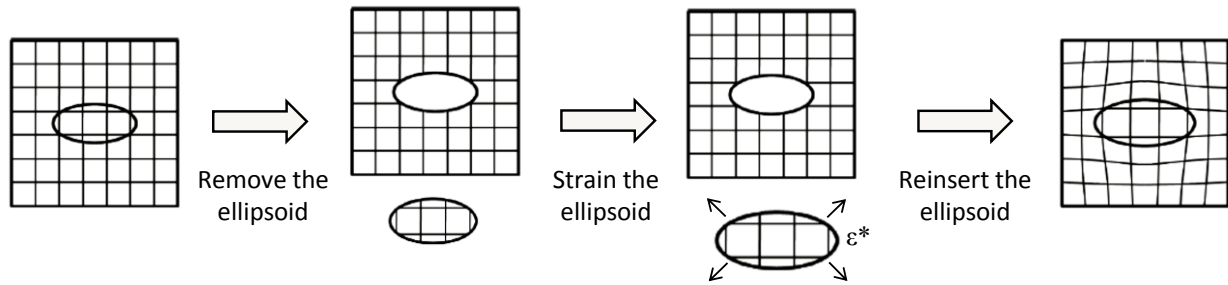


Figure 2-12 – Eshelby's problem of an elliptical inclusion [45]

Eshelby's model was later adapted to deal with multi-inclusion problems. For instance, Mori-Tanaka [46] (and Benveniste [47]) used Eshelby's expression to approximate behaviour of a multi-inclusion composite by assuming that each inclusion behaves as an isolated inclusion and “sees” a far-field strain equivalent to the average matrix strain [43]. Using the Mori-Tanaka method, stiffness of the composite (C_C) is calculated based on Eq. 2-1, where C_M is the matrix stiffness tensor, C_I is the inclusion stiffness tensor, I is the identity matrix, A_S is the strain-concentration factor given by Eq. 2-2 and S is the Eshelby tensor. The Eshelby tensor represents the shape of the inclusion and depends on the diameter (d) and the length (L) of the ellipsoid. Components of the Eshelby tensor can be found in [6, 48]. Overall, this model is adequate for V_f up to 20 % [45]. A summary of other models that were developed based on the Eshelby method can be found in Tucker [43].

$$C_C = C_M + V_f(C_I - C_M)A_S[(1 - V_f)I + V_fA_S]^{-1} \quad \text{Eq. 2-1}$$

where

$$A_S = [I + S(C_M)^{-1}(C_I - C_M)]^{-1} \quad \text{Eq. 2-2}$$

Even though Eshelby's solution was originally derived for ellipsoidal inclusions, it has been used to model platelets and flakes, spherical particles, and cylindrical fibres and nanotubes [6, 45, 48]. The actual geometry of the inclusion can be approximated by an ellipsoid with the same aspect ratio (L/d), as is demonstrated in Figure 2-13.

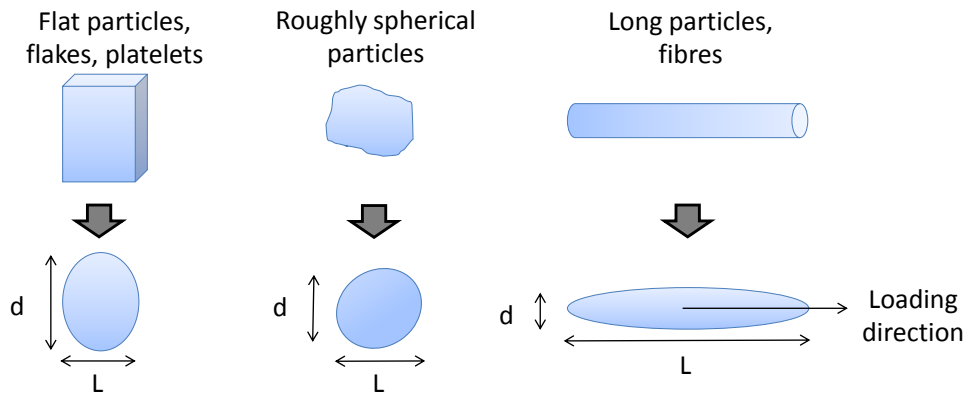


Figure 2-13 – Approximation of various inclusions with an ellipsoidal geometry [45]

2.2.1.2 Cylindrical inclusions

There are two well-known models that describe the stress distribution along the length of a cylindrical fibre embedded in resin: Kelly-Tyson [49] and Cox [50]. These models are based on the following assumptions [41]:

- fibre is straight and cylindrical
- matrix and fibre are isotropic
- fibre ends carry no load
- fibre carries only axial stress
- matrix sustains only shear stress
- load transfer occurs through the fibre-matrix interface.

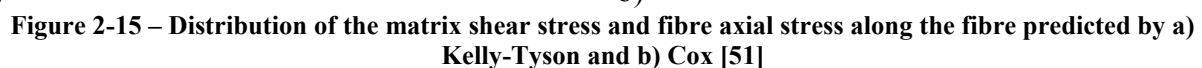
The load distribution along the fibre is derived by considering the equilibrium of forces acting on a small fibre element, as shown in Figure 2-14. Stress distribution in the fibre (σ) is proportional

Literature review



a)

b)



By first considering the Kelly-Tyson approximation, the maximum load sustained by the fibre in the center (σ_{\max}) is given by the Eq. 2-4. This equation can be rearranged to define a critical length (L_{cr}), as shown in Eq. 2-5, which signifies the transition between fibre failure and fibre pull-out (i.e. matrix shear failure), by recognizing that maximum stress that can be sustained by the fibre is limited by its strength (σ_f) and the interlaminar shear strength is given by τ_i . Hence, fibres that are longer than L_{cr} will fail due to fibre failure, while fibres shorter than L_{cr} will eventually debond, because σ_f will never be obtained in the center. The effect of fibre length on stress distribution is shown in Figure 2-16.

$$\sigma_{\max} = \frac{2\tau_i L}{d} \quad \text{Eq. 2-4}$$

$$L_{cr} = \frac{\sigma_f d}{2\tau_i} \quad \text{Eq. 2-5}$$

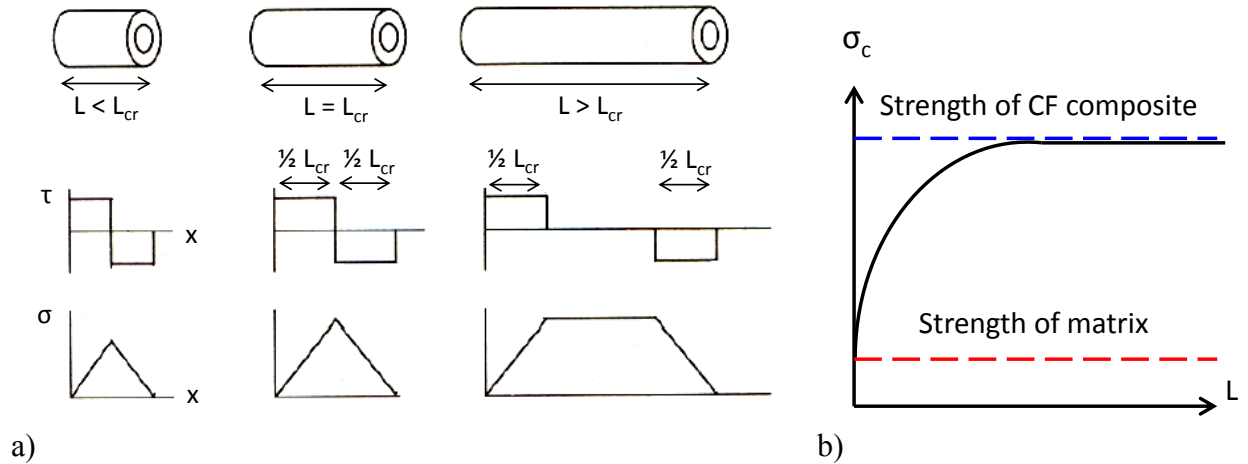


Figure 2-16 – The effect of fibre length on a) stress distribution along the fibre based on the Kelly-Tyson model and b) the composite strength [51]

From Figure 2-16 it is evident that higher fibre reinforcing efficiency is achieved with longer fibres, since a larger portion of the fibre is loaded to its maximum capacity. In fact, Kelly-Tyson proposed a length efficiency factor (χ_L), which represents the average load carried by the fibre and can be used in conjunction with the rule of mixtures (ROM) to account for fibre length, as is shown by Eq. 2-6-Eq. 2-8, where E and σ represent modulus and strength, and subscripts c , m

and f strand for composite, matrix and fibre. Kelly-Tyson's expression for critical length is widely used in relation to cylindrical and non-cylindrical inclusions [6, 45, 52, 53]. For instance, L_{cr} for platelet-type reinforcement can be estimated by replacing the fibre diameter by the platelet thickness in Eq. 2-5 [52]. Alternatively, Harper used the same approach as Kelly-Tyson and re-derived the expression for L_{cr} for a cylinder with an elliptical rather than a circular cross-section.

$$E_c = X_L E_f V_f + E_m (1 - V_f) \quad \text{Eq. 2-6}$$

$$\sigma_c = X_L \sigma_f V_f + \sigma_m (1 - V_f) \quad \text{Eq. 2-7}$$

where

$$X_L = \begin{cases} L/2L_{cr} & , \quad L < L_{cr} \\ 1 - L_{cr}/2L & , \quad L \geq L_{cr} \end{cases} \quad \text{Eq. 2-8}$$

Expression for Cox's length-efficiency factor is given by Eq. 2-9, where G_m is the matrix shear modulus and β is defined in Eq. 2-10. Cox's formulation is more complicated than Kelly-Tyson's, because shear and axial stresses along the fibre are described by hyperbolic functions (i.e. \cosh , \tanh) and are dependent on the fibre stacking arrangement though the D/d ratio, refer to Figure 2-15b. Cox assumed a hexagonal stacking arrangement and derived Eq. 2-11 for the D/d ratio [41]. Modifications of this model for other stacking arrangements are given in [43]. This family of models was used in [52, 54].

$$X_L = \left[1 - \frac{\tanh(\beta L/2)}{\beta L/2} \right] \quad \text{Eq. 2-9}$$

$$\beta^2 = \frac{8G_m}{d^2 E_f \ln(D/d)} \quad \text{Eq. 2-10}$$

$$\frac{D}{d} = \sqrt{\frac{2\pi}{\sqrt{3}V_f}} \quad \text{Eq. 2-11}$$

2.2.2 Orientation averaging

There are numerous techniques found in the literature that can be used to approximate properties of composites with multi-directional oriented inclusions. They can be separated into two categories: (i) direct averaging and (ii) pseudo-grain method. The following two sections will summarize these methods. Overall, these methods can be used in conjunction with the previously discussed micro-models to account for inclusion size and orientation.

2.2.2.1 Direct averaging

This is a fairly broad category of models that are based on simple expressions that represent the dependence of a particular property on the orientation and can be averaged out by direct integration. The simplest method by far is the modified ROM equations, Eq. 2-12-Eq. 2-13. The ROM equation for strength and/or modulus is modified to include an orientation efficiency factor (\mathcal{X}_O) to represent the effect of orientation on the corresponding property. This method has been used by [9, 52, 53, 55, 56]. A well-known expression for \mathcal{X}_O was introduced by Krenchel [57], see Eq. 2-14. In this equation, a_n denotes the proportion of fibres with the off-axis angle θ_n . For a perfectly planar random distribution, this efficiency factor is 0.375. Another option for random planar orientations is to use $\mathcal{X}_O = 1/\pi$, which simply represents equal probability of occurrence for each angle over the range of π radians [52].

$$E_c = \mathcal{X}_L \mathcal{X}_O E_f V_f + E_m (1 - V_f) \quad \text{Eq. 2-12}$$

$$\sigma_c = \mathcal{X}_L \mathcal{X}_O \sigma_f V_f + \sigma_m (1 - V_f) \quad \text{Eq. 2-13}$$

$$\mathcal{X}_O = \sum a_n \cos^4 \theta_n \quad \text{Eq. 2-14}$$

Alternatively, the Nielsen and Chen [58] equation for modulus or the Baxter [59] expression for strength can be integrated over the possible range of orientations to get an equivalent property, as is shown in Eq. 2-15 - Eq. 2-18. In these equations ν_{12} is Poisson's ratio; E_1 , E_2 and G_{12} are the

longitudinal, transverse and shear moduli; and σ_L , σ_T and σ_S are the longitudinal, transverse and shear strengths of a unidirectional ply or fibre.

$$E_c = \frac{\int_0^{\pi/2} E(\theta) d\theta}{\int_0^{\pi/2} d\theta} \quad \text{Eq. 2-15}$$

$$\frac{E_1}{E(\theta)} = \cos^4\theta + \frac{E_1}{E_2} \sin^4\theta + \left(\frac{E_2}{G_{12}} - 2\nu_{12} \right) \cos^2\theta \sin^2\theta \quad \text{Eq. 2-16}$$

$$\sigma_c = \frac{1}{\pi} \int_0^\pi \sigma(\theta) d\theta \quad \text{Eq. 2-17}$$

$$\sigma(\theta) = \left[\frac{\cos^4\theta}{(\sigma_L^T)} + \frac{\sin^4\theta}{(\sigma_T^T)} + \left(\frac{1}{(\sigma_S^L)} - \frac{1}{(\sigma_L^T)} \right) \cos^2\theta \sin^2\theta \right]^{-1/2} \quad \text{Eq. 2-18}$$

2.2.2.2 Pseudo-grain method

In this modelling technique, the representative volume element (RVE) is decomposed into a set of aggregates or grains that represent inclusions with a particular orientation. Each pseudo-grain is a two-phase composite with aligned inclusions and the same V_f as the parent material. The relative volume fraction of each grain V_r in the RVE is proportional to the probability of each orientation $\psi(\theta_n)$. These pseudo-grains can then be re-assembled to form a laminate, such that “thickness” of each grain matches its V_r . Effective composite properties can be determined by the classical laminate theory (CLT), as shown in Figure 2-17. This modelling technique was used in [60, 61].

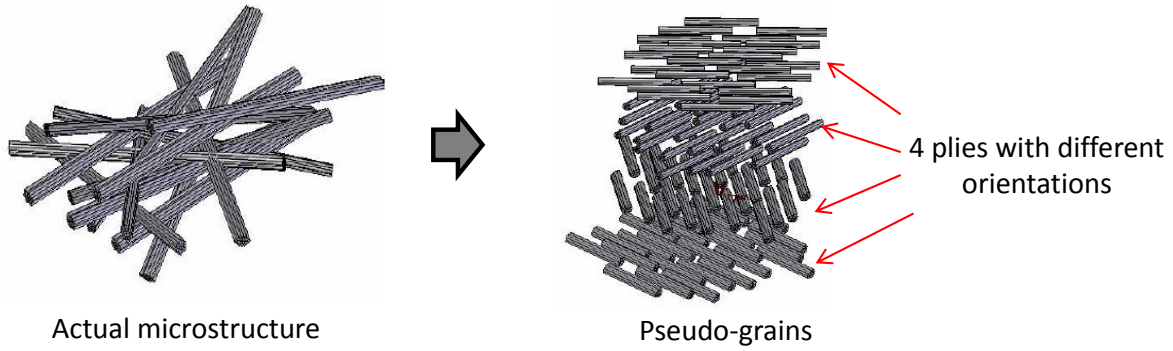


Figure 2-17 – Application of the pseudo-grain concept and CLT to randomly-oriented fibres [6, 62]

Alternatively to the CLT, the tensor averaging method can be used. Its main advantage over CLT is that it considers in-plane and out-of-plane orientations. This technique was proposed by Advani and Tucker [63]. Elastic properties of a multi-directional composite material are represented by a stiffness tensor $\langle C_C \rangle$, where $\langle \rangle$ means that properties are averaged over all directions. Orientation of a fibre is described by a unit directional vector \mathbf{p} , Figure 2-18.

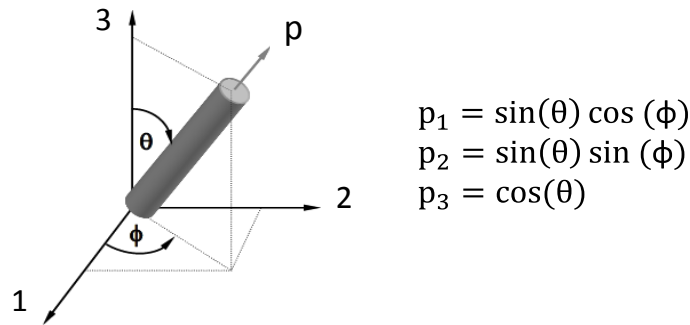


Figure 2-18 – Directional vector \mathbf{p} used in the tensorial approach for orientation averaging [45]

The effective stiffness tensor $\langle C_C \rangle$ can be expressed as a linear combination of five independent constants B (i.e. invariants) which represent properties of a pseudo-grain, and the 2nd and 4th orientation tensors λ , which represent the average orientation of all the inclusions. $\langle C_C \rangle$ is calculated using Eq. 2-19, where δ_{ij} is the Kronecker delta function, $\psi(\theta, \phi)$ is the probability distribution function that characterizes the inclusion orientations in the composite and $i, j, k, l = 1, 2, 3$ (refer to Figure 2-18). Invariants are computed from the stiffness tensor C of the pseudo-grain using Eq. 2-20a-e, and orientation tensors are computed using Eq. 2-21a-b. This averaging

method was successfully used by [6] and is implemented in Digimat® (e-Xstream Engineering). A more detailed explanation of this model is given in [6, 42, 45].

$$\langle C_{ijkl} \rangle = B_1 \lambda_{ijkl} + B_2 (\lambda_{ij} \delta_{kl} + \lambda_{kl} \delta_{ij}) + B_3 (\lambda_{ik} \delta_{jl} + \lambda_{il} \delta_{jk} + \lambda_{jl} \delta_{ik} + \lambda_{jk} \delta_{il}) \quad \text{Eq. 2-19}$$

$$+ B_4 (\delta_{ij} \delta_{kl}) + B_5 (\delta_{ik} \delta_{jl} + \delta_{il} \delta_{jk})$$

$$B_1 = C_{1111} + C_{2222} - 2C_{1122} - 4C_{1212} \quad \text{Eq. 2-20a}$$

$$B_2 = C_{1122} - C_{2233} \quad \text{Eq. 2-20b}$$

$$B_3 = C_{1212} + \frac{1}{2}(C_{2233} - C_{2222}) \quad \text{Eq. 2-20c}$$

$$B_4 = C_{2233} \quad \text{Eq. 2-20d}$$

$$B_5 = \frac{1}{2}(C_{2222} - C_{2233}) \quad \text{Eq. 2-20e}$$

$$\lambda_{ij} = \int_0^{2\pi} \int_0^\pi p_i p_j \psi(\varphi, \theta) \sin(\theta) d\theta d\varphi \quad \text{Eq. 2-21a}$$

$$\lambda_{ijkl} = \int_0^{2\pi} \int_0^\pi p_i p_j p_k p_l \psi(\varphi, \theta) \sin(\theta) d\theta d\varphi \quad \text{Eq. 2-21b}$$

2.2.3 Evaluation of the basic models

To evaluate the applicability of the basic analytical models to ROS composites, strength and modulus were computed using the modified ROM equations (Eq. 2-12-Eq. 2-13) and compared with Eguemann's experimental results [35]. In these expressions fibre strength, modulus and diameter were replaced by strand longitudinal strength, modulus and thickness. The contribution of matrix in the ROM equations was ignored, because the strand volume fraction in the composite is essentially 1. The orientation efficiency factor was assumed to be 0.375 for random strand orientation, and the length efficiency factor was calculated using Eq. 2-8.

Results of this calculation are summarized in Figure 2-19. It is evident that basic analytical models can predict modulus reasonably well, but significantly overestimate strength of ROS composites. The main downfall of these models is that they do not take into account the complex microstructure and failure mechanisms that govern damage initiation and propagation in ROS composites. For instance, test results show that ROS specimens fail due to strand pull-out, while analytical models predict strand failure (i.e. $L > L_{cr}$). Hence, the literature review is expanded to encompass models that are more representative of actual matrix properties and of the stresses at the fibre-matrix interface. For example, the effect of matrix fracture toughness on the failure strength of composites is considered [42, 64].

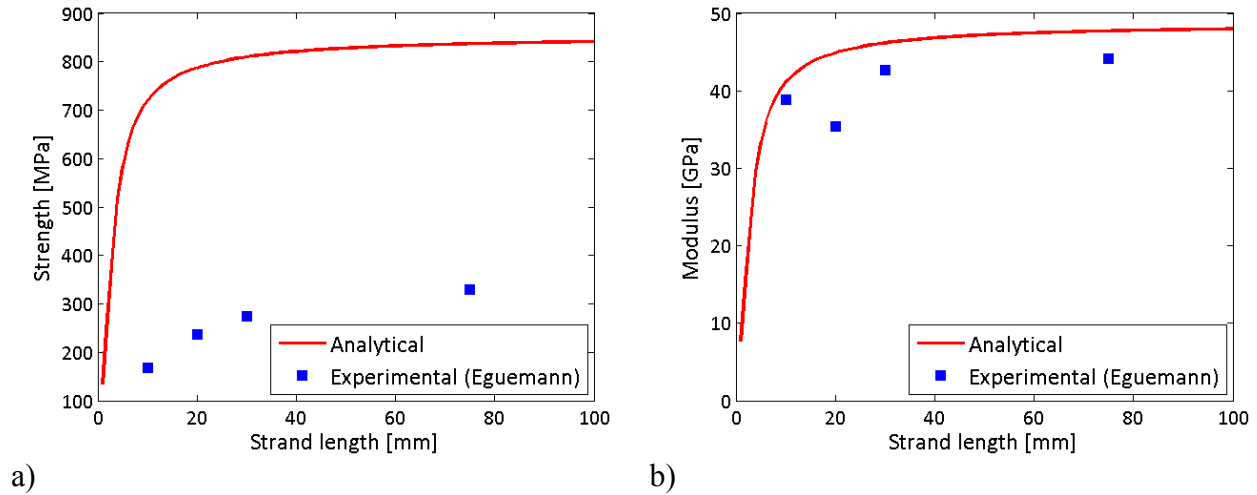


Figure 2-19 – Comparison between the calculated and the measured a) strength and b) modulus as a function of strand length. Experimental data from [35]

2.2.4 Additional considerations

When fibre volume fraction is high, it is important to take into account the interaction between the neighbouring fibres. For instance, Rexer and Anderson [65] described the effect of stacking pattern on the level of stress concentrations that develop in the fibres. Figure 2-20 depicts two stacking arrangements and the resultant stress distributions in the fibres. It is evident that in Case A, stress concentrations in the fibres are really high, because at the weakest cross-section there are only half as many fibres as there are at other locations. Thus, strength of this arrangement is $\sigma_c \approx 0.5\sigma_f$, where σ_f is the fibre strength. Alternatively, when fibre ends are well distributed (Case B), the stress profile in the fibres is more uniform and higher fibre efficiency is attained.

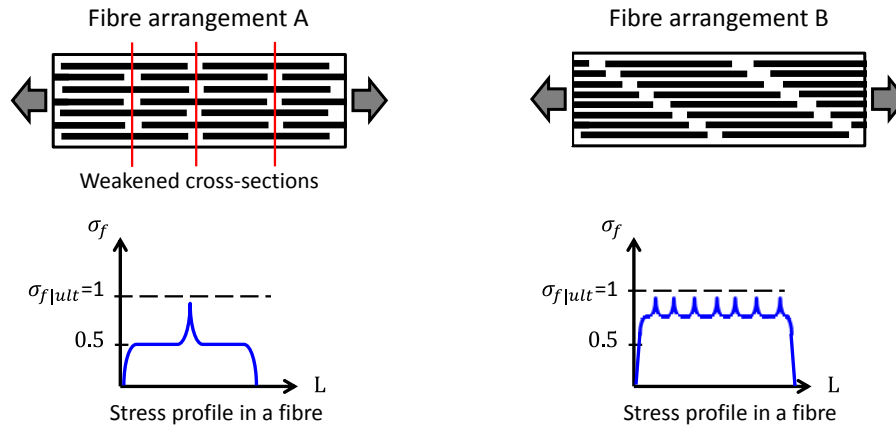


Figure 2-20 – The effect of different fibre arrangements on the stress profile in a fibre [adapted from [65]]

Moreover, fibre pull-out strength depends on the overlap length rather than fibre length [53]. Based on the stacking arrangement, if the overlap length between the fibres is short, fibres will be prone to debonding even if their length exceeds the L_{cr} . For instance, as shown in Figure 2-21, fibres of the same length will either debond or fracture depending on their location with respect to the failure plane. The same concept was described by Wyser *et al.* [66] when trying to predict whether crack growth in the vicinity of a fibre will cause it to break or to pull-out. The transition between the two failure modes is governed by the location of the crack tip with respect to the fibre end. Concepts described in [53, 66] help to explain why ROS composites with long strands tend to fail by strand pull-out, even though based on the basic models for length efficiency they are expected to fail by strand breakage.

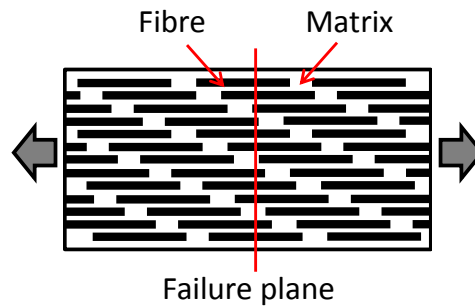


Figure 2-21 – Failure plane intersecting fibres at a different location from their ends [53]. Distance between the fibre end and the failure plane determines the failure mode being fibre pull-out or breakage

The recently published paper by Pimenta *et al.* [64] proposed a comprehensive modelling approach for composites with discontinuous staggered inclusions (or platelets), as shown in

Figure 2-22a. Authors acknowledged that there are two criteria for matrix failure: (i) strength-based (Eq. 2-22) and (ii) toughness-based (Eq. 2-23). The former is a modified version of the Kelly-Tyson expression (Eq. 2-4), where L_o is the overlap length and t_b is the platelet thickness. The latter is based on the assumption that matrix fails due to the propagation of a mode-II crack that initiates at the overlap end due to high strain concentrations. In Eq. 2-23 E_b and t_b represent platelet modulus and thickness, and $G_{IIc,IL}$ is the matrix mode II interlaminar fracture toughness. The combined effect of the two criteria on the strength of the composite, if inclusions do not fracture, is shown in Figure 2-22b. The existence of the strength plateau caused by the toughness criterion helps to explain why the strength of ROS composites is significantly lower than that of QI CF laminates even though strands are sufficiently long to achieve high fibre length efficiency. Moreover, the strength of thermoplastic ROS composites is known to be higher than that of thermoset ones (Figure 2-3), and the toughness-based criterion can potentially capture this difference, since thermoplastic resins are more ductile and tougher than the thermoset ones.

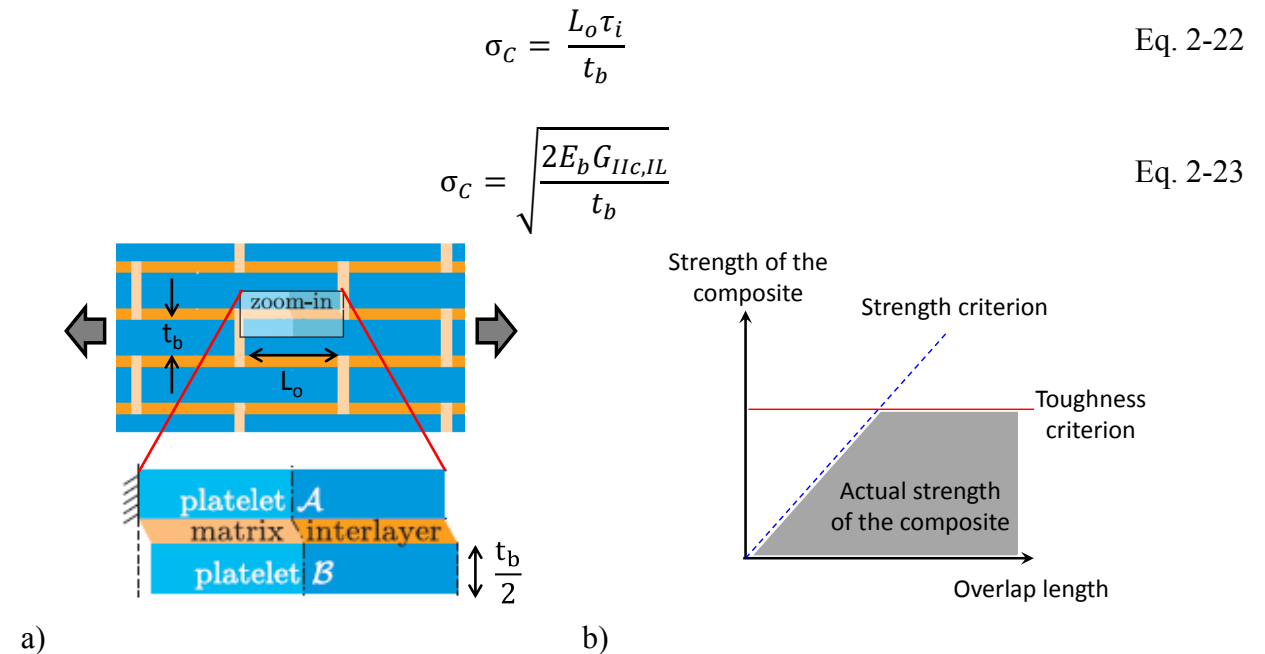


Figure 2-22 – a) Unit cell used by Pimenta to represent discontinuous staggered inclusions and b) the effect of overlap length on the composite's strength, as determined by the strength and toughness-based criteria [64]

In fact, theories developed for single-lap joints (Figure 2-23a) also predict the existence of a strength plateau for joints with long overlaps, as shown in Figure 2-23b. For a given joint geometry and mechanical properties of the adhesive and adherends, there is an upper limit on the

load that can be sustained by the joint regardless of its length, because delamination will inevitably originate at the ends of the overlaps due to stress and strain concentrations. The ability of the joint to withstand crack initiation is dependent on the strain-energy (SE) of the adhesive, as is given Eq. 2-24, where t_a is the adhesives thickness. This equation is derived in the Composite Materials Handbook [67] and is based on the works of Volkersen [68] and Hart-Smith [69]. This equation has a similar form to that proposed by Pimenta, since fracture toughness and strain-energy represent the same material property (i.e. ductility).

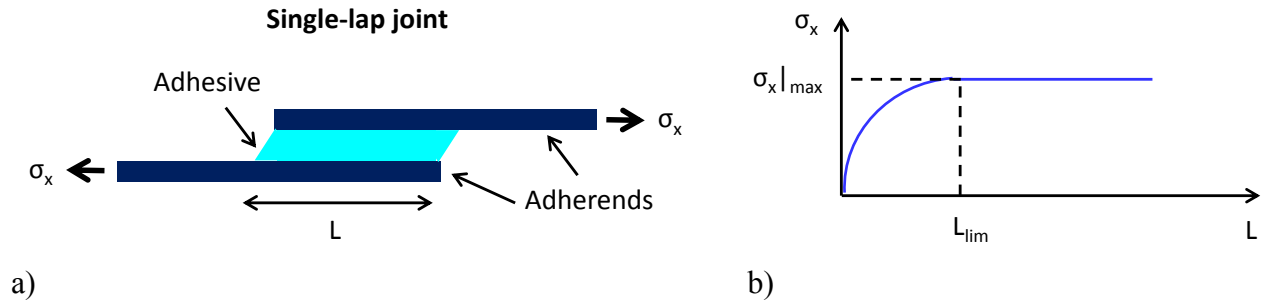


Figure 2-23 – a) Geometry of a single-lap joint and b) the concept of strength plateau for joint strength [70]

$$\sigma_c = \sqrt{\frac{2E_b}{t_b} \cdot 2(SE)t_a} \quad \text{Eq. 2-24}$$

The modelling technique proposed by Pimenta was validated experimentally by Czel *et al.* [71]. In this work, the authors manufactured UD panels with slits staggered in such a way that overlaps of different lengths, for simplicity referred to as short and long, were achieved, as shown in Figure 2-24. They showed that strength of specimens with short overlaps can be predicted by the strength-based failure criterion, whereas strength of specimens with long overlaps is well predicted by the toughness-based criterion. Moreover, stress-strain curves of specimens with long overlaps were non-linear before the ultimate failure, which is indicative of slow and progressive delamination.

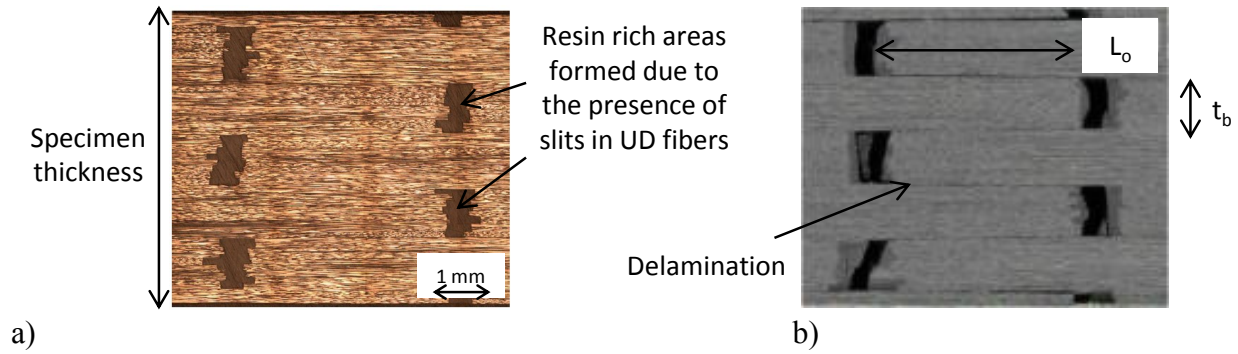


Figure 2-24 – Microstructure of UD laminates with slits a) virgin state and b) broken state [71]

Similar results were obtained by Tateka *et al.* [72], who tested slit-UD laminates with long overlaps and different slit depths (i.e. adherends or platelet thickness). They relied on the fracture mechanics formulation for the laminate of columns to predict strength of their specimens, Eq. 2-25. The schematic representation of this model is shown in Figure 2-25. This equation can be simplified by noting that modulus in the UD laminate is constant (i.e. $E_{b2} = E_{b1}$), so that Eq. 2-25 simplifies to Eq. 2-26. This equation is similar to the one proposed by Pimenta, and for thin adherends or platelets (i.e. $t_{b1} \ll t_{b2}$ and $t_{b2} \approx t_{b2} + t_{b1}$) the two models become identical. Overall, Taketa demonstrated good correlation between the test results and the toughness-based strength model. Additional information on the properties of UD and QI slit-ply laminates can be found in [10, 73, 74].

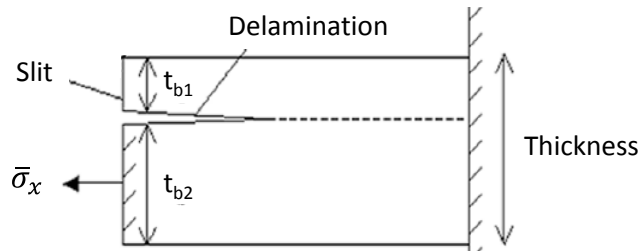


Figure 2-25 – Propagation of delamination in a laminate of columns [72]

$$\sigma_c = \frac{1}{t_{b1} + t_{b2}} \sqrt{\frac{2E_{b2}t_{b2}(E_{b1}t_{b1} + E_{b2}t_{b2})G_{IIc,IL}}{E_{b1}t_{b1}}} \quad \text{Eq. 2-25}$$

$$\sigma_c = \sqrt{\frac{2E_b t_{b2} G_{IIc,IL}}{(t_{b1} + t_{b2})t_{b1}}} = \sqrt{\frac{2E_b G_{IIc,IL}}{t_{b1}} \cdot \frac{t_{b2}}{(t_{b1} + t_{b2})}} \quad \text{Eq. 2-26}$$

Overall, papers reviewed in this section suggest that it is the strand stacking arrangement rather than length, and matrix fracture toughness rather than shear strength that determine the maximum strength achievable by ROS composites with high V_f .

2.2.5 Summary of analytical models

Analysis of the literature review suggest that models that are typically used for discontinuous-fibre composites are not representative of the micromechanics of load transfer and sharing that are intrinsic to ROS composites. Nonetheless, modelling approaches and concepts that were developed for other applications, such as bonded joints, can form the backbone of the model developed for ROS composites. In total there are six main parameters that need to be accounted for in an ROS strength model:

- strand orientation
- strand length
- strand strength
- matrix shear strength
- matrix toughness
- strand overlap length

The first four were address in the basic models, while the latter two were identified through the extended review. One aspect that is yet to be touched upon is the heterogeneity of material properties. There are some interesting FE based approaches that quite elegantly capture the effect of random strand or platelet placement on the effective properties of composites. Such models will be described in the next section on FE analysis.

2.3 Finite element models

The final section of this literature review will briefly summarize the main finite element (FE) models that were developed for composites with microstructures similar to that of ROS composites. Finite element models undoubtedly have the potential of capturing the mechanics of

load transfer between the matrix and the reinforcement more accurately than analytical models, but they are usually more difficult to implement.

2.3.1 2D models

FE models that were developed specifically for ROS composites capture the in-plane stiffness as well as its variability. Sato *et al.* [38] and Feraboli *et al.* [31] proposed modelling schemes, in which a specimen is discretized into regions (or elements) with different ply layups, and hence different properties. Localized modulus is calculated by applying the CLT to each element. Global modulus of the entire specimen is calculated by either analytically superimposing the effect of local moduli in the widthwise and lengthwise directions [38] or by modelling the entire specimen in an FE software [31]. The latter method is shown in Figure 2-26. These approaches were able to capture the average modulus and its variability from one specimen to another. Feraboli's model also demonstrated the heterogeneous strain fields that develop in ROS composites when loaded. However, since there are no actual repeating units, it is difficult to choose an appropriate size for a representative element. The use of large elements, whose layups are completely random and not dependent on the neighbouring elements, leads to large variation of properties across the element boundaries and large strain discontinuities, as shown in Figure 2-26b. In fact, the size of features that have high and low strains is directly related to the size of the representative element. Nonetheless, it would be interesting to incorporate failure criteria into this model and to evaluate the ability of this stochastic CLT-based approach to estimate strength of ROS composites.

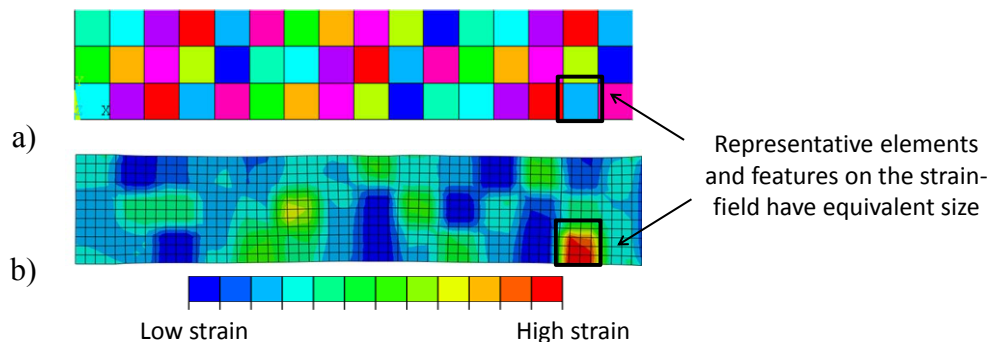


Figure 2-26 – a) Model of an ROS composites proposed by [31] in which a specimen is subdivided into regions with different properties (shown with different colours) and b) the resultant strain-field under loading (colour map corresponds to strain variability)

Moreover, a set of papers by Qian *et al.* [75-77] outlined an FE modelling scheme for estimation of elastic properties of DCFP, which in comparison to ROS composites have narrower fibre bundles and lower V_f . Fibre bundles were modeled as 1D beam elements and matrix was modeled using regular 2D plane stress elements, Figure 2-27a. An RVE was constructed by randomly generating fibre locations and orientations. Fibres were allowed to intersect to simplify the model and to generate high V_f .

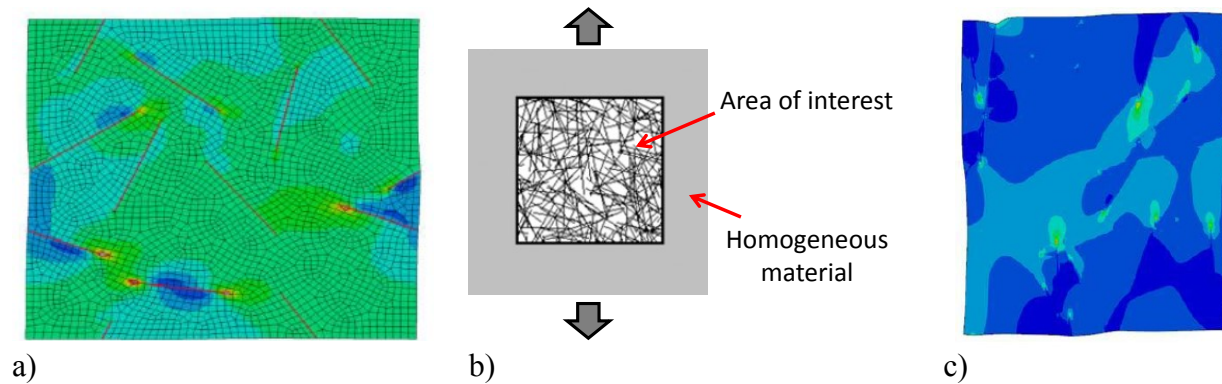


Figure 2-27 – 2D FE model for in-plane properties of DCFP: a) mesh of the matrix with embedded 1D beam elements that represent fibres, b) application of the boundary conditions using a homogeneous material and c) Von-Mises stress contour plots for an RVE [75, 77]

Authors noted that the means of applying boundary conditions to an RVE can affect the stress-strain response of the material [75]. Since this material does not have repeating units, it is inappropriate to apply periodic boundary conditions. Instead authors made use of the Saint-Venant's principal which postulates that an approximation to the solution can be found if a sub-domain (i.e. region of interest) is embedded in a homogeneous material, which is used to transmit the applied load (see Figure 2-27b). The homogenous region was assigned average properties of DCFP. Finally, as shown in Figure 2-27c the edges of the deformed RVE (under tensile loading) are not straight, therefore conventional boundary conditions for this RVE model would be inappropriate [77]. Moreover, authors provide an interesting discussion in relation to the appropriate RVE size, which can be found in [40]. It was shown that in order to achieve the same statistical confidence, it is more efficient to run fewer large models. Overall, their model was able to accurately predict elastic properties of the material and their variability, but failure of the material was not simulated.

The aforementioned models predicted elastic properties of ROS composites by creating 2D models that were representative of the in-plane meso-structure of the material. Alternatively, the through-the-thickness microstructure can be modelled in order to capture the interlaminar interactions between the strands and the matrix. One such model was developed by Bekah *et al.* [78] for nacre (sea shells), which is made of strong and stiff platelets and tough matrix, as is shown in Figure 2-28a.

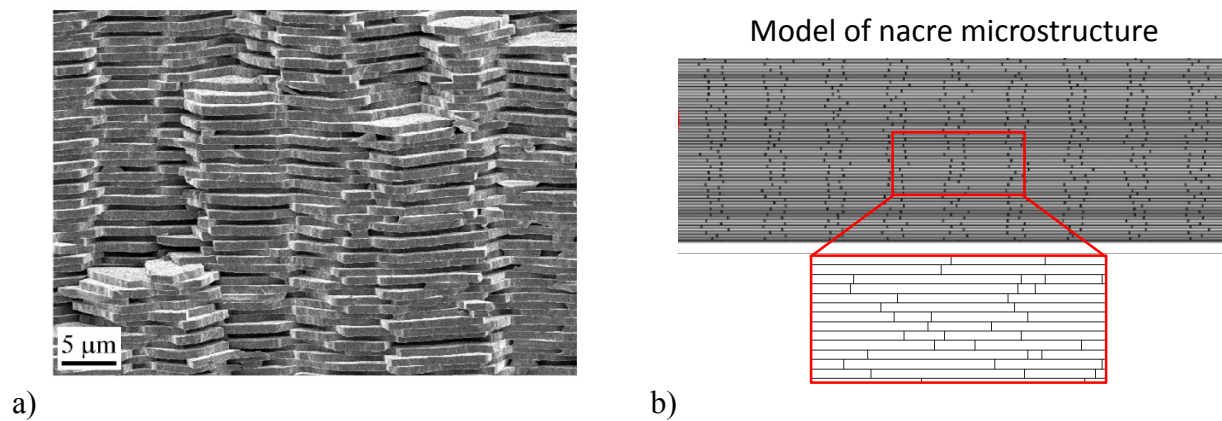


Figure 2-28 – a) Micrograph of nacre that depicts the staggered arrangement of reinforcing platelets and b) microstructure captured by the FE model proposed by [78]

In the proposed model, an RVE representative of the microstructure is generated (Figure 2-28b) and interfaces between the platelets and matrix are modelled by cohesive elements. This model captures the non-uniform contour of the axial displacement and a stair-like failure path (Figure 2-29), which is similar to that observed with ROS composites. Modelling results also demonstrate that failure develops along the weakest-path.

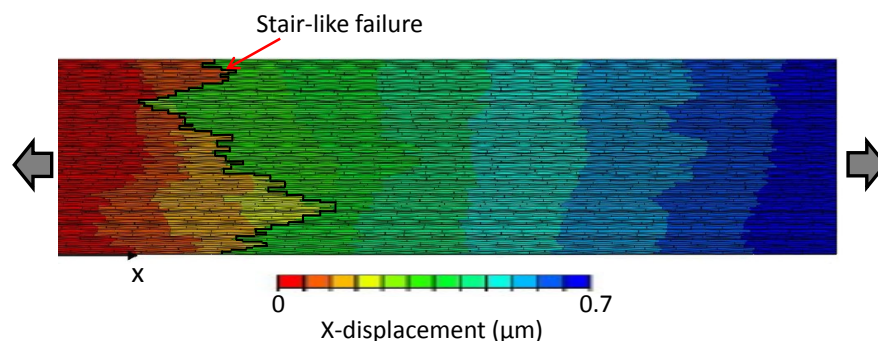


Figure 2-29 – Displacement contour plot obtained with the nacre model [78]. The black line shows the location of final failure

2.3.2 3D models

The most accurate way of modelling elastic properties and failure mechanisms in ROS composites would be to create a 3D model. However, it is rather difficult to generate an RVE containing a high volume fraction of inclusions with large aspect ratios and random orientations. For instance, models with straight fibres are limited to V_f of about 20 % [42], as shown in Figure 2-30a. To address this issue, Pan [42] developed an algorithm which allowed fibres to curve around other fibres at intersection points and was able to achieve V_f up to 40 %, Figure 2-30b. He used a cohesive zone model and a strain-based failure criterion for the fibre-matrix interface, and was able to successfully predict properties of his material. Overall, Pan concluded that fracture toughness and strength of the interface have a strong effect on strength of the composite. This is a very powerful and comprehensive model, but it would be difficult to implement for ROS, because volume fraction of strands in the material is close to 100 %. Such high volume fraction is obtained because extra resin is not added to the strands, and only a minimal amount of resin flows out of the strands during moulding.

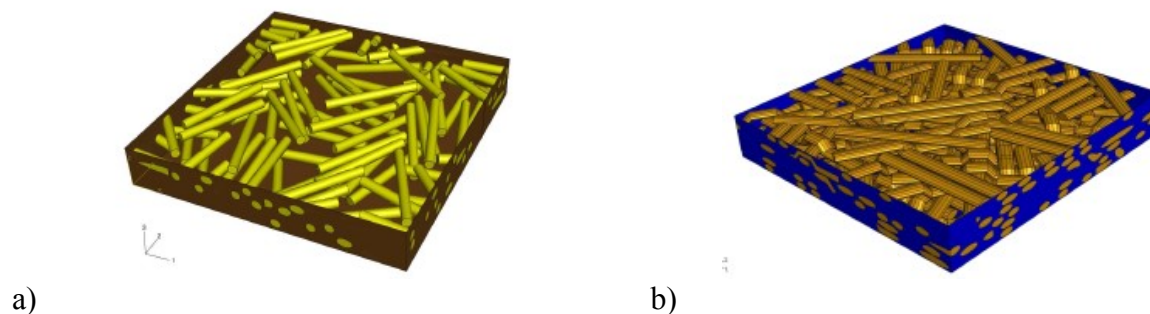


Figure 2-30 – RVEs generated using a) straight fibres ($V_f = 13.5\%$) and b) curved fibres ($V_f = 35\%$) [42]

Finally, Kilic [25, 79] from Green, Tweed & Co developed a homogenization approach and a 3D element, which can be used to predict the stress-strain response of an actual ROS component. Outline of the model is given in Figure 2-31. The micromechanical model on itself is not fully representative of the ROS material and requires some calibration against the stress-strain curves of test-coupons. Nonetheless, this modelling technique has great industrial potential, since it can predict the response of an ROS part under loading.

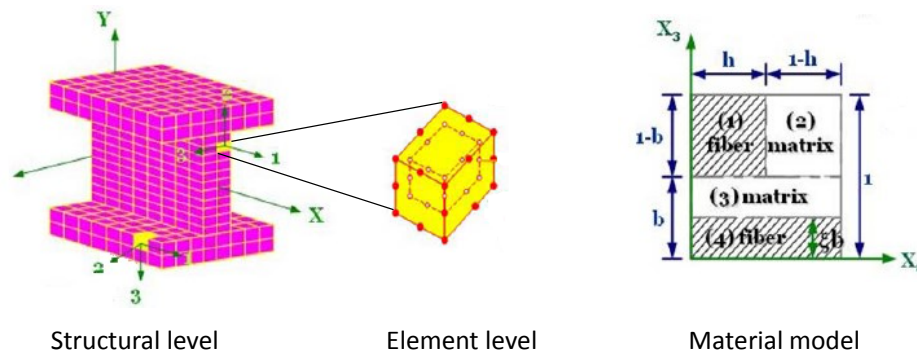


Figure 2-31 - Combined micromechanical and structural framework [25, 79]

2.3.3 Summary of the FE models

From the literature review it is evident that generation of a detailed 3D model representative of an ROS microstructure would be really labor and power intensive. At this stage it seems more appropriate to focus on 2D models to study the fundamental properties of ROS composites. A simplified 2D model can be created by focusing on: (i) in-plane (Feraboli) or (ii) through-the-thickness (Bekah) strand placement. It would be interesting to adapt these techniques for strength modelling of ROS composites.

2.4 Concluding remarks and thesis outline

Experimental work on ROS composites that has been accomplished to date describes the main properties of this material system and highlights some of its unique traits, such as notch-insensitivity. However, the amount of experimental data available, at least in the public domain, is rather limited and warrants additional testing. Hence, the main portion of this thesis is dedicated to the characterization of ROS composites:

- **Chapter 3** will describe how ROS panels were fabricated, discuss the effect of processing parameters on part quality and identify defects that can develop during manufacturing.
- **Chapters 4-6** will describe the experimental procedures for tensile, compressive and shear (in- and out-of-plane) properties, present the main findings regarding the effect of

strand size and panel thickness on these properties and give practical recommendations in relation to testing.

ROS composites have already found industrial applications, but their widespread use is hindered due to limited modelling capabilities. There are analytical and FE models that can predict modulus of an ROS composite from the properties its constituents, but models for strength are yet to be developed. The modelling objectives defined in this thesis are to predict and explain the strength difference between QI CF and ROS composites and to capture the effect of strand size on material heterogeneity and strength. Two modelling strategies are considered:

- **Chapter 7** will describe the workings of a 2D in-plane FE model for strength, which is essentially an extension of Feraboli's model, and will discuss its applicability and limitations.
- **Chapters 8** will describe the development of a 2D through-the-thickness analytical model for strength, which is a simplified adaptation of the FE model for nacre. The model will be evaluated against experimental data for carbon/PEEK and carbon/epoxy ROS composites and subsequently, areas for future modelling work will be identified.

Finally, main conclusions and recommendations for future work will be outlined in **Chapter 9**.

Chapter 3

Manufacturing process

This chapter will present an overview of the manufacturing process used for making ROS composite test samples and discuss the influence of processing parameters on part quality.

3.1 Overview of the manufacturing process

The bulk moulding carbon/PEEK compound, which was used in this work, is currently available from the manufacturer and can be ordered in different strand sizes [33]. However, in the beginning of the project it was not available commercially and had to be produced onsite from a precursor prepreg. Unidirectional slit tape, which came in different widths, was cut into strands of desired length using an automated tape cutter (Kingsing Machinery Co. Limited, model KS-915) at NRC-Montreal. The following strand sizes (length x width) were cut: 6 x 3, 12 x 3, 12 x 6, 25 x 6, 50 x 6, 25 x 12 and 50 x 12 mm, as summarized in Table 3-1. Strands were then placed in small batches into a steel mould and shuffled back-and-forth each time to minimize their out-of-plane orientation. The mould was placed into a press (Wabash MPI V150-36-CX) and minimal pressure was applied to close it. Once the processing temperature of 380°C was reached, full pressure of 34 bar (500 psi) was applied. Following a 15 min dwell, the mould was cooled down at an average rate of 10°C/min. The panel was then demoulded and trimmed by 10 mm on each side. The final panel dimensions were 280 x 330 mm with thicknesses of 2.5 or 6 mm. An overview of the manufacturing process of ROS panels can be seen in Figure 3-1. CF

unidirectional and quasi-isotropic panels with $[0/\pm 60]_{3s}$ layup were manufactured to allow for benchmarking of the results. For consistency, the same moulding cycle was used for all CF panels. The following sections will describe how and why these processing conditions were chosen.

Table 3-1 – Summary of all test cases

Panel thickness	Strand width Strand length	3 mm	6 mm	12 mm
2.5 mm	6 mm			
	12 mm			
	25 mm			
	50 mm			
6 mm	6 mm			
	12 mm			
	25 mm			
	50 mm			

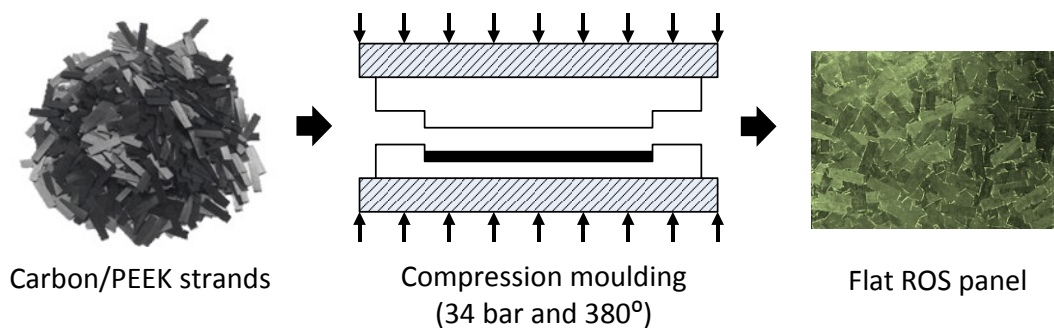


Figure 3-1 - Manufacturing process of flat ROS panels

3.2 Selection of the processing parameters

The first stage of the experimental work encompassed the selection of the processing parameters that would ensure good quality of the moulded panels. For compression moulding, pressure, temperature, dwell time and cooling rate had to be defined, and the following ranges were recommended by the manufacturer:

- Pressure: 34 - 70 bar (for ROS) and 7 – 20 bar (for CF).
- Temperature : 370 - 400°C
- Dwell time: 15 - 30 min
- Cooling rate: 5 - 20°C/min

Since the focus of the thesis is on mechanical properties rather than optimization of the manufacturing process, it was necessary to investigate the effect of these parameters on panel quality without conducting a full-scale sensitivity study. To reduce the number of variables, it was decided to consider only the influence of pressure and cooling rate. This simplification was made based on the assumption that temperature and dwell time do not affect the mechanical properties, and any combination of them would be adequate as long as complete filling of the mould cavity by ROS is achieved. Temperature of 380°C and dwell time of 15 min were chosen.

On the contrary, pressure and cooling rate govern void content and matrix crystallization, both of which are expected to have a direct impact on mechanical properties. The recommended pressure range was large, so three different pressures were considered corresponding to low (10 bar), intermediate (20 bar) and high (60 bar) values. It was difficult to control the cooling rate due to the large thermal mass of the press platens, so two cooling rates were considered corresponding to the fastest (16°C/min) vs. the slowest (0.5°C/min) options. Rapid cooling was achieved by using a mixture of air and water to cool the press platens (more details are given in section 3.2.2). The slow cooling was attained by letting the mould cool under the ambient conditions (i.e. cooling system was not turned on). For this study 2.5 mm thick panels were manufactured using 25 x 6 mm strands.

3.2.1 Panel defects

Surface defects were observed with panels moulded using a fast cooling rate, as can be seen in Table 3-2. Some regions of these panels looked white due to the presence of a thin layer of PEEK resin on the surface, which is identified by red lines in the pictures in Table 3-2. These white regions were larger in panels moulded at lower pressures. On the other hand, panels moulded with slow cooling rates did not develop this defect. These observations imply that fast cooling rates can have an effect on surface quality, while high pressures can help to alleviate it. Also in the case of the panel moulded at the lowest pressure (10 bar), surface voids were visible in the resin deprived areas between the strand ends. In order to evaluate the significance of these surface defects, panels were c-scanned and mechanically tested.

Table 3-2 – Effect of pressure and cooling rate on surface quality of ROS panels (with 25 x 12 mm strands)

	Fast cooling (16°C/min)	Slow cooling (0.5°C/min)
Low pressure (10 bar)		
Intermediate pressure (20 bar)		
High pressure (60 bar)		

The ultrasonic c-scans were performed at NRC-Ottawa and had a resolution of 1 x 1 mm, meaning that they could detect large voids and delaminations. Comparisons between the c-scans of panels with and without surface defects are shown in Figure 3-2. The c-scan image of a pristine panel did not reveal any defects, whereas the c-scan image of a low pressure panel showed that areas with potential internal defects had the same shape as the white regions on the surface. Since c-scans are sensitive to both surface quality and voids, the low pressure panel was sanded down to remove the resin layer and rescanned. Same results were obtained meaning that defects that were detected by the ultrasound were in fact internal rather than purely external. This result signifies that surface discoloration is a sign of potential internal defects, such as voids.

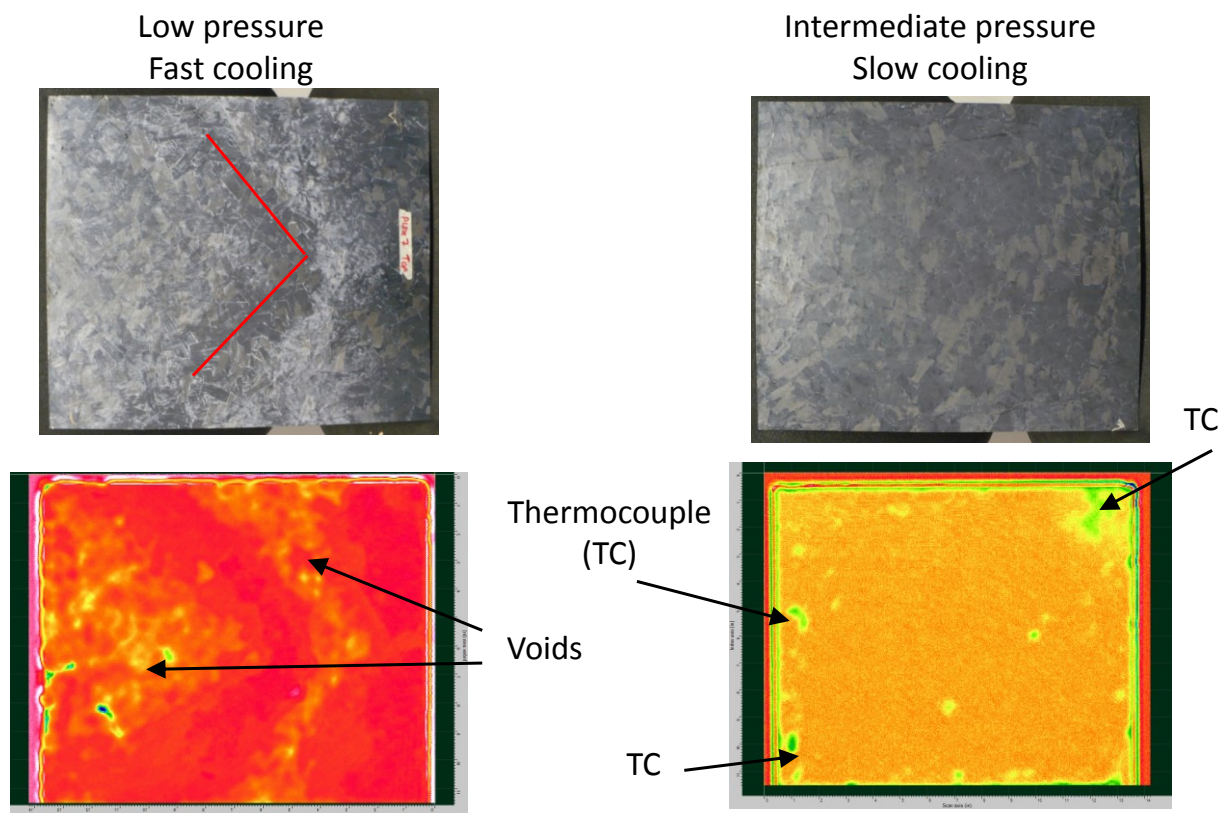


Figure 3-2 – Correlation between surface defects and ultrasonic c-scans of ROS panels with 25 x 6 mm strands

The next step was aimed at evaluation of mechanical properties. Panels were cut into tensile specimens (275 x 25 mm) which had an active gauge section of 200 x 25 mm. A total of 8 specimens per panel were tested. An Instron machine with hydraulic grips and 100 kN load cell

was used at NRC-Boucherville. A loading rate of 1.5 mm/min was used. A summary of tensile results is shown in Figure 3-3. These results show that the average strength values are unaffected by these defects, but the scatter is larger with low pressure panels. The fact that voids have a minimal effect on tensile strength can be explained by the fact that this material is considered to be notch-insensitive [30]. Nonetheless, it was interesting to determine the real cause of these defects and to find a way to mitigate them in order to avoid any problems or uncertainties that could arise with future tests (i.e. compression and shear).

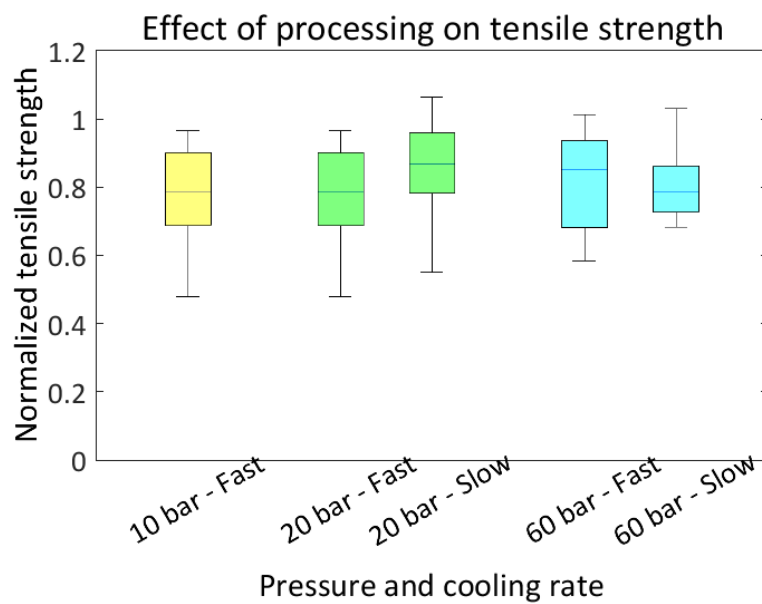
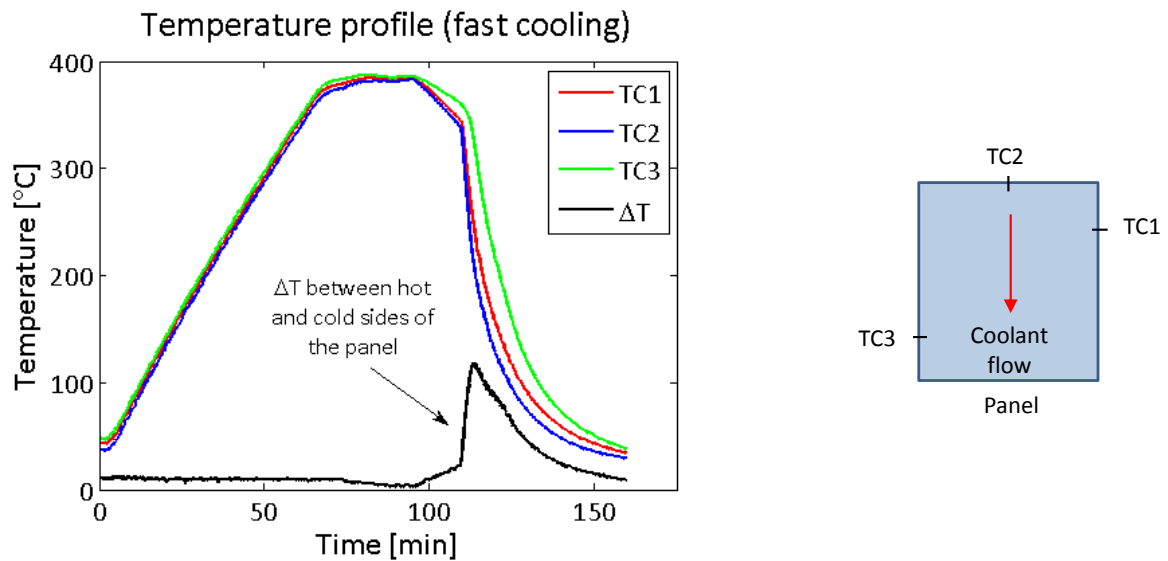


Figure 3-3 – Effect of processing conditions on tensile strength of ROS panels with 25 x 12 mm strands

3.2.2 Cause of the problem

The main clue for understanding the origins of the surface defects came from the thermocouple (TC) data. Figure 3-4 shows temperature profiles measured at different locations in the panel during the moulding cycling with a fast cooling rate. It is evident that there is a large in-plane temperature gradient during cooling, with the difference in temperature (ΔT) between the cold and the hot side being as large as 120°C. This gradient is caused by the design of the cooling system, which is shown in Figure 3-5. As the coolant flows through the press platens, it warms up and loses its cooling efficiency, hence creating a temperature gradient between the inlet and the outlet.



a) Figure 3-4 – a) Temperature profile measured at different locations in a panel and b) schematic indicating TC locations

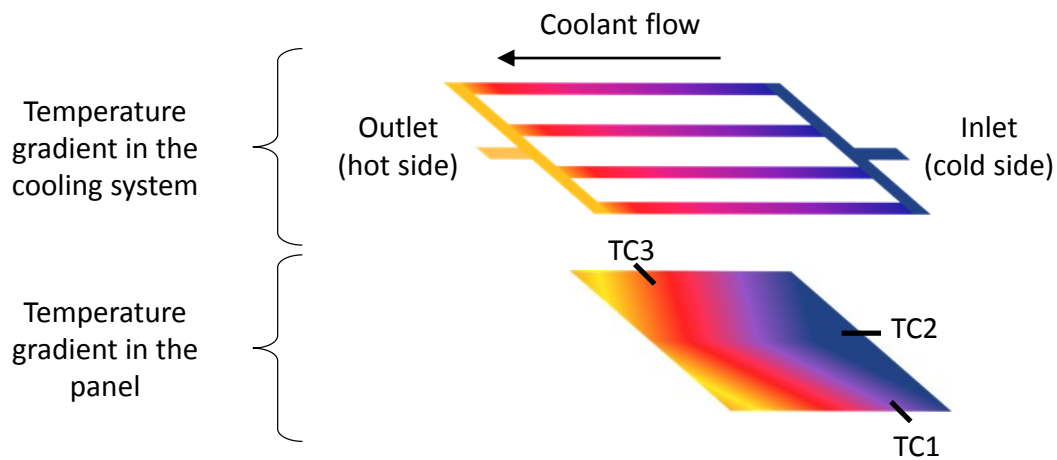


Figure 3-5 – Temperature gradient that develops in the cooling system and in the panel during fast cooling

This temperature gradient causes the colder portion of the panel to crystallize and/or shrink at a faster rate than the hotter portion. This non-uniform shrinkage might lead to formation of a gap between the colder thinner side and the mould, while the hotter thicker side would carry all the pressure, as shown in Figure 3-6. Such loss of pressure on the cold side causes the resin on the panel surface to pull away from the mould, hence creating a rough surface finish on the panel and leaving a layer of resin residue on the mould. Also, if this pressure loss occurs during the

early stages of the cool down before the material is fully crystallised, voids might form in the panel.

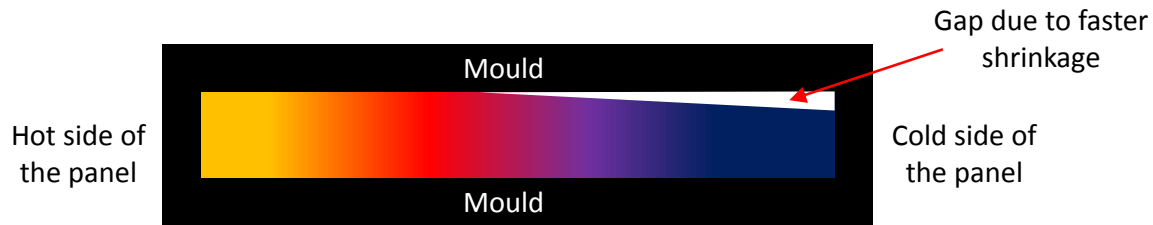


Figure 3-6 – Gap between the mould and the cold side of the panel due to non-uniform shrinkage

Whether or not the colder side of the panel will actually experience a pressure loss depends on the amount of mould pressure. The use of higher pressure will either prevent the localized pressure loss all together or at least off-set it to a lower temperature at which the material is fully crystallized and void formation is avoided. Hence, if presence of a temperature gradient cannot be avoided, higher moulding pressures should be used to mitigate these problems. Table 3-2 clearly shows the improvement in surface quality of panels that were moulded at higher pressures.

When no coolant was used, temperature was uniform throughout the panel, and hence there were no problems with surface discoloration. Overall, it was not per say the cooling rate that caused the problem, but rather the temperature gradient that was induced by the coolant flow.

3.2.3 Reduction of the temperature gradient

It was advantageous to reduce the temperature gradient, which is the primary cause of the surface defects, in lieu of trying to use high pressures or refraining from using the cooling system all together, which would lead to unacceptably long cooling time (8 hours). A solution was proposed by S. Roy from NRC-Montreal. The press was modified to include passive devices to improve the temperature uniformity. The resultant temperature profile can be seen in Figure 3-7, and the maximum temperature difference was 18°C. Due to this modification, the cooling rate was reduced to 10°C/min. The moulding pressure was set to 34 bar which is the lowest

recommended pressure for ROS. Panels moulded using these settings had minimal if any surface discoloration.

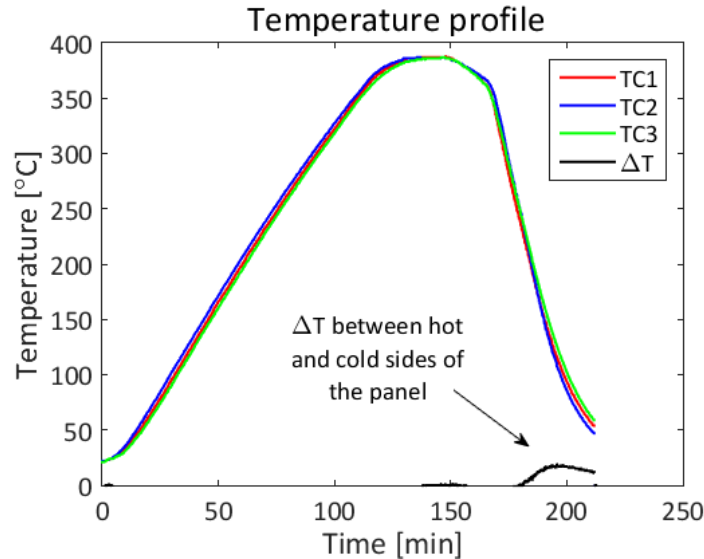


Figure 3-7 - Temperature profile in a panel manufactured with the use of passive devices to improve temperature uniformity

3.3 Warpage

The main manufacturing defect which was observed with all ROS panels, regardless of the strand size or manufacturing conditions, was out-of-plane warpage. In order to document warpage, all panels were scanned by a coordinate measurement machine (CMM) at 5 mm intervals. The shapes of ROS panels were “unique” and irregular, and could not be described by a commonly used constant curvature value. Since it was desired to compare the degree-of-warpage among the different types of ROS panels (i.e. different strand lengths), a D-value was proposed as the means of quantifying warpage. The definition of the D-value is shown in Figure 3-8.

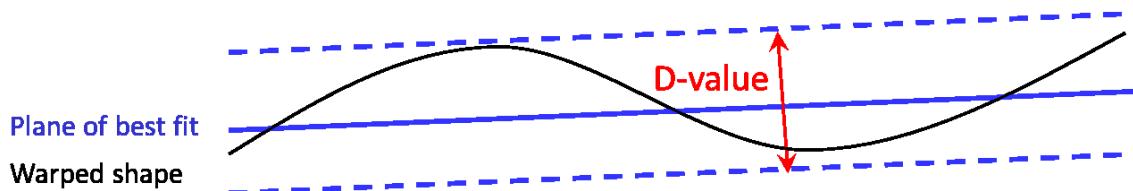


Figure 3-8 – Schematic definition of the D-value used to quantify warpage

Warpage can be caused by the material microstructure (i.e. ply layup) and/or the processing conditions (i.e. thermal gradient, part-tool interaction). Microstructure of ROS composites is heterogeneous, and hence the local properties, such as modulus and coefficient of thermal expansion (CTE), are also variable. Thus, some degree-of-warpage could be expected. The processing conditions could affect warpage, but their effect would be consistent for each panel. Since each panel had a different warped geometry (Figure 3-9), microstructure was a more likely cause of warpage, because it was also unique to each part, rather than the processing conditions, which were the same. Also, with the aim to eliminate thermal gradients during cooling, some panels were cooled overnight at a slow rate of 0.5°C/min. No improvement in geometrical integrity was observed.

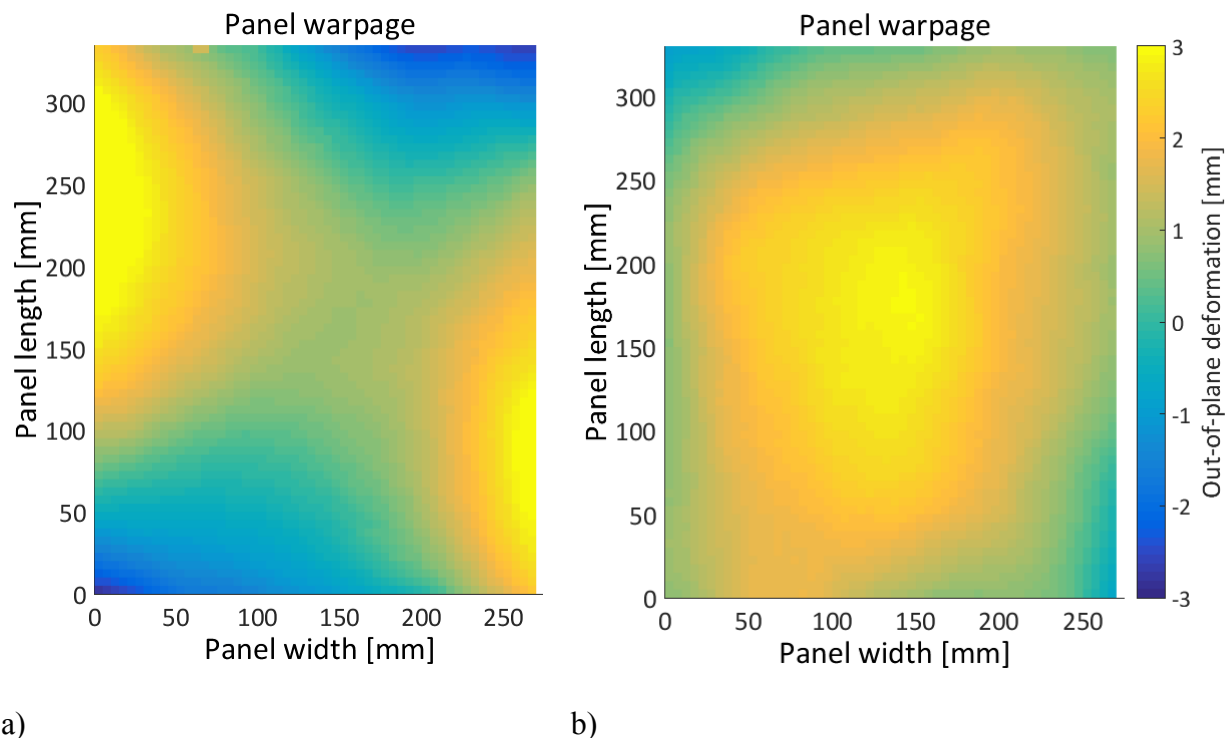


Figure 3-9 – Warped shapes of ROS panels with 25 x 6 mm strands. Panels have D-values of a) 9 and b) 4

The effects of stand size and panel thickness on warpage are summarized in Figure 3-10. Two panels per category were manufactured and measured, with the exception of 2.5 mm thick panels with 25 x 6 mm strands, in which case 6 panels were measured. Foremost, it is evident that in the case of thin panels, warpage decreases with decreasing strand size. This trend can be explained by the fact that homogeneity of the composite improves with shorter strand lengths.

Interestingly, thick panels are only slightly warped. Panel thickness has a twofold effect: homogeneity is improved and flexural stiffness is higher due to the larger moment of inertia. It is noteworthy that even though warpage of thick panels is minimal, they are still at a state of complex residual thermal stress, which is caused by the mismatch of the CTEs in the through-the-thickness as well as the in-plane directions. Figure 3-10 also shows that quasi-isotropic CF laminates (QI CF) were slightly warped. This type of warpage can be attributed to the slight misalignment of the plies and/or the processing conditions. Overall, since minimal warpage was obtained with CF panels and thick ROS panels, it can be concluded that large warpage of thin ROS panels and its variability were caused by the material heterogeneity and not adverse processing conditions.

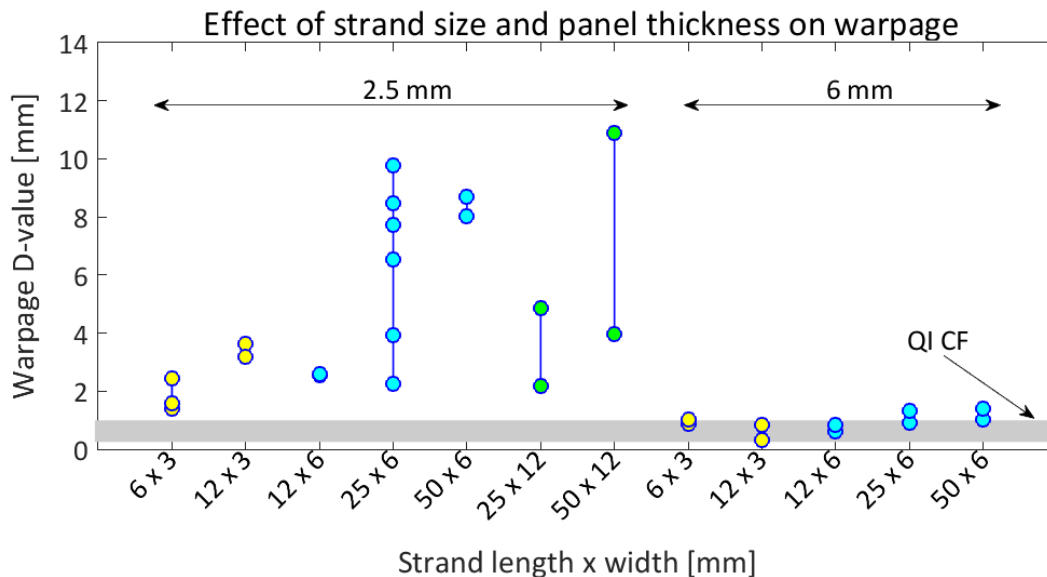


Figure 3-10 – The effect of strand size and panel thickness on warpage

3.4 Variability of CTE

As discussed in the previous section, warpage of ROS panels is believed to be caused by large variability of CTE. To demonstrate this variability, in-plane CTE was measured at different locations in a panel. While variability of in-plane CTE would not cause warpage in balanced and symmetric laminates, it would lead to irregular warpage of unbalanced and unsymmetrical ones, as is the case with strand layup in ROS composites. CTE measurements were done using a

Thermal Mechanical Analyzer (TMA). A total of six samples were cut from a 2.5 mm thick ROS panel with 25 x 6 mm long strands. Samples were 8 x 8 mm, which is the biggest size that could fully fit between the base plate and the probe of the TMA fixture, which have a diameter of 9 mm. Figure 3-11 shows a sample installed in the fixture. The TMA works by slowly heating up the specimen in a closed-off chamber and measuring the expansion of the sample between the base and the probe. Data recorded during the second heating cycle was used in the analysis, since it is considered to be more reliable. The first thermal cycle is used to “erase” the thermal history of the resin. For each sample, CTE was measured in two in-plane directions. The following procedure was used:

1. Force of 0.1 N was applied onto the specimen
2. Temperature was allowed to stabilize at 25°C
3. Temperature was increased from 25°C to 140°C at a rate of 1°C/min
4. Temperature was kept constant at 140°C for 10 min
5. Temperature was reduced to 25°C at a rate of 1°C/min
6. Steps 2-5 were repeated.

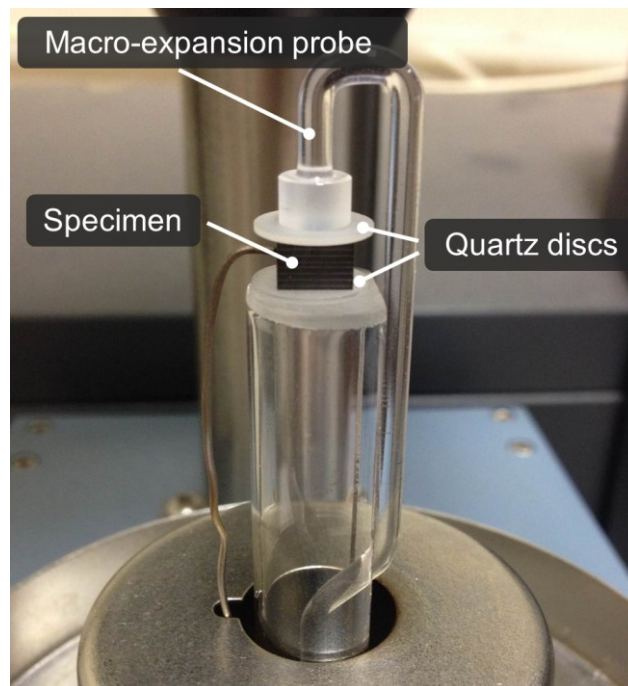


Figure 3-11 – Sample in the TMA apparatus

Thermal expansion curves for the two in-plane directions of each ROS specimen are presented in Figure 3-12. It is evident that the variability of data is rather large. For comparison, approximated curves of UD carbon/PEEK specimens in the longitudinal (fibre) and transverse (matrix) directions are also given (based on the data from [80]). Thus far, TMA results demonstrate the large variability of in-plane CTE, which seems to be the principal cause of warpage. These results will be revisited in Chapter 7 which deals with modelling of in-plane properties of ROS composites and their variability.

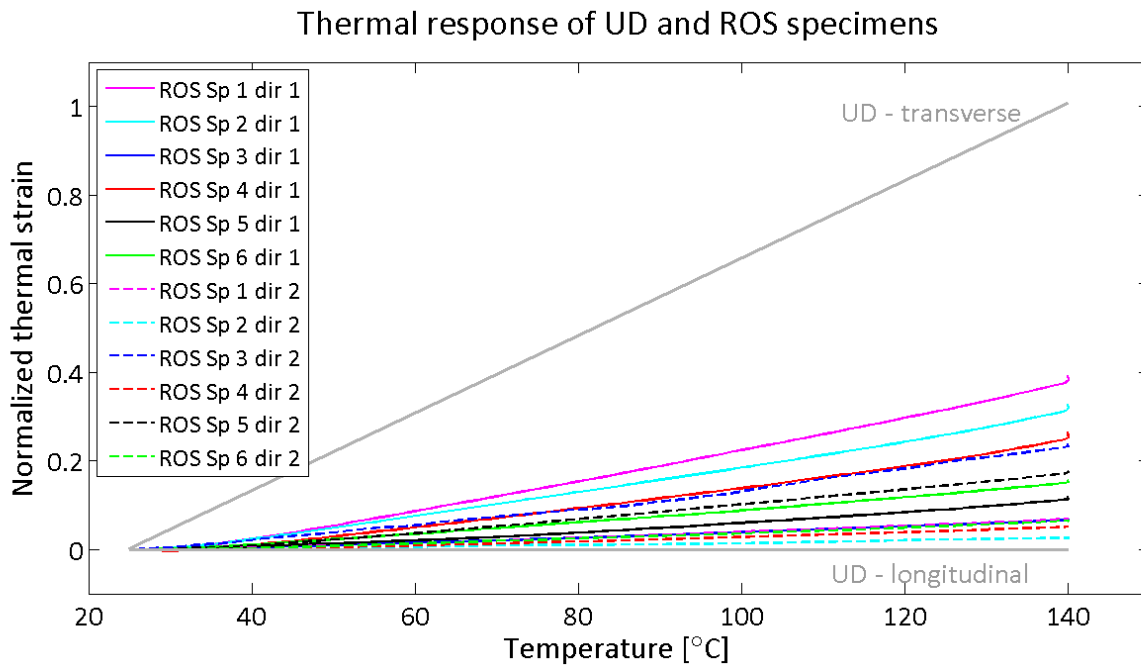


Figure 3-12 – Thermal expansion curves of UD and different ROS samples with 25 x 6 mm strands. *Sp* stands for specimen number and *dir* stands for directions

3.5 Concluding remarks

This chapter presented an overview of the manufacturing process and gave an explanation behind the choice of different processing parameters. The main manufacturing defects that might occur in ROS panels are: (i) the white discoloration of the surface caused by the loss of pressure during cooling due to temperature gradients and (ii) warpage of the panels caused by in-plane heterogeneity of the material. The former problem can be mitigated with a better mould or press design. The latter is inherent to the material and is improved for panels or parts that contain

smaller strands and have higher design stiffness. In general, the influence that strand size and intrinsic material heterogeneity have on the properties of ROS composites will be an ongoing theme in this thesis. The following chapters will discuss the experimental work done to investigate the effect of aforementioned parameters on mechanical properties of ROS composites.

Chapter 4

Tensile properties

This chapter will cover the experimental work that was done to characterize and explain tensile properties of ROS composites. Initially preliminary tests were conducted to evaluate the significance of size effects associated with material microstructure (i.e. strand size) and test parameters (i.e. specimen width). For these tests carbon/PEEK prepreg from a different manufacturer than that selected by the industrial partners was used. While the properties corresponding to the two carbon/PEEK systems were different, the overall trends were the same. Next, full scale tests were designed and performed based on the preliminary results. Finally, supplementary tests were ran with the aim to explain the size effects in ROS composites by illustrating the load transfer mechanisms in a simple laminate with discontinuous fibres. All data pertaining to ROS composites had to be normalized. This was required by our industrial partners.

4.1 Preliminary tests

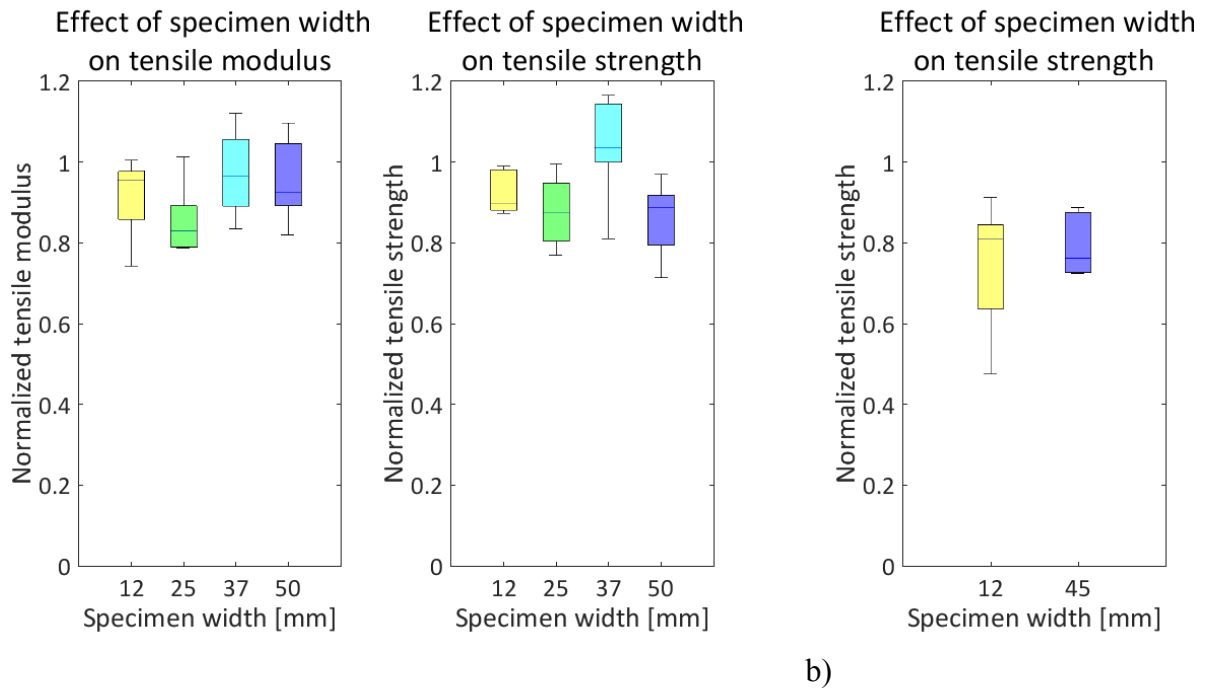
It is a common practice to follow standardized test procedure when measuring mechanical properties. For tensile properties, ASTM 3039 can be used for discontinuous and continuous-fibre composites. However, it does not fully account for the size effects associated with ROS composites. For instance, a gauge section has to be at least one characteristic repeating unit (or unit cell) in size in order to represent average properties of a heterogeneous material, but definition of a unit cell size for an ROS material has yet to be established. Hence, the first set of

preliminary tests was performed to evaluate the sensitivity of tensile properties to the specimen width, as will be presented in section 4.1.1. At the start of the project, only papers by Feraboli *et al.* [27-31], which dealt with thermoset-based ROS composites, were available in the public domain, and it was interesting to see how sensitive thermoplastic-based ROS composites would be to the strand size. Results of these tests will be discussed in section 4.1.2.

4.1.1 Effect of specimen width

To evaluate the effect of specimen width on tensile properties, panels with a common strand size of 25 x 6 mm and thickness of 3 mm were manufactured. From the panels, specimens were cut to a length of 250 mm and had different widths: 12, 25, 38 and 50 mm. Six specimens per width were tested. Two pieces of retro-reflective tape (i.e. markers) were placed on the coupon surface 75 mm apart to allow for strain measurement with a laser extensometer (MTS LX500). A piece of silicon carbide mesh (McMaster Carr #30715) was placed between the specimen and the grips to prevent slippage. Specimens were tested using a hydraulic MTS 100kN machine and were loaded at a rate of 1 mm/min.

The summary of strength and modulus data is presented in Figure 4-1a. No major differences were found between the results pertaining to different coupon widths, since the average modulus and strength were within the variability bounds for each width category. These results suggest that there is no need to use excessively wide coupons (i.e. twice the strand length) for tensile testing of ROS materials. These results were later repeated using the carbon/PEEK material, which was meant for the full-scale investigation. Same strand size and loading conditions were used, and two specimen widths (12 and 45 mm) were considered. Similar results were obtained as shown in Figure 4-1b. However, even though the average measured strength was the same for both specimen widths, the variability was significantly higher for narrow specimens. Hence, it should be noted that the use of specimens that are narrower than the strand length can lead to large variability in the measured data and would require a large number of test coupons in order to achieve viable statistical significance.

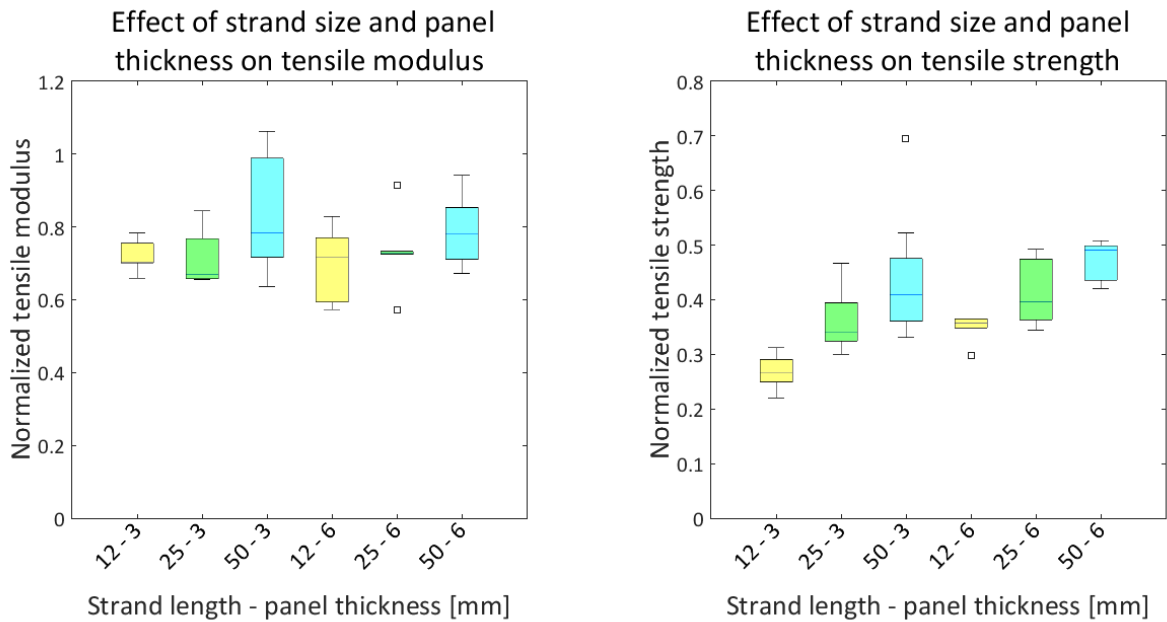


a) **Figure 4-1– Effect of specimen width on tensile properties of ROS composites made of carbon/PEEK material**
a) used only for preliminary studies and b) used predominantly for full scale tests

4.1.2 Effect of strand length and panel thickness

In order to evaluate the effect of strand length and panel thickness on tensile properties, six panels were fabricated with strand lengths of 12, 25 or 50 mm and panel thickness of 3 or 6 mm. Strand width was kept constant at 6 mm and specimen width was 25 mm. The same test method as described in section 4.1.1 was used. Test results were normalized using approximate properties of QI CF laminates and are summarized in Figure 4-2.

From Figure 4-2a, it appears that average modulus increases slightly with increasing strand length. However, statistical analysis using ANOVA showed that due to large variability of the data, strand length does not affect modulus. Similarly, Feraboli *et al.* [27] showed that in the case of thermoset-based ROS composites strength increases with increasing strand length, while modulus is unaffected by it. The fact that modulus is unaffected by strand length (in the range of 12-50 mm) is in line with the assumption of fibre continuity, as was discussed in Chapter 2. Also from Figure 4-2a, it seems that panel thickness does not have a significant effect on modulus.



a)

b)

Figure 4-2 - The effect of strand length and panel thickness on a) modulus and b) strength

Results presented in Figure 4-2b indicate that higher tensile strength is achieved with ROS panels that consist of longer strands. In the case of 3 mm thick panels, strength increases from 0.25 to 0.5 as strand length increases from 12 to 50 mm. Nonetheless, even the highest strength obtained with 50 mm long strands is still significantly lower than that of QI CF laminates. Since the strength of ROS composites is low despite the fact that the continuity assumption is met, there must be other factors besides fibre length efficiency that influence strength. This relationship will be explored in more detail in the subsequent sections. It is also noteworthy that the high strength of the 3 mm panel with 50 mm long strands is also accompanied by high variability. This variability is related to the heterogeneous microstructure of these specimens. Overall, lower variability is observed in the case of 6 mm thick panels. ROS panels are expected to become more statistically homogeneous when they consist of smaller strands and are thicker. It was of particular interest to find a strand size which would provide good compromise between mechanical properties and repeatability, thus within the scope of the full scale tests were:

- characterization of the strand length effect, and
- explanation of the mechanisms behind it

4.2 Full scale tests

4.2.1 Procedure

The following strand sizes (length x width) were studied: 6 x 3, 12 x 3, 12 x 6, 25 x 6, 50 x 6, 25 x 12 and 50 x 12 mm (Table 3-1). Two panel thicknesses were considered: 2.5 or 6 mm. CF UD $[90]_{18}$ and QI panels with $[0/\pm 60]_{3S}$ layup were manufactured to allow for benchmarking. These panels had a thickness of 2.5 mm. For each strand size, eight specimens were tested in tension as per the ASTM D3039. Specimens were 250 x 25 mm in size and had a gauge section of 150 x 25 mm. QI CF panels were cut such that specimens had $[0/\pm 60]_{3S}$ or $[90/\pm 30]_{3S}$ fibre orientations.

During testing, strain was measured using the DIC technique. The validity of this technique will be demonstrated in the next section. The speckle pattern was created by using white spray paint (Rust-Oleum) and black air-brushing paint (Badger, air-opaque). A single 5 megapixel camera (Point Grey, model Flea2 FL2G-50S5M) with AF75-300 mm Tamron lens was used. Specimens were loaded at 2 mm/min, and LVDT data and DIC images were captured at 5 Hz. Image analysis was performed using VIC-2D software from Correlated Solutions. Stress-strain curves were created by using the average strain from each DIC image. Modulus was computed by finding the slope of the stress-strain curve in the strain interval of 2000 – 4000 $\mu\epsilon$. Also, DIC data was used to compute the Poisson's ratio of the material. It was calculated by finding the ratio between the slopes of the longitudinal and the transverse stress-strain curves in the range between 2000 – 4000 $\mu\epsilon$. This strain range was chosen for the calculation of modulus and Poisson's ratio, because it was close to the range recommended by the ASTM D3039 test standard (1000 – 3000 $\mu\epsilon$) and was not as affected by the noise from the DIC strain data.

To analyze the state of damage of ROS composites after failure, post-mortem microscopy was performed on short (6 x 3 mm), mid (25 x 6 mm) and large (50 x 12 mm) strand ROS specimens. In preparation for microscopy, specimens were mounted into EpoThin2 epoxy system (Buehler), then polished using Forcipol 1V (Metkon automatic polisher) and finally examined under an automatic microscope (Nikon L150 and Clemex Tango/Captiva). The exact grinding and polishing sequence was as follows:

- Diamond disks with 220 grit until plane → 600 grit for 4 min → 1200 grit for 4 min
- Polishing cloth (MetLab) and 12.5 μm Al_2O_3 particles for 5 min → 0.3 μm part. for 5 min

4.2.2 Validation

The overall applicability of DIC was checked by testing an aluminum specimen in tension and comparing stress-strain curves generated with full-field DIC and 25 mm long extensometer (634.11F-25, MTS), as shown in Figure 4-3. The gauge section used for DIC measurements was 100 x 25 mm. From Figure 4-4, it is evident that correlation between the two stress-strain curves is good.

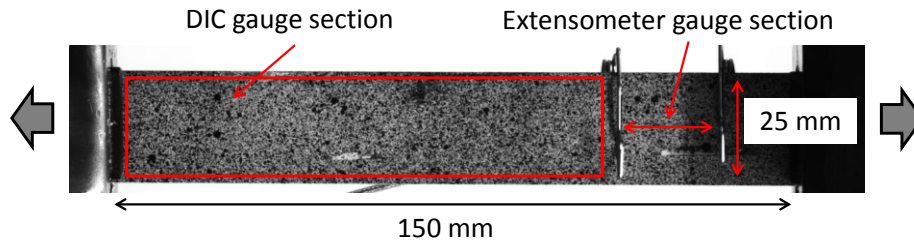


Figure 4-3 – Painted tensile specimen instrumented with an extensometer

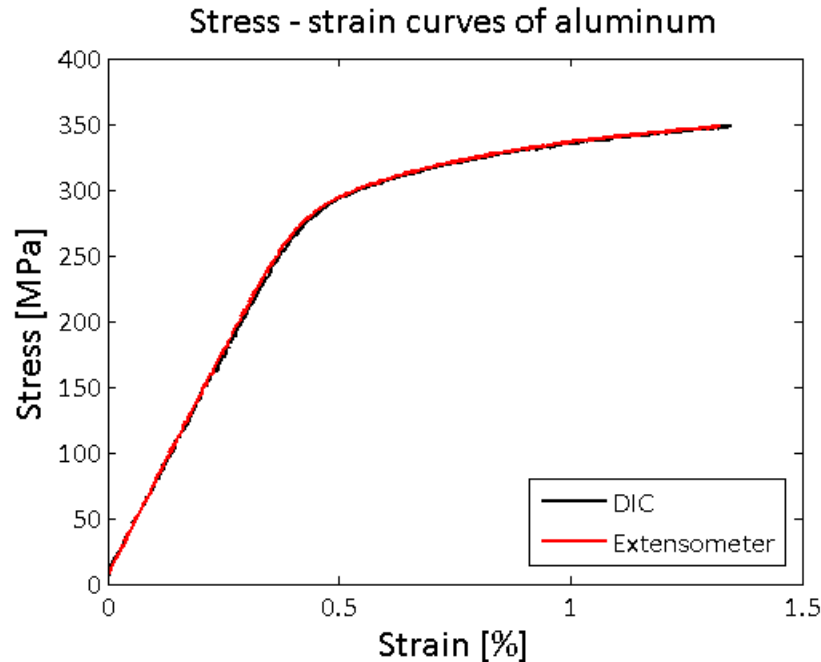


Figure 4-4 – Comparison between stress-strain curves measured using DIC and an extensometer

Variability in the strain-field obtained with DIC can be caused by actual material variability or simply by the noise in the data, hence it was important to distinguish between the two. DIC is sensitive to test conditions such as lighting and vibrations caused by the MTS machines, as well as analysis parameters like subset and step size, to name a few. While noise could not be completely eliminated, it could be minimized and quantified. Prior to running the actual tests, sample photos of a gripped but stationary specimen were recorded and analysed. While the strain was expected to be constant since the load was constant, non-zero strain values were always obtained and the pattern of the strain-field would appear to flicker from one image to the next. Such strain variability is indicative of the noise. The test conditions were adjusted to keep the strain variability within each image to at most $\pm 300 \mu\epsilon$. This ensured that areas of actual high and low strains would be easily identifiable as the load increased, since the strain difference between them is greater than $\pm 300 \mu\epsilon$, as shown in Figure 4-5b. Also, the scatter of the average strains was checked and was kept below $50 \mu\epsilon$, since the average strains were used to construct the stress-strain curves. From Figure 4-4 is evident that despite this level of noise in the measured data, the stress-strain curve is smooth. For DIC analysis, the following settings were used and they yielded good results:

- Subset size of 35 pixels, which correlated to about 3 mm
- Step size of 15 pixels, which correlated to about 1 mm.

A relatively large subset and step size were used to minimize the amount of noise observed on the strain-fields especially at low loads. The use of a large subset and step size resulted in a coarser averaged out strain-field, which may be inappropriate for monitoring of local strain inhomogeneities. ROS composites are heterogeneous on the meso-scale, and despite the use of large subset and step size, the presence of high and low-strain regions was clearly visible, as shown Figure 4-5. Overall, the chosen settings were deemed to be reasonable, because they do not have an effect on the average strains (i.e. measurement of global modulus) and because, accurate measurement of local strains was not required. The same settings were used for the analysis of compression and shear test data.

4.2.3 Modulus

The strain maps obtained with DIC show that strain-fields of ROS composites are significantly more variable than those of CF laminates. This difference is shown in Figure 4-5, where both specimens exhibit an average strain of 4000 $\mu\epsilon$, but the standard deviation corresponding to an ROS composite is 1350 $\mu\epsilon$ while that of a CF laminate is 250 $\mu\epsilon$. The large variability of the strain-field signifies that modulus of ROS materials is also highly variable. It would be difficult to measure global modulus of the specimen with a strain gauge since it would capture localized strain, which would not be representative of the entire specimen. Whereas, strain-fields captured with DIC can be averaged out to get mean strain and modulus.

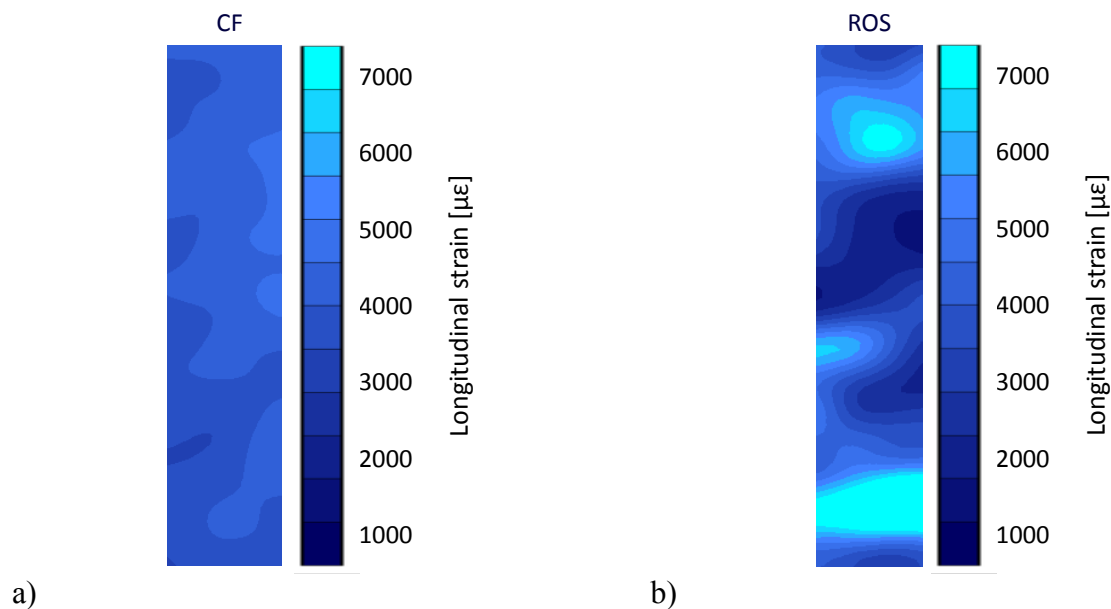


Figure 4-5 – Comparison between the DIC full-field strain maps of a) QI CF and b) ROS (6 x 3 mm strand) composite

An alternative way of demonstrating strain variability is to plot histograms that represent the strain evolution with increasing loading, as is shown in Figure 4-6. The shape of the CF histogram curves remains the same as the load increases meaning that scatter in the strain values is caused by the noise associated with the DIC technique rather than the actual material variability. On the contrary, the shape of ROS histograms becomes more spread out, since strain increases at different rates at different locations of the specimens. Thus, evolution of ROS histograms demonstrates variability of modulus.

The effect of strand size on modulus is summarized in Figure 4-7. The presence of scatter in the results makes it difficult to identify a particular trend. Nonetheless, if only the moduli of the composites with the shortest (6 mm) and the longest (50 mm) strands are compared, it is clear that longer strands yield higher modulus (70 vs. 80 %).

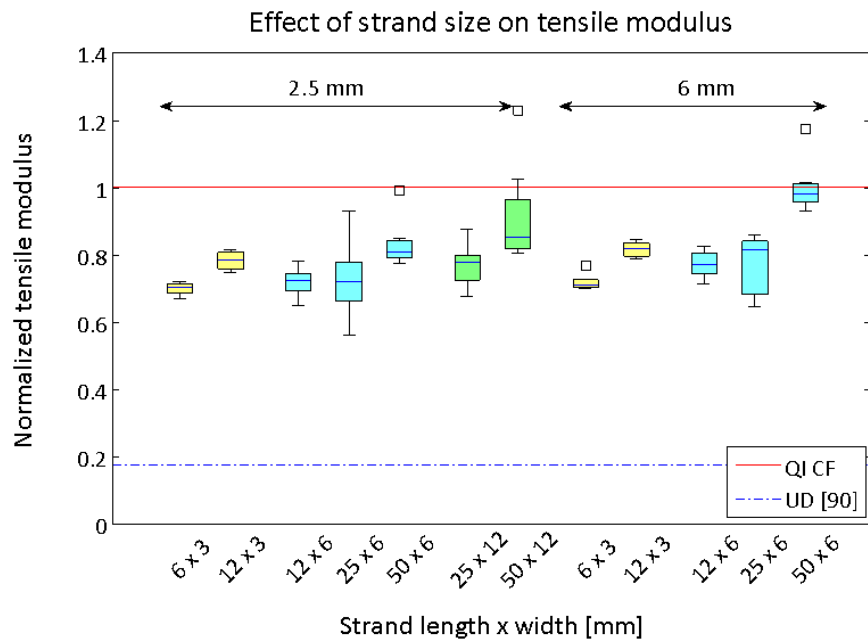
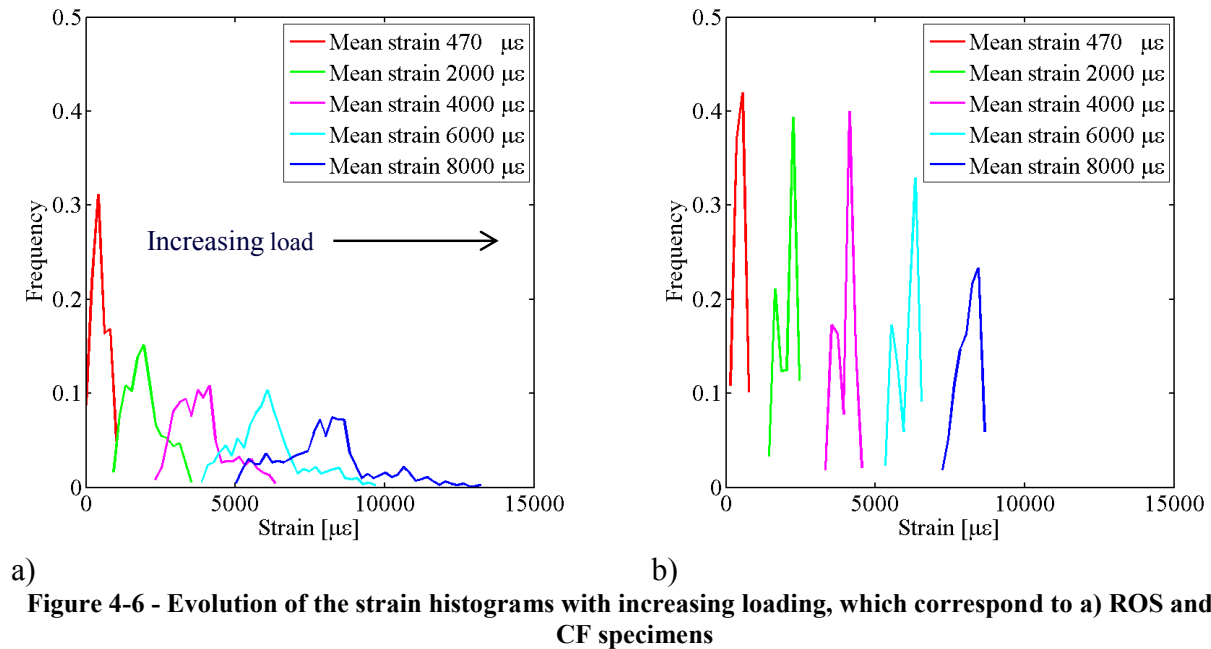
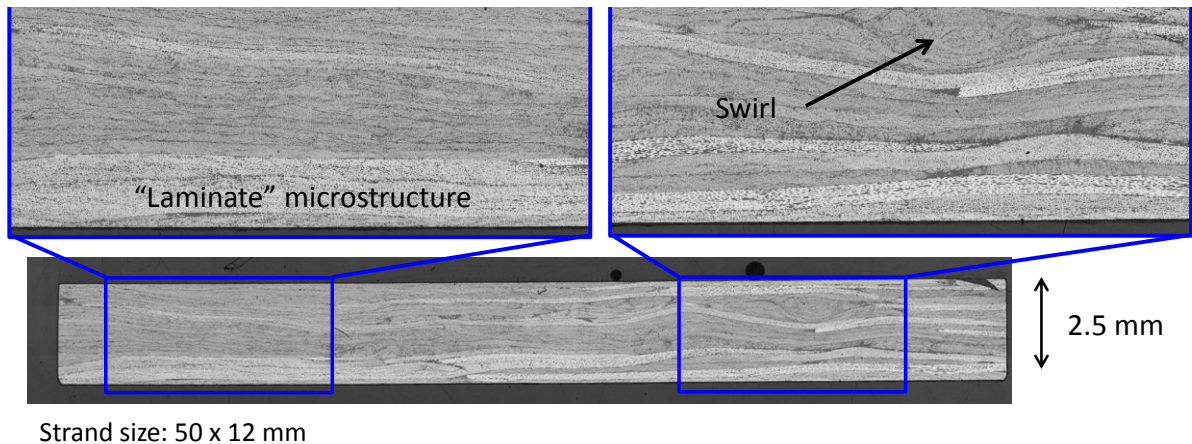
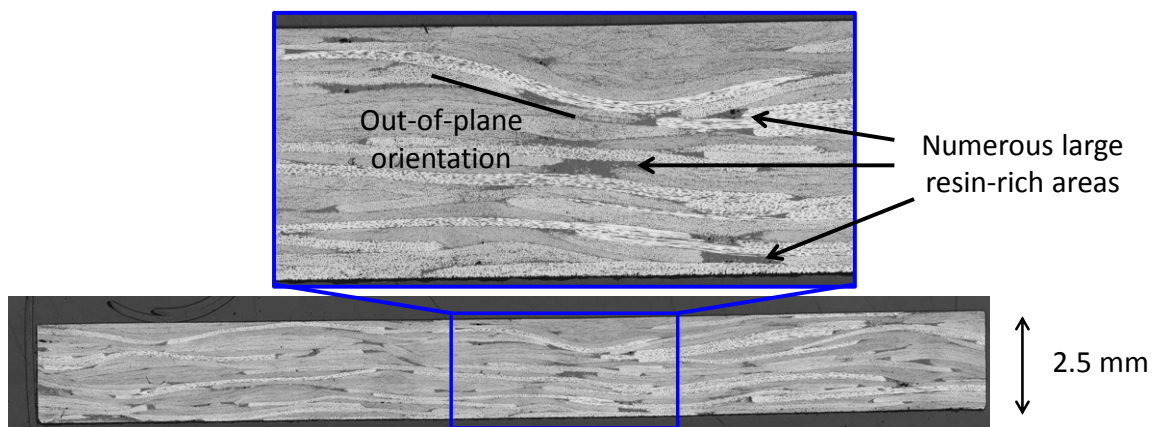


Figure 4-7 – Effect of strand size on tensile modulus

Dependency of modulus on the strand size can be explained by examining the micrographs of ROS composites, as depicted in the Figure 4-8. There is a striking difference between the microstructure of short and long-strand ROS specimens. In the case of the former, numerous strands are curving out-of-plane, while in the latter strands are neatly stacked resembling a CF laminate. This observation explains why the modulus of short-strand ROS is lower than that of QI CF laminates, but for long-strand ROS it is more comparable to that of QI CF. While short-strand ROS composites have lower in-plane modulus, they also offer improved repeatability of the results. The effect of strand size on the homogeneity of the material, as was shown previously in the case of warpage, is once again demonstrated. Panel thickness does not seem to have a significant effect on modulus.



a)



b)

Figure 4-8 – Microstructure of ROS composites with a) long and b) short strands

Results of the Poisson's ratio measurements are presented in Figure 4-9. It is evident that Poisson's ratio is in the same range as that of QI laminates. However, it is accompanied by large variability, which can be explained by the fact that transverse strain is small and is of the same order of magnitude as the DIC noise. Hence, given the accuracy of the current test set up, variability of Poisson's ratio should be attributed to noise rather than actual material variability.

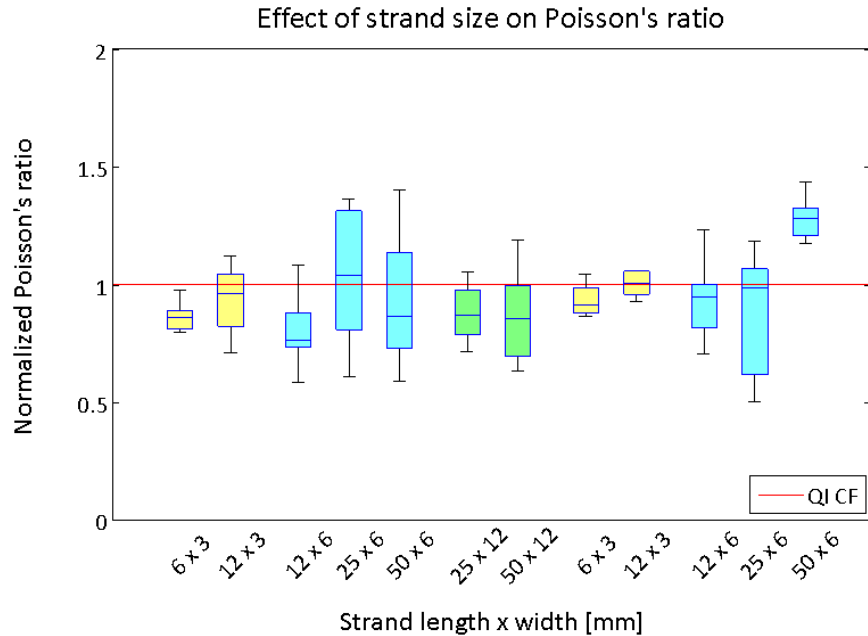


Figure 4-9 – Effect of strand size on Poisson's ratio (normalized to QI CF value)

4.2.4 Strength

Measured strength of ROS composites is summarized in Figure 4-10. Overall, strength obtained with ROS panels is less than 60 % of the strength of QI CF laminates. Performance of ROS composites is significantly lower than that of QI CF laminates even though fibres are fairly long and have high length efficiency. The reasons behind strength reduction are believed to be material heterogeneity and matrix-dominated properties, both of which will be explored in more detail in the next section where failure mechanisms will be investigated.

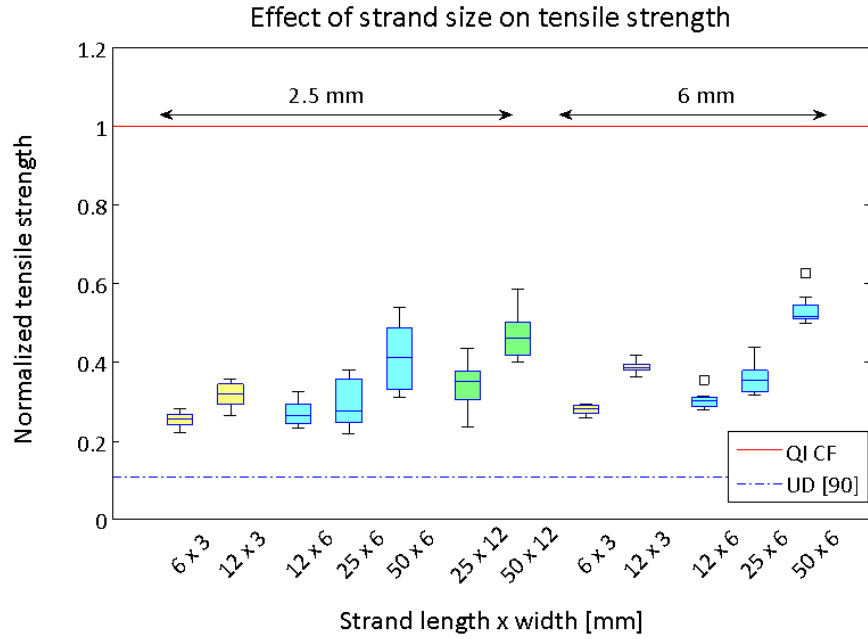


Figure 4-10 - Effect of strand size on tensile strength

Another important aspect to examine (in addition to the average strength) is the variability in the measurements, because it has to be taken into account when calculating design allowables. The common practice in aerospace industry is to use the b-basis (or the a-basis) design allowables, which take into account the average strength value (σ_C) and the standard deviation (s) associated with the property of interest. A similar approach is used in this thesis to capture the influence of scatter by computing the 95 % confidence level for strength, which will be termed as an allowable for simplicity, using the following equation:

$$\text{allowable strength} = \sigma_C - 2s \quad \text{Eq. 4-1}$$

Results are summarized in Figure 4-11. For the case of thinner panels, it is evident that while longer strands offer higher average strength, the design allowables for different strand lengths are essentially the same due to the increased variability in the data. The only exception is the strength of 50 x 12 mm strand ROS specimens, but it is difficult to say whether this result represents an actual improvement of properties or is just an artifact caused by a small gauge section. Nonetheless, the computed design allowables demonstrate once again that heterogeneity associated with ROS composites has a detrimental effect on material properties and has to be

carefully considered at the design stages. A similar result was also reported in a paper by Eguemann *et al.* [8]. Improvement in homogeneity is achieved with thicker panels which exhibit lower variability and consequentially offer higher strength allowables.

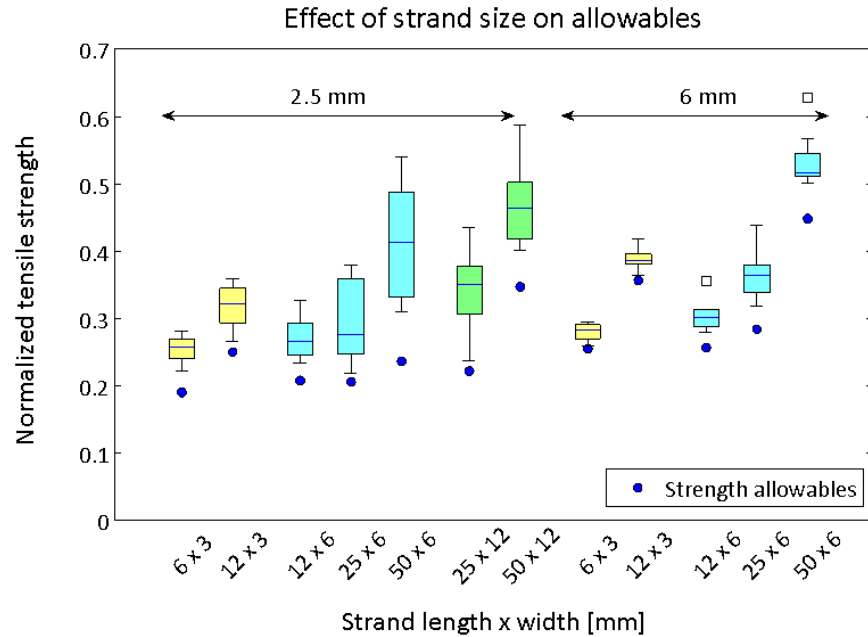


Figure 4-11 – Effect of strand size on design strength (allowables)

An alternative way of presenting the strength and modulus data is to compare stress-strain curves of CF and ROS composites with different strand lengths, as is shown in Figure 4-12. It is evident that stress-strain curves of ROS composites with short strands overlap and fall in-between the curves of continuous-fibre QI and UD [90] laminates. On the other hand, curves corresponding to long-strand ROS composite band the QI CF curves, at least with respect to the slope of these curves. This difference highlights that modulus of short-strand ROS composites is more matrix dependent than that of long-strand ROS.

It is also noteworthy, that while the range of failure strengths of ROS composites falls somewhere between that of UD [90] and QI laminates and little correlation can be made between them, the failure strain of ROS composites is actually close to the failure strain of CF [90]. Hence, failure strength of ROS is more matrix-dominated than fibre-dominated. This point will

be further explored in the chapters on modelling. Subsequent sections in this chapter will rely on post-mortem analysis and additional tests in order to explain the origin of the strand-size effect.

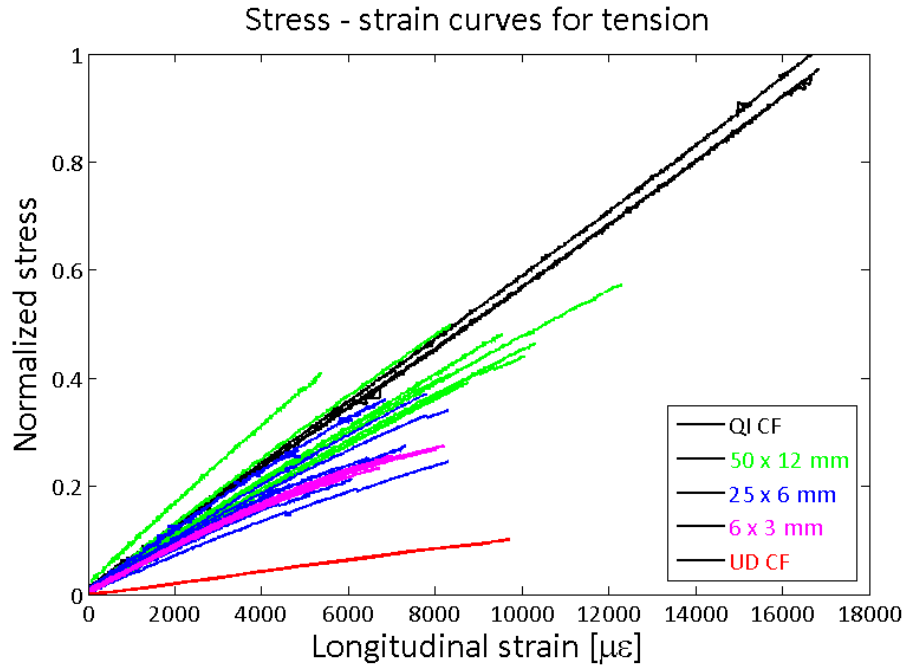


Figure 4-12 - Comparison between the stress-strain curves of CF and ROS specimens

4.2.5 Failure

The two possible explanations for the large reduction in strength of ROS composites in comparison to QI laminates are matrix-dominated failure modes and material heterogeneity.

Continuous-fibre quasi-isotropic laminates fail due to fibre failure; while ROS composites experience a matrix-dominated failure in a form of step-wise disband between the strands (i.e. interlaminar shear between the strands). This type of failure is shown in Figure 4-13. This failure mode is typical for discontinuous reinforcement, whether it is short fibres, ceramic platelets or nacre (shells [78, 82]). The longer are the strands and the overlap among them the higher is the ability of the material to withstanding crack propagation, which occurs in the direction of the least resistance, as shown in Figure 4-13. Hence, composites with longer strands are expected to be stronger, because statistically they have longer overlaps. This is actually evident from the failure regions taken from long and short strand ROS, as is shown in Figure 4-14. Strand

overlaps and the crack path are noticeably longer in the case of long-strand ROS, and the failure strength is higher. Also, by referring back to Figure 4-8, it is evident that short-strand ROS composites have large resin-rich areas around the strand ends, which is understandable considering the chaotic strand placement. These resin-rich areas would act as crack initiation sites and the ability of that cross-section to withstand crack propagation will depend on the overlap efficiency of the strands. Hence, it is not surprising that short-strand specimens have lower strength than their long-strand counterparts, since they are more prone to crack initiation and are less capable of hindering crack growth.

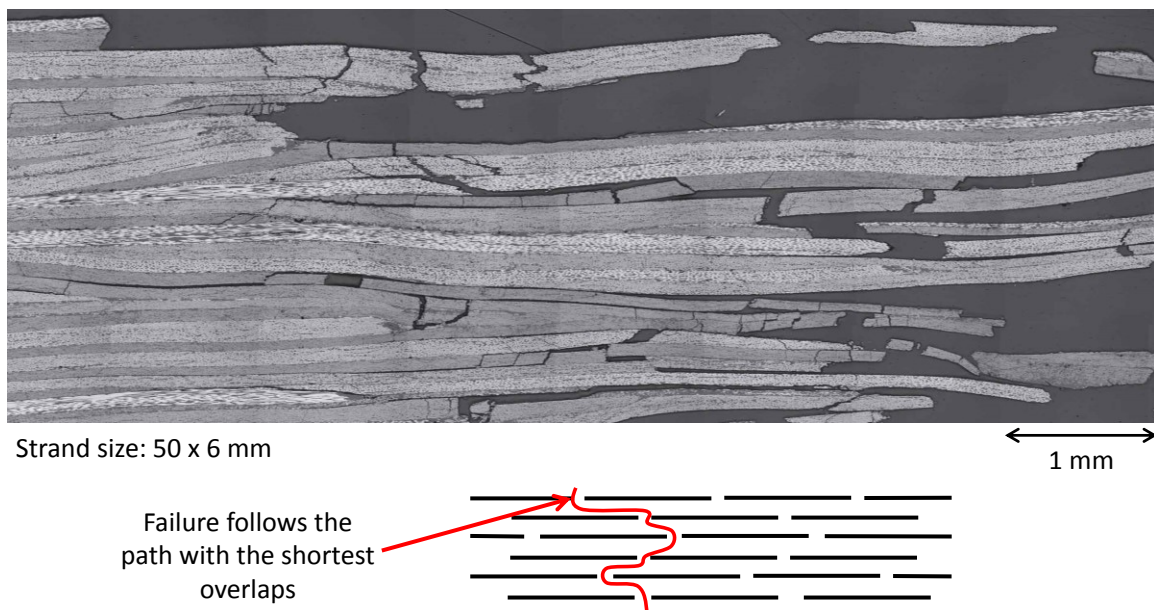


Figure 4-13 – Crack propagation mechanism in ROS composites

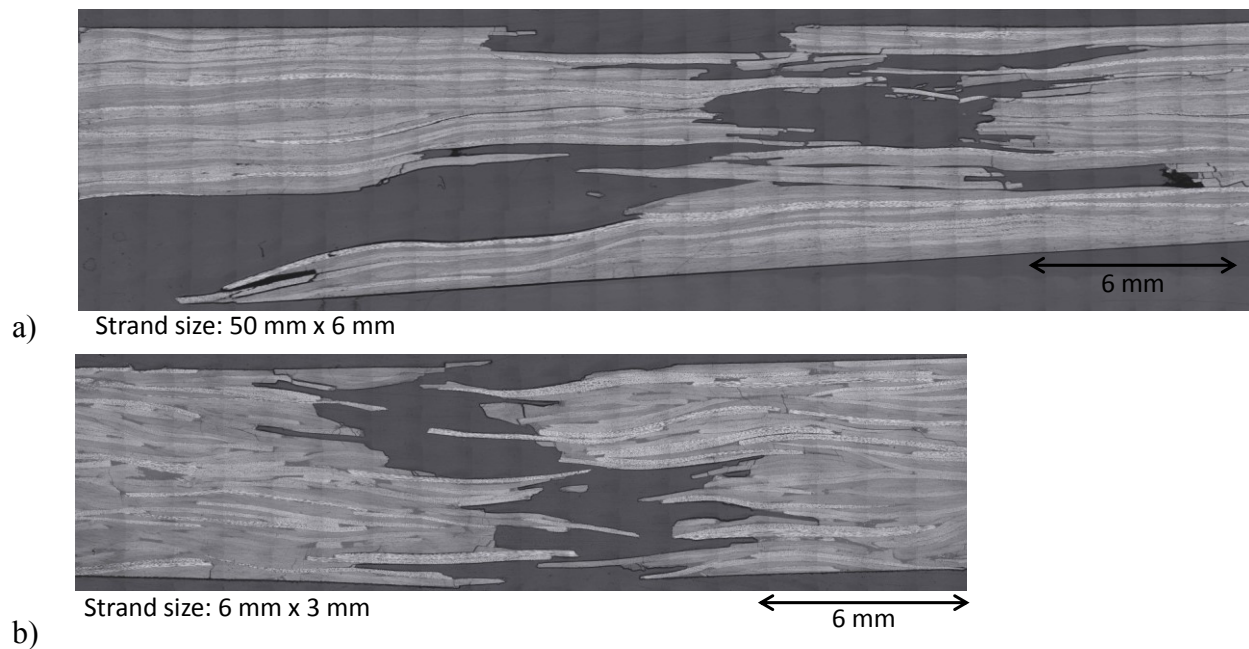
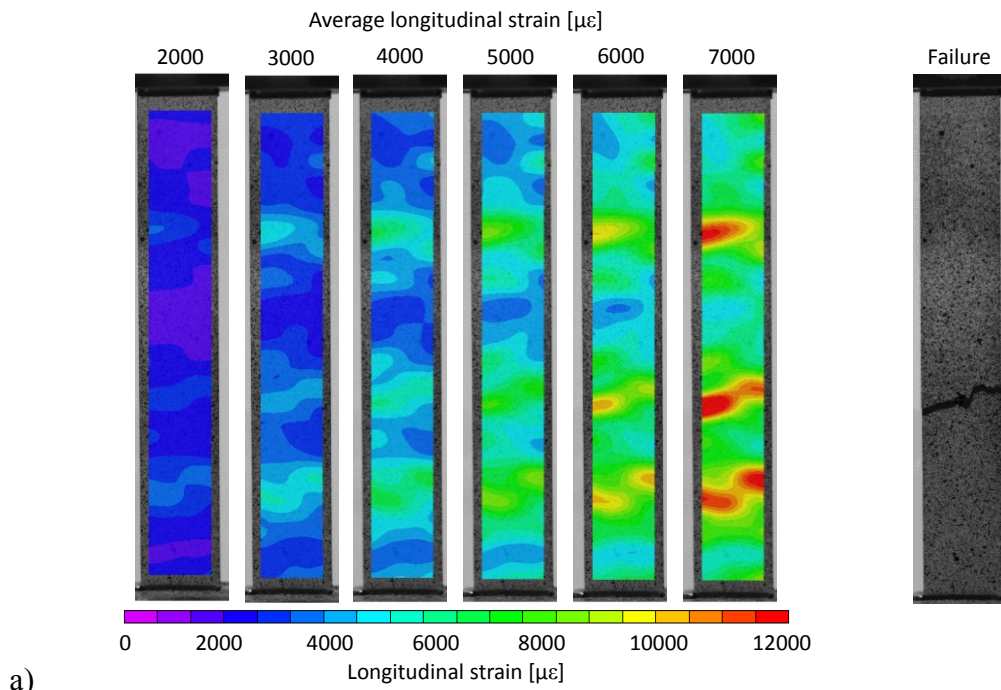


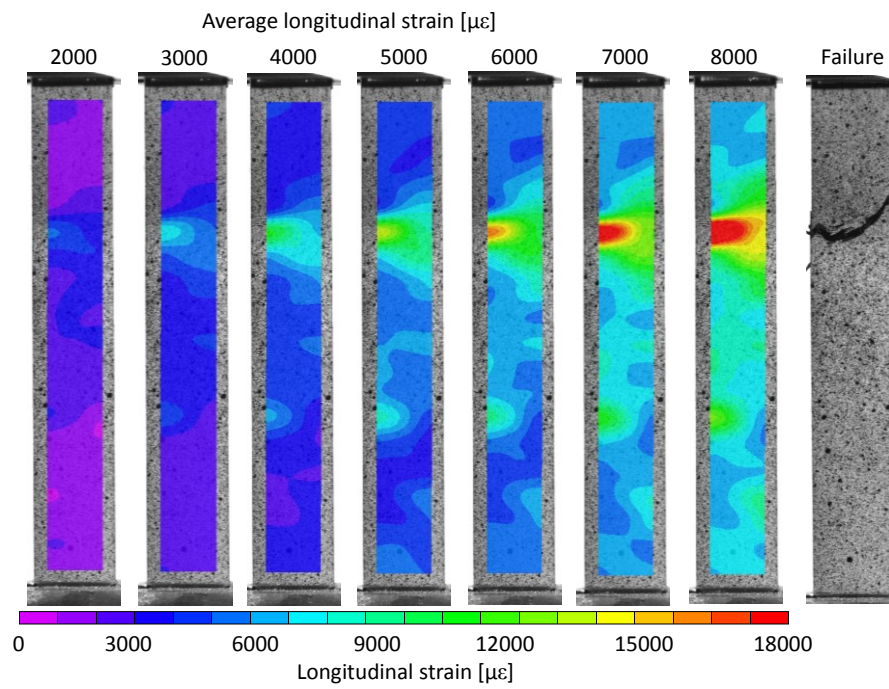
Figure 4-14 - Failure region of ROS composites with a) long and b) short strands

Moreover, due to material heterogeneity, ROS specimens fail at a weak-spot while little damage develops away from the failure region. This localization of damage could be observed from the evolution of the strain-field (Figure 4-15) and the post-mortem microscopy (Figure 4-8).

From Figure 4-15 it is evident that the strain-field is non-uniform and that failure occurs in the vicinity of a high-strain region presence of which is noticeable even at low loads. Since regions with high strain are more compliant than the rest of the specimen, it can be postulated that material properties in that region are more matrix-dominated (i.e. have fewer fibres oriented in the loading direction) than in the other areas, and hence high-strain regions serve as weak-spots for failure. Interestingly, these weak-spot usually occur close to the edge. The length of the strands along the edge is reduced due to cutting of the specimens, hence making that region weaker than the mid-section which is composed of strands of nominal length. It can be hypothesized that net-moulded specimens and parts would have higher properties than the cut-to-shape specimens. Specimens with large strands have at most two regions of high strain while specimens with small strands have multiple high-strain regions, demonstrating the effect of homogeneity.



a)



b)

Figure 4-15 – Evolution of the full-field strain with loading, corresponding to ROS composites with a) short and b) long strands

After failure, specimens were sectioned in the regions that were identified as weak-spots by DIC to check for the presence of any defects or cracks, as is shown in Figure 4-8. Overall very little damage was observed, which implies that specimens failed at the weakest-spot while the rest of the material was still intact. It is also possible that damage propagated quickly once it initiated, and hence only a few small cracks were detected. It was difficult to identify any major defects in these sections. Figure 4-8a shows one defect (curling of strands), which could potentially cause a high-strain region. Similar defects were also reported by Feraboli *et al.* [28].

4.2.6 Summary

The foremost conclusion of tensile tests is that mechanical properties, especially strength, are dependent on strand length. In general, while average strength and modulus increase with increasing strand size, so does the variability. Variability is an important property to consider on its own, because it is involved in the calculation of the design allowables. Also, even in the case of long-strand ROS composites, their strength is significantly lower than that of QI laminates. This strength reduction is attributed to matrix-dominated failure modes and material heterogeneity.

The principle failure mode associated with ROS composites is delamination among the strands, in which case longer strands are expected to be more resistant to this type of failure. This hypothesis will be further explored in the next section.

4.3 Additional experiments

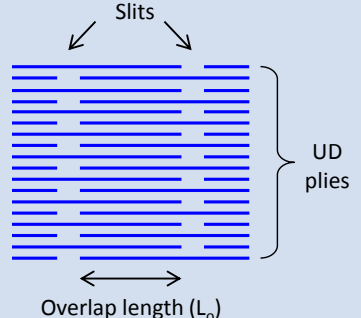
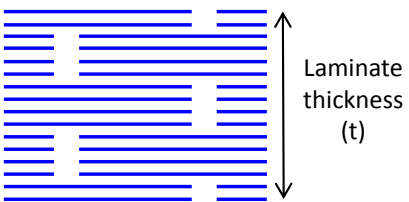
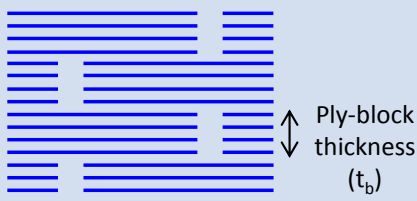
To further study the effect of strand length on strength, specimens with a simplified and controllable microstructure were used. That being said, UD slit laminates with different overlap lengths and stacking configurations were manufactured and tested. These experiments were an extension to work done by Czel [71] and Taketa [72] but for a thermoplastic instead of a thermoset resin. The objective of this study was to compare how matrix strength and toughness influence failure characteristics of such laminates and to generate experimental results that would facilitate the development of a strength model for ROS composites, which will be described in Chapter 8.

4.3.1 Experimental procedure

Laminates with slit plies were prepared by first cutting each ply the right size to fit into the mould, and then slitting it in the direction perpendicular to the fibres. In order to facilitate handling of the cut plies, a few millimeters along one of the edges were left uncut and the cut line was welded together using a hot gun. Plies were stacked with alternating slit locations to create overlaps. A summary of different overlap configuration that were manufactured and tested is shown in Table 4-1. It is noteworthy that layups A and B are not entirely symmetric in terms of the slit location with respect to the centerline.

Panels were manufactured using the same cure cycle as that used for the ROS panels, which was described in Chapter 3. The effect of the overlap length was studied through tensile testing of UD specimens in the fibre direction. Overall, the test set-up was the same as for the ROS specimens (section 4.2.1) including the specimen size, the loading conditions and the use of DIC for monitoring of the strain field.

Table 4-1 – Summary of different overlap configurations that were tested

Type	Number of plies	Number of overlaps (n)	Overlap length (L_o) [mm]	Stacking diagram
A	18	17	1.5, 3.5, 9.5, 20	
B	16	3	9.5	
C	16	4	9	

It was anticipated that failure of these specimens would occur due to one of these criteria: (i) matrix shear strength (Eq. 2-22), (ii) matrix toughness (Eq. 2-23) and (iii) fibre strength (Eq. 4-4). The first two criteria represent interlaminar ply failures, whereas the last criterion represents longitudinal normal ply failure. More detailed explanation can be found in Chapter 2.

$$\sigma_c = \frac{nL_o\tau_i}{t} \quad \text{Eq. 4-2}$$

$$\sigma_c = \sqrt{\frac{2E_b G_{IIc,IL}}{t_b}} \quad \text{Eq. 4-3}$$

$$\sigma_c = \frac{\sigma_L^T}{2} \quad \text{Eq. 4-4}$$

In these equations:

- n is the number of overlaps
- L_o is the overlap length
- τ_i is interlaminar shear strength (64 MPa see Chapter 5)
- E_b is the longitudinal modulus of UD plies (130 GPa [83])
- $G_{IIc,IL}$ is the mode II fracture toughness (1930 J/m² [84])
- t_b is the ply or the ply-block thickness
- σ_L^T is the longitudinal strength of UD plies (2280 MPa [83])

4.3.2 Results and discussion

The DIC results clearly capture the effect of slits on the strain-field in the specimen, as is shown in Figure 4-16. The strain at the slit location is twice as high as the global strain, since there are only half as many fibres carrying the load. Also, comparison between the stress-strain curves of Type A slit-ply laminates with short (1.5 mm) and long (20 mm) overlaps is shown in Figure 4-17. Strain values that were used to construct these curves were taken from a section that enclosed the overlap and the slits, as shown in Figure 4-16. Overall, it is evident that laminates with short overlaps have a non-linear stress-strain response, whereas the response of specimens with long overlaps is linear. Similar trends were observed with ROS composites, where specimens with short strands also exhibited non-linear behaviour, as shown in Figure 4-12. The non-linearity of the stress-strain curves can be attributed to matrix-dominated material response, meaning that the fibres are not long enough to achieve a high fibre length efficiency (i.e. are not fully loaded) and the matrix in the overlap region undergoes large plastic deformation. In the case of long overlaps, the fibres are fully loaded, while the resin deforms elastically over the major portion of the overlap.

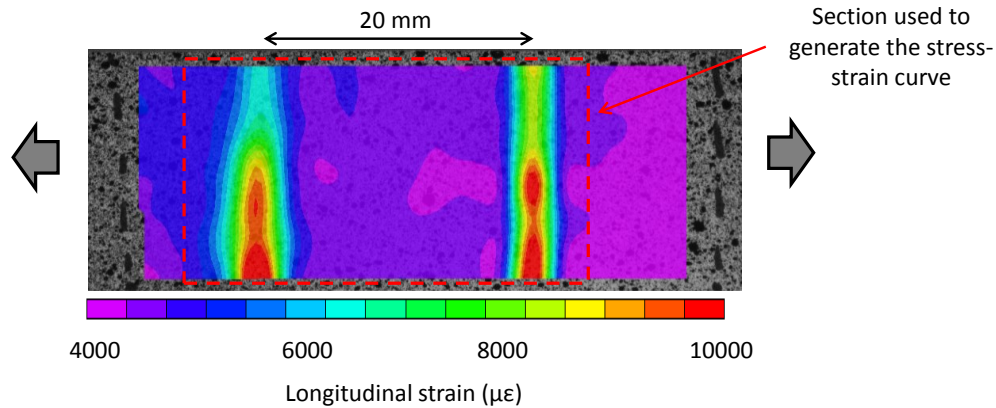


Figure 4-16 – Strain-field in a UD specimen with 20 mm overlap

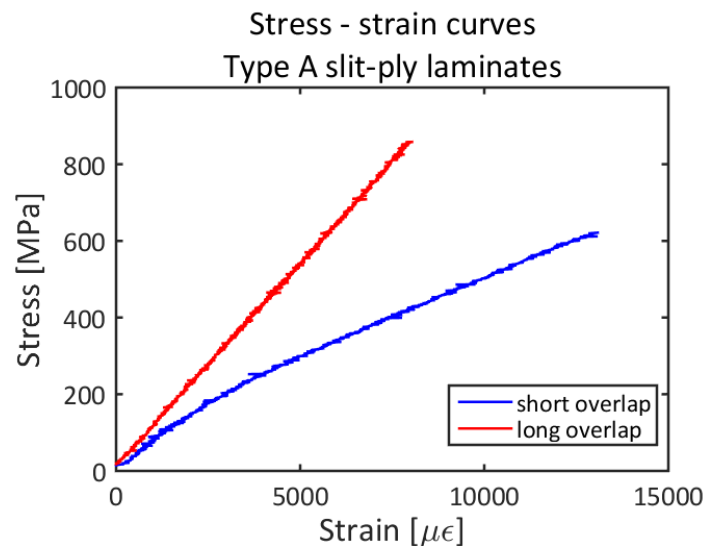


Figure 4-17 – Strain-field in a UD specimen with 20 mm overlap

Table 4-2 summarizes results pertaining to each specimen type (A, B, C) including the measured and the calculated strength values and micrographs depicting the failure morphology. Also for each overlap configuration, cells that correspond to the failure criterion/criteria that is/are representative of specimen strength and failure characteristics are highlighted in the table.

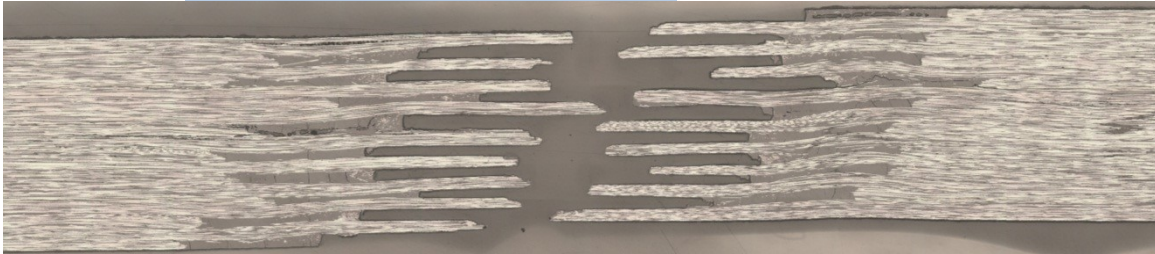
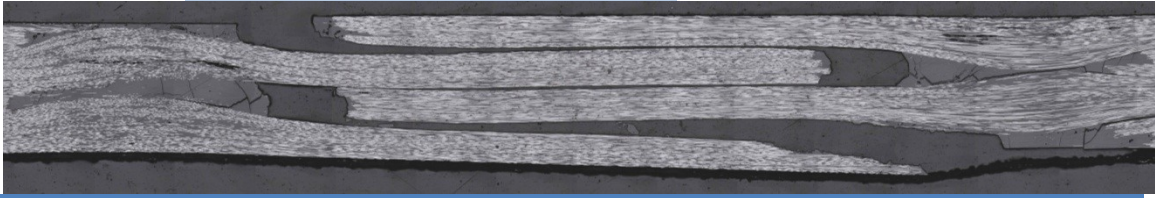
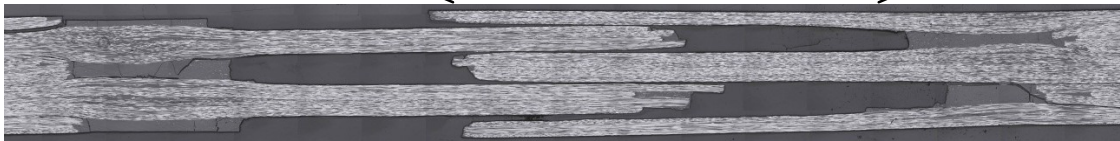
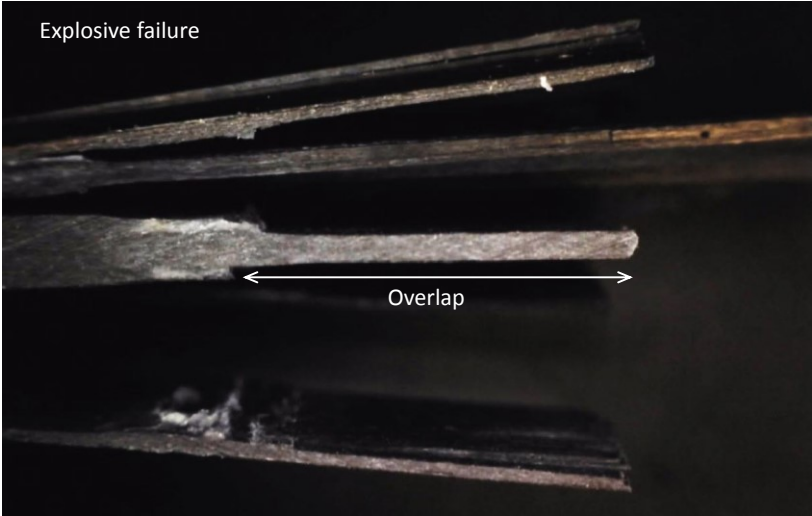
In the case of Type A, only specimens with the shortest overlap length (1.5 mm) failed through stable delamination or pull-out, and their strength could be reasonably estimated using the matrix shear strength criterion. The rest of the specimens failed due to fibre tension at the slits, and based on the three strength criteria, fibre strength was the lowest.

Type B specimens failed due to stable delamination. However, their measured strength was only 60 % of the calculated one. This difference can be explained by the premature delamination of the outer ply-blocks (i.e. four outer plies forming the outmost overlap) due to peel stresses. During the test, it was evident that failure initiated at the surface, and it was possible to hear the progressive cracking of each overlap. This problem was addressed in the paper by Czel *et al.* [71], and they recommended using thinner surface ply-blocks.

To mitigate the problem of peel-stresses, outmost ply-blocks in the Type C specimens were thinner than the inner ones (2 vs. 4 plies). As a result, the measured strength was as high as the predicted strength. Interestingly, matrix shear strength and toughness criteria predicted very similar strength values, and both failure modes were observed. Some specimens showed stable pull-out or delamination of the overlaps, which was the same failure mode as that observed with the Type A and B configurations. The other specimens underwent unstable or explosive failure where they essentially disintegrated into small pieces. It was evident that the ply blocks were fully delaminated, hence signifying that overlap or specimen strength was independent of the length of the delaminated region and was governed by the fracture toughness of the material.

It is also noteworthy that failure modes observed with slit UD laminates resemble those of ROS composites (Figure 4-13 - Figure 4-14). Hence suggesting that slit laminates, which can be designed and manufactured in a controlled way, can be used to study the fundamentals of failure mechanics of ROS composites.

Table 4-2– Summary of measured and calculated strength data and failure morphologies of the slit panels

Type	Overlap length [mm]	Measured strength [MPa]	Matrix strength criterion [MPa]	Matrix toughness criterion [MPa]	Fibre strength criterion [MPa]
A	1.5	744	774	1907	1140
					
	3.5	1050	1535	1907	1140
	9.5	1080	4170	1907	1140
	20	931	8775	1907	1140
B	9.5	520	880	950	1140
					
C	9	1100	1050	950	1140
	<div>Stable pull-out</div> <div>Overlap</div> 				
	<div>Explosive failure</div> <div>Overlap</div> 				

4.3.3 Summary

Overall, the results of this short additional study highlight the important role that the three failure criteria have on the strength and failure mechanics of slit UD laminates. It can be anticipated that the same failure criteria dictate the strength of ROS composites. The adaptation of the aforementioned failure criteria to strength modelling of ROS composites seems to be rather promising, since these criteria can capture the effect of strand length and the correct failure modes.

4.4 Concluding remarks

Thus far, investigation of the mechanical properties of ROS composites has shown that strength and modulus increase with increasing strand length. One reason for this effect is that longer strands increase the chance of having larger overlaps and improving the load transfer mechanism among the strands. Nonetheless, with respect to industrial design, better properties can be attained with long-strand ROS only if adequate level of homogeneity can be achieved. Thus, for relatively small and thin parts it is recommended to use short strands in order to achieve better geometrical stability, mechanical properties and repeatability. For larger and thicker parts, longer strands can potentially offer higher mechanical properties without compromising repeatability and are worth a consideration. Subsequent chapters will further explore the effect of strand size on compressive (chapter 5) and shear (chapter 6) properties, and finally will propose in-plane (chapter 7) and through-the-thickness (chapter 8) methods that could be used to predict properties of ROS composites from the properties of the constituents.

Chapter 5

Compressive properties

This chapter will discuss the effect of strand size on compressive properties of ROS composites and more notably will give recommendations for achieving an effective test set up.

5.1 Experimental procedure

Compressive strength and modulus were measured for 2.5 mm and 6 mm thick ROS specimens with the following strand sizes (length x width): 6 x 3, 12 x 3, 12 x 6, 25 x 6, 50 x 6, 25 x 12 and 50 x 12 mm (Table 3-1), as well as for 2.5 mm thick QI $[0/\pm 60]_{3S}$ and $[90/\pm 30]_{3S}$ laminates. Specimens were 140 x 25 mm in size, which allowed for a 12 mm long gauge section. Longer gauge sections were tested, but they resulted in unacceptable failure modes due to buckling. These results will be discussed in more detail in Section 5.2.2. Specimens were cut with a high precision diamond saw (Discotom 60, Struers) to ensure that all angles were at 90°. This is a requirement of the combined loading compression fixture (ASTM D6641), as will be discussed in the next paragraph.

There are two commonly used test fixtures, shear loading (ASTM D3410) and combined loading (ASTM D6641). The main difference between these fixtures is the way compressive load is introduced into the specimen, as shown in Figure 5-1. In the case of the former fixture, compressive load is applied through shear between the grips and the specimen surfaces. And in

the latter, compressive load is introduced by two means: directly at the ends of the specimen and through surface shear. Since the ends of the specimen are loaded, it is essential for the specimens to have 90° between the edges to ensure uniform stress distribution. There was no particular advantage of choosing one fixture over the other to test ROS composites, so the combined loading fixture was initially selected because of its availability in the lab. However, certain problems arose due to the selection of this method, and the shear loading fixture had to be used for certain specimens. These issues will be discussed in the next section.

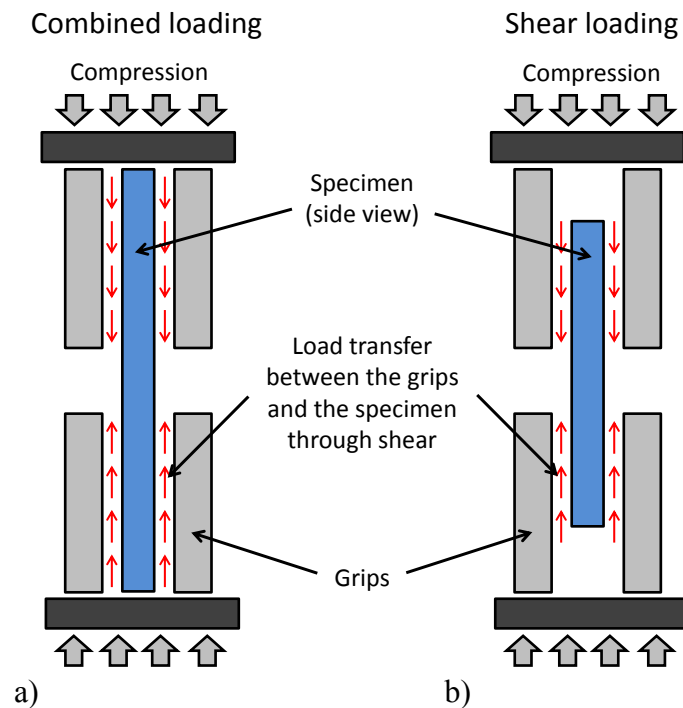


Figure 5-1 – Comparison between a) combined loading and b) shear loading methods for compression testing

One of the main issues associated with compression tests is buckling of the specimens. Usually back-to-back strain gauges (SG) are used to check for this problem, such that a difference of more than 10 % between the SG readings would indicate buckling. However, since instrumentation of all the specimens with SG is time consuming and expensive, it is customary to test five specimens of the same type (layup, thickness, gauge length) with SG, and if acceptable behaviour is obtained, to continue testing without the SG. In this study, testing of 5 specimens per category was considered to be too extensive, since seven different types (i.e. strand lengths) of ROS composites were tested, which would require 70 SG. Moreover, SG were proven to be

ineffective for measurement of tensile properties [29], and hence their applicability for monitoring of ROS specimens for buckling was also considered to be questionable.

In this study, strain was measured using the DIC technique by monitoring the speckle pattern on the edge of the specimen, because the test fixture blocked the view of the specimen faces. DIC results were also compared with the SG data. Back-to-back SG (C2A-06-250LW-350, Vishay) were bonded onto QI, short strand (6 x 3 mm), mid strand (25 x 6 mm) and long strand (50 x 12 mm) ROS composites using M-Bond adhesive (Vishay). Two specimens per category were tested. Comparison between these strain measurement techniques and their ability to detect buckling will be discussed in Section 5.2.2.

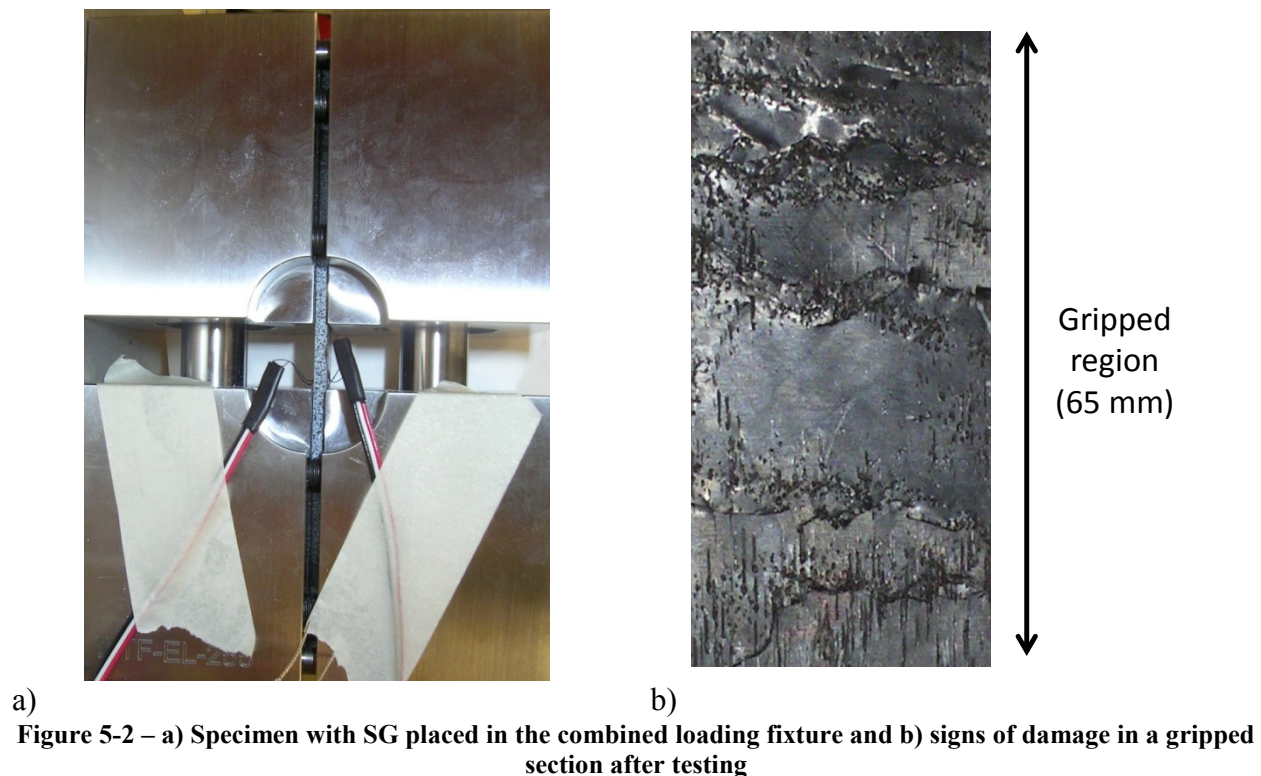
During testing, specimens were loaded at a rate of 1 mm/min and data was recorded at 4 Hz. Strain was monitored using a DIC system with a 5MP camera, Schneider CM120 BK15 lens and a 25 mm extension tube. VIC-2D software was used for the analysis. Modulus was calculated by finding the slope of the stress-strain curve between 1000 - 3000 $\mu\epsilon$. The max strength was taken as the failure strength.

5.2 Experimental results

5.2.1 Effect of test fixture

Figure 5-2a shows a specimen instrumented with SGs clamped in the combined loading fixture. In order to properly grip the specimens, bolts had to be tightened to a torque between 5 and 9 N·m depending on the specimen type. In general, specimens with shorter strands failed at lower loads and required lower torque, while specimens with long strands or continuous fibres failed at higher loads and required higher torque. Even though gauge section failure was obtained in most specimens, some damage was observed in the gripped sections. Figure 5-2b shows that specimens underwent localized crushing inside the grip. Sometimes in-grip failure was so pronounced that the specimen slipped and gauge section failure could not be achieved. The presence of damage was more drastic in specimens with longer strands (25 and 50 mm), and it was difficult to obtain gauge section failure, regardless of the bolt torque. This problem occurred

with thin and thick specimens. Interestingly, this problem was not observed with QI specimens. It can be hypothesised that since a fraction of the load is applied directly at the specimen ends, a large enough compression stress might develop in the gripped portion of the specimen to cause failure if there is a weak spot. Since 127 mm out of 140 mm are in the grips, the probability of a weak-spot being in the gripped section rather than in the gauge section is quite high. On the other hand, QI CF laminates are homogeneous throughout the entire length of the specimen and are more likely to fail in the gauge section since it is the area of the highest stress.



To check this hypothesis and to potentially mitigate this problem, half of the specimens with 50 mm long strands were tested with the shear loading method. Theoretically the easiest way of inducing compressive stresses through shear loading is to use hydraulic grips, which are commonly used for tensile testing. This set up is shown in Figure 5-3a. Unfortunately, this method was found to be impractical for compression tests. In this set up, the lower grip is free to rotate, hence making these grips self-aligning during tensile loading. However, during compressive loading grips would actually rotate increasing the misalignment further, resulting in twisting of the specimen, as shown in Figure 5-3b. Also, any axial misalignment of the grips

would cause a more drastic effect when used for compression than tension tests due to a smaller gauge section. Nonetheless, minimal damage was observed in the gripped section of the specimens, suggesting that the shear loading method should be used in lieu of the combined loading method for testing of ROS composites.

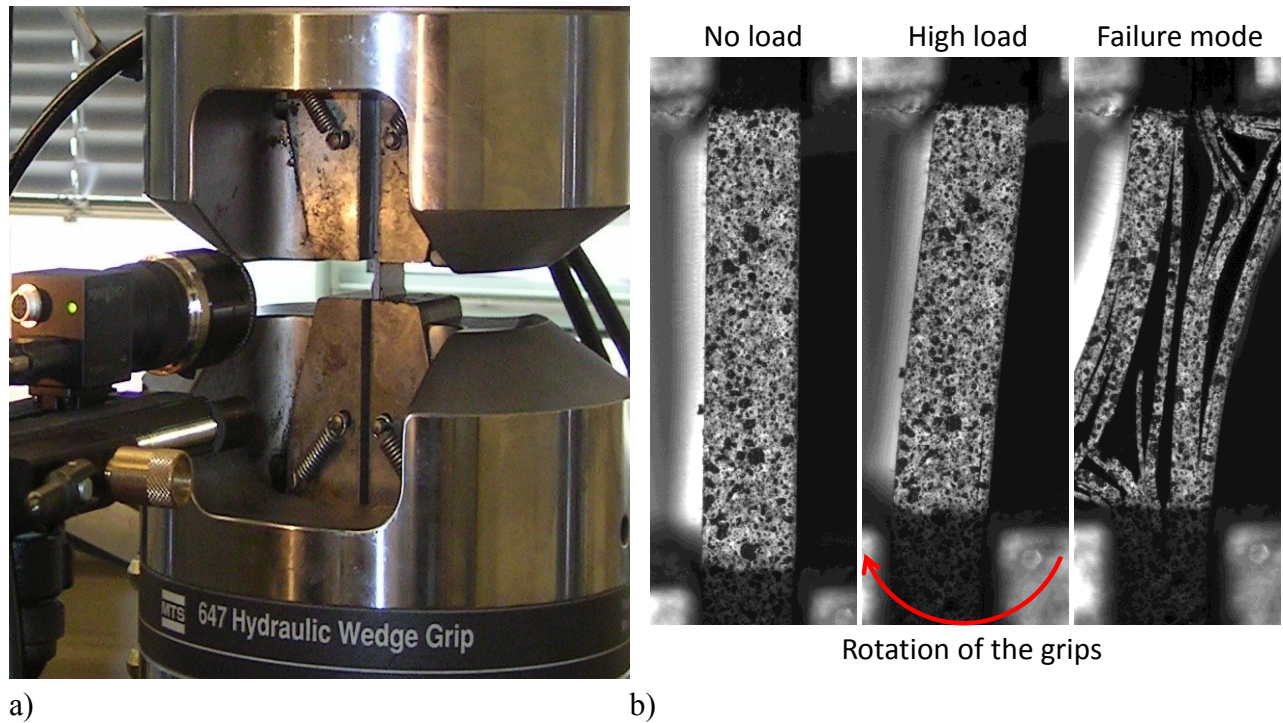


Figure 5-3 - a) Specimen placed in the hydraulic grips and b) twisting of the specimen during loading

Finally, ROS specimens were tested with a proper shear loading fixture, with the set up shown in Figure 5-4a. Glass/epoxy end-tabs were bonded onto the specimens using superglue, because 2.5 mm thick specimens were too thin for the fixture (Figure 5-4b). Nonetheless, 6 mm thick specimens were successfully tested without the use of end tabs. No problems with specimen misalignment or excessive damage in the grip section were observed. This fixture was later extensively used for other studies of ROS composites and no problems with misalignment, slippage or excessive grip section damage were observed.

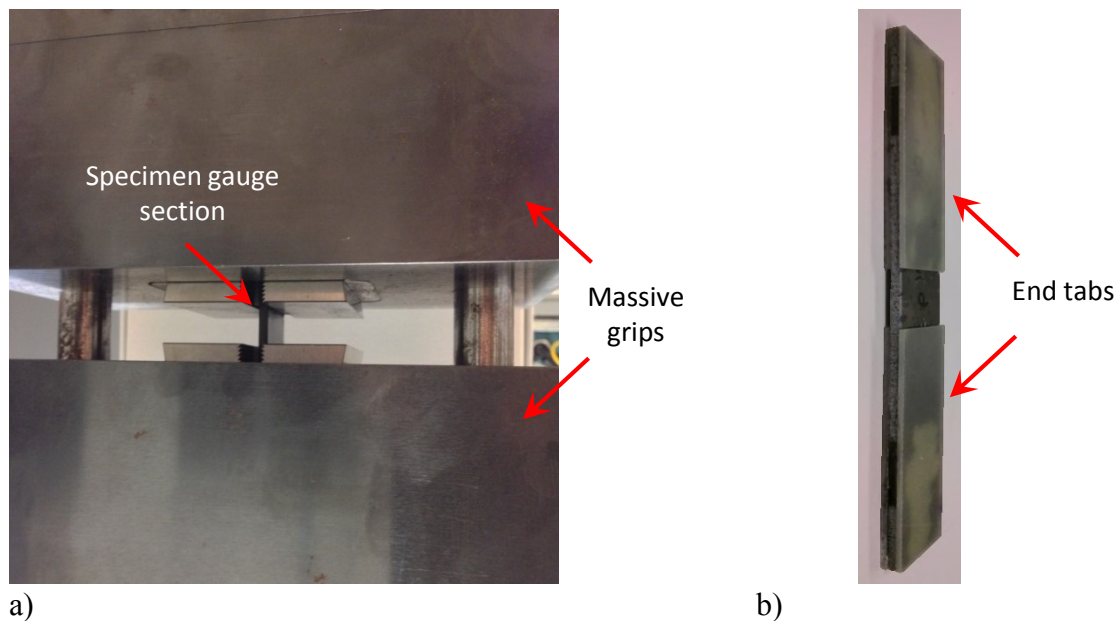


Figure 5-4 – a) Specimen placed in the shear loading fixture and b) specimen with bonded end tabs

Overall the use of shear loading fixture to test ROS composites in compression is recommended. Moreover, specimen preparation is easier since they do not have to be perfectly perpendicular, and gripping procedure is easier since the wedge grips are self-tightening based on their design.

5.2.2 Checking for buckling

The strain readings obtained with DIC and SG for QI specimens were in close agreement, as shown in Figure 5-5, hence signifying that DIC measurements taken from the edge of a sample can provide accurate strain data. In this figure, red lines represent the location of the strain gauges, which had to be bonded off-centre to accommodate for the wire terminals. Also, the fact that two SG curves overlap verifies that there is no buckling of the specimen. It is also noteworthy that the strain field is fairly uniform, and the slight variability can be attributed to noise.

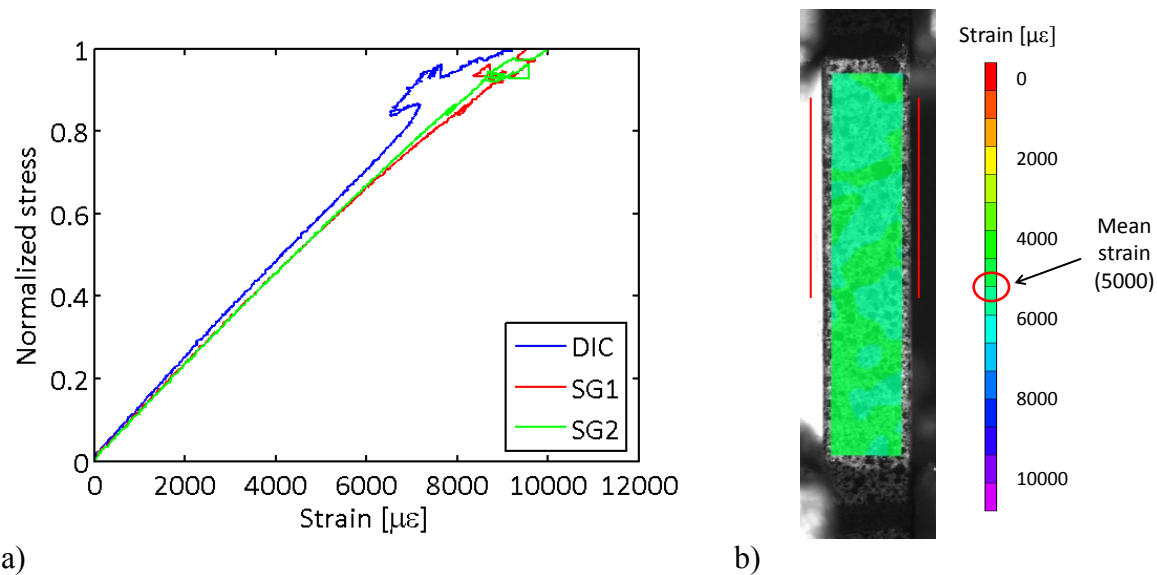


Figure 5-5 – a) Stress-strain curves measured by SG and DIC and b) strain-field captured with DIC corresponding to a QI CF specimen

Next, stress-strain curves for a sample with small strands show that SG curves are still close enough to say that there is no buckling (percent bending $< 10\%$), but there is a significant discrepancy between the SG and the DIC data, as shown in Figure 5-6. The strain-field shows that there is an area of high strain that is outside of the SG zone. As a result, DIC measures higher strains than SG for a given load. Alternatively, DIC strains can be extracted from a smaller region that coincides with the SG region. From Figure 5-7 it is evident that while the overall strain is 5000 $\mu\epsilon$, strain in the smaller section, which is highlighted by a red rectangle, is 3500 $\mu\epsilon$. Also, the updated stress-strain curve correlates better with SG data. Comparison between the strain-fields of QI and ROS specimens shows significantly higher strain variability observed with the latter.

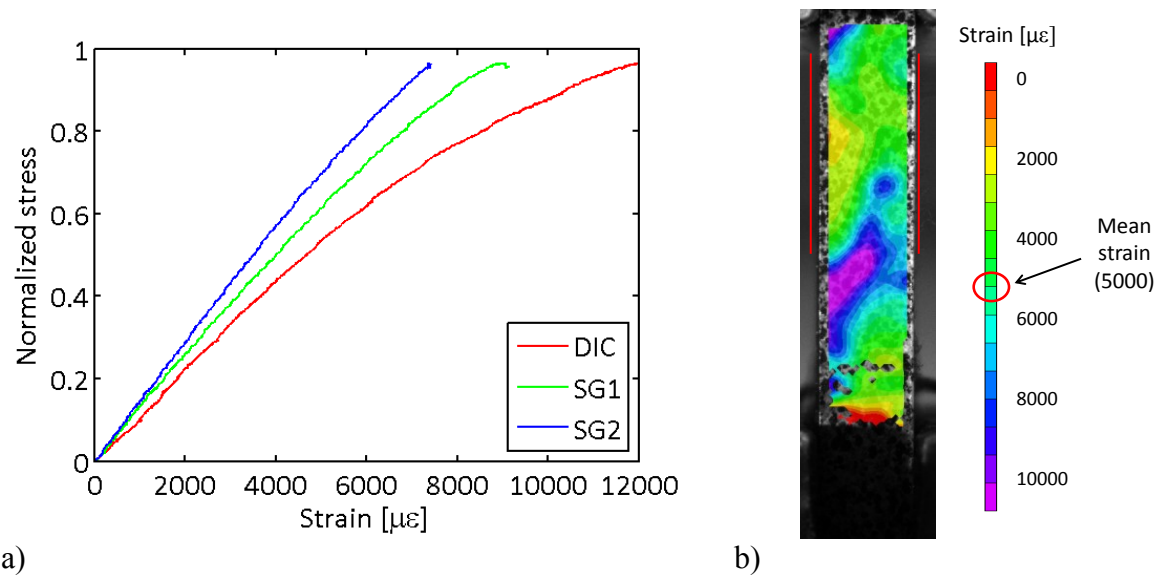


Figure 5-6 - a) Stress-strain curves measured by SG and DIC and b) strain-field captured with DIC corresponding to a short-strand ROS specimen

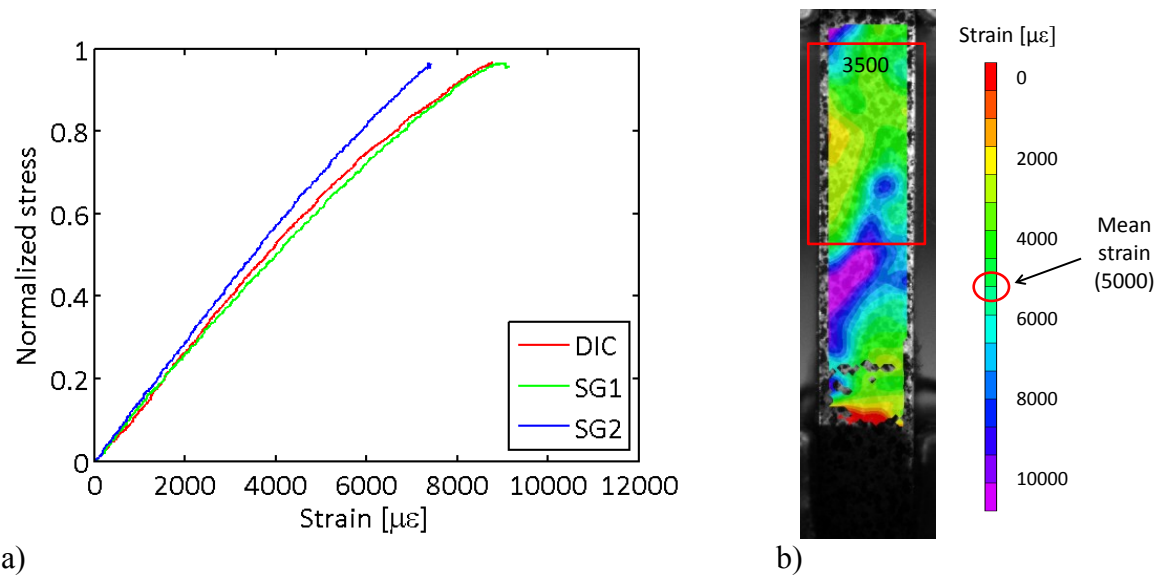


Figure 5-7 - a) Stress-strain curves measured by SG and DIC while using a smaller gauge section and b) strain-field captured with DIC corresponding to a short-strand ROS specimen

Finally, in the case of mid and long-strand ROS composites, there was a large difference between the SG curves, and the DIC curve was somewhere in the middle, as shown in Figure 5-8. This result suggests of buckling, but the strain-field did not show the typical strain pattern associated with flexural strains. Hence, it is possible that the discrepancy in SG readings is associated with heterogeneity of properties and (surface) strains in long-strand ROS composites rather than with bending or buckling. In general, problems with buckling are expected when the

gauge section is too long, or the specimen is too compliant. In this study, it was shown that QI and short-strand ROS composites are not susceptible to buckling given the 12 mm gauge section. Since all the thin specimens had the same thickness, and since QI and short-strand ROS composites mark the high and the low range of possible ROS stiffness, it can be hypothesised that long-strand ROS composites would not be prone to buckling problems for a 12 mm gauge section.

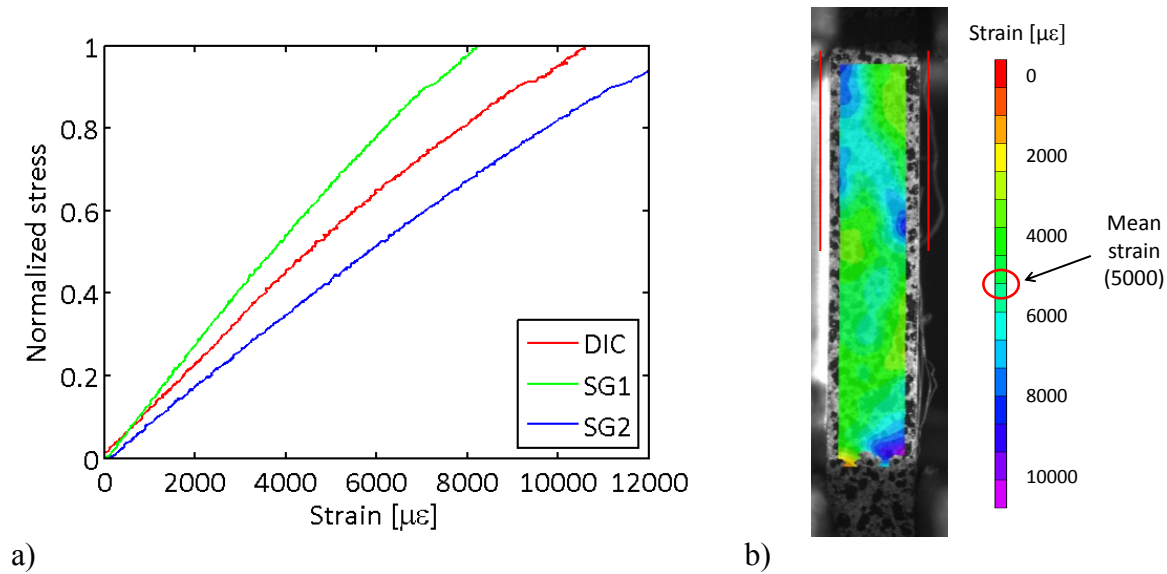


Figure 5-8 - a) Stress-strain curves measured by SG and DIC and b) strain-field captured with DIC corresponding to a long-strand ROS specimen

Thus far, it can be concluded that when testing a new ROS composite in compression, SG can be used to check for buckling only in the case of short-strand composites. However, in the case of long strands composites, SG give questionable or inconclusive results. An alternative way to check for buckling is to use DIC. To test this option, an extra set of tests was conducted with ROS composites with 25 mm long strands and 25 mm gauge section, which was too long and led to visible bending. DIC was used to capture the out-of-plane displacement, which clearly depicted bending in the case of 25 mm long gauge section. Comparison between the out-of-plane displacements observed with 12 and 25 mm gauge sections is shown in Figure 5-9. Failure due to buckling resulted in strength being 18 % lower than when specimens failed properly due to compression. Hence, for long-strand ROS composites, DIC is the preferred method over SG for monitoring of buckling during compression loading.

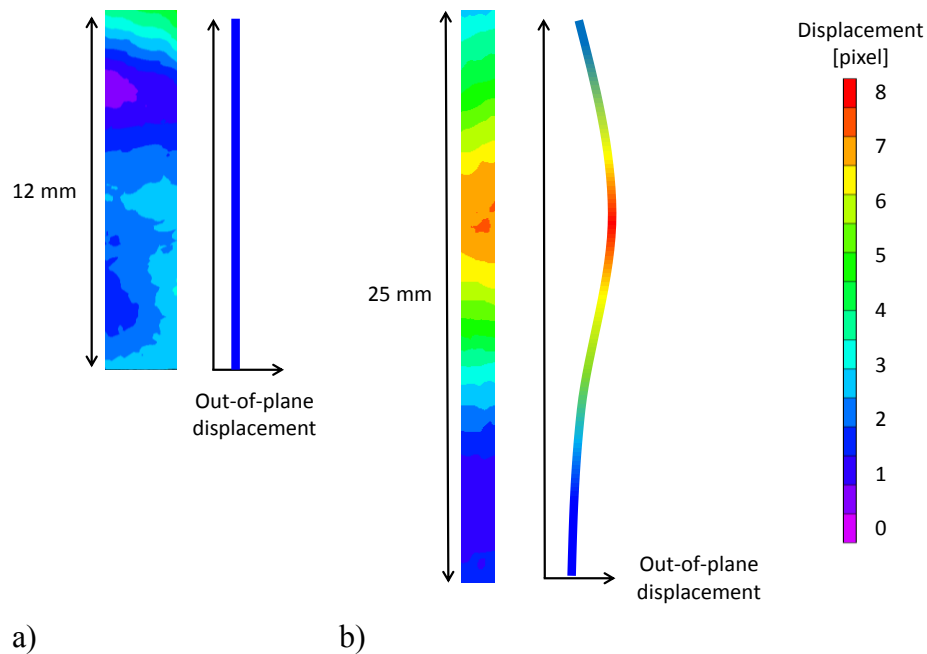


Figure 5-9 – Out-of-plane displacement of an ROS specimen with a a) 12 mm and b) 25 mm gauge section captured with DIC

5.2.3 Failure modes

ROS specimens failed mainly due to strand debonding with minimal fibre breakage. Overall, the failure region had a combination of different failure features namely transverse shear, brooming and through-the-thickness failure, which are typically observed with CF composites. Typical failure modes that were observed with thin and thick specimens regardless of the strand size are shown in Figure 5-10. The main difference was that delamination cracks often extended beyond the gauge section of long-strand composites, which is understandable since individual strands were longer than the gauge section. No connection between the failure modes and strengths was found.

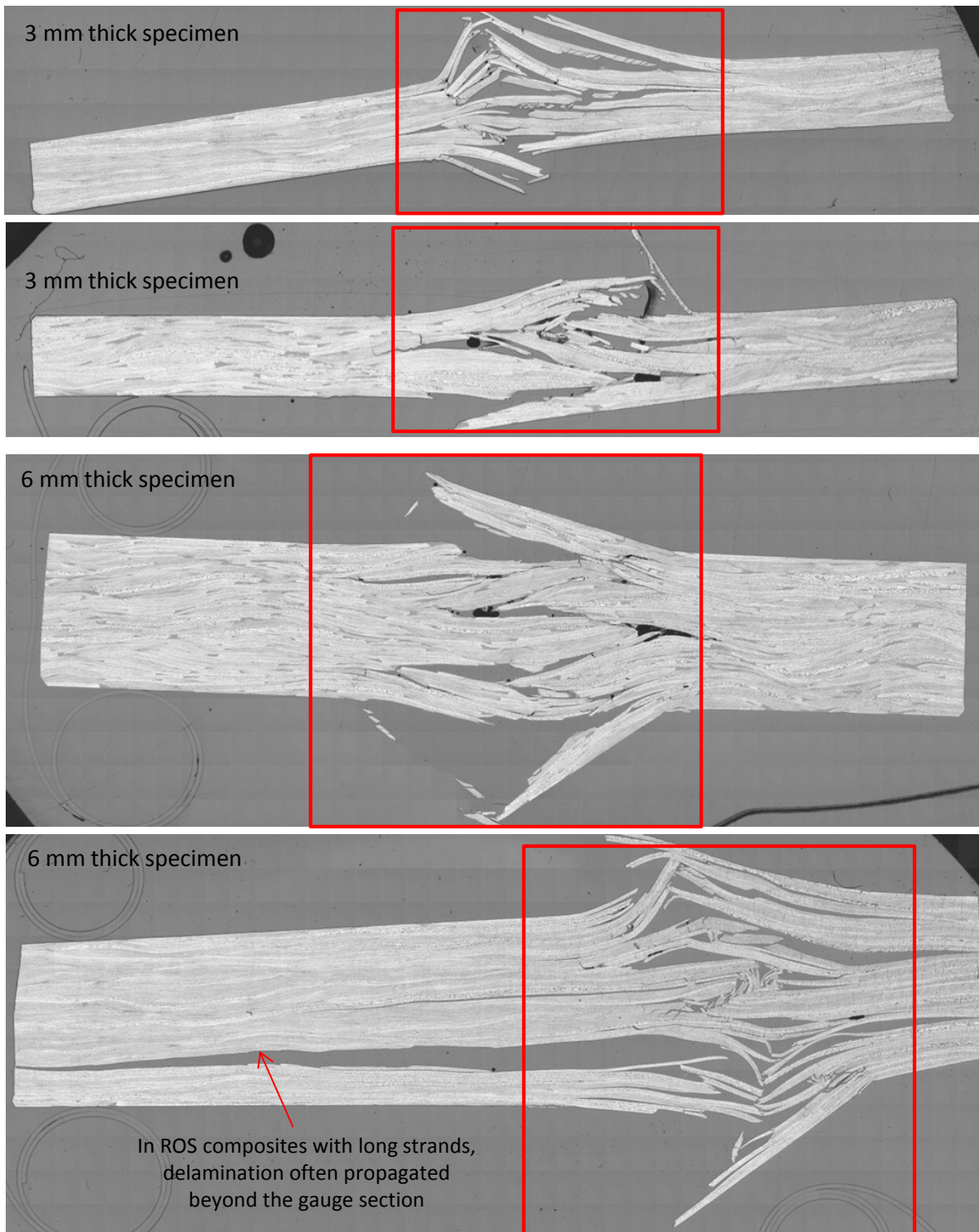


Figure 5-10 – Failure modes of thin and thick ROS composites. Gauge section is identified with a red rectangle

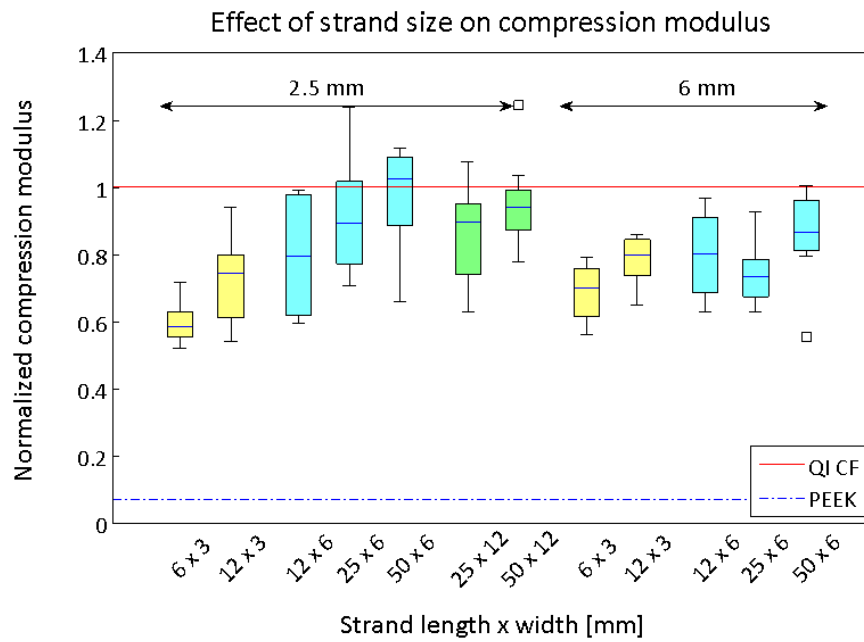
5.2.4 Strength and modulus

The summary of compressive strength and modulus results is shown in Figure 5-11. Values are normalized based on the properties of QI CF laminate. It is evident that variability in the measured data is higher than what was observed with tensile properties in Chapter 4 probably due to the smaller gauge section. Similarly to tensile properties, compressive modulus and strength increased with strand length. Interestingly, ROS composites have a similar, if not higher, compressive than tensile strength; whereas, CF composites are significantly stronger in tension. This can be explained by the fact that strength of ROS composites depends on the resin-dominated interlaminar properties, but strength of CF composites is fibre-dominated and is sensitive to the loading direction (i.e. (+) tension and (-) compression).

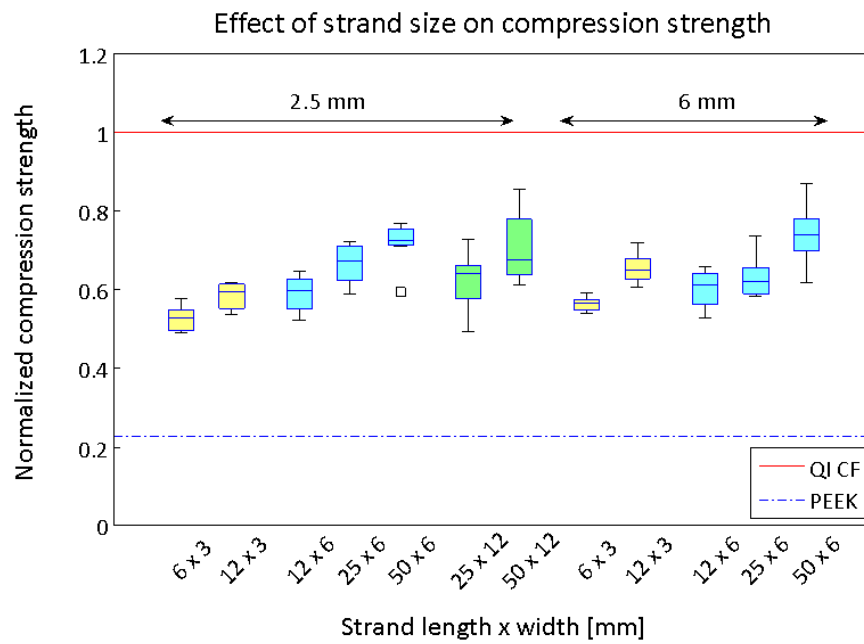
The same trends were observed in the case of carbon/epoxy ROS composites [27, 33, 85, 86]. However, the fact that compressive strength of the carbon/epoxy ROS composites is lower than that of the PEEK-based ones is probably due to PEEK being a tougher resin than epoxy, hence offering better interlaminar properties. Overall, compressive properties of ROS composites compare better with the strength of QI CF laminates than tensile properties. Hence, it can be concluded that ROS composites are more suitable for applications where components will experience compressive rather than tensile loading, since strength reduction in the latter case is too high.

5.3 Concluding remarks

This chapter presented experimental results pertaining to compressive properties of ROS composites. Strength and modulus increased with increasing strand length. The same trend was observed with tensile properties, but the knockdown of compressive strength from CF to ROS was not as drastic as that of tensile strength. Thus, ROS composites are more suitable for applications where components have to withstand compressive rather than tensile loads. The next chapter will discuss shear properties of ROS composites.



a)



b)

Figure 5-11 - Effect of strand size on compressive a) modulus and b) strength of ROS panels

Chapter 6

Shear properties

This chapter will discuss the effect of strand size on in-plane and out-of-plane shear properties of ROS composites. The opening section will describe the available test methods and the reasoning used for selection of the most suitable ones for this study.

6.1 Selection of test methods

The material coordinate plane and the definition of shear stresses with respect to ROS and single strand microstructure are shown in Figure 6-1. For ROS composites, shear stresses (τ) in the 1-2 plane are referred to as the in-plane, and those in the 1-3 and 2-3 planes (note that 1-2 is the plane of isotropy) represent the out-of-plane stresses. In the case of a UD lamina or a single strand, Y-Z is the plane of isotropy, and τ_{yz} and τ_{zy} represent the out-of-plane shear stresses. The in-plane (X-Y) and the interlaminar (X-Z) properties are assumed to be the same. This difference in the planes of isotropy between the ROS and the UD composites is noteworthy when comparing experimental results and using approximations to calculate shear modulus.

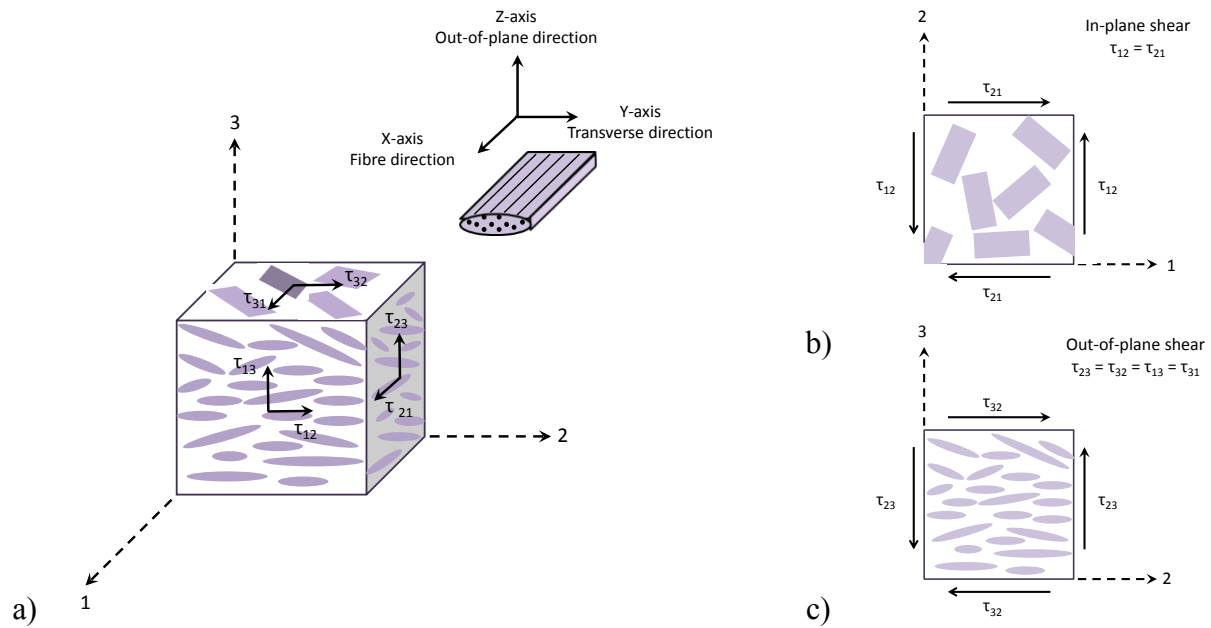
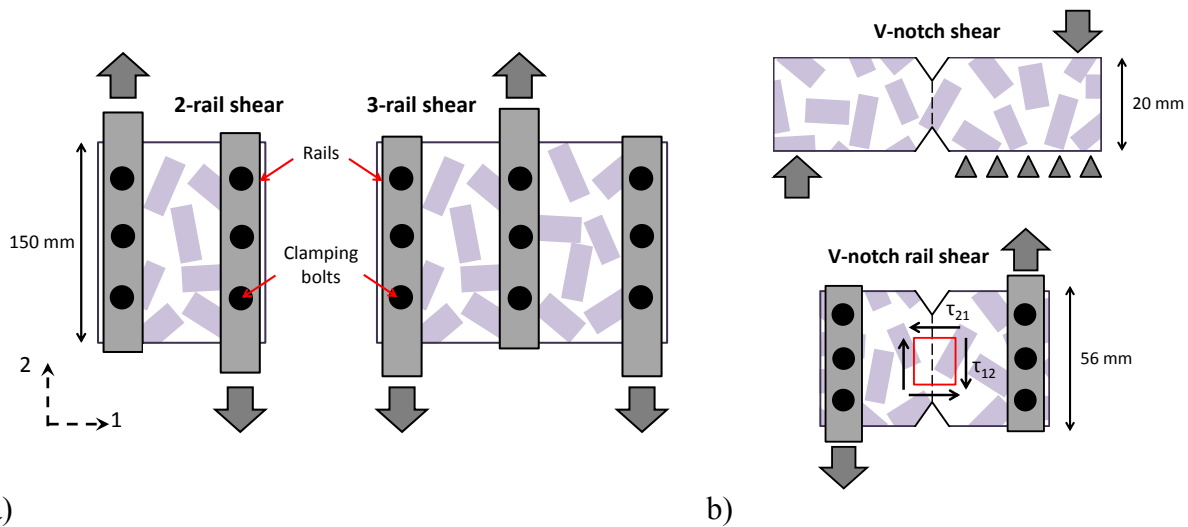


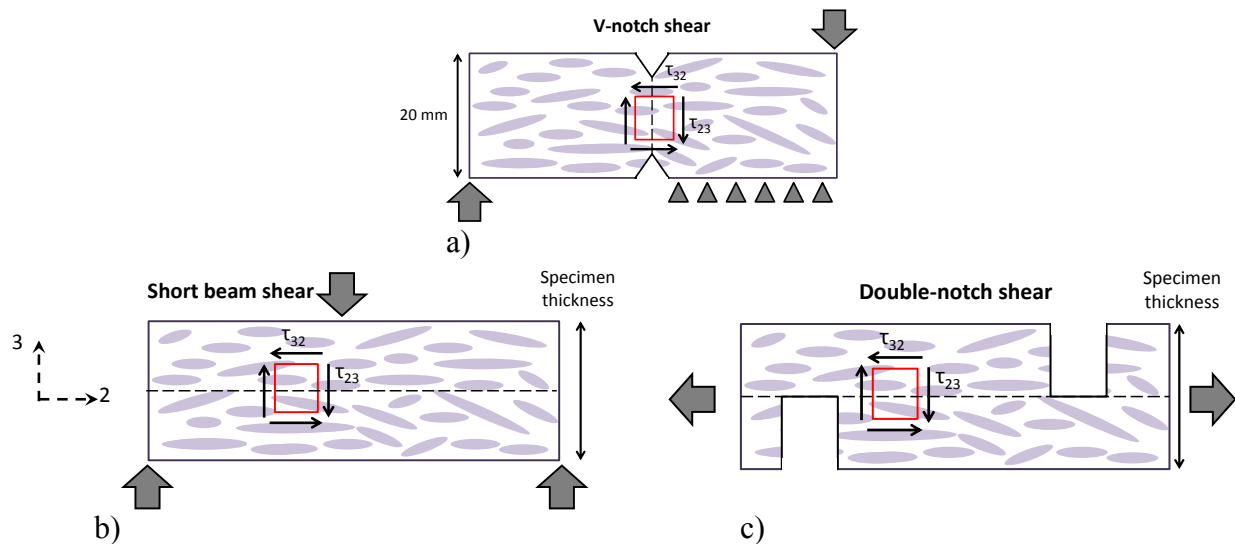
Figure 6-1 – a) Material coordinate plane and definition of shear stresses, and b) in-plane stresses and c) out-of-plane stresses in ROS composites

There are two types of ASTM test methods available for measurement of in-plane shear strength and modulus: rail shear (ASTM D4255) and v-notch shear (ASTM D5379 and ASTM D7078), which are schematically shown in Figure 6-2. The rail shear method requires the use of large specimens (at least 150 x 75 mm) and thus was considered to be too material consuming for this study. Nonetheless, due to a large gauge section, the use of this method is advisable for studies where consistency and low scatter of data are of great importance, such as when determining the design allowables. There are two variations of the v-notch method available, as shown in Figure 6-2b. The v-notch rail test was chosen because it allows for a larger gauge section (30 vs. 10 mm). Even though this gauge length is too small given the scale of material heterogeneity it is thought to produce acceptable results for comparing the properties and for capturing the general trends.



a) **Figure 6-2 – Test methods for in-plane shear properties: a) 2-rail and 3-rail, and b) v-notch and v-notch rail**

There are three ASTM test methods for measuring the out-of-plane shear strength (S_{23}): v-notch shear (ASTM D5379), short beam shear (SBS) (ASTM D2344) and double-notch shear (DNS) (ASTM D3846). Figure 6-3 shows these three methods and in turn illustrates the different ways of inducing out-of-plane shear stresses in the material. The dashed lines in these figures indicate the centerlines along which the state of pure shear exists.



a) **Figure 6-3 – Test methods for out-of-plane shear properties: a) v-notch, b) short beam and c) double-notch**

While the v-notch shear test is conventionally used to measure in-plane properties, its use is troublesome for out-of-plane measurements, because it requires manufacturing of really thick specimens (20 mm). It is noteworthy that the v-notch shear method is the only method that

allows for direct measurement of out-of-plane shear modulus (G_{23}). Alternatively, for UD laminas shear modulus can be approximated based on the assumption of transverse isotropy in the X-Z plane, as shown in Eq. 6-1. Since, in the case of ROS composites, the 1-2 plane is the plane of isotropy, this assumption cannot be used for calculation of the G_{23} .

$$G_{23} = \frac{E_2}{2(1 + \nu_{23})} \quad \text{Eq. 6-1}$$

In the case of SBS and DNS, typical specimen thicknesses used are in the range of 2.5 - 6.5 mm. The fundamental problem with the DNS test is that significant stress concentrations occur at the notches, potentially leading to premature failure. It is also difficult to machine the notches accurately, hence potentially resulting in overcuts or undercuts, which would further complicate the stress state and induce failure. SBS is commonly used to test laminated composites due to the simplicity of specimen preparation, in particular since cutting of the notches is avoided. The main disadvantage of this test is that the specimen is always under the state of complex stress. The state of pure-shear exists along the centerline, but away from the center there are non-zero tensile and compressive stresses caused by bending, as well as stress concentration under the loading nose. Overall, out-of-plane properties are difficult to measure and accuracy of the results obtained with these methods is always subject to scrutiny. Nonetheless, as an accepted practice, any one of these methods can be used to compare properties of different materials, as long as the same method is used for all tests. A more in-depth discussion of these methods can be found in [87, 88].

The v-notch method was rejected on the basis of practicality, since it is difficult to manufacture thick samples, which actually may or may not be representative of thin ROS samples. As the consequence G_{23} could not be measured and was excluded from the study. Overall, it appears that strand size has a more pronounced effect on strength than on modulus, and hence more emphasis was placed on strength measurements. In the future it would be advisable to manufacture thick specimens and use the v-notch method to measure G_{23} .

For this study the DNS method was chosen because clear failure between the notches could be achieved. Specimens subjected to SBS loading showed signs of a mix-mode failure (i.e. tension, compression and shear), and it was difficult to judge which failure mode caused the onset of damage, as shown in Figure 6-4. Due to the concern that DNS measurements would underestimate strength due to stress concentrations, UD specimens were tested using the DNS method and were used as a benchmark. Also, the DNS test results were compared against the SBS results found in other publications [13].

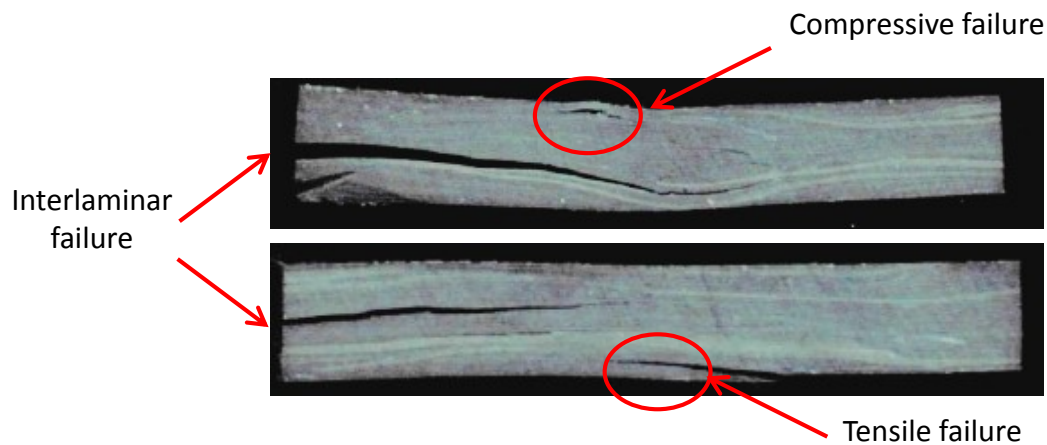


Figure 6-4 – Failure mode of SBS ROS specimens

6.2 In-plane shear

6.2.1 Experimental procedure

In-plane shear strength and modulus was measured for 2.5 mm and 6 mm thick ROS specimens with the following strand sizes (length x width): 6 x 3, 12 x 3, 12 x 6, 25 x 6, 50 x 6, 25 x 12 and 50 x 12 mm (Table 3-1), as well as UD $[90]_{18}$, and QI $[0/\pm 60]_{3S}$ and $[90/\pm 30]_{3S}$ laminates. Specimens were cut at NRC-Ottawa and were painted with a black-and-white speckle pattern to allow for strain measurement with DIC, as shown in Figure 6-5a. A torque wrench was used to clamp the specimens in the fixture (Figure 6-5b), and the amount of required torque varied depending on the specimen type.

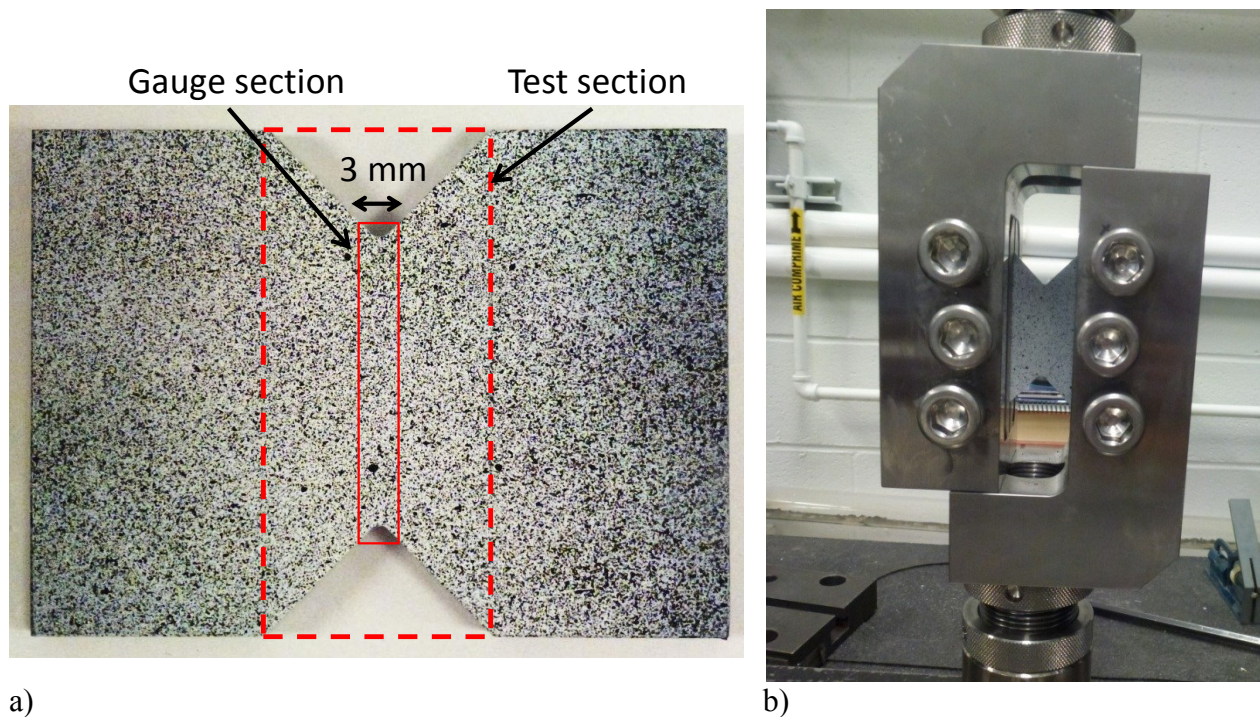


Figure 6-5 – V-notch rail: a) painted specimen and b) clamped specimen in the fixture

Generally, torque has to be chosen so that it is high enough to prevent the specimen from slipping in the grips, and yet low enough to avoid premature failure. Thin specimens with small strands (6 x 3 mm) were weaker and required lower torque (27 N·m) while stronger QI specimens required higher torque (76 N·m), it can be noted that torque recommended by the ASTM standard is 45-55 N·m (30-40 lb·ft). In the case of thicker specimens, torque loads higher than 76 N·m were required, since force-to-failure was also higher in comparison to thin specimens. However, it was not recommended by the manufacturer (Wyoming Fixtures) to exceed torque of 83 N·m, since the fixture was simply not designed for it. As a result, only thick specimens with 3 mm wide strands were tested, because in other cases slippage became a problem and it was decided to abort testing so as not to damage the fixture (i.e. cause permanent deformation). It is possible to test thicker samples but a custom made fixture that can sustain higher torques would be required. For example, Wyoming Fixtures offers a combined loading fixture, which is a merge between the v-notch and the v-notch rail setup such that combined edge and face loading is achieved. This fixture can be used with specimens that require higher force-to-failure.

During testing, specimens were loaded at a rate of 1.5 mm/min and data was recorded at 4 Hz. Strain was monitored using a DIC system with a 5 megapixel camera (Point Grey, model Flea2 FL2G-50S5M) and a Tamron lens (23FM75L), and VIC-2D software was used for the analysis. For strain measurement, ASTM recommends strain gauges with an active gauge length of 1.5 mm or longer for textile reinforcement, such that gauge length would be at least as great as the characteristic repeating unit of the fabric. For this study, in order to calculate modulus, shear strain was averaged over a 3 mm wide region as shown in Figure 6-5a. Even though the choice for an appropriate gauge length for ROS is subject to discussion, CF and ROS data can be adequately compared if the same gauge section is used. Modulus was calculated by finding the slope of the stress vs. engineering strain ($\gamma_{12} = 2 \cdot \epsilon_{12}$) curve between 1500 - 5500 $\mu\epsilon$. For strength results, the ultimate strength is presented.

6.2.2 Experimental results

The main difference between the response of ROS and CF specimens to shear loading is the variability of the strain field. Comparison between the shear strain fields of ROS, and CF UD and QI can be seen in Figure 6-6. These images were obtained with DIC analysis and illustrate strain field in the specimen when gauge section strain is 5000 $\mu\epsilon$ (0.5 % ϵ). The gauge section area is highlighted with a red rectangle in Figure 6-5a. It is clear that while CF composites develop a classical strain pattern with the highest strain observed in the gauge section, ROS specimens show an unsymmetrical shear pattern with regions of high strain present at different locations in the specimen. Similarly, failures obtained with CF specimens were repeatable and developed clearly along the fibres, but failure paths with ROS specimens were random, as shown in Figure 6-6. Failure paths are marked with a red line.

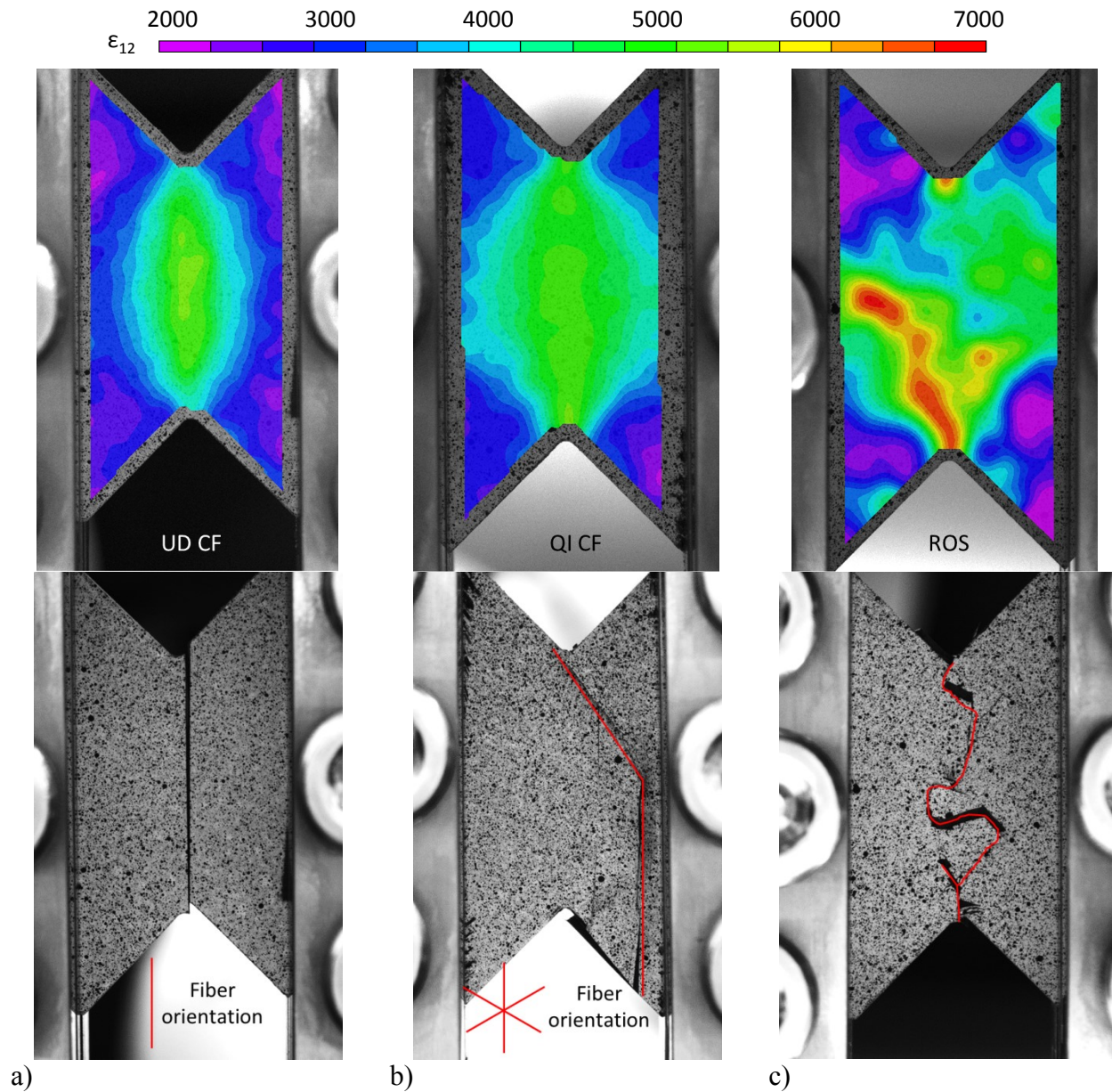
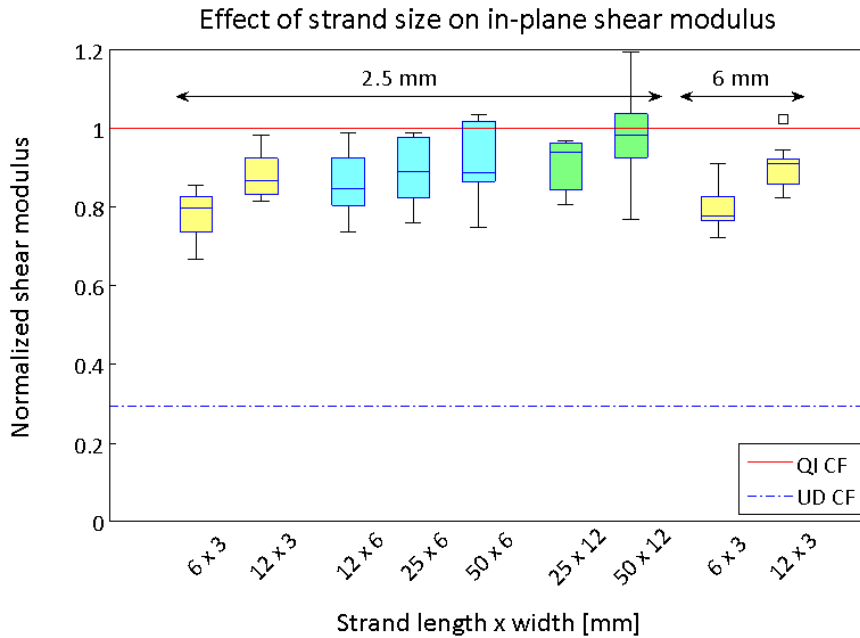


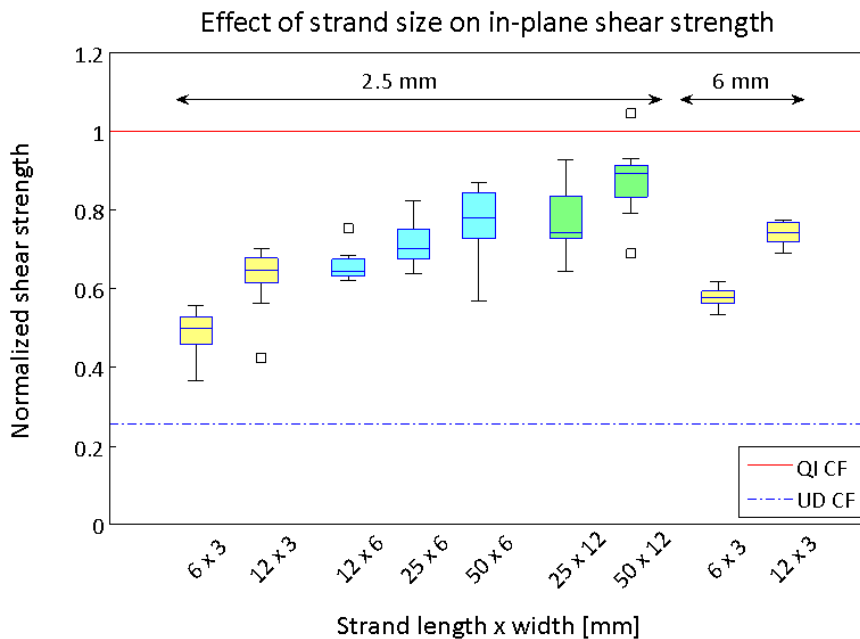
Figure 6-6 – Shear strain field and failure region of a) UD CF, b) QI CF and c) ROS specimens

The summary of in-plane strength and modulus results is shown in Figure 6-7. Values are normalized based on the properties of QI CF laminate. There is a clear trend that shear modulus and strength increase with strand length. In fact, properties of some ROS specimens with long strands are actually higher than those of QI CF laminates. The same trend was observed with tensile and compressive properties. The main difference is that in-plane shear strength of ROS composites compares better with the strength of CF laminates. Thus far, it seems that composites

are more suitable for applications where components will experience shear rather than tensile loading, since strength reduction in the latter is too high.



a)



b)

Figure 6-7 – Effect of strand size on in-plane shear a) modulus and b) strength of ROS panels

Another way of comparing the results is shown in Figure 6-8. It is evident that the stress-strain response of ROS composites is between the response of CF UD and QI laminates. Strength and

modulus of ROS composites increases with strand length and in the case of the longest 50 mm strands sometimes surpass the stiffness of CF composites. Also, response of short strand ROS specimens is more non-linear, whereas stress-strain curves of ROS composites with 50 mm long strands are essentially straight. Overall it can be said that properties of short strand ROS composites are more matrix-dominated, and properties become more fibre-dominated as strand length increases.

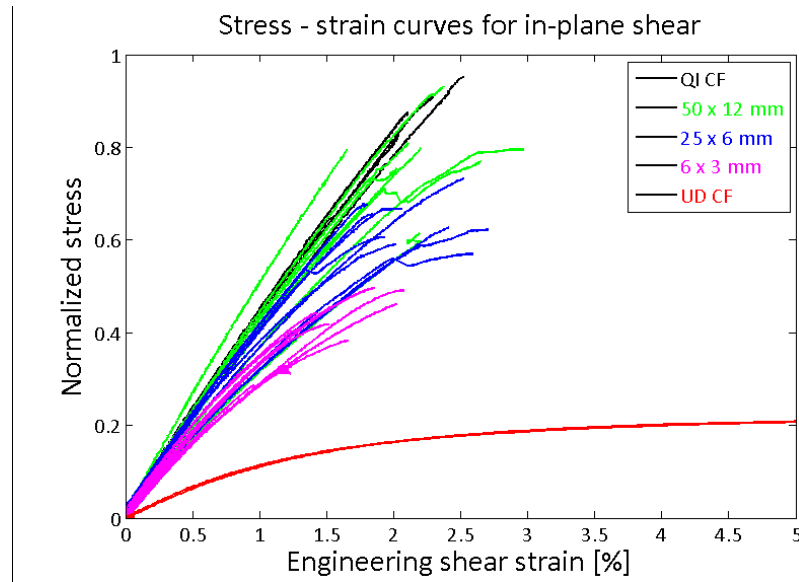
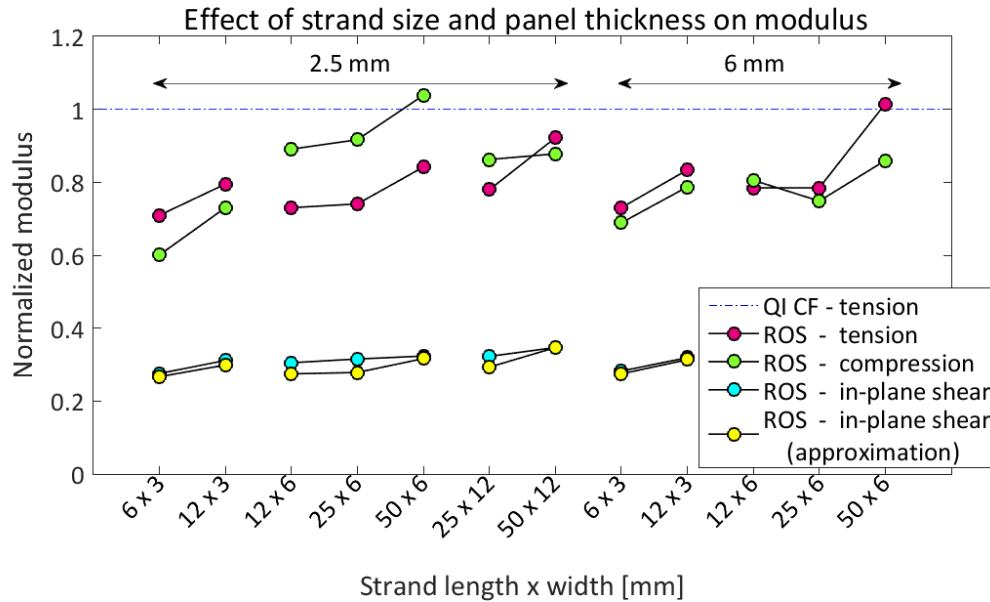


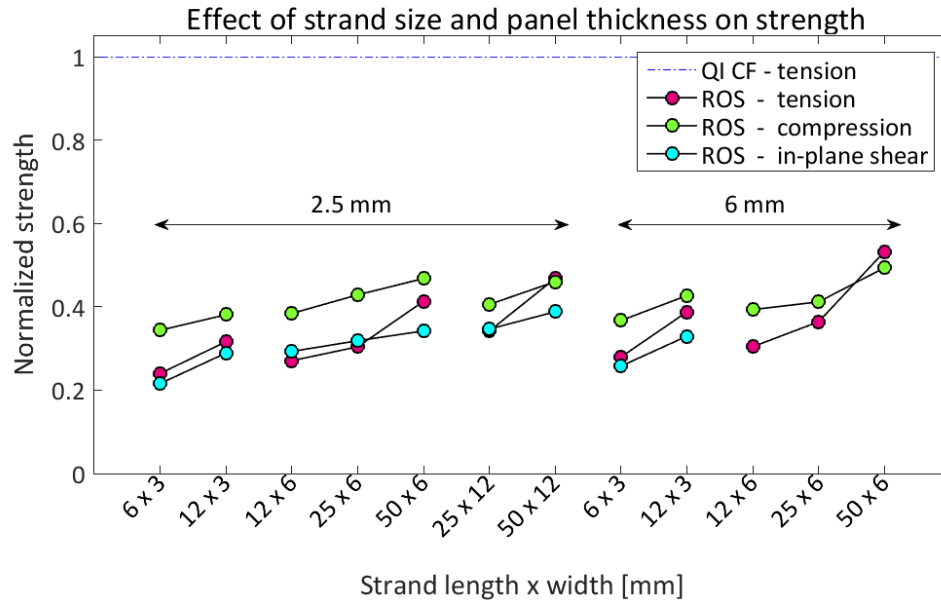
Figure 6-8 – Comparison between the stress-strain curves of CF and ROS specimens

Final comparison of the in-plane properties is presented in Figure 6-9, where tensile, compression and shear strength and modulus are plotted as normalized values based on tensile properties. Interestingly, strengths corresponding to different loading conditions are very close to each other in magnitude, especially tensile and shear strengths. Hence, tensile strength can be used as an approximation of shear strength and as a conservative approximation of compression strength. Figure 6-9 also provides a comparison between the measured and the estimated shear modulus, which was calculated based on the assumption of transverse isotropy of the 1-2 plane (Eq. 6-1). Error between the measured and the approximated values was on average 5 %, hence tensile modulus can be used to approximate shear modulus of ROS composites. These observations help to reduce the number of preliminary tests that need to be conducted when

trying to evaluate the performance of a new ROS material, at least when it has carbon fibres and thermoplastic matrix as its constituents.



a)



b)

Figure 6-9 – Effect of strand size on tensile, compression and shear properties of ROS composites

6.3 Out-of-plane shear

6.3.1 Preliminary tests

Preliminary tests were performed to find the largest distance between the notches that would result in the desired failure mode (i.e. between the notches) and to compare whether or not the loading direction made a difference (i.e. tension or compression). Three distances between the notches (L_o) were considered: 6, 12 and 25 mm. Eight samples per length were tested: four in tension and four in compression. A 2.5 mm thick ROS panel with 25 x 12 mm strands was used for testing. Specimens, as shown in Figure 6-10, were cut to 150 x 25 mm and had parallel notches machined at NRC-Montreal using a 1.6 mm ($1/16$ in) end mill. A support jig was used to minimize the out-of-plane deformation caused by the eccentricity in loading, as shown in Figure 6-10. Based on the ASTM standard, the bolts must be tightened to a torque of 0.113 N·m. However, an appropriate torque wrench was not available, and the bolts were finger-tight. Specimens were subjected to tensile or compressive loading at a rate of 0.5 mm/min using a 100 kN MTS machine.

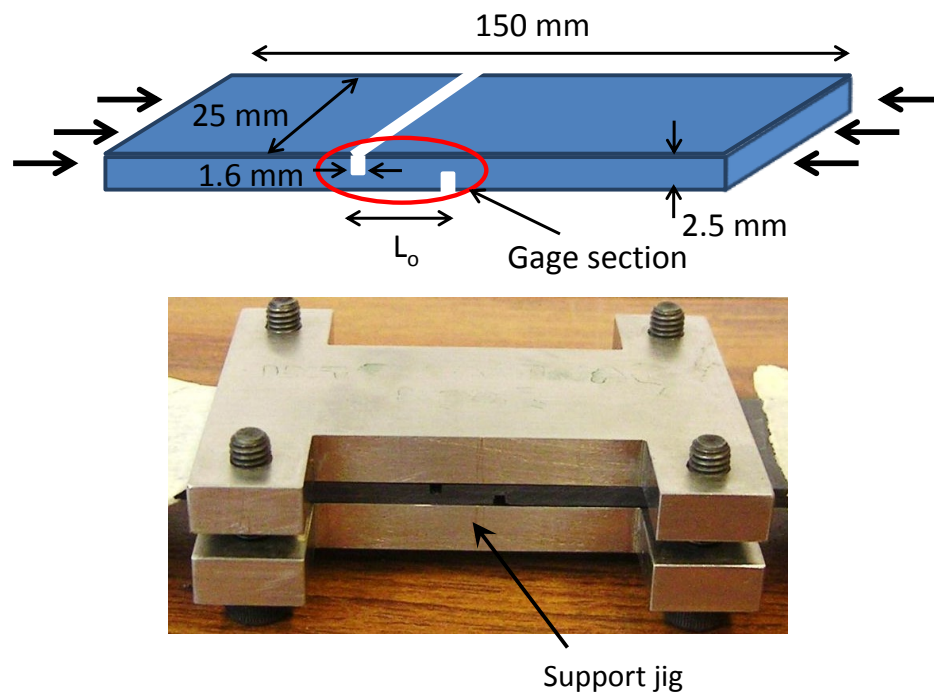


Figure 6-10 – DNS specimen with a support jig

Only the shortest distance of 6 mm led to adequate failure because longer distances led to tensile or compressive failure at the notch, as shown in Figure 6-11. From the specimens with 6 mm distance, all four tension specimens but only two compression specimens failed properly. Hence for the subsequent full scale tests, 6 mm notch distance and tensile loading were used.

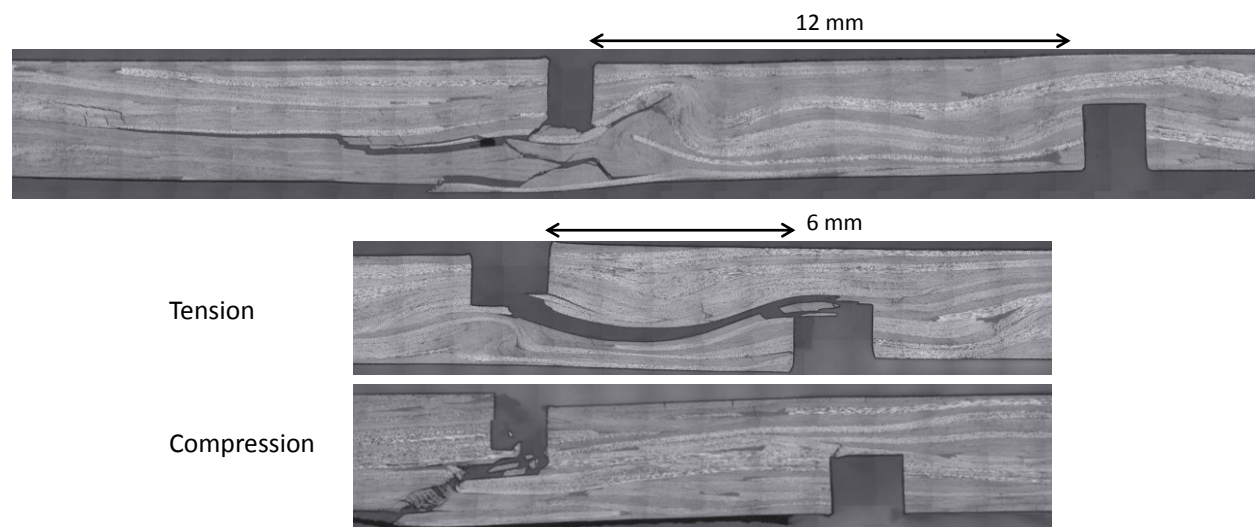


Figure 6-11 – Comparison between failure modes of DNS specimens with 6 mm and 12 mm distances between the notches

6.3.2 Full scale tests

Out-of-plane shear strength was measured for 2.5 mm thick ROS specimens with the following strand sizes (length x width): 6 x 3, 12 x 3, 12 x 6, 25 x 6, 50 x 6, 25 x 12 and 50 x 12 mm (Table 3-1). It was also desired to measure the interlaminar (X-Z) and out-of-plane (Y-Z) properties of UD laminates, which would require specimens to be tested in the 0° and 90° directions. The 0° fibre direction signifies that fibres are oriented lengthwise in the specimen. Test conditions were the same as those used for the preliminary tests.

Unfortunately, 90° UD specimens could not be failed in shear with a 6 mm gauge length, because matrix normal strength was too low and the specimens failed in either compression or tension; both types of loading were tried. In order to ensure proper failure of 90° UD specimens, the distance between the notches would have to be reduced or the thickness of the panel would have to be increased. Both of these options were undesirable since they would affect the stress-

concentration at the notches and would make the comparison between UD and ROS specimens inaccurate. As a result, only the data for 0° UD specimens was used for benchmarking. The summary of ROS results, which were normalized by strength of UD specimens, can be seen in Figure 6-12.

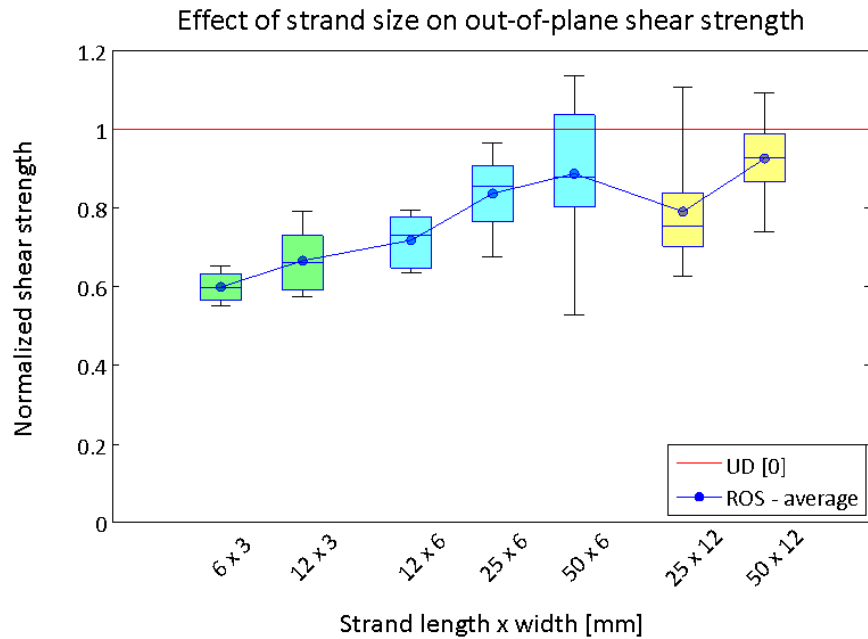


Figure 6-12 – Effect of strand size on out-of-plane strength of ROS panels

The main observation is that out-of-plane strength and variability increase with strand length, which is consistent with the results for other loading conditions (i.e. tension, compression and in-plane shear). Interestingly, the strength of ROS specimens with strands longer than 25 mm sometimes surpasses the strength of UD specimens. This result is not surprising, since 25 mm long strands are a lot longer than the 6 mm gauge section of the specimen and could easily bridge the notches, hence alleviating the strength reduction associated with discontinuous fibres. Also, the out-of-plane orientation of fibres would help to impede growth of a delamination crack between the notches. The failures associated with different strand sizes are shown in Figure 6-13. From these images it is evident that failure surface of ROS specimens is in fact curvilinear due to the out-plane strand orientation, whereas failure surface of UD specimens is straight. Also, failure paths corresponding to specimens with longer strands are smoother in comparison to those related to shorter strands, which show a lot of jaggedness due to strand discontinuity.

Delamination propagates along the length of the strand, and in the case of longer strands it might actually progress beyond the two notches, as shown in the last image in Figure 6-13.

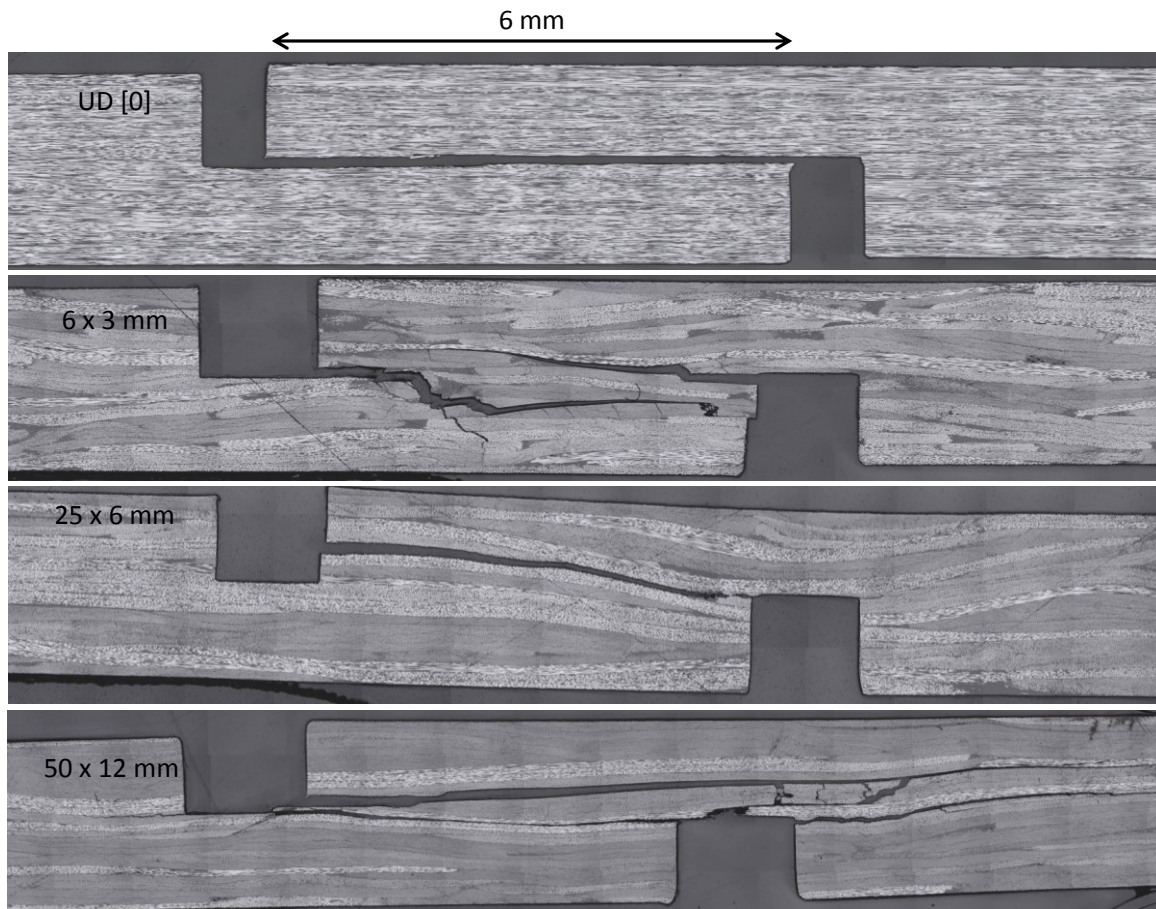


Figure 6-13 – Failure modes of DNS UD and ROS specimens with 6, 25 and 50 mm long strands

The DNS results were further compared against the SBS data [13]. In that test specimens were 25 x 7 mm and had a thickness of 3.5 mm. These results are shown in Figure 6-14, and all the data is normalized against the SBS strength of UD specimens. By comparing the strength of UD specimens measured with SBS and DNS, it is apparent that the DNS method significantly underestimates the results. Hence, it can be concluded that notches create stress concentrations which induce premature failure. Interestingly, both tests yield similar comparison between the properties of ROS and UD specimens. For example, based on Figure 6-12 and Figure 6-14, ROS composites with the shorter strands have shear strength that is 60 % of the UD strength.

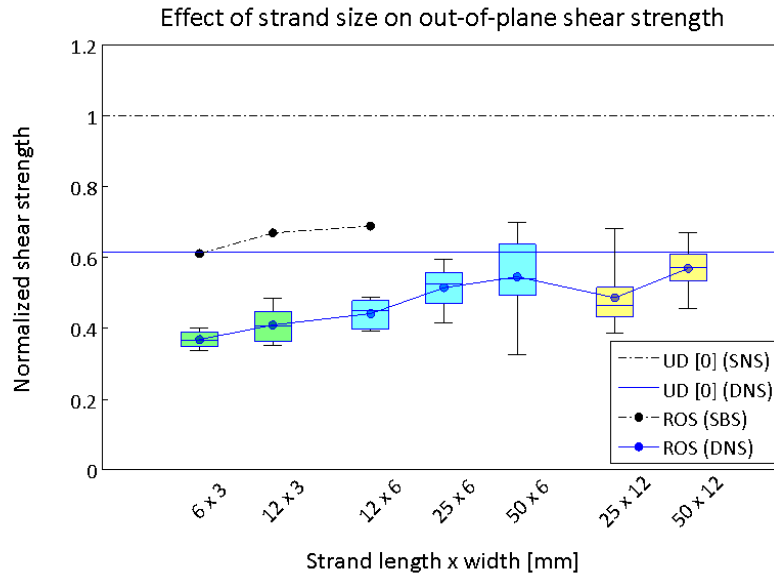


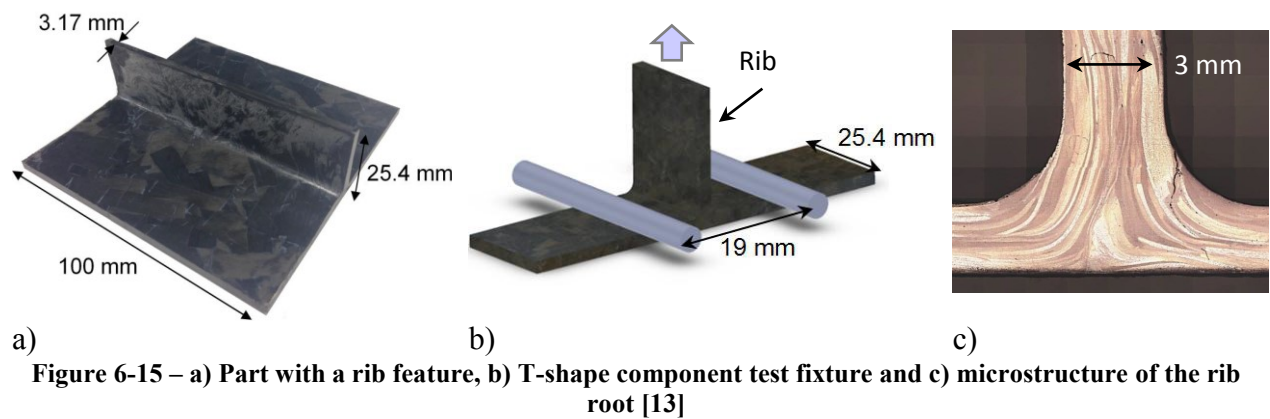
Figure 6-14 – Comparison between out-of-plane strength measured with SBS and DNS methods

6.4 Concluding remarks

This chapter presented experimental results pertaining to in-plane and out-of-plane shear properties of ROS composites. Shear strength and modulus both increased with increasing strand length. The same trend was observed in both tension and compression (Chapters 4 and 5). The knockdown of shear strength from CF to ROS was not as drastic as in the case of tensile or compressive loading. Thus, the use of ROS is recommended for application where shear is the dominant load. It is noteworthy that tensile, compressive and shear strengths had similar magnitudes. Hence, tensile strength, which is an easier property to measure, can be used as an approximation for other two strengths. Analogously, tensile and compression modulus are similar, and shear modulus can be computed (approximated) based on the assumption of transverse isotropy.

It is also noteworthy that accurate interpretation of test data is complicated by the fact that the size of the microstructural features of ROS composites is similar to some dimensions of the test specimens. For instance, the gauge section of the DNS and SBS specimens is actually smaller than most of the strand sizes that were considered. It is possible to test large specimens in order to measure the global properties; however, such specimens would be significantly larger than the

typical ROS parts. Hence, properties measured using large specimens may or may not be representative of the stress-strain response of the actual parts. For instance, the rib feature shown in Figure 6-15 would experience out-of-plane stresses at the root during loading, and the size of that region is actually similar in size to the DNS and SBS specimens. Hence, even though small specimens are not representative of the global material properties, they seem to be representative of the part properties. Also, in order to obtain a large gauge section with DNS and SBS test, really thick specimens must be manufactured, and they might develop defects and microstructural features that are absent from the thin part. For example, a through-the-thickness temperature gradient during cooling might have an adverse effect on part quality. Overall, the use of specimen sizes prescribed by the ASTM standards allows to compare properties between ROS composites and typical laminates and illustrates the negative effects of material heterogeneity, which will inevitable be present in industrial parts.



a) b) c)
Figure 6-15 – a) Part with a rib feature, b) T-shape component test fixture and c) microstructure of the rib root [13]

There are two consistent trends that interweave through all the experimental results, which are the dependency of mechanical properties and even warpage on strand length, and the high variability of data caused by material heterogeneity. The main goal of the subsequent chapters on modelling is to predict mechanical properties of ROS composites from the properties of UD carbon/PEEK, while accounting for strand length and heterogeneity of strand placement.

Chapter 7

In-plane model

This chapter will describe the stochastic finite element (FE) technique that was developed for modelling of the effective properties and behaviours of ROS composites from the basic properties of unidirectional prepreg. The main objective of this model is to predict strength and modulus of ROS composites, while also capturing the variability of properties and demonstrating the “weakest-link” principle that dictates failure. Modelling results will be compared to the experimental results and in particular to the DIC strain-field data.

7.1 Modelling overview

The modelling scheme proposed in this chapter is a modification and an extension of the earlier model created by Feraboli [31] for calculation of elastic properties of ROS composites. He proposed a 2D modelling scheme, which is illustrated by Figure 7-1, in which a specimen was discretized into partitions (or regions) and different ply layups were assigned to each partition. Global modulus of the entire specimen is calculated by evaluating the stress-displacement response of such specimen using a finite element software [31]. This approach was able to capture the average modulus and its variability. However, as there is complete discontinuity between neighbouring partition layups, the strain-field is highly dependent on the partition size and large strain discontinuities occur between partitions, as shown in Figure 7-1. Moreover, this model was not used to calculate strength.

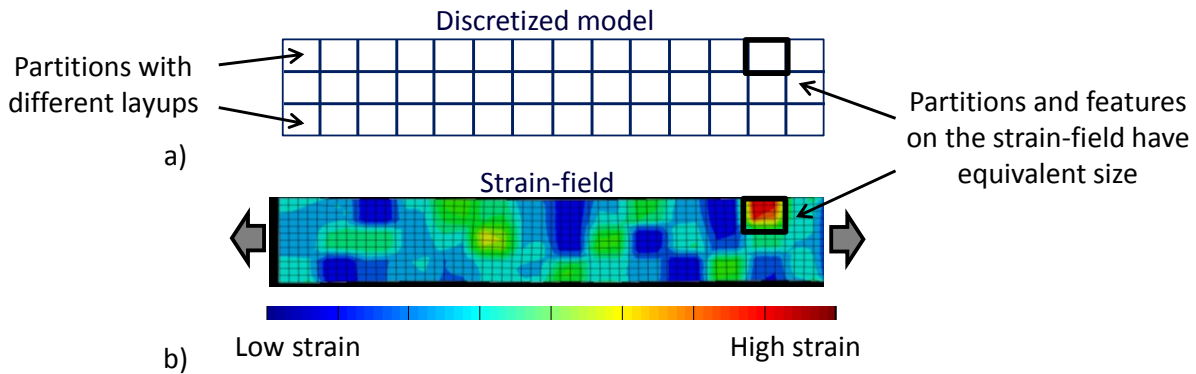


Figure 7-1 - Model of an ROS composite proposed by Feraboli in which a specimen is subdivided into regions with different properties (shown with different colours) and the resultant strain-field under loading (colour map corresponds to strain variability). These images were adapted from [31]

The modelling technique proposed in this thesis employs a different discretization technique, which is inspired by the models developed for Oriented Strandboard (OSB) wood-based composites. OSB and ROS composites have certain geometric similarities. Strand shape, aspect ratio and volume fraction are comparable between the two material systems. Analytical models developed for OSB panels capture the in-plane density variability in the material; density is related to strength and stiffness of OSB composites [89-91]. This modelling concept and the discretization technique are depicted in Figure 7-2, which shows the in-plane view of a panel populated with randomly oriented and positioned strands. The overall thickness of the panel is assumed to be uniform, and hence overlap regions constitute areas of high density, whereas voids lead to low density. It can be noted that partitions in Figure 7-2 are smaller than the individual strands. This methodology can be summarized as follows: (1) create a network of strands by randomly generating their in-plane orientation and position within a panel, (2) calculate the total number of strands at every partition, (3) convert the number of strands in each partition into localized panel density by assuming constant strand and panel thicknesses, and (4) finally, use density to estimate the strength and the stiffness of that OSB panel [89-91]. With some justification and changes, it is believed that this method of strand generation can be applied to ROS composites to generate a layup which captures the variability of ROS while taking into account strand size.

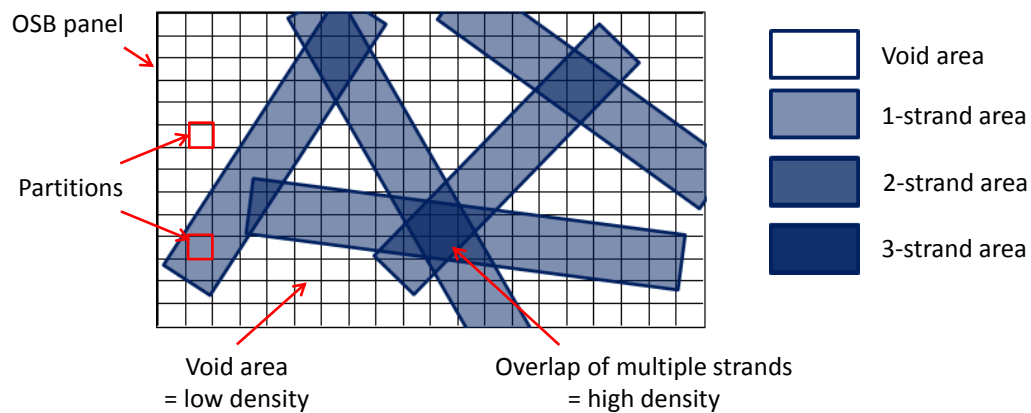


Figure 7-2 – Method for determining spatial density variability in an OSB panel (adapted from [89])

While no papers were found that deal specifically with strength modelling of ROS composites, Naderi and Khonsari [92] considered the variability of properties of CF laminates to capture arbitrary crack growth in an open-hole tensile specimen. Random stochastic properties were assigned to elements based on the Gaussian distribution function with 1 % variation. Failure initiation and propagation were modelled with Hashin's failure criteria and fracture energy evolution law. In this thesis, the strength modelling of ROS is developed using failure initiation and propagation methods [92] coupling with the Hashin's failure criteria.

To this day, no model can predict the strength of ROS composites from the properties of the constituents. Although the variability of modulus could be captured [31], a number of important factors such as the discontinuities in the strain-field, the undesired coupling between partition size and strain-field was not reported. This chapter presents a new modelling technique that includes strength modelling and provides an improvement over the existing stiffness model by ensuring that results are independent of the partition size, while capturing the variability inherent to the random strand orientation.

The outline of the proposed modelling scheme is shown in Figure 7-3. The geometry and the resultant properties of a typical tensile specimen are modelled and evaluated. The modelled specimen is populated with randomly oriented and positioned strands in order to account for the variability in the ROS microstructure, as shown in Figure 7-3 (step 1). This network of strands is then discretized using partitions and each partition contains information about the local layup, as

shown in Figure 7-3 (step 2). Since layups that are assigned to each partition result from the random strand placement, some partitions will have more layers of strands than others. Next, a 2D model is created in ABAQUS software and the layup information associated with each partition is transferred to this FE model, as shown in Figure 7-3 (step 3). Overall, the adopted modelling approach is typical to that used to model regular laminates (e.g. shell elements are used), with the main difference being that instead of assigning a single layup to the geometry, different layups are assigned to different partitions (i.e. areas) in order to represent the in-plane variability of the ROS microstructure. Finally, strength of the material is determined by applying Hashin's failure criteria and fracture energy evolution law. The entire procedure is repeated to capture the variability in modulus and strength among the different FE simulations. In this paper modelling results are compared against experimental work, which encompasses testing of CF laminates and ROS composites with different strand sizes.

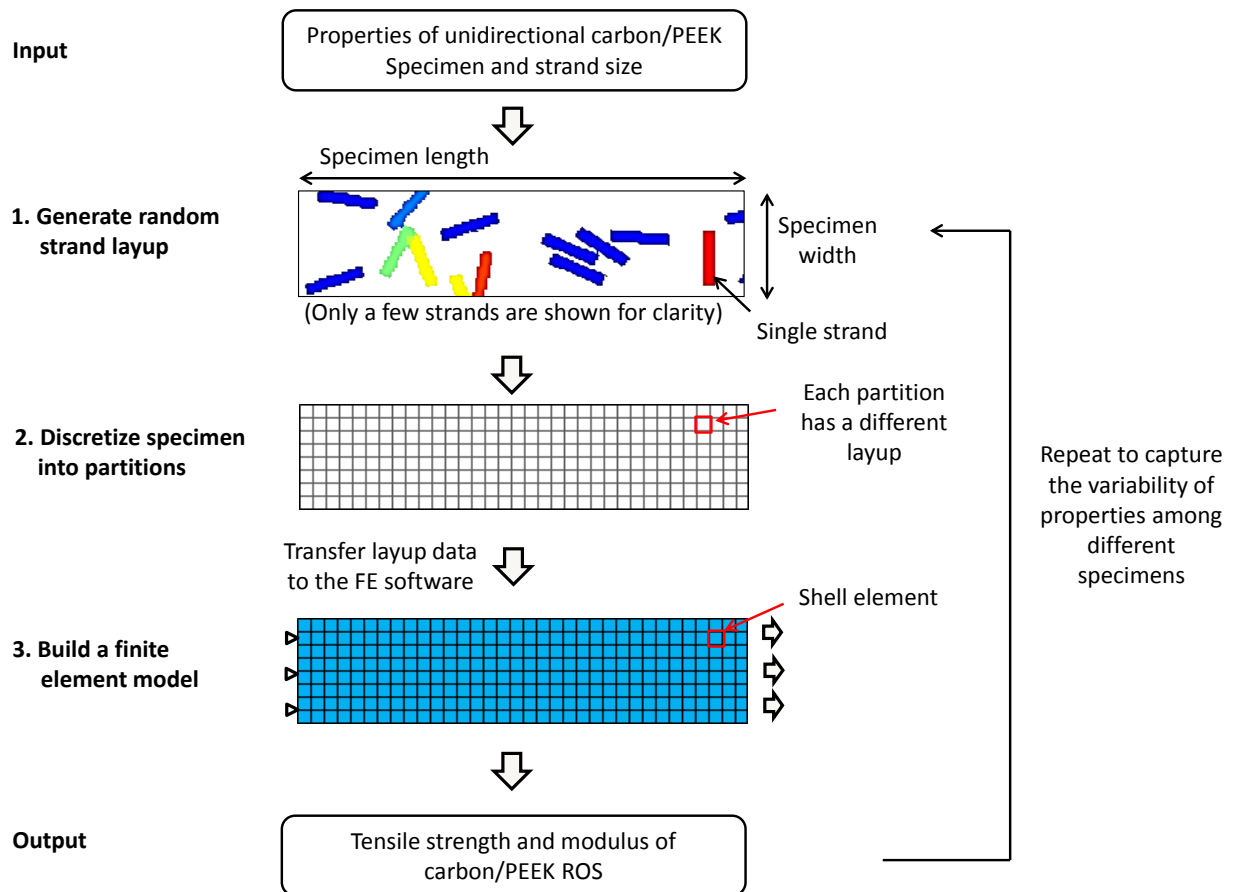


Figure 7-3 - Overview of the modelling structure

7.1.1 Steps 1 and 2 Generate random strand layup and partition the specimen

7.1.1.1 Assumptions

A 2D model is generated to represent the in-plane properties of a tensile specimen. The model takes into account the specimen length, width and thickness, and the strand size (12 - 50 mm) and off-axis orientation, but it ignores the following micro- and macro-structural features:

- strand out-of-plane orientation,
- defects (i.e. voids and resin rich areas),
- interlaminar shear between strands,
- residual thermal stresses.

Microstructure of ROS composites resembles that of a CF laminate, at least when it is discretized into smaller sections. Figure 7-4 shows a cross-sectional image of an ROS composite. The image shows the randomness of the strand layup and its 3D features such as strand out-of-plane orientation. Despite the randomness of the layup, when observed locally on a smaller scale (e.g. in 1 mm intervals) it resembles a laminate (refer to the red rectangles in Figure 7-4). The assumptions of planar strand orientation and defect-free microstructure is appropriate for large-strand ROS specimens, because strand placement is fairly orderly and planar as is shown in Figure 7-4b. On the other hand, small-strands have a more chaotic placement which results in large out-of-plane angles and numerous resin-rich areas, as shown in Figure 7-4a. Thus, the proposed model is expected to over-predict strength and modulus of short-strand ROS composites.

The effect of interlaminar shear properties and failure mechanisms are without a doubt non-negligible, since strand delamination was shown to be one of the primary failure modes. Overall, the model is expected to over predict strength, since only one failure mode is permitted but nonetheless, to capture the effect of variability on mechanical properties.

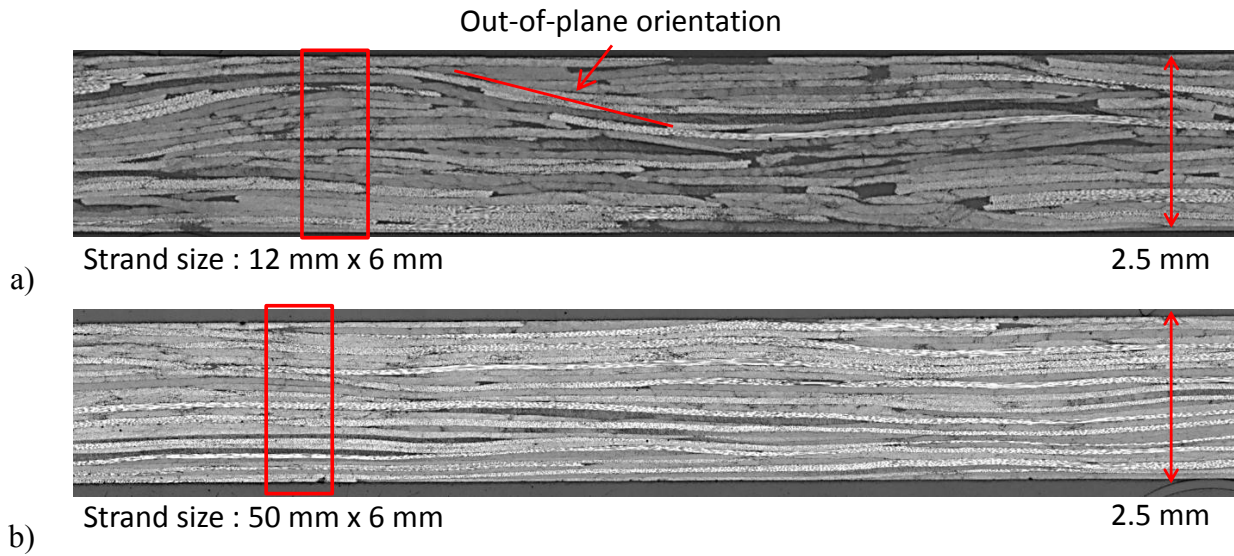


Figure 7-4 – Microstructure of a) short and b) long strand ROS specimens

Carbon/PEEK composites are expected to develop large residual thermal stresses, since during manufacturing they are cooled down from 340°C (melting temperature of PEEK). The proposed model can be extended to account for residual stresses by incorporating the COMPRO module (Convergent Manufacturing Technologies Inc) into the ABAQUS script. COMPRO is a commercially available program for calculation of cure or crystallinity and thermal residual stresses in polymer based composites. Unfortunately, at this stage it does not have a proper model for PEEK, but ongoing work is being done by our research partners at the University of British Columbia and Convergent Manufacturing Technologies Inc. Hence, calculation of residual stresses is part of the recommended future work.

7.1.1.2 Procedure

As opposed to continuous fibre composites with a uniform layup, ROS materials exhibit an almost infinite amount of different layups. In order to capture this variability in a model, an algorithm was written in MATLAB software to generate randomized strand layups and assign them to the geometry or component being simulated. In this case, the simulated geometry corresponds to the gauge section of an actual tensile specimen, which is 150 x 25 x 2.5 mm (6 x 1 x 0.1 in.). Three strand sizes are considered: 12 x 6 mm, 25 x 6 mm and 50 x 6 mm. The simulated specimen is discretized into partitions that store information about strand layups. As

more and more strands with random orientation are generated (or laid up) in the model, the layup properties stored in the partitions are automatically getting updated. For example, Figure 7-5 shows the placement of three strands within the modelled geometry. In this example, some partitions have only one strand associated with them, while others contain information about the overlap regions of two strands ([45 0] and [0 -60]). Since partitions are smaller than the individual strands and each strand spans across multiple partitions, there is a gradual transition of layups from one partition to the next. If a portion of the strand protrudes outside of the simulated geometry, it is cut off and is not reinserted from the other side (i.e. “torus conversion” is not used).

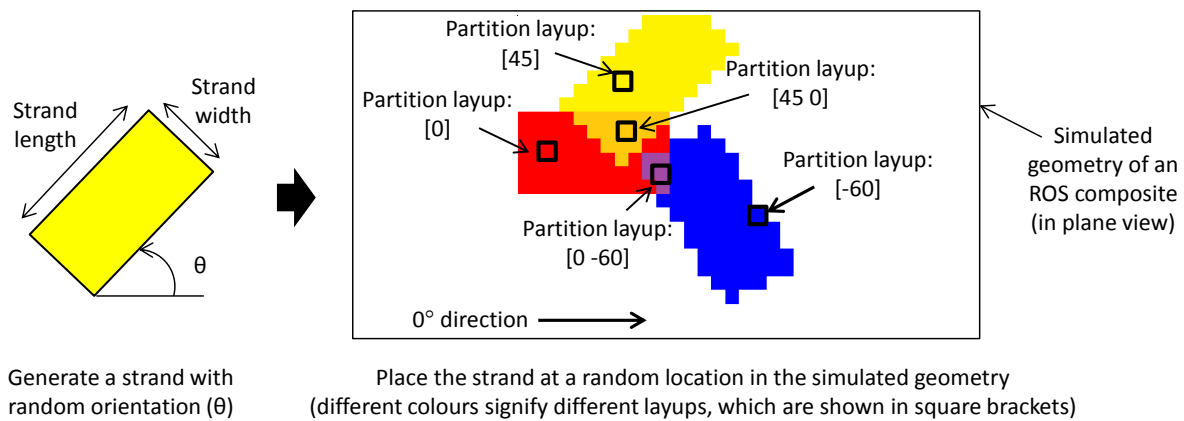


Figure 7-5 - Strand generation algorithm

Strand generation is continued until the average number of plies over all the partitions reaches the number of plies that a CF laminate of the same thickness would have. For instance, a 2.5 mm CF laminate would have 18 plies. Thus, on average a 2.5 mm thick ROS composite is also expected to have 18 strands through-the-thickness, but locally this number will vary, as shown in Figure 7-6. Once strand generation is complete, thickness of each ply in a given partition is adjusted such that the total partition thickness (t) is 2.5 mm, as shown in Figure 7-6. This step is implemented in order to achieve constant thickness everywhere in the simulated geometry. It is also noteworthy that symmetry and balance of the layups are not enforced during strand generation.

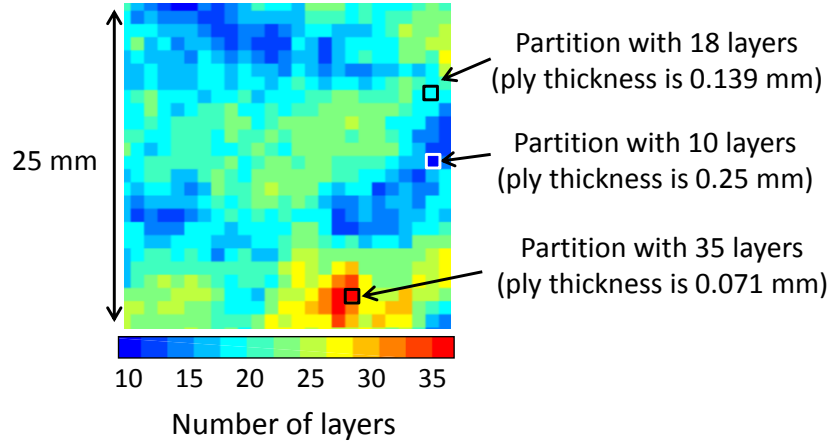


Figure 7-6 - Variability in the number of layers among partitions in 2.5 mm thick simulated ROS composite

7.1.1.3 Equivalent elastic properties

Global properties of the specimen are estimated by evaluating the equivalent properties of each partition and averaging them out. This calculation is based on the layup of the individual partitions and does not consider the load sharing between them, which is accounted for by the FE model (next section). For every partition the CLT is used to calculate the equivalent engineering properties (Eq. 7-1-Eq. 7-3). The laminate ABD stiffness matrix defines a relationship between stress and moment resultants (N , M), and laminate strains and curvatures (ϵ , κ) (Eq. 7-1).

$$\begin{Bmatrix} N \\ M \end{Bmatrix} = \begin{bmatrix} A & B \\ B & D \end{bmatrix} \begin{Bmatrix} \epsilon \\ \kappa \end{Bmatrix} \quad \text{Eq. 7-1}$$

And ABD matrices are computed from the ply off-axis stiffness matrix (Q_{126}):

$$\begin{aligned} A_{ij} &= \int_{-t/2}^{t/2} Q_{ij} dz & i, j &= 1, 2, 6 \\ B_{ij} &= \int_{-t/2}^{t/2} Q_{ij} z dz & i, j &= 1, 2, 6 \\ D_{ij} &= \int_{-h/2}^{h/2} Q_{ij} z^2 dz & i, j &= 1, 2, 6 \end{aligned} \quad \text{Eq. 7-2}$$

Engineering constants are then computed from the laminate abd compliance matrix using the following formulations:

$$\begin{bmatrix} a & b \\ b & d \end{bmatrix} = \begin{bmatrix} A & B \\ B & D \end{bmatrix}^{-1}$$

$$E_1 = \frac{1}{a_{11}t}$$

$$E_2 = \frac{1}{a_{22}t}$$

$$G_{12} = \frac{1}{a_{12}t}$$

Eq. 7-3

where E_1 , E_2 and G_{12} are the longitudinal, transverse and shear moduli.

Additionally, the CLT can be used to find the equivalent CTE of a laminate (Eq. 7-4 – Eq. 7-11). The general approach is to first compute the stress-free thermal strains ($\{\epsilon_{xys}\}^T$) that a UD ply would experience due to a change in temperature (ΔT), Eq. 7-4. For this calculation a dummy $\Delta T = 1$ can be used, because this term will get factored out during the last calculation (Eq. 7-11). The next step is to compute the thermal force and moment results ($\{N^T\}$ and $\{M^T\}$) that would develop in a laminate by recognizing that plies are bonded together and cannot expand freely when a ΔT is applied, Eq. 7-5 - Eq. 7-9. Finally, the equivalent thermal laminate strains ($\{\epsilon_{126}\}_0$), Eq. 7-10, and the effective laminate CTE (α_{126}), Eq. 7-11 are calculated.

Eq. 7-4 defines the relationship between applied ΔT and the on-axis ply strains, where (α_{xys}) represents the longitudinal (α_x), transverse (α_y) and shear ($\alpha_s = 0$) CTE of a UD ply.

$$\{\epsilon_{xys}\}^T = \begin{Bmatrix} \alpha_x \\ \alpha_y \\ \alpha_s \end{Bmatrix} \Delta T$$

Eq. 7-4

Expressions for laminate thermal force and moment resultants are given by Eq. 7-5 and Eq. 7-6 in terms of the off-axis (i.e. subscripts 1, 2, 6) ply strains and stiffness.

$$\{N\}^T = \int_{-t/2}^{t/2} [Q_{126}] \{\varepsilon_{126}\}^T dz \quad \text{Eq. 7-5}$$

$$\{M\}^T = \int_{-t/2}^{t/2} [Q_{126}] \{\varepsilon_{126}\}^T z dz \quad \text{Eq. 7-6}$$

Alternatively, the force resultant can be expressed in terms of the on-axis ply properties (Eq. 7-7) and more conveniently in terms of the on-axis ply CTE (Eq. 7-9) by combining Eq. 7-4 and Eq. 7-7. The moment resultant can be expressed in the same form.

$$\{N\}^T = \int_{-t/2}^{t/2} [T]^{-1} [Q_{xys}] \{\varepsilon_{xys}\}^T dz \quad \text{Eq. 7-7}$$

$$\text{where } [T]^{-1} = \begin{bmatrix} \cos^2\theta & \sin^2\theta & -2\sin\theta\cos\theta \\ \sin^2\theta & \cos^2\theta & 2\sin\theta\cos\theta \\ \sin\theta\cos\theta & -\sin\theta\cos\theta & \cos^2\theta - \sin^2\theta \end{bmatrix} \quad \text{Eq. 7-8}$$

$$\{N\}^T = \Delta T \int_{-t/2}^{t/2} [T]^{-1} [Q_{xys}] \begin{Bmatrix} \alpha_x \\ \alpha_y \\ 0 \end{Bmatrix} dz \quad \text{Eq. 7-9}$$

Finally, the equivalent laminate thermal strains and CTE are calculated using Eq. 7-10 - Eq. 7-11. By comparing Eq. 7-9 - Eq. 7-11, it is evident that ΔT gets factored out.

$$\{\varepsilon_{126}\}_o = [a \quad b] \begin{Bmatrix} N^T \\ M^T \end{Bmatrix} \quad \text{Eq. 7-10}$$

$$\{\alpha_{126}\} = \frac{\{\varepsilon_{126}\}_o}{\Delta T} \quad \text{Eq. 7-11}$$

7.1.2 Step 3 – Build a finite element model

Finite element model was created in ABAQUS to evaluate the stress-strain response of the material. A *Python* script, which is a programming language used to interface with ABAQUS, is used to generate the FE model (geometry, mesh, boundary conditions, etc.) and to assign layups

to each partition. Partition refers to an area of the specimen with distinct layup assigned to it. For this reason, the mesh size has to be the same as the partition size or finer, and each mesh element has to be fully within a partition (i.e. it cannot be split between two partitions with different layups). The same mesh and partition size are used, such that each element is 1 x 1 mm and has its own layup. The effect of mesh and partition size will be discussed in the next section. The model is meshed using 4-node quad shell elements (S4). The stress-strain curve is captured by incrementally applying a displacement and measuring the force resultants. For the boundary conditions, a constant displacement is applied along one edge, and the opposite edge is restrained in the longitudinal direction. Two nodes, one along each restraint edge, are fully restrained, and the rest of the specimen is free to deform in any direction, as shown in Figure 7-7.

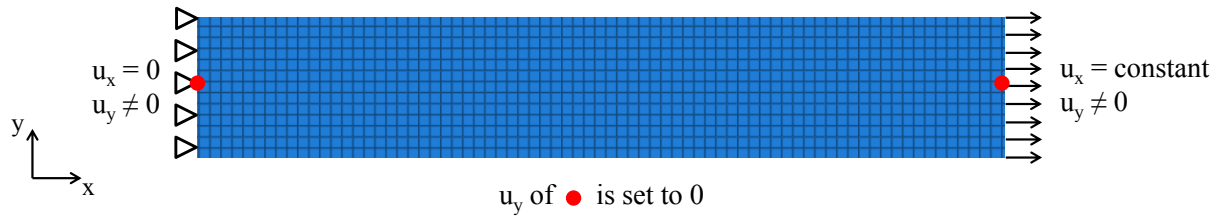


Figure 7-7 - Boundary conditions imposed on the simulated tensile specimen. X and Y refer to longitudinal and transverse directions, and u represents displacement

7.1.2.1 Mesh and partition size

Sensitivity of the model to mesh and partition sizes was evaluated in the range of 0.5 – 3 mm. All the models showed the same features on the stress, strain and damage plots, and predicted the same modulus. For example, the effect of partition size on the damage state of a simulated tensile specimen is shown in Figure 7-8. The only difference among these images is that larger partition size results in a coarser pattern.

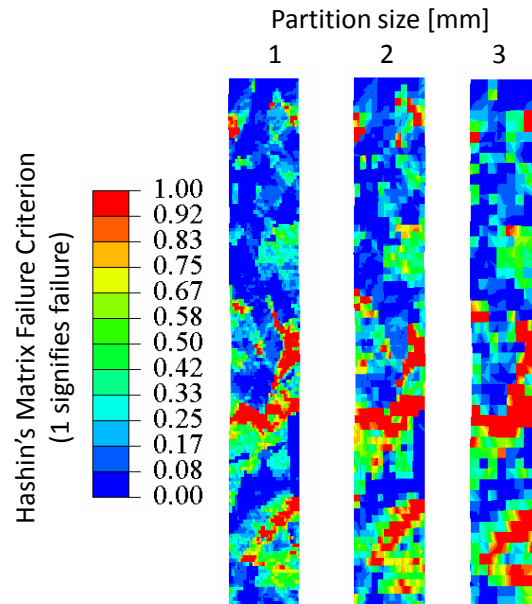


Figure 7-8 – Damage state of simulated tensile specimens at the time of failure

Since the mesh size had no effect on the results, for the sake of consistency, it was kept the same size as the partition size during modelling. Effect of the partition size on the average strength, which was normalized by the strength of CF laminates, is summarized in Figure 7-9. Overall, partition size (and corresponding mesh size) of 0.5 mm provided the most accurate results (with respect to convergence). However, partition size of 1 mm was used for the rest of the study, as it required shorter run times and provided results within 6%. For the purpose of this study, given the random nature of the strength, this accuracy was considered good enough.

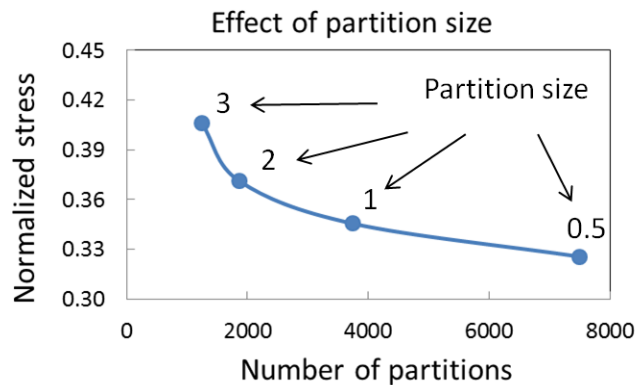


Figure 7-9 – Effect of partition size on predicted strength

7.1.2.2 Failure criteria and damage propagation

Damage initiation is determined by the Hashin's failure criteria [93] and is combined with the fracture energy dissipation [94] methods to model damage propagation. This is done on ply-by-ply bases. Once any of the plies in a particular partition reach one of the Hashin's failure criteria (i.e. fail), their individual properties are degraded at a rate which is defined by the fracture energy dissipation formulation. The rate at which ply properties are degraded depends on the failure criterion that was triggered. For instance, matrix failure is accompanied by gradual decrease in transverse stiffness (E_{22}), whereas fibre failure results in an abrupt drop in longitudinal stiffness (E_{11}). These formulations will be discussed in more detail in this section.

Hashin's failure criteria (Eq. 7-12 -Eq. 7-15) criteria were chosen because they consider the combined effect of different stress components on each failure mode, can differentiate between fibre and matrix failure modes and are available in ABAQUS.

Fibre tension ($\sigma_f \geq 0$):

$$F_f^T = \left(\frac{\sigma_f}{\sigma_L^T} \right)^2 + \left(\frac{\tau}{\sigma_S^L} \right)^2 \quad \text{Eq. 7-12}$$

Fibre compression ($\sigma_f \leq 0$):

$$F_f^C = \left(\frac{\sigma_f}{\sigma_L^C} \right)^2 \quad \text{Eq. 7-13}$$

Matrix tension ($\sigma_m \geq 0$):

$$F_m^T = \left(\frac{\sigma_m}{\sigma_T^T} \right)^2 + \left(\frac{\tau}{\sigma_S^L} \right)^2 \quad \text{Eq. 7-14}$$

Matrix compression ($\sigma_m \leq 0$):

$$F_m^C = \left(\frac{\sigma_m}{2\sigma_S^T} \right)^2 + \left[\left(\frac{\sigma_T^C}{2\sigma_S^T} \right)^2 - 1 \right] \frac{\sigma_m}{\sigma_T^C} + \left(\frac{\tau}{\sigma_S^L} \right)^2 \quad \text{Eq. 7-15}$$

In the above equations, σ_f , σ_m and τ represent the components of the effective stress tensor; σ_L^T and σ_T^T denote longitudinal and transverse tensile strength; σ_L^C and σ_T^C denote longitudinal and transverse compressive strength; σ_S^L and σ_S^T denote longitudinal (in-plane) and transverse (out-of-plane) shear strength.

Damage propagation is modelled by linearly softening the material (i.e. ply) based on the concept of fracture energy (G) dissipation. In this method, stress-displacement behaviour for each failure mode is represented by a bi-linear relation shown in Figure 7-10. The slope O-A represents linear elastic behaviour prior to damage initiation (or peak stress). After the onset of damage, material stiffness decreases, which is represented by the line O-B. The area under OAC represents the total fracture energy. The equivalent displacement (δ_{eq}) is used to calculate the damage variable (d) corresponding to the particular failure mode, which is then used to compute the damaged stiffness matrix (C_d) of the particular ply [94]:

$$d = \frac{\delta_{eq}^f (\delta_{eq} - \delta_{eq}^o)}{\delta_{eq} (\delta_{eq}^f - \delta_{eq}^o)} \quad \text{Eq. 7-16}$$

Where δ_{eq} is the current displacement; δ_{eq}^o is the displacement at which the damage initiation criterion for that mode is met, and δ_{eq}^f is the displacement at which the material is completely damaged.

$$C_d = \frac{1}{D} \begin{bmatrix} (1-d_f)E_1 & (1-d_f)(1-d_m)v_{21}E_1 & 0 \\ (1-d_f)(1-d_m)v_{12}E_2 & (1-d_m)E_2 & 0 \\ 0 & 0 & (1-d_s)G_{12}D \end{bmatrix} \quad \text{Eq. 7-17}$$

$$\text{Where } D = (1-d_f)(1-d_m)v_{12}v_{21} \quad \text{Eq. 7-18}$$

In this expression, d_f , d_m and d_s are the damage variables that denote the current state of fibre, matrix and shear damage.

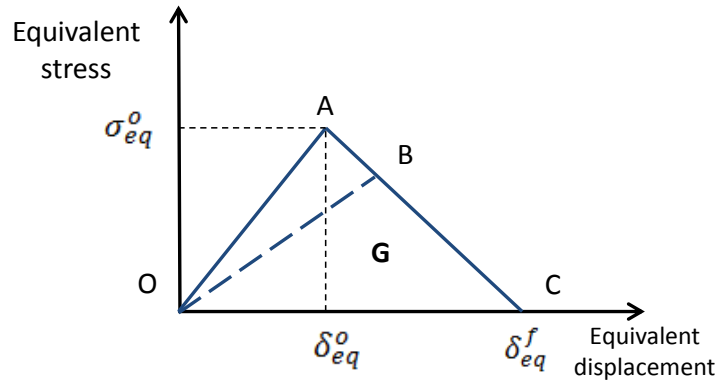


Figure 7-10 – Stress-displacement relationship for each damage mode.

Mechanical properties of carbon/PEEK are readily available from the manufacturer and are summarized in Table 7-1. No experimentally measured values for fracture energies of carbon/PEEK were found in the open literature. In this thesis, fracture energies were chosen so that stress-strain curves of $[0/\pm 60]_{3S}$ and $[90/\pm 30]_{3S}$ laminates obtained from FE analysis would match the experimental results. The benchmark energy values were taken from the literature [92, 95], which relied on approximate values to model progressive crack growth in open-hole GLARE [95] and CF carbon/PEEK laminates [16]. The effect of fracture energies on stress-strain response was the most evident in the case of $[0/\pm 60]_{3S}$ laminates, as shown in Figure 7-11. With benchmark values, there is a dip in the stress-strain curve when the $\pm 60^\circ$ plies fail; whereas, the experimental curve is straight. If all fracture energies are increased by a factor of 10, then the stress-strain curve becomes straight but properties degrade too slowly after the failure of 0° plies. Overall, values that gave best results for $[0/\pm 60]_{3S}$ and $[90/\pm 30]_{3S}$ layups are summarized in Table 7-2.

As noted in ABAQUS [94], materials that are experiencing stiffness degradation often lead to convergence difficulties in implicit analysis. These difficulties can be mitigated with a viscous regularization scheme, which ensures that the tangent stiffness matrix is positive definite for a sufficiently small time increment. In general, viscous coefficient has a similar effect on results as fracture energy. The higher are the values, the higher is the failure load. Hence, for simplicity viscosity coefficient was set to zero and only the effect of fracture energies was considered.

Table 7-1 - Mechanical and material properties of carbon/PEEK plies. Mechanical properties were taken from the datasheet provided by the manufacturer [83] and thermal properties were taken from the literature [80]; * Out-of-plane shear modulus was calculated based on the transverse isotropic assumption; and ** Transverse tensile and compressive strengths were assumed to be the same

Material properties of Carbon/PEEK		
Modulus [GPa]	Longitudinal	130
	Transverse	10
	In-plane shear	5.2
	Out-of-plane shear	3.759*
Poisson's ratio	In-plane	0.33
Strength [MPa]	Longitudinal tension	2280
	Longitudinal compression	1300
	Transverse tension and compression	86**
	In-plane shear	152
	Out-of-plane shear	94
Fracture energy [N/mm]	Longitudinal tension	1
	Longitudinal compression	1
	Transverse tension	10
	Transverse compression	10
Coefficient of thermal expansion [$\mu\epsilon/^{\circ}\text{C}$]	Longitudinal	-0.3
	Transverse	34.3

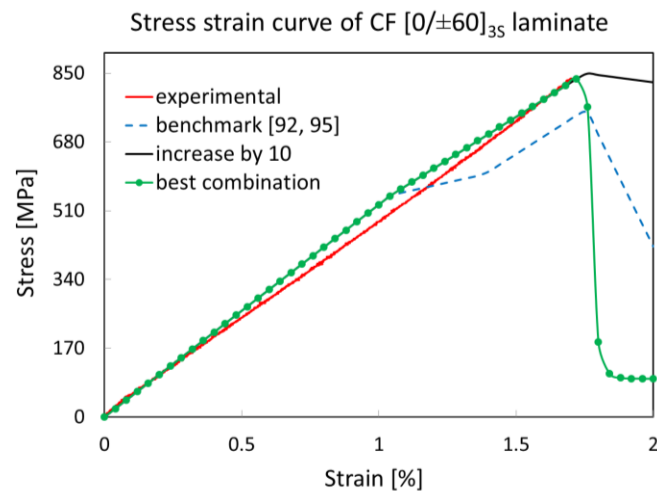


Figure 7-11 – Effect of fracture energy on the stress-strain curve of $[0/\pm 60]_{3S}$ laminate. Stress values are normalized with respect to the failure load obtained experimentally.

Table 7-2 – Fracture energies used to model failure of carbon/PEEK.

Fracture energy [N/mm]	From [92, 95]	This thesis
Longitudinal tension	12.5	1
Longitudinal compression	12.5	1
Transverse tension	1	10
Transverse compression	1	10

In the case of ROS composites, ten simulations with different randomized layups were run for each strand size, and failure was assumed to occur when the model failed to converge. Loading was applied incrementally with a constant step size, but as the element properties began to degrade, the step size was reduced automatically with the aim to achieve convergence. Overall, a sample set of stress-strain data obtained from an FE model, shown in Figure 7-12, demonstrates that the analysis converged to a failure load.

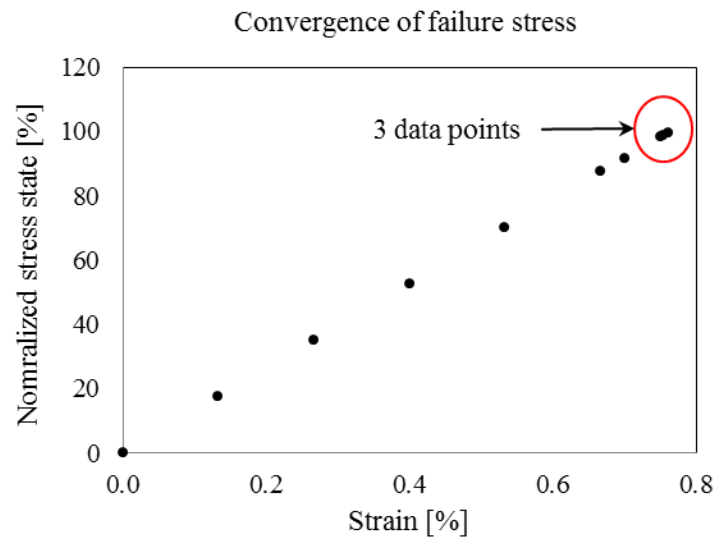


Figure 7-12 – Convergence of the stress values to failure strength. Stress values are normalized with respect to the failure load

7.2 Results and discussion

7.2.1 Analytical model (elastic properties)

Firstly, results of the analytical module of the model are discussed. Figure 7-13 shows typical equivalent stiffness plots that were generated using the CLT algorithm for a 250 x 250 mm panel; red rectangle in this figure represents a tensile specimen. It is evident that local properties are highly variable (e.g. $E_1 = 15\text{-}90$ GPa). It is noteworthy, that features of low and high modulus patterns on these plots are larger than the partition size, which is 1 mm, hence highlighting that these results are independent of the partition size.

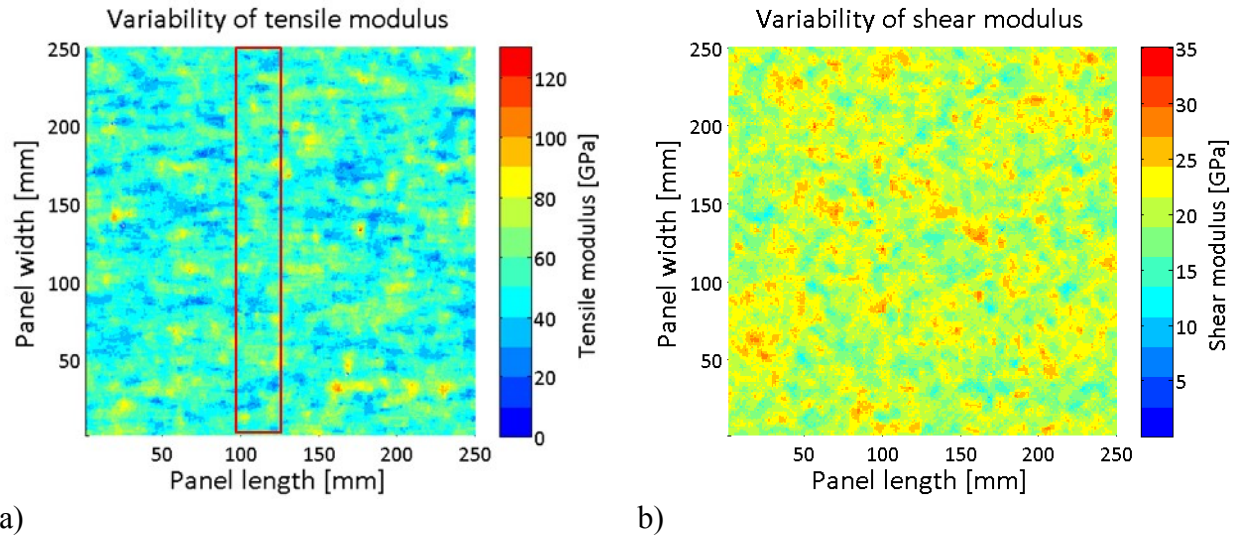


Figure 7-13 – Variability of the local a) tensile and b) shear modulus in 2.5 mm thick discretized specimen with 25 x 6 mm strands. Rectangle in (a) represents size of a tensile specimen

Next, the effect of coupling matrices B and D on the calculation of equivalent properties is examined. Two methods of calculating equivalent stiffness were considered: (i) only A matrix was used, thus implying symmetric and balanced layup, and (ii) the A, B and D matrices were used to account for coupling between the normal and flexural strains and loads. Fifty simulations were run using each option. Figure 7-14 gives a comparison between modelling and experimental results, which were normalized based on the properties of a QI CF laminate. Overall, it is evident that ROS composites have lower stiffness than CF laminates. Modelling results obtained by using the coupling matrices (i.e. Model-ABD matrix) are more representative of actual ROS specimens, while those that were calculated using only the A matrix (i.e. Model-A matrix) over predict the results and are closer to the properties of QI CF laminates. Hence, it can be postulated that ROS composites exhibit a lower modulus than QI CF laminates during testing because of their unsymmetrical and unbalanced strand layups.

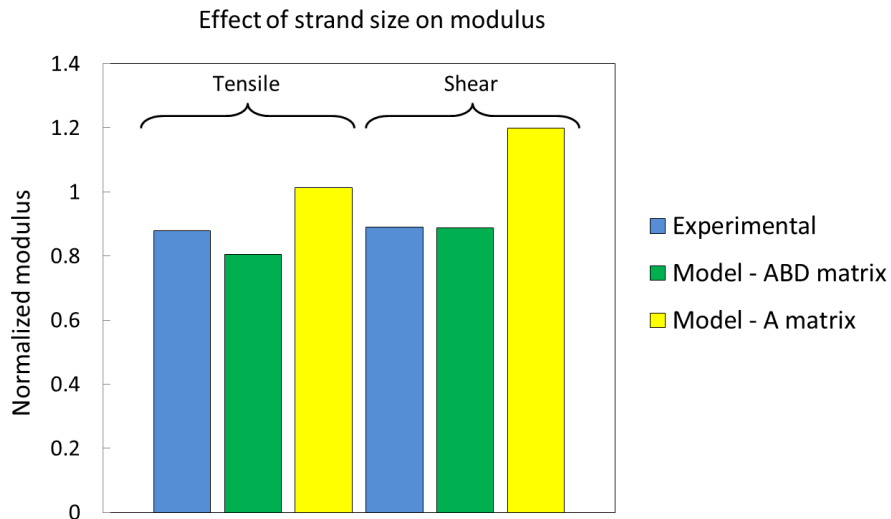


Figure 7-14 – Comparison between experimental and modelling results for tensile modulus of a 2.5 mm thick ROS panel with 25 x 6 mm strands. Results are normalized based on the strength of QI CF laminates

It is also possible to demonstrate the variability of CTE in ROS specimens. Sample image is shown in Figure 7-15. Experimental results obtained with the TMA showed that CTE of 8 x 8 mm samples varied between 1 - 13 $\mu\epsilon/^\circ\text{C}$, and analogous range was observed with the modelling results. These modelling results further support the hypothesis that panel warpage is caused by heterogeneity of in-plane properties.

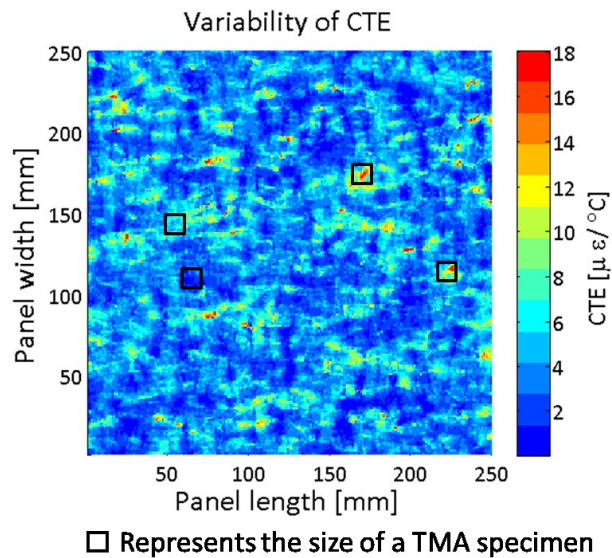


Figure 7-15 – Variability of the coefficient of thermal expansion (CTE) in an ROS panel

7.2.2 FE model (elastic properties)

A one-to-one comparison between the model and the experiments cannot be obtained since the exact strand orientation and placement in an ROS specimen are unknown and hence cannot be simulated. However, general trends can still be compared. Figure 7-16 shows evolution of the strain-field during loading of a) an actual and b) a randomly simulated ROS specimen. Both show that there are regions of high strain which are noticeable even at low loads, while the rest of the specimen experiences significantly lower strains. The earlier model developed by Feraboli *et al.* [31] was also able to capture regions of high and low strain, but their size and shape depended on the partition size, which is a modelling and not a physical parameter, as shown in Figure 7-1. The current model captures the shape and size of these regions independently of the partition size, since strands span across multiple partitions and the change in layups from one partition to the next is gradual.

Comparison between the measured and the calculated global modulus is shown in Figure 7-17. Both sets of data indicate that global modulus is variable among the specimens (eight specimens/strand length were tested and ten specimens/strand length were simulated), as shown by the error bars in Figure 7-17. Also, modulus of CF laminates is higher than that of ROS composites due to the unsymmetrical and unbalanced strand layups in the latter. Same results were noted in Section 7.2.1.

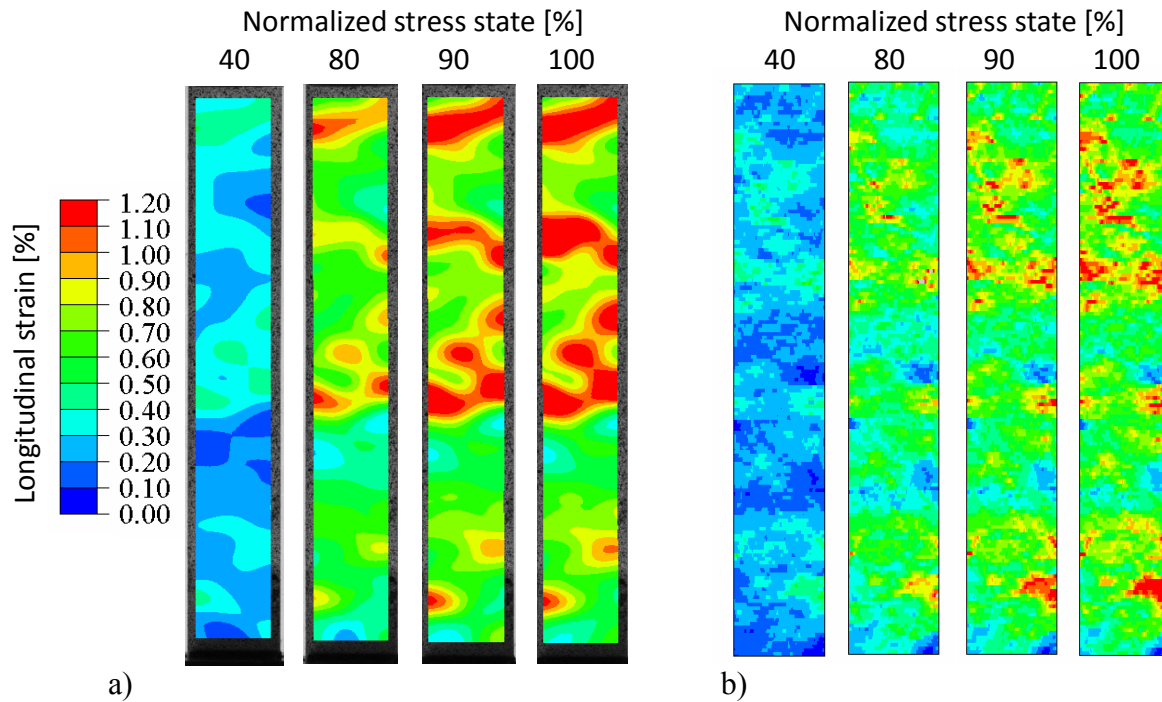


Figure 7-16 - Evolution of the strain-field captured with a) DIC and b) FE model. Stress values are normalized with respect to the failure load

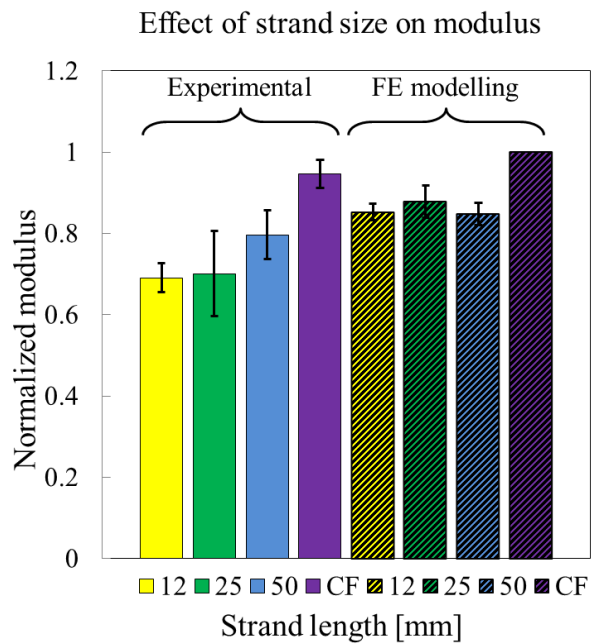


Figure 7-17 - The effect of strand length on modulus. Error bars show the standard deviation

Overall, the model predicts well the modulus of ROS composites with longer strands and over-predicts for composites with shorter strands. Some of this discrepancy can be explained by the fact that smaller strands are more prone to be oriented out-of-plane, as depicted in Figure 7-4a, and hence have lower in-plane modulus. The most accurate way of accounting for the out-of-plane orientation is to create a 3D model, which would be very complex considering heterogeneity. Simplified methods which can be used with a 2D model entail: (i) the use of the orientation efficiency factor, such as that proposed by Krenchel (Eq. 2-14), which would be applied to the computed global properties or (ii) the modification of the elastic properties of each strand by using something analogous to the Nielsen and Chen formulation for off-axis laminates (Eq. 2-15 -Eq. 2-16). Both of these methods require knowledge of the probability distribution for off-axis angle. Additionally, elastic properties can be scaled by the Kelly-Tyson length efficiency factor to account for the effect of strand length. Overall, the proposed model provides a good estimation of the elastic properties and can be slightly fine-tuned to improve the accuracy of results pertaining to short-strand ROS composites.

7.2.3 FE model (failure properties)

Measured and predicted strengths of ROS composites are summarized in Figure 7-18. Overall, strength obtained with ROS panels is less than 40 % of the strength of CF quasi-isotropic laminates. Performance of discontinuous-fibre composites is expected to be lower than that of CF composites in part due the reduced ability of short fibres to carry load. As the fibre length increases, mechanical properties are expected to increase eventually approaching those of CF composites. As was shown in section 2.2.3 of the literature review, based on the simple analytical models (e.g. Kelly-Tyson) even the 12 mm long fibres should attain high properties similar to those of CF laminates. Hence, there must be other factors besides fibre length that affect strength.

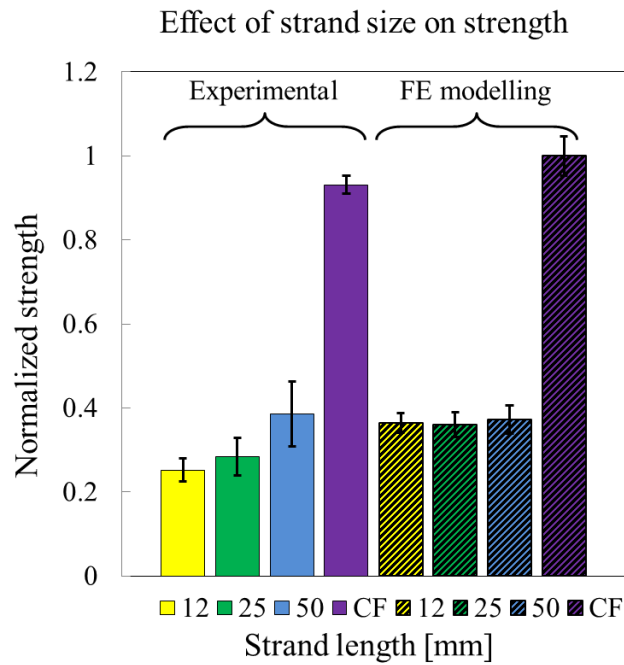


Figure 7-18 - The effect of strand length on strength. Error bars show the standard deviation

Two possible explanations for the large reduction in strength are material heterogeneity and matrix-dominated failure mode. The matrix-dominated failure mode pertains to transverse strand failure and strand delamination, but the current model considers only the former. Examination of the cross-sectional micrographs of failed specimens showed that little damage developed away from the main failure region, signifying that specimens failed at the weakest point while the rest of the specimen was still intact. Similar results were obtained through simulation. For instance, Figure 7-19 shows progressive failure of a simulated tensile specimen in terms of the evolution of Hashin's a) matrix tension and b) fibre tension criteria. Only the first ply is shown, but it is representative of the general state of the entire specimen. There are a few regions with extensive matrix damage, but little fibre damage can be detected. It is evident that failure is localized, while a large portion of the specimen remains undamaged, which explains why strength of ROS composites is significantly lower than that of CF laminates. Strength of ROS composites is highly variable and even FE simulations predicted a wide range of failure loads, as shown by the error bars in Figure 7-18. Material heterogeneity makes it difficult to predict the exact failure strength of ROS composites, and a statistical method is required to predict the range of possible

outcomes. The modelling technique proposed in this paper captures the non-uniform damage development within a specimen as well as a difference in load bearing capacity among them.

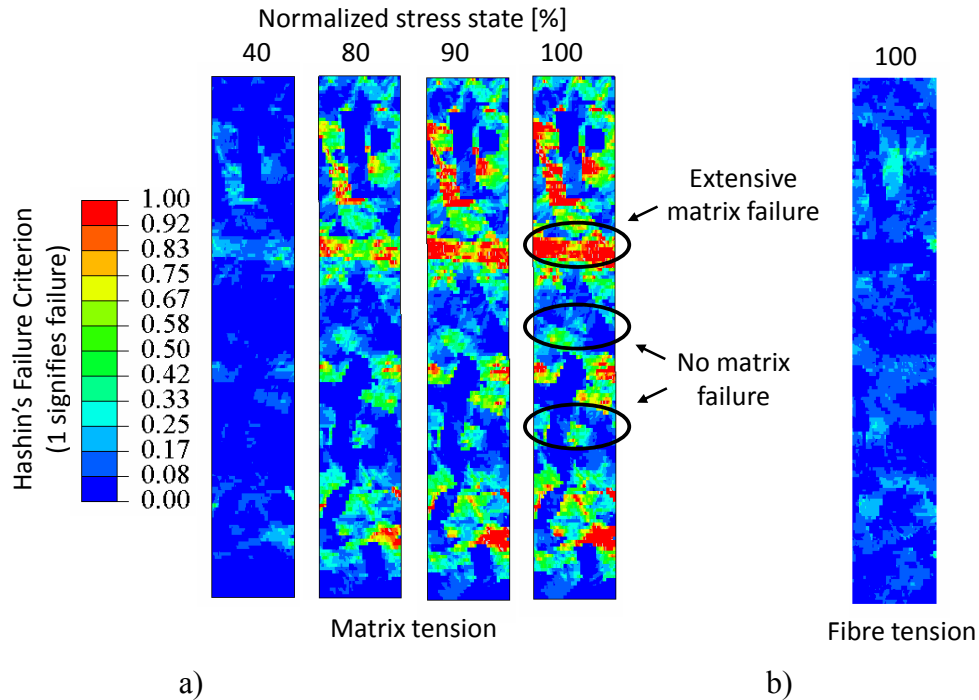


Figure 7-19 - Progressive failure depicted by Hashin's a) matrix tension and b) fibre tension failure criteria, where the value of "1" signifies failure. Stress values are normalized with respect to the failure load

Experiments show that this material undergoes extensive delamination of the strands during failure; however, the current model is a simple 2D case, which does not capture delamination. Test results also show that strength increases with strand length Figure 7-18. This trend is not captured with the FE model, because the model does not include delamination, which is governed by the strand overlap length. Nonetheless, the proposed model predicts a significant drop in strength when going from CF to ROS layups and shows that failure is a matrix-dominated event. Hence, it can be concluded that while strand size has an effect on strength, the biggest knockdown of strength comes from material heterogeneity which leads to the presence of "weak-spots". As stated in the introductory paragraph the main goal of the proposed modelling technique was to demonstrate the effect of heterogeneity of ROS composites on their properties, since variability of experimental data was high.

7.3 Concluding remarks and future work

This chapter described a modelling technique for estimation of strength and modulus of ROS composites. This is the first strength model found in the open literature that was developed for ROS composites. The earlier stiffness model that was proposed by Feraboli [31] predicted strain-fields that are partition size dependent, and the current model alleviates this problem. The main concept of the model is to discretize the simulated geometry into small regions or partitions, which can have different layup, in order to account for the material heterogeneity. To achieve this, strands with random orientation and position are generated and placed within the geometry being simulated. As a result, each partition has a different layup assigned to it. Strength and modulus are estimated by building an FE model in ABAQUS, applying a displacement to obtain modulus and using Hashin's failure criteria and fracture energies to predict failure.

Experimental and modelling results showed that strength and modulus of ROS composites are variable from one specimen to another due to the heterogeneity of the material. From an industrial standpoint, variability is an important parameter since it is involved in the calculation of design allowables. Also, ROS composites fail at relatively low loads in comparison to CF laminates, mainly because failure occurs based on the "weakest-link" principle and is matrix-dominated. The main downfall of the model is that it does not capture interlaminar shear and delamination, dominant factors influencing strength of the shorter strands. Hence, the effect of these factors will be studied in the next chapter. Overall, the stochastic approach presented in this paper can successfully capture the heterogeneity of strength and stiffness of ROS materials, and it can be implemented into more complex strength models or adapted for other purposes, such as modelling of thermal residual stresses.

An interesting future application of the model would be the calculation of warpage caused by the residual thermal stresses. This can be done by using COMPRO once the proper material model for carbon/PEEK is implemented. Overall, it would be interesting to reproduce different warped shapes through modelling and to investigate the ways of minimizing distortion.

Chapter 8

Through-the-thickness model

This chapter will describe the analytical model that was developed to predict strength of ROS composites from the basic properties of unidirectional prepreg. The previously developed model (refer to Chapter 7 – In-plane model) showed that strength of ROS composites is significantly lower than that of QI CF laminates due to the presence of localized weak-spots. Unfortunately, that model could not predict the effect of strand size, because it did not take into account interlaminar failure (i.e. debonding of the strands). As was previously discussed in the experimental chapters (4-6), strand delamination is one of the principal failure modes and hence must be considered in the strength calculations. The main objective of the model presented in this chapter is to predict strength of ROS composites, while also capturing the strand size effects and the correct failure mechanisms.

8.1 Modelling overview

The modelling methodology proposed herein is based on the modelling technique used to predict strength of nacre, which is a bio-composite made of stiff staggered platelets held together by a ductile matrix. The microstructure of nacre can be seen in Figure 8-1a. Rabiei *et al.* [96] predicted the strength of nacre by creating an FE model of the microstructure, which captured the inherent variability in the material (i.e. platelet size and arrangement varied from one layer to the next), as shown in Figure 8-1b. It was found that failure was triggered by local shear stress-

concentrations and propagated due to platelet debonding forming a stair-like failure path. Since the microstructure and the stair-like (or zig-zagging) failure path characteristic to nacre resemble those of ROS composites, this modelling approach provided the basis for developing an ROS model.

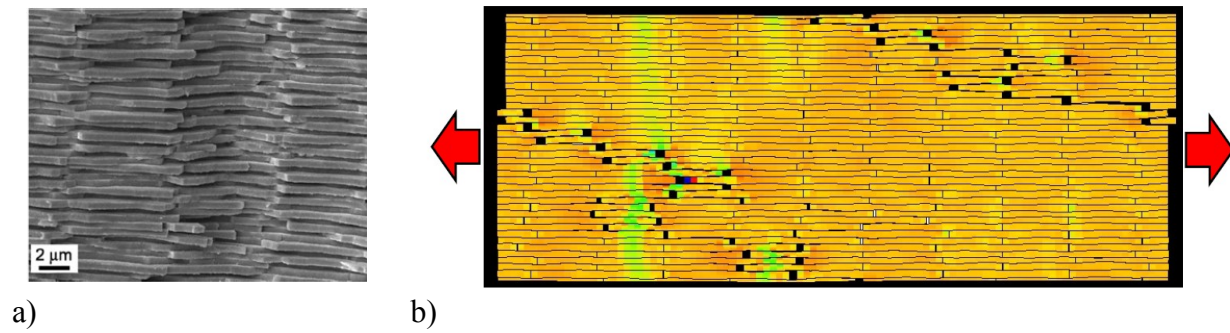


Figure 8-1 – a) Microstructure and b) failure mechanism of nacre [96].

In comparison to the nacre model, the ROS strength model is purely analytical, which makes it simpler to implement. It is possible in the future to extend the modelling analysis to FE to improve accuracy, and capture crack initiation and propagation in more detail. The outline of the technique is shown in Figure 8-2. The first step is to create a microstructure that is representative of the size of the specimen and the strands, and of the general strand placement. The generated microstructure would be unique to each run of the model, and hence multiple simulations can be run to capture variability of material properties from one specimen to another. In the next step, multiple possible failure paths are generated by considering all the possible combinations of strand delamination and failure. Finally, the weakest path is found and the strength is calculated by summing up the strength components of all the elements in that path. This type of failure analysis is a simplification over a more accurate progressive failure analysis, which would be quite complex to incorporate into the given analytical model. Hence, the model is expected to over-estimate and set the upper-bound on strength of ROS composites, but it is considered to be a good starting point in developing a strength model for this type of material.

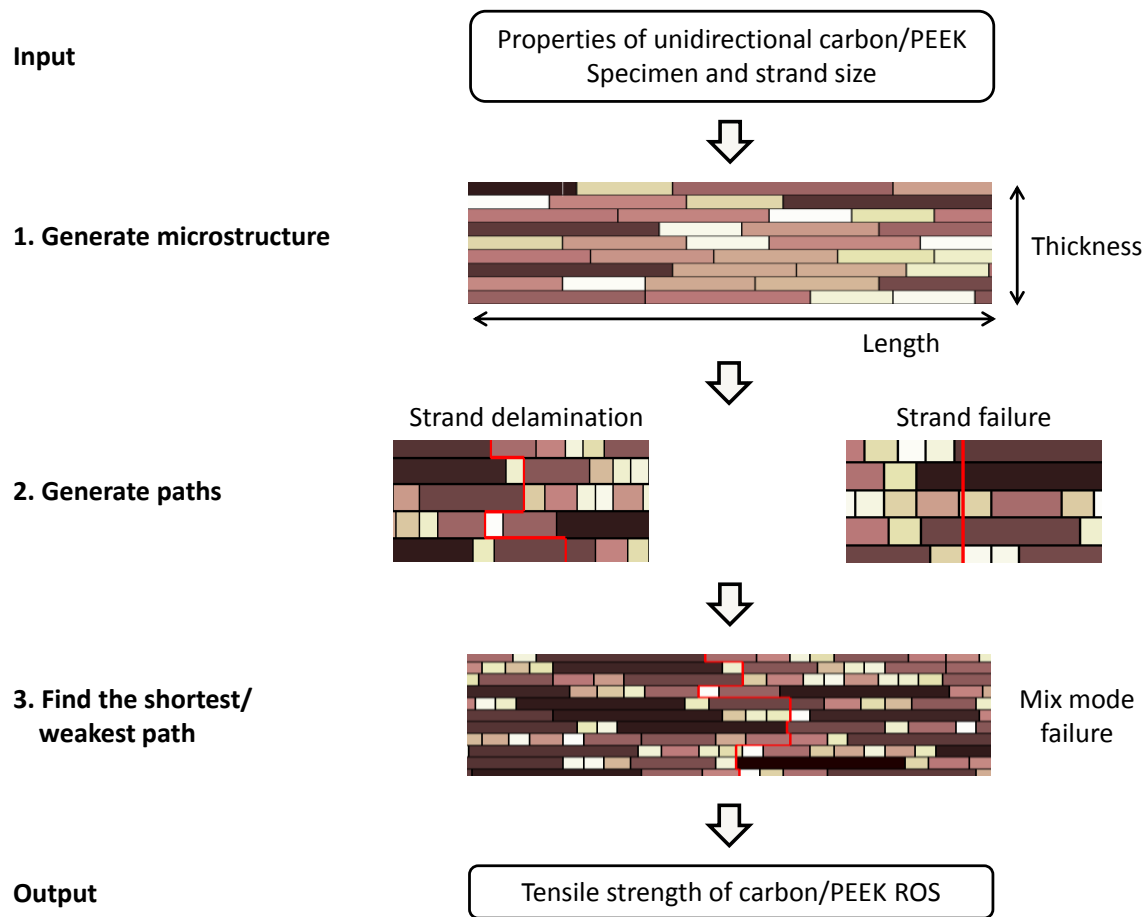


Figure 8-2 – Overview of the modelling structure

8.2 Step 1 - Generate microstructure

8.2.1 Assumptions

A 2D microstructural model is generated to represent the length-wise cross-section of a tensile specimen. The modelled cross-section includes the specimen length and thickness, the strand size and off-axis orientation, but it ignores the following micro- and macro-structural features (Figure 8-3a vs. b):

- Specimen width
- Variability in the number of strands
- Strand out-of-plane orientation
- Defects (i.e. voids and resin rich areas)

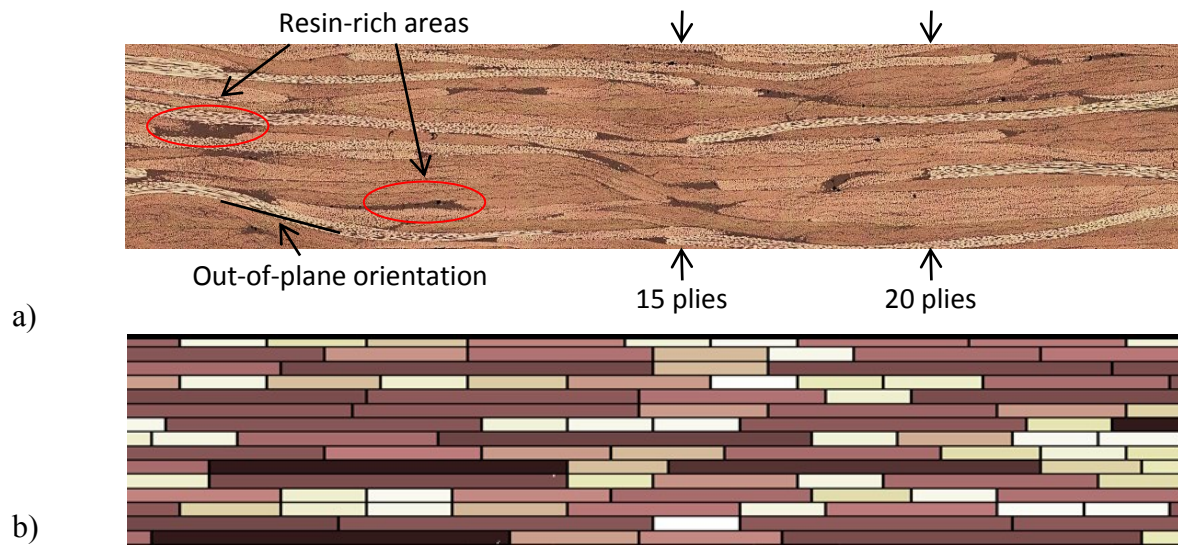


Figure 8-3 – Comparison between a) actual and b) modelled microstructure

Based on experimental results, the effect of specimen width on strength is not clear. Some studies showed that there is an effect [30], while others concluded that there is none [17, 37]. A better understanding of the effect of specimen width on strength supported by experimental results is needed before an accurate 3D model can be developed. While the current model is a 2D simplification of the actual microstructure, it was developed to demonstrate the general modelling methodology and can be extended to 3D when a better understanding of the specimen width effects is available.

It is assumed that the number of strands through-the-thickness is constant throughout the specimen. In reality it varies and is expected to have an effect on the average strength and variability. It was excluded from this analysis because it was considered to be a secondary rather than a primary factor (i.e. strand length) responsible for tensile properties of ROS coupons.

The two simplifications (2D modelling and constant number of strands through-the-thickness) are appropriate for large-strand ROS specimens, because strand placement is fairly orderly and planar as is shown in the micrographs (Figure 4-8). On the other hand, small-strands have a more chaotic placement, which results in large out-of-plane angles and resin-rich areas. This model is expected to over-predict strength of short-strand ROS composites.

8.2.2 Procedure

First an empty cross-section is created with dimensions of specimen length and the number of plies. The number of plies represents the average number of strands through-the-thickness. This cross-section is then populated with strands that have different in-plane orientations. Strand orientation affects the effective length (L_{eff}) of the strand when it is observed from the edge. This notion of the effective length and the calculations involved are summarized in Figure 8-4. The location of the first strand in each ply is randomly off-set in the length-wise direction so that the plies do not all start in the same spot.

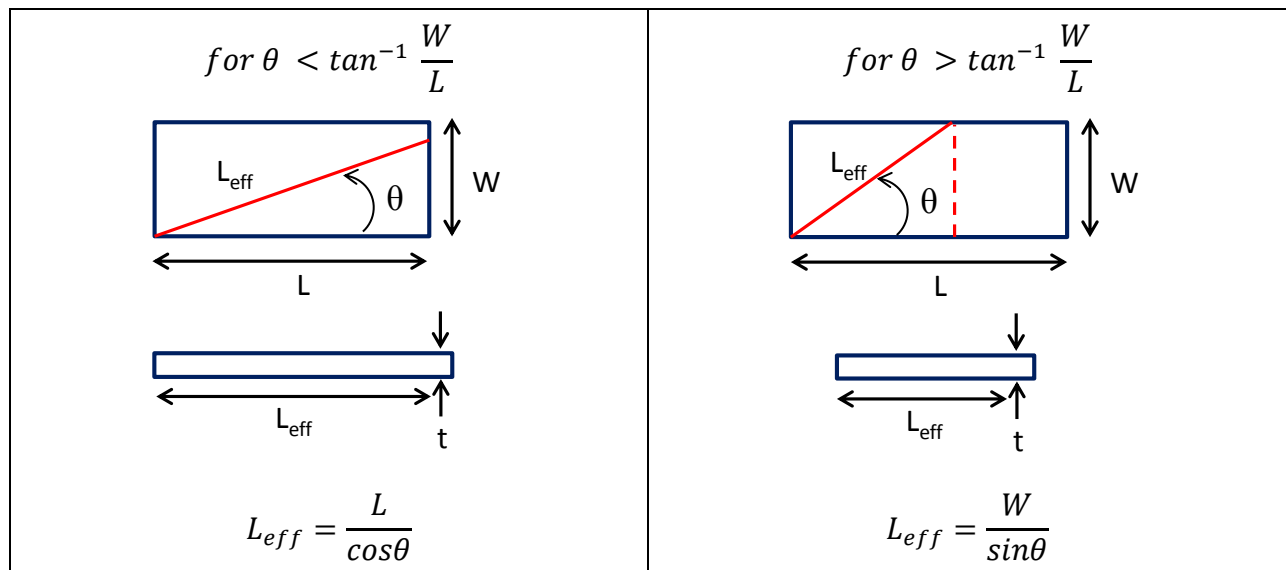


Figure 8-4 – Definition of the effective length

Sample cross-sections of small and large-strand ROS specimens are shown in Figure 8-5, and the difference in overlap lengths is apparent. The colour map corresponds to different strand off-axis angles and the resultant effective lengths.

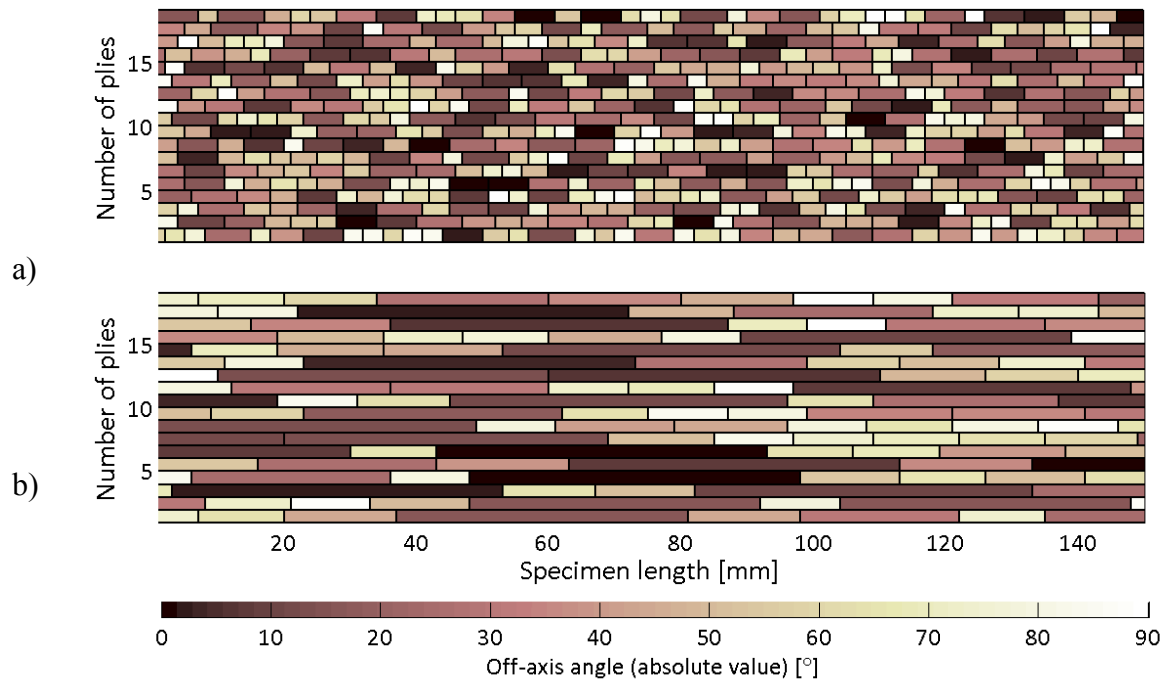


Figure 8-5 – Comparison between the modelled microstructure of a) short (6 x 3 mm) and b) long (50 x 12 mm) strand ROS specimens. These specimens are 150 mm long and 2.5 mm thick

8.3 Step 2 - Generate paths

Two failure modes are observed in ROS specimens tested experimentally: strand failure and strand pull-out. Consequently, possible failure paths are generated by considering all combinations of strand failure and strand pull-out. For this purpose the failure strength of each strand and the bond strength of each overlap are calculated.

8.3.1 Strand failure

In general, strength of each strand is calculated based on its orientation angle (θ). Initially, to approximate the off-axis strand strength (σ_s) of each strand, without going into progressive failure analysis, the Tsai-Hill model was considered. It was an easy-to-implement formulation (Eq. 8-1) that has been used in the literature to represent strength of off-axis laminates [97] and discontinuous fibres [45]. However, it led to significantly under-estimated results (as will be shown in Section 8.6 - Results). The reason for under-estimation is that Tsai-Hill does not consider the interaction and the load sharing with the neighbouring strands. Other models, such as Chen's and Baxter's lamina analogies were reviewed (Chapter 2 and [41]), but were dismissed

because they also did not take into account the presence of neighbouring strands. Finally, classical laminate theory (CLT) with simplified failure analysis was implemented, as will be discussed next.

$$\left(\frac{1}{\sigma_s}\right)^2 = \left(\frac{\cos^2\theta}{\sigma_L^T}\right)^2 + \left(\frac{1}{(\sigma_S^L)^2} - \frac{1}{(\sigma_L^T)^2}\right)^2 (\cos^2\theta \sin^2\theta) + \left(\frac{\sin^2\theta}{(\sigma_T^T)^2}\right)^2 \quad \text{Eq. 8-1}$$

The CLT-based approach is explained by first considering a single layup. CLT is used to compute laminate stiffness and compliance matrices (see previous chapter). Then a dummy load such as $N = [1 \ 1 \ 1]$ (force per unit width) is applied to calculate the laminate strains (ϵ_{126}), as shown in Eq. 8-2. These laminate strains can be transformed into on-axis ply strains (ϵ_{xys}) for each ply through a transformation matrix (T), Eq. 8-3 - Eq. 8-4.

$$\{\epsilon_{126}\} = \begin{bmatrix} a & b \\ b & d \end{bmatrix} \{N\} \quad \text{Eq. 8-2}$$

$$\{\epsilon_{xys}\} = [T] \{\epsilon_{126}\} \quad \text{Eq. 8-3}$$

$$\text{where } [T] = \begin{bmatrix} \cos^2\theta & \sin^2\theta & \sin\theta\cos\theta \\ \sin^2\theta & \cos^2\theta & -\sin\theta\cos\theta \\ -2\sin\theta\cos\theta & 2\sin\theta\cos\theta & \cos^2\theta - \sin^2\theta \end{bmatrix} \quad \text{Eq. 8-4}$$

Next, on-axis strains are used to compute the on-axis stresses (σ_{xys}) for each ply, Eq. 8-5.

$$\{\sigma_{xys}\} = [Q_{xys}] \{\epsilon_{xys}\} \quad \text{Eq. 8-5}$$

At this stage Hashin's failure criteria (see Eq. 7-12 - Eq. 7-15) are used to determine the strength ratio (R) between the on-axis stresses, which were created by the load N , and the material strength ($R=1$ means that ultimate stress is reached). An example of the calculation is shown for the fibre compression criterion below (Eq. 8-6 - Eq. 8-7).

$$\left(\frac{R\sigma_f}{\sigma_L^c}\right)^2 = 1 \quad \text{Eq. 8-6}$$

$$R = \left(\frac{\sigma_L^c}{\sigma_f}\right) \quad \text{Eq. 8-7}$$

A common practice to calculate laminate strength of continuous fibre composites is either to use strength at which the weakest ply fails or to use progressive failure analysis. However, in this work, only the strength of the current strand (ply) is of interest as it will be combined at a later stage with other strand strengths and overlap strengths to enable mixed failure modes. The maximum off-axis stress in the loading direction (i.e. $\sigma_1 = \sigma_s$) is computed for each strand while assuming that the other strands maintain the same stiffness characteristics even though they might fail at a lower load, as shown in Eq. 8-8. The same assumption was made by Halpin and Kardos when developing a strength model for discontinuous-fibre composites [61]. This assumption was permitted, because stress-strain curves of ROS and QI carbon/PEEK specimens were smooth until final failure (i.e. there were no kinks or abrupt stiffness changes that would mark the ply-by-ply failure sequence). Nonetheless, this is a significant assumption, and it is expected to lead to over-prediction of the overall strength associated with strand failure.

$$\{\sigma_{126}\} = R_{min}[Q_{126}]\{\varepsilon_{126}\} \quad \text{Eq. 8-8}$$

where R_{min} corresponds to the smallest safety factor calculated for a particular strand or ply.

As the fibre architecture varies along the specimen length, strand strength is calculated in 1 mm intervals and the evolution of strand strength along its length is captured. This step is illustrated in Figure 8-6, where the black dashed areas correspond to localized layups and the red section shows a single strand that is affected by these layups. For simplicity, the average strength value is assigned to each strand; in this example it is 640 MPa.

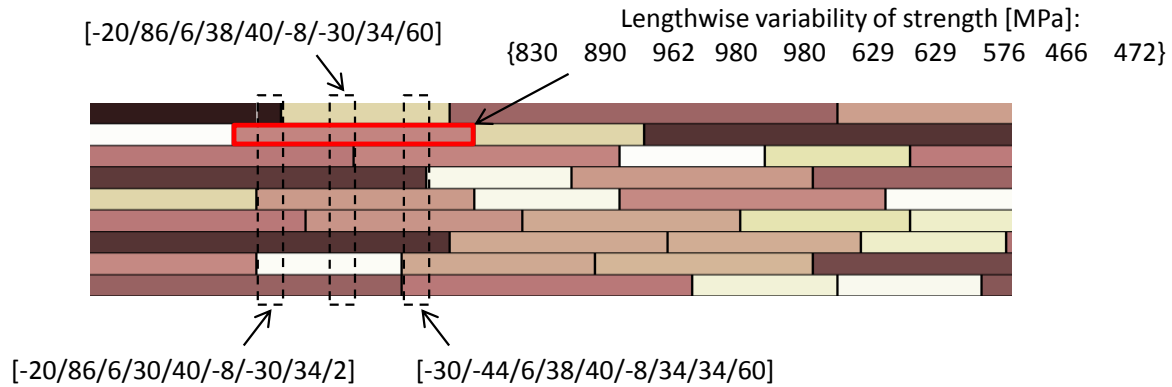


Figure 8-6 – Effect of layup variability on strength of a particular strand

The effect of strand orientation on strength is summarized in Figure 8-7. It is evident that the Tsai-Hill criterion significantly under-predicts strand strength, and that the scatter in the CLT-based strength is large. The latter observation signifies that strand or ply strength depends not only on the off-axis angle but also on ply stacking sequence. Overall, the interaction and the load-sharing that occur among the strands lead to a non-trivial stress-state in each strand.

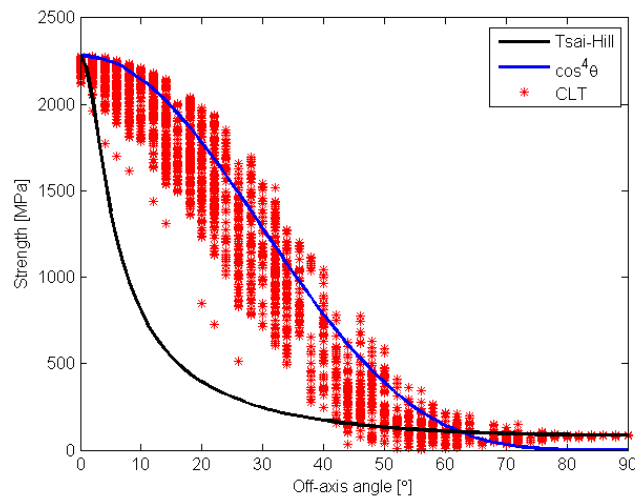


Figure 8-7 – Effect of orientation on strand strength

Interestingly, from the different equations for discontinuous fibre composites that were reviewed, one equation was found to provide a reasonable approximation of strength based on the off-axis angle, Eq. 8-9. This equation is used to compute the Krenchel's orientation efficiency factor (see

Eq. 2-14). Hence, it is possible to use Eq. 8-9 instead of the previously described CLT-method to simplify and speed up the model.

$$\sigma_s = \cos^4 \theta \quad \text{Eq. 8-9}$$

8.3.2 Strand debonding

In this model, approximation of bond strength between the adjacent strands is based on the theories and concepts that were derived and have been extensively used over the years to calculate the strength of joints [67-69]. Figure 8-8 highlights the similarity in the load transfers mechanisms that occur between the adherends in a joint and between strands in an ROS composite. Overall, two failure criteria for the calculation of the overlap strength were considered: (i) strength-based and (ii) toughness-based [64]. The former equation is based on the assumption of a ductile matrix that will yield plastically but never fails, and the strength of the joint depends solely on the strength of the adhesive (or the interface). The latter formulation was developed for brittle matrices and takes into account the possibility of a mode-II crack originating in the matrix due to the stress concentration at the ends of the overlap and propagating inwards. In this case, strength of the overlap is governed by the material's ability to withstand delamination (i.e. fracture toughness). Figure 2-22 shows the combined effect of the two criteria on the overlap strength. Next two sections will explain how these failure criteria were incorporated into the model.

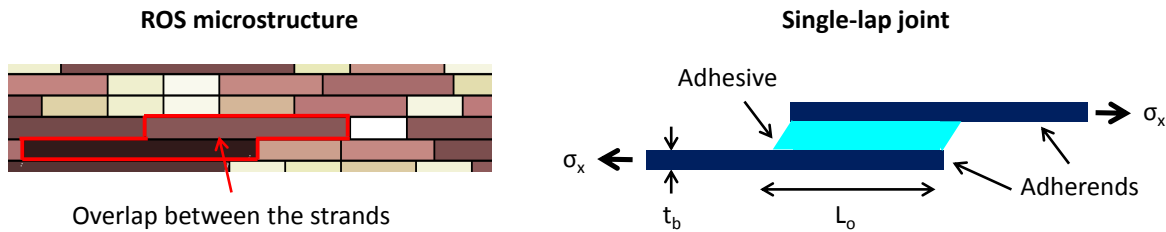


Figure 8-8 – Comparison between strand overlap and joint overlap

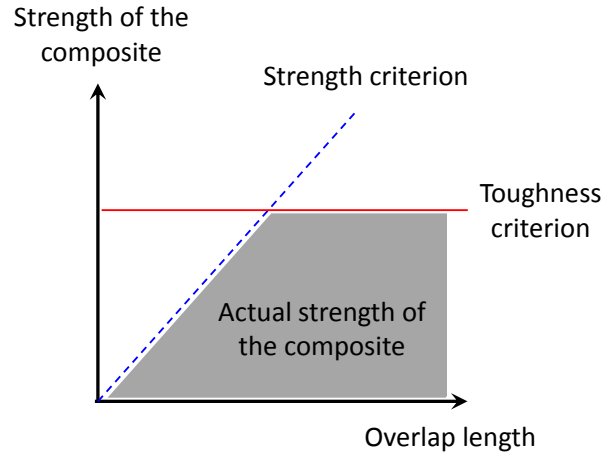


Figure 8-9 – Effect of the overlap length on the composite's strength, as determined by the strength-based and toughness-based criteria [64]

Recently, Pimenta *et al.* [64] have successfully applied these criteria for modelling of the stress-strain response of discontinuous-fibre composites. Moreover, these criteria were used to predict strength of slit-ply UD laminates, for more information see Chapter 2 and [71, 72].

8.3.2.1 Criterion 1: strength-based

In this method, the maximum load that can be handled by the overlap is calculated by simply multiplying its length by shear strength, as shown in Eq. 8-10. This method is based on the assumption that shear stress is uniform between the adherends, hence ignoring the presence of stress concentrations at the ends of the overlap. This assumption is fairly inaccurate for a generic joint, but is justifiable for joints with ductile adhesives, as will be explained next.

$$\sigma_c = \frac{L_o \tau_i}{t_b} \quad \text{Eq. 8-10}$$

where σ_c is the strength of the joint/composite, L_o is the overlap length, t_b is thickness of the adherend or strand, and τ_i is the interface shear strength.

The evolution of shear stress and strains with respect to the applied load in the case of ductile adhesives is illustrated in Figure 8-10. For simplicity, the adhesive is assumed to exhibit elastoplastic behaviour. At low loads, while the adhesive is in the elastic regime of its properties, the

distribution of shear stress is non-uniform (Figure 8-10a). As the load is increased, shear stresses at the ends surpass the plasticity limit and begin to plateau while the rest of the adhesive is still in the elastic regime and exhibits non-uniform stresses. Finally, the entire length of the adhesive is in the plastic regime, stress-distribution is uniform, and the maximum load that this joint can sustain is expressed by Eq. 8-10. PEEK, being a thermoplastic matrix, is expected to exhibit an elasto-plastic shear behaviour, which was observed with in-plane shear of UD carbon/PEEK specimens (see Chapter 6). This criterion alone cannot be used to approximate the overlap strength, because it assumes that the adhesive can be stretched to an infinite plastic strain, which in reality is not true. This issue is addressed by criterion 2.

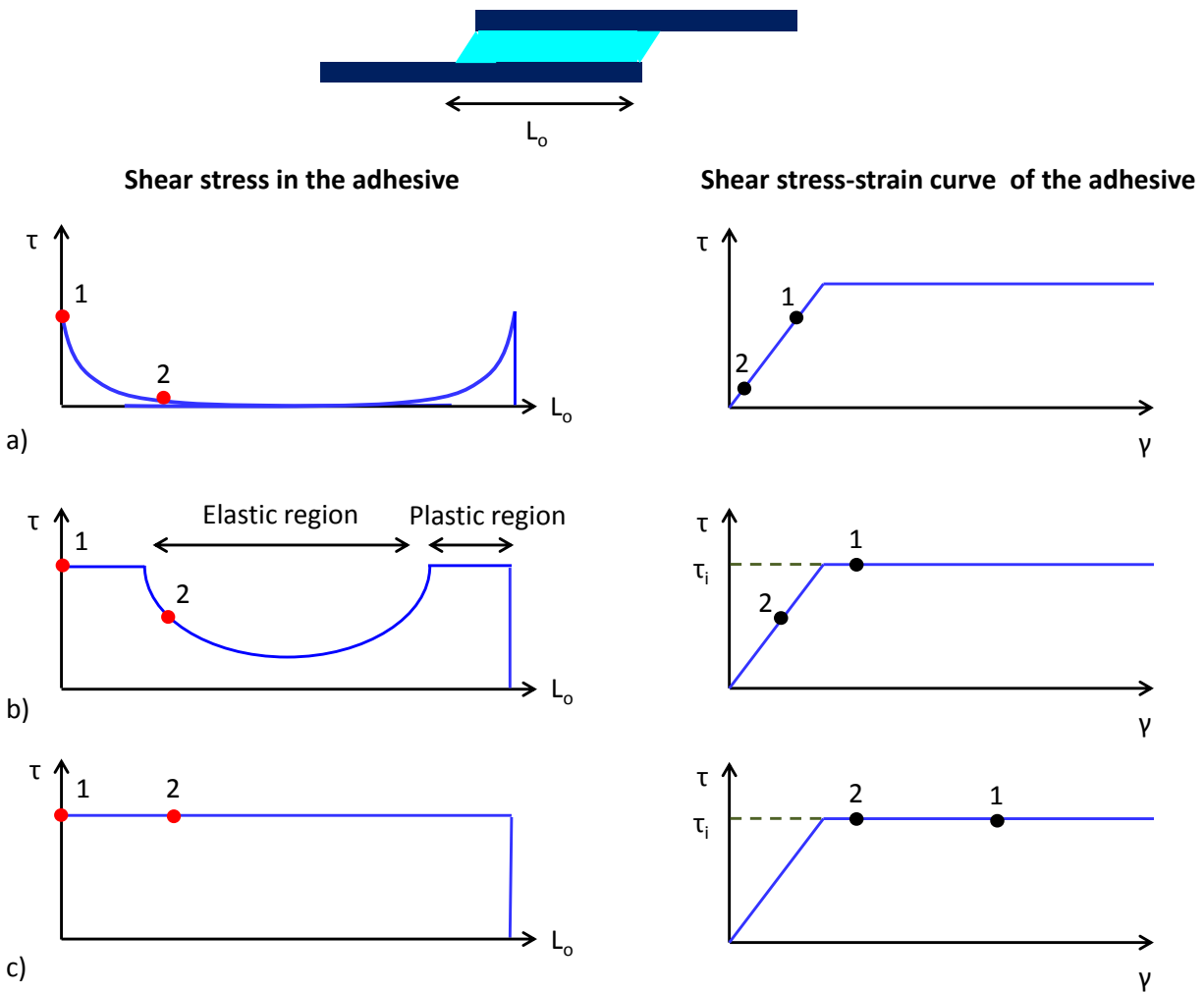


Figure 8-10 – Evolution of shear stress in a joint with increasing loading a) → c), assuming elasto-plastic behaviour of the adhesive (adapted from [70])

8.3.2.2 Criterion 2: toughness-based

The loading scenario described in the previous section can be further improved by considering a finite failure strain associated with the adhesive. The effect that failure strain (γ_{\max}) has on the stress evolution in the joint is shown in Figure 8-11. In the case of long joints it is possible that failure strain at the ends of the overlap is reached before the plastic regime (i.e. uniform stress) develops along its full length. As a result debonding will initiate as soon as failure strain is reached. Hence, there is an upper limit on the load that can be sustained by an overlap regardless of its length. This limit depends on the fracture toughness of the adhesive/interface [67-69].

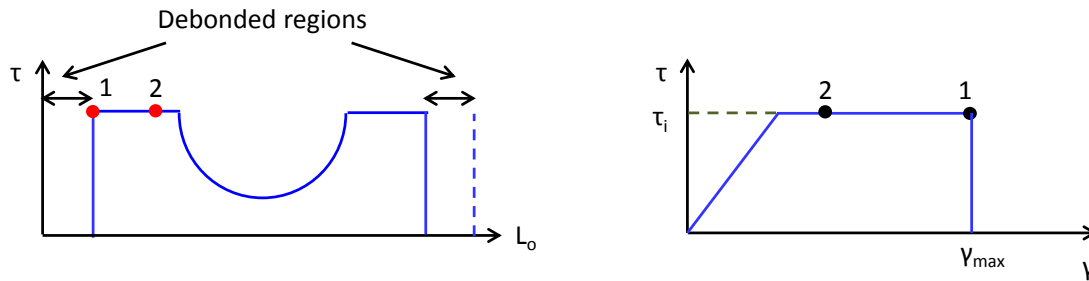


Figure 8-11 – Effect of debonding on shear stress distribution in a long joint (adapted from [70])

Based on the fracture toughness criterion, strength plateau ($\sigma_{x|_{\max}}$) of a joint can be calculated using Eq. 8-11 [72]. This form of the criterion considers the possibility of having two adherends with different thickness and modulus. If the two adherends are the same, the expression for the strength plateau takes on a simpler form, Eq. 8-12 [64]. This latter form was used to calculate strength of slit-ply UD laminates [71]. It would be cumbersome to implement Eq. 8-11 into the ROS model. A single strand can overlap with multiple strands, which have different orientations, along its length, and it would be difficult to select an appropriate combination of (E_{b1} and E_{b2}). Also, no experimental data is yet available to validate the applicability of this expression for general slit-ply laminates (i.e. not just UD). For these reasons, Eq. 8-12 instead of Eq. 8-11 is implemented into the model and a single E_b was chosen to represent the average modulus of all the strands. Hence, E_b was approximated as modulus of a QI CF laminate (E_{QI}) by using CLT. The results are shown in Table 8-1.

$$\sigma_c = \frac{1}{t_{b1} + t_{b2}} \sqrt{\frac{2E_{b2}t_{b2}(E_{b1}t_{b1} + E_{b2}t_{b2})G_{IIc,IL}}{E_{b1}t_{b1}}} \quad \text{Eq. 8-11}$$

$$\sigma_c = \sqrt{\frac{2E_b G_{IIc,IL}}{t_b}} \quad \text{Eq. 8-12}$$

where $G_{IIc,IL}$ is the critical mode-II fracture toughness of the adhesive/interface and E_b is the modulus of the adherends or strands or inclusions.

To implement this concept into the model, the notion of limit length (L_{lim}) is introduced, as described by Eq. 8-13. The shortest failure path is found by looking at the effective “lengths” rather than strengths of each component (i.e. strand or overlap). Hence, the strength plateau is represented by a length value (L_{lim}). In relation to Figure 2-22, L_{lim} occurs at the intersection point of the two criteria. Overall, for short overlaps (i.e. $L_o < L_{lim}$) strength-based criterion is used, and for long overlaps (i.e. $L_o > L_{lim}$) toughness-based criterion is used.

$$L_{lim} = \frac{\sigma_c n t_b}{(n - 1) \tau_i} \quad \text{Eq. 8-13}$$

where n is the number of plies and $n-1$ is the number of overlaps.

It is noteworthy that peel stresses are not considered by these criteria. Peel stresses are not negligible as was evident from tensile tests of slit-ply UD laminates (Chapter 4). Calculation of the peel stresses is excluded from this model because of the complex interaction among the strands. A more elaborate model (e.g. FE-based) is required to adequately capture the effect of peel stresses. Overall, the model is expected to over-predict the results due to this simplification.

8.4 Step 3 - Find the shortest path

Failure strength of the modelled microstructure is determined by finding the path of least-resistance for the crack to grow. The actual sequence of crack initiation and propagation is not modelled, and only the overall load required to break the cross-section is estimated. The path of least-resistance is found by using the shortest path algorithms (function `shortest_distance()` in MATLAB), which are commonly used to solve network problems. A network is a representation of physical connections (e.g. roads between cities) or abstract connections (e.g. relationships between people). It can be visually depicted through a graph diagram, which shows all the nodes (objects) and the links (connections) between them.

In order to apply the network analogy to the current strength model, a graph detailing all the possible failure paths has to be assembled, as shown in Figure 8-12 and Figure 8-13. The microstructure is represented by a set of nodes (i.e. strand ends: 1, 2, 3...5) and the links between them ($L_{12} \dots L_{45}$). These links represent either the overlap strength or the strand strength that connect the nodes. It is assumed that in order for the ultimate failure to occur a crack must merge the two opposite sides (\mathcal{A} and \mathcal{B}) of the specimen and pass through at least one strand end (i.e. node) even though in reality the crack may never pass through a strand end.

First, all the possible delamination paths are assembled into a network. Figure 8-12 shows a simple microstructure and a graph diagram that represents different delamination paths (for clarity only a few links are labelled). In this example, the shortest path for delamination is $\mathcal{A} \rightarrow 1 \rightarrow 3 \rightarrow 5 \rightarrow \mathcal{B}$, and the resultant failure strength is $\sigma_{\max} = (L_{13} + L_{35}) \tau_i / nt_b$.

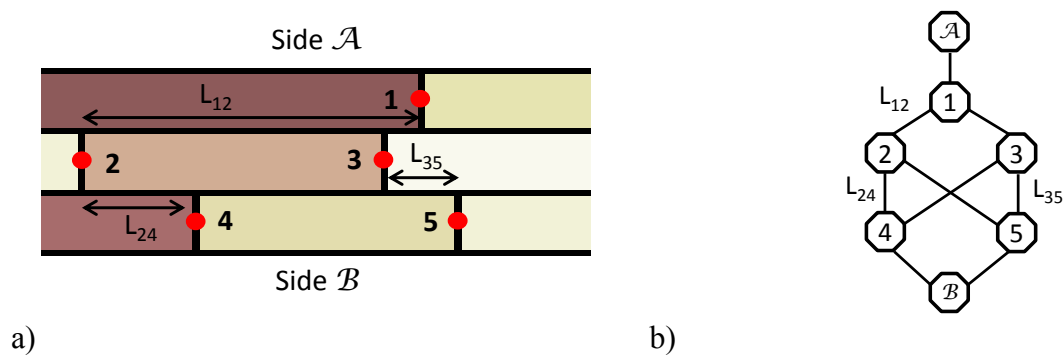


Figure 8-12 – a) Modelled microstructure and b) graph schematic that shows links related to strand delamination

It is noteworthy that load transfer between the strand ends is assumed to be negligible and that load carrying capacity of the matrix is excluded from the calculation of the total strength. The same assumption has been made in other papers that dealt with strength of discontinuous-fibre, slit-ply and nacre based composites [64, 71, 72, 82] and good results were obtained.

Next, all the links associated with strand failure are added to the graph. Figure 8-13 shows two examples of strand failures that link nodes $1 \rightarrow 5$ and $2 \rightarrow \mathcal{B}$. In the former, two failure scenarios can occur: (i) the strand between nodes 1 and 5 can be pulled-out ($L_{13} + L_{35}$), or (ii) it can break (σ_{15}) and debond along the distance L_{15} . To define all the links, the same units had to be used and for this model the unit of length was selected. Hence, the bond strength was expressed as the overlap length and the strand strength was scaled using Eq. 8-14.

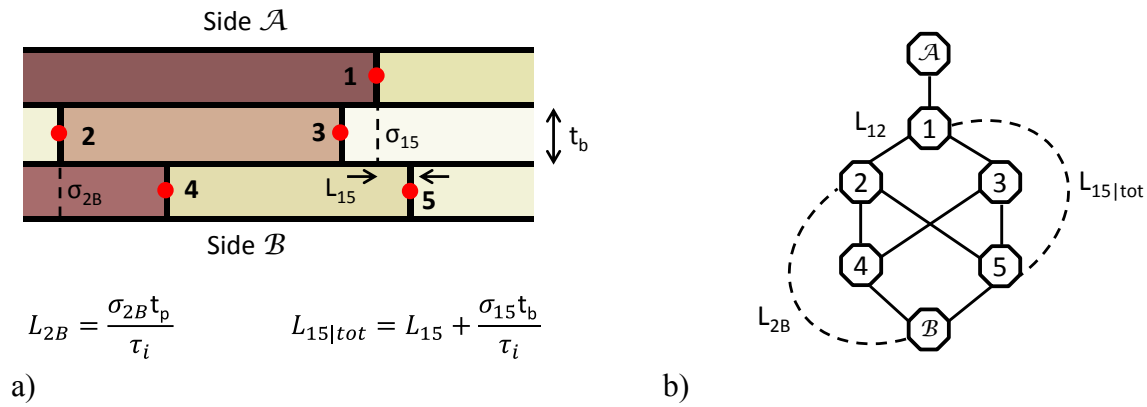


Figure 8-13 – a) Modelled microstructure and b) graph schematic that shows links related to strand failure

$$L = \frac{\sigma_s t_b}{\tau_i} \quad \text{Eq. 8-14}$$

Once the full graphical representation is generated, the shortest path algorithm is run to find the shortest path (L_{short}) between nodes \mathcal{A} and \mathcal{B} . This length value is then converted into laminate strength using Eq. 8-15.

$$\sigma_{ROS} = \frac{L_{short} \tau_i}{n t_b} \quad \text{Eq. 8-15}$$

8.5 Material properties

To validate the model, strength properties of ROS carbon/PEEK (thermoplastic) and carbon/epoxy (thermoset) composites were calculated and compared against experimentally measured data [27, 35]. The model uses standard material properties of UD CF carbon/PEEK and carbon/epoxy from the literature [13, 22, 83, 98, 99], as shown in Table 8-1. By comparing mechanical properties of these materials, the only significant difference is fracture toughness, which is three times higher for carbon/PEEK. Based on the experimental data that was published so far, strength of thermoplastic-based ROS composites is superior to that of thermoset-based ones. Hence, it will be interesting to see if the proposed ROS strength model can capture that difference in performance. The next two sections will show how plateau strength and limit length were calculated for these materials.

Table 8-1 - Properties of carbon/PEEK and carbon/epoxy laminates [13, 22, 83, 98, 99]. Abbreviations SBS and DNS stand for short-beam shear and double-notch shear

Property	carbon/PEEK	T700/2510	Property	carbon/PEEK	T700/2510
σ_L^T [MPa]	2280	2200	E_1 [GPa]	130	127
σ_L^C [MPa]	1300	1470	E_2 [GPa]	10	8.42
σ_T^T [MPa]	86	48.9	G_{12} [GPa]	5.2	4.21
σ_T^C [MPa]	86	199	ν_{12}	0.33	0.309
σ_S^L [MPa]	152	154	t_b [mm]	0.139	0.127
SBS [MPa]	100	86	$G_{II,CL}$ [J/m ²]	1930	633
DNS [MPa]	64	-	E_{QI} [GPa]	51.9	48.6

8.5.1 Strength plateau - carbon/PEEK

Based on Eq. 8-12 and Eq. 8-13 sample calculations of the strength plateau and of the limit length for carbon/PEEK ROS specimens are shown in equations Eq. 8-16 - Eq. 8-18. Two values for interlaminar shear strength (100 and 64 MPa) were available from two different tests (short-beam shear and double-notch shear). Since it was uncertain which one is more appropriate for this problem, both values were used, and two limit lengths were calculated, Eq. 8-17a vs. Eq. 8-17b. Also, two specimen thicknesses were considered (2.5 and 6 mm) and the calculations for L_{lim} had to be adjusted to account for the different number of overlaps. A UD specimen that is

2.5 mm thick would have 18 plies and 17 overlaps, while a 6 mm thick specimen would have 43 plies and 42 overlaps, Eq. 8-17 and Eq. 8-18.

$$\sigma_c = \sqrt{\frac{2E_{QI}G_{ILc,IL}}{t_b}} = \sqrt{\frac{2(51.9)1930}{0.139}} = 1200 \text{ MPa} \quad \text{Eq. 8-16}$$

$$L_{\text{lim}|\tau=100} = \frac{\sigma_c n t_b}{(n-1)\tau_i} = \frac{1200 \cdot 2.5}{(18-1)100} = 1.77 \text{ mm} \quad \text{Eq. 8-17a}$$

$$L_{\text{lim}|\tau=64} = \frac{\sigma_c n t_b}{(n-1)\tau_i} = \frac{1200 \cdot 2.5}{(18-1)64} = 2.77 \text{ mm} \quad \text{Eq. 8-17b}$$

$$L_{\text{lim}|\tau=100} = \frac{\sigma_c n t_b}{(n-1)\tau_i} = \frac{1200 \cdot 6}{(43-1)100} = 1.68 \text{ mm} \quad \text{Eq. 8-18a}$$

$$L_{\text{lim}|\tau=64} = \frac{\sigma_c n t_b}{(n-1)\tau_i} = \frac{1200 \cdot 6}{(43-1)64} = 2.63 \text{ mm} \quad \text{Eq. 8-18b}$$

8.5.2 Strength plateau - carbon/epoxy

Calculations of the strength plateau and of the limit length for carbon/epoxy ROS specimens are shown in equations Eq. 8-19 and Eq. 8-20. Specimens tested by Feraboli *et al.* [27] were 2 mm thick and had 16 plies.

$$\sigma_c = \sqrt{\frac{2E_{QI}G_{ILc,IL}}{t_b}} = \sqrt{\frac{2(48.6)633}{0.127}} = 696 \text{ MPa} \quad \text{Eq. 8-19}$$

$$L_{\text{lim}|\tau=86} = \frac{\sigma_c n t_b}{(n-1)\tau_i} = \frac{696 \cdot 2}{(16-1)86} = 1.08 \text{ mm} \quad \text{Eq. 8-20}$$

8.6 Results and discussion

Prior to reviewing the modelling results, it is worthwhile to revisit the test results. Figure 8-14 summarizes the strength data for carbon/PEEK ROS composites with different strand lengths. The two curves were obtained from different studies: test data from this thesis (Chapter 4) and Eguemann [86]. The curve that represents results from Chapter 4 has two average data points associated with some length values, because strands of different widths were tested. It is evident that there is noticeable discrepancy between the two sets of experimental data. This difference can be caused by any difference in the manufacturing process, such as strand placement. Also, the scatter associated with each (average) data point is quite large, as is indicated by the error bars (vertical lines), which represent the maximum and minimum measured values.

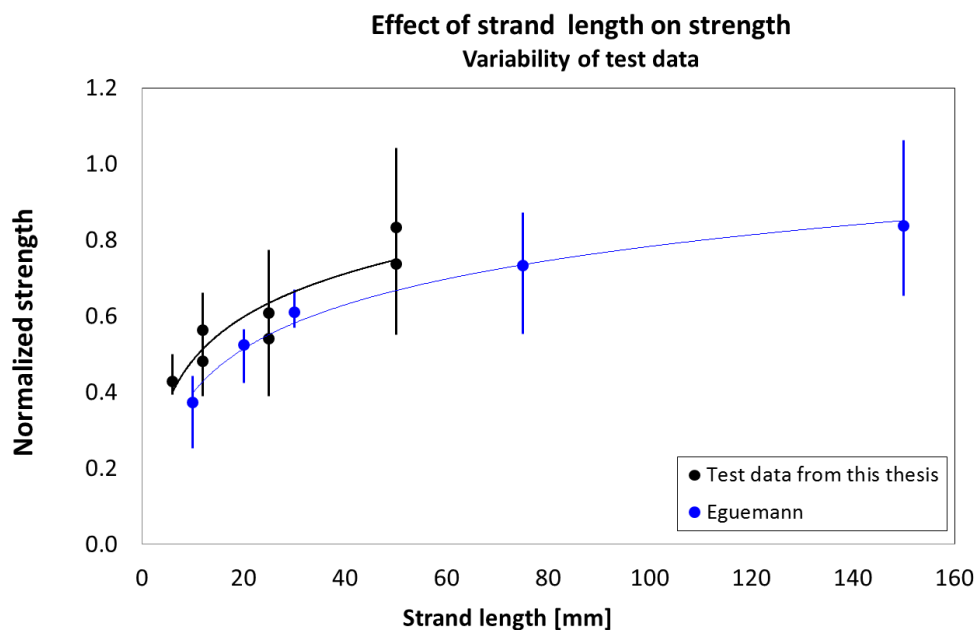


Figure 8-14 – Variability of the strength data. Error bars are plotted as vertical lines without caps

Figure 8-15 compares experimental and modelling results for carbon/PEEK. The modelling data was generated using two values for interlaminar shear strength: 64 MPa (double-notch shear) vs. 100 MPa (short-beam shear), and two methods for modelling strand failure: Tsai-Hill vs. CLT and Hashin. During the initial stages of the model development, Tsai-Hill failure criterion was considered as a criterion for strand failure (Section 8.3.1). However, it significantly

underestimated the off-axis strand strength and inevitably predicted really low strength for ROS composites, as is shown in Figure 8-15. In these simulations, specimens failed predominantly due to strand failure rather than debonding. Subsequently, the model was modified to include CLT analysis to account for load sharing among the strands.

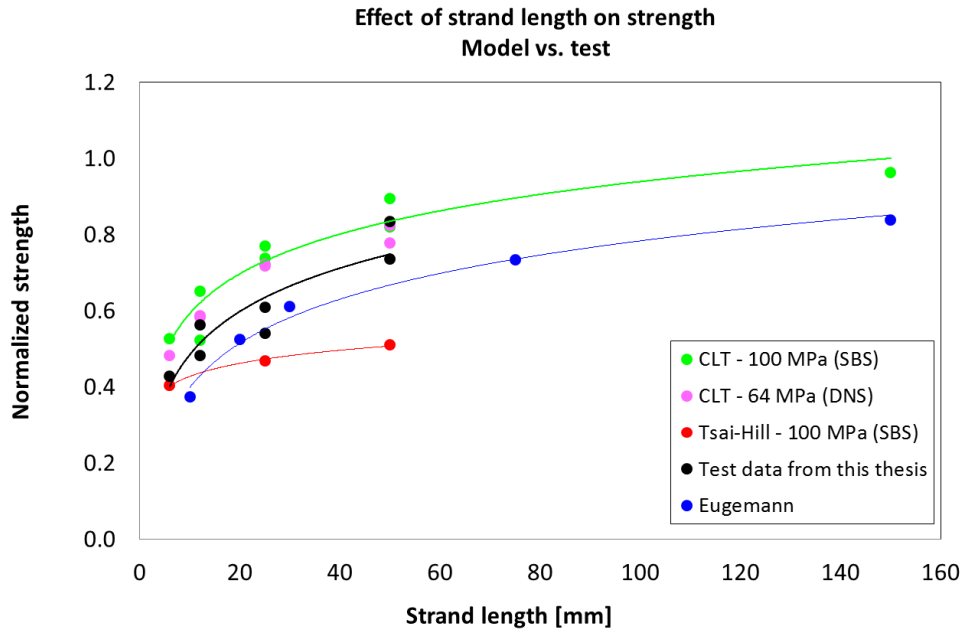


Figure 8-15 - Comparison between experimental and modelled (CLT vs. Tsai-Hill) strength data. Abbreviations SBS and DNS stand for short-beam shear and double-notch shear test methods and represent matrix shear strength that was used in the model (100 or 64 MPa)

The modelling results obtained with the CLT approach capture the effect of strand length but over-predict strength of ROS composites (Figure 8-15). It was anticipated that the model would over-predict the results, because all the assumptions that were made were non-conservative. These results represent the upper-limit of strength achievable with carbon/PEEK ROS.

Interestingly, interlaminar shear strength only seems to have an influence on the strength of short-strand (< 25 mm) ROS composites, while strength of long-strand composites is more dependent on fracture toughness. This trend could be expected since the limit length for carbon/PEEK is at most 2.8 mm, and the probability of having overlaps longer than 2.8 mm increases with strand length. Overall, based on these results and the results of slit-ply UD laminates (Chapter 4), interlaminar shear strength that was measured by the double-notch shear

test is more representative of the interlaminar properties of these materials. Even though the accuracy of that test is debatable [87, 88], it appears to be more representative of the general stress-state and the load transfer mechanism which are present in ROS composites.

Another way of comparing measured and predicted strength is to consider its variability, as is shown by the max/min error bars in Figure 8-16. Both simulation and experimental results show significant variability in strength. Although, the model is over-predicting the average strength, it captures the variability and its relationship with strand size quite well. As was discussed in the opening section, variability plays an important role in the calculation of design allowables and is an important parameter for the model to capture.

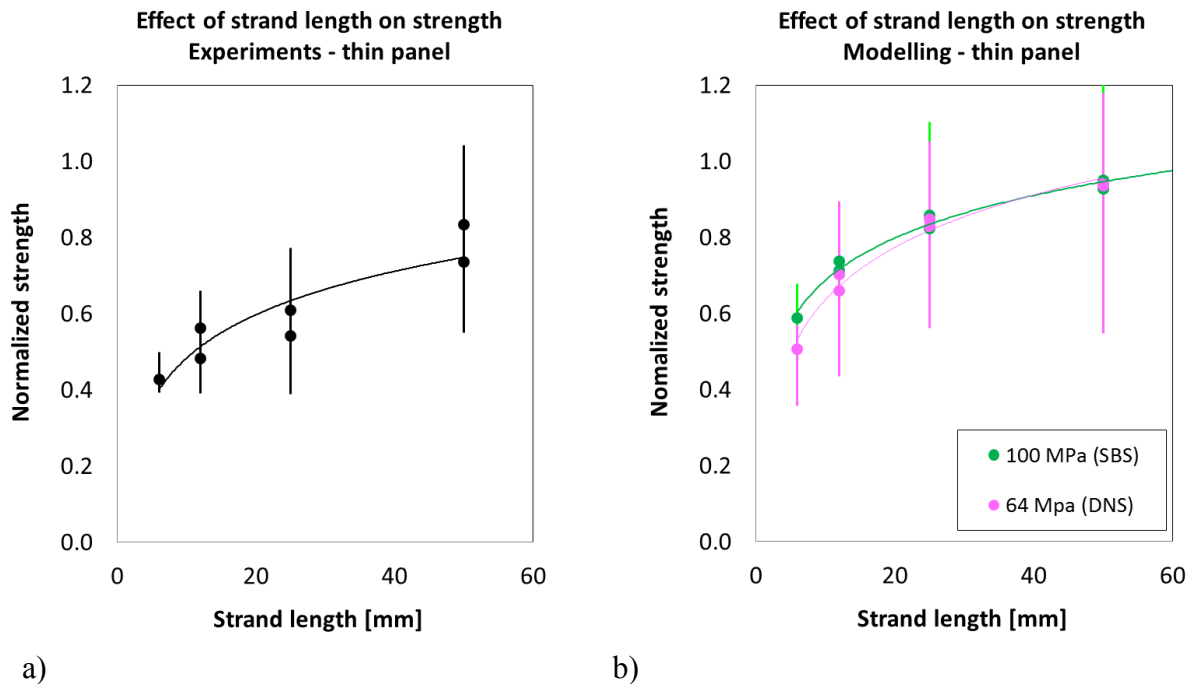


Figure 8-16 - Variability of strength observed in a) experimental and b) modelled data of thin (2.5 mm) ROS composites. Abbreviations SBS and DNS stand for short-beam shear and double-notch shear test methods and represent matrix shear strength that was used in the model (100 or 64 MPa). Error bars are plotted as vertical lines without caps

Both the model and the experiments show that strength increases with panel thickness, as shown in Figure 8-17. One possible explanation for this trend is an improvement in material homogeneity with increased thickness. Also, by comparing Figure 8-16 and Figure 8-18 it is evident that variability is lower for thicker panels.

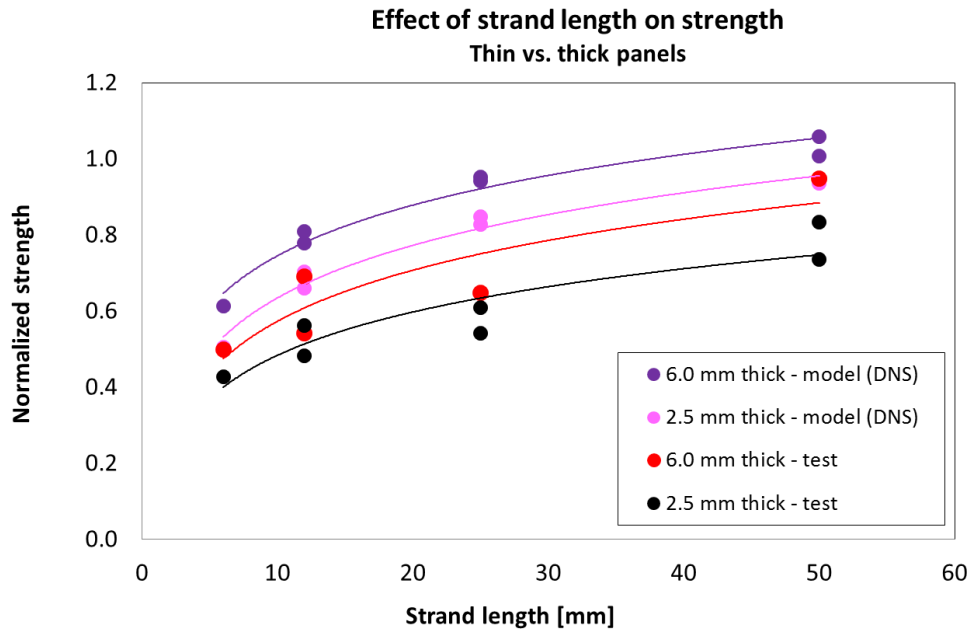
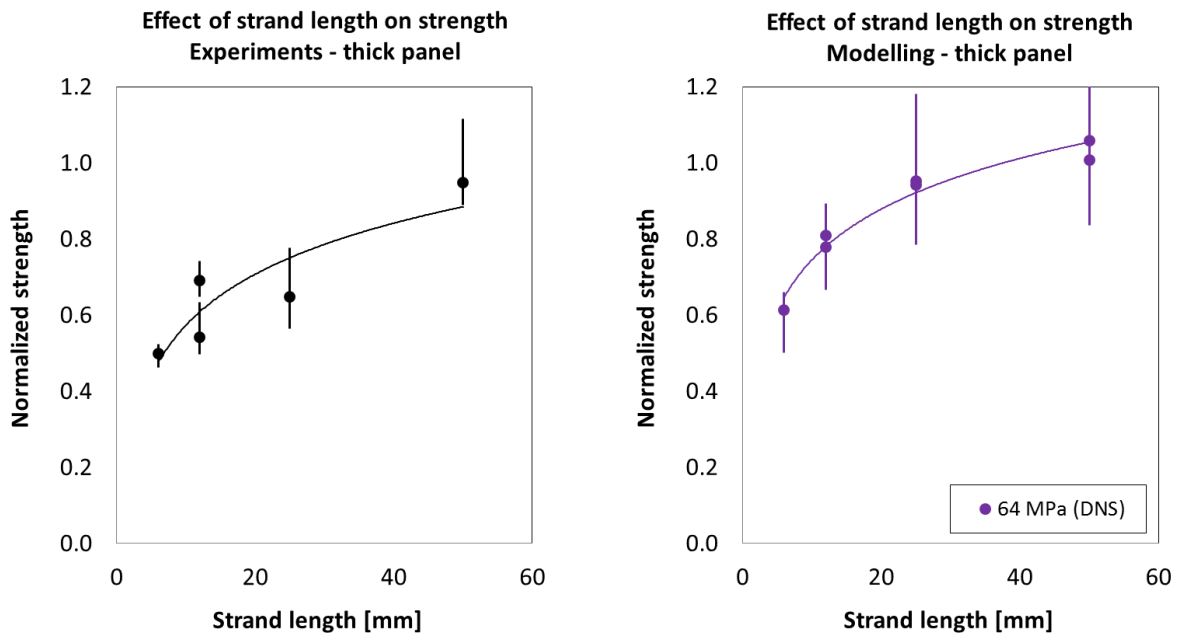


Figure 8-17 - Comparison between strength of thin (2.5 mm) and thick (6 mm) ROS composites. Abbreviations SBS and DNS stand for short-beam shear and double-notch shear test methods and represent matrix shear strength that was used in the model (100 or 64 MPa)



a) b)
Figure 8-18 – Variability of strength observed in a) experimental and b) modelled data of thick (6 mm) ROS composites. Abbreviation DNS stands for double-notch shear test methods and represent matrix shear strength that was used in the model (64 MPa). Error bars are plotted as vertical lines without caps

Finally, results between carbon/epoxy and carbon/PEEK are compared, as shown in Figure 8-19. Unfortunately, only the short-beam shear strength of carbon/2510-epoxy was found in the literature [98, 99], so both sets of results were generated using SBS strength values. Overall, the model is capable of picking up the large difference between the strength of PEEK and epoxy-based ROS composites. This difference can be attributed to the difference in toughness, especially since it is the only property that is significantly different. Thus, thermoplastic-based ROS composites have more potential in this niche of composite materials.

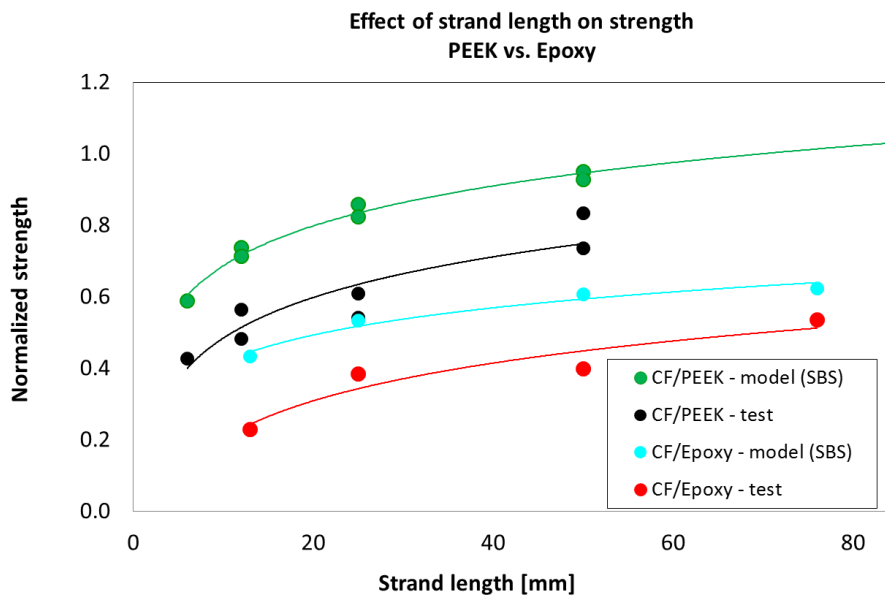


Figure 8-19 – Comparison between strength of thermoset and thermoplastic-based ROS composites. Abbreviation SBS stands for short-beam shear test method and represent matrix shear strength that was used in the model (100 MPa)

Finally, the simulated failure paths are compared to those observed in actual test specimens, and there is a clear resemblance between them, as shown in Figure 8-20. Lengths of the debonded sections are longer than the 2.8 mm length limit, hence proving the importance of incorporating the toughness-based failure criteria into the model. The simulated failure paths depict strand and interface failure modes, hence highlighting the importance of accurately modelling both of them. The fact that strand failure has a prominent presence in the overall failure path explains why the modelling technique proposed in Chapter 7 was able to predict strength of ROS composites fairly accurately even though it did not consider strand delamination.

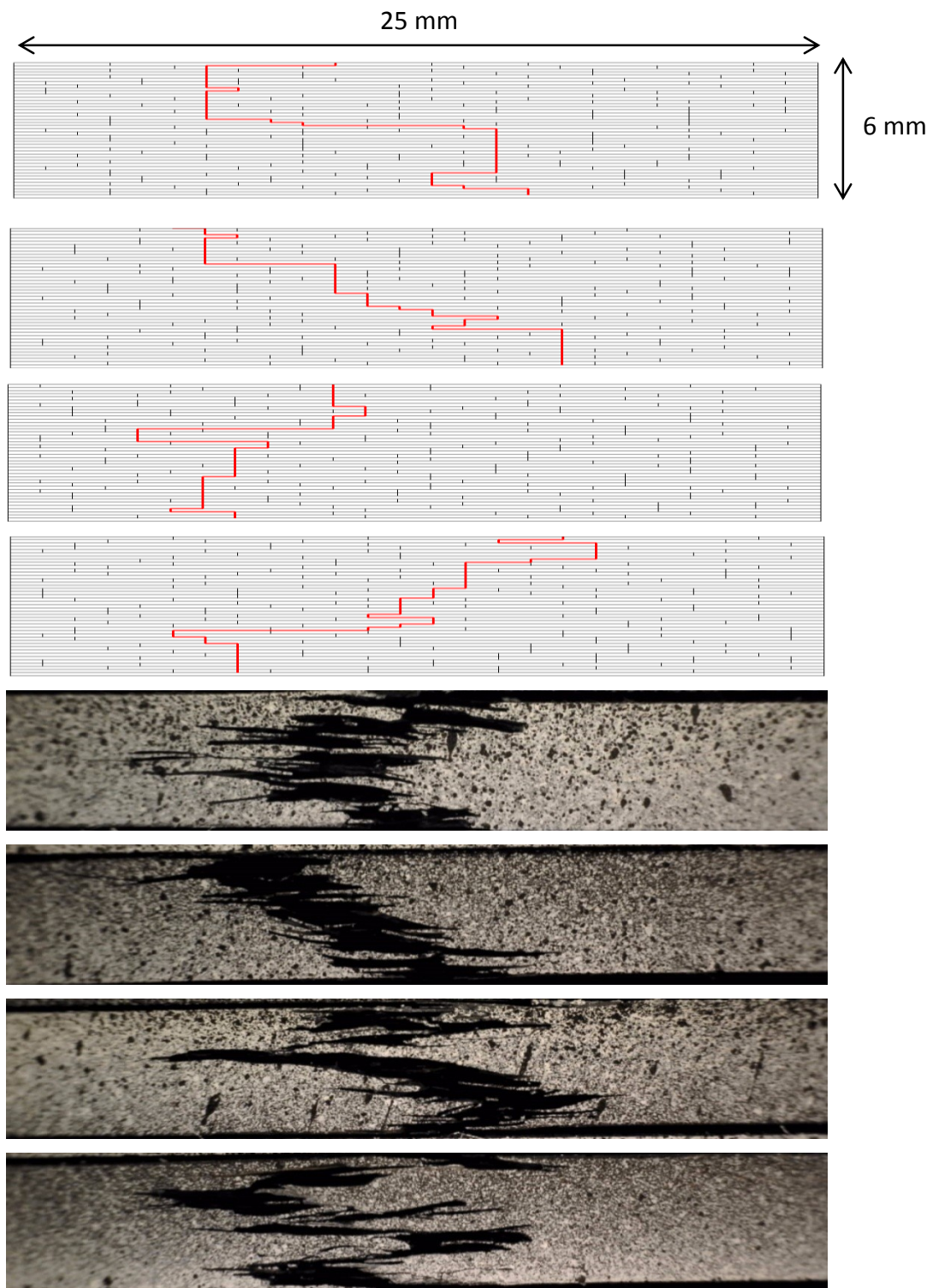


Figure 8-20 – Examples of different failure morphologies obtained with modelling and testing of ROS composites with 6 x 3 mm strands

8.7 Concluding remarks and future work

This chapter presented a modelling technique that can predict strength of ROS composites from basic properties of unidirectional laminates of the same material by employing simple analytical formulations. The proposed model is a 2D representation of the microstructure and takes into account the possibility of strand failure and delamination when subjected to tensile loading. Strand failure strength is estimated using the CLT and Hashin's failure criteria, and overlap strength is calculated using the shear strength and fracture toughness criteria. With respect to interlaminar shear strength, it is recommended to use the data measured by the double-notch shear test. An example of how this model is used can be found in Appendix B.

Overall, this model successfully captures the effect of strand size and panel thickness on the strength and its variability in ROS composites, hence signifying that the proposed modelling approach is appropriate for this type of material architecture. The main downfall of this model is that it over-predicts strength, which was expected since all of the assumptions are non-conservative. Nonetheless, it predicts the upper bound for strength of ROS composites which is more realistic than the one produced by the basic analytical models, as is shown in Figure 2-19 and was previously discussed in the Chapter 2.

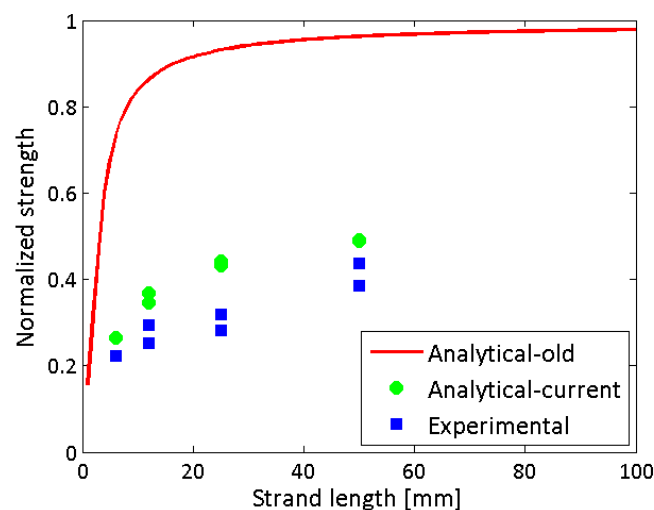


Figure 8-21 – Comparison between the older (basic) analytical models, the currently proposed model and the experimental strength data for ROS composites. Explanation of the analytical models used to generate this graph can be found in Chapter 2

As a part of the future work, it is recommended to reconsider the validity of all the assumption through more detailed experiments and FE modelling. In particular, it is necessary to implement the physics of progressive failure into the model and to determine the effect of peel stresses on strand delamination. Another important parameter to implement into the model would be the residual thermal stresses, which develop during manufacturing, and as was discussed in Chapter 3, are substantial.

Also, it is advisable to consider the 3D nature of the material, since currently only one slice of the 3D microstructure is considered, as shown in Figure 8-22. It is unclear at this stage how failure propagates through the entire specimen and more experimental work is required to characterize this mechanism. It would be interesting to extend the current model to a 3D network of cracks and study their propagation.

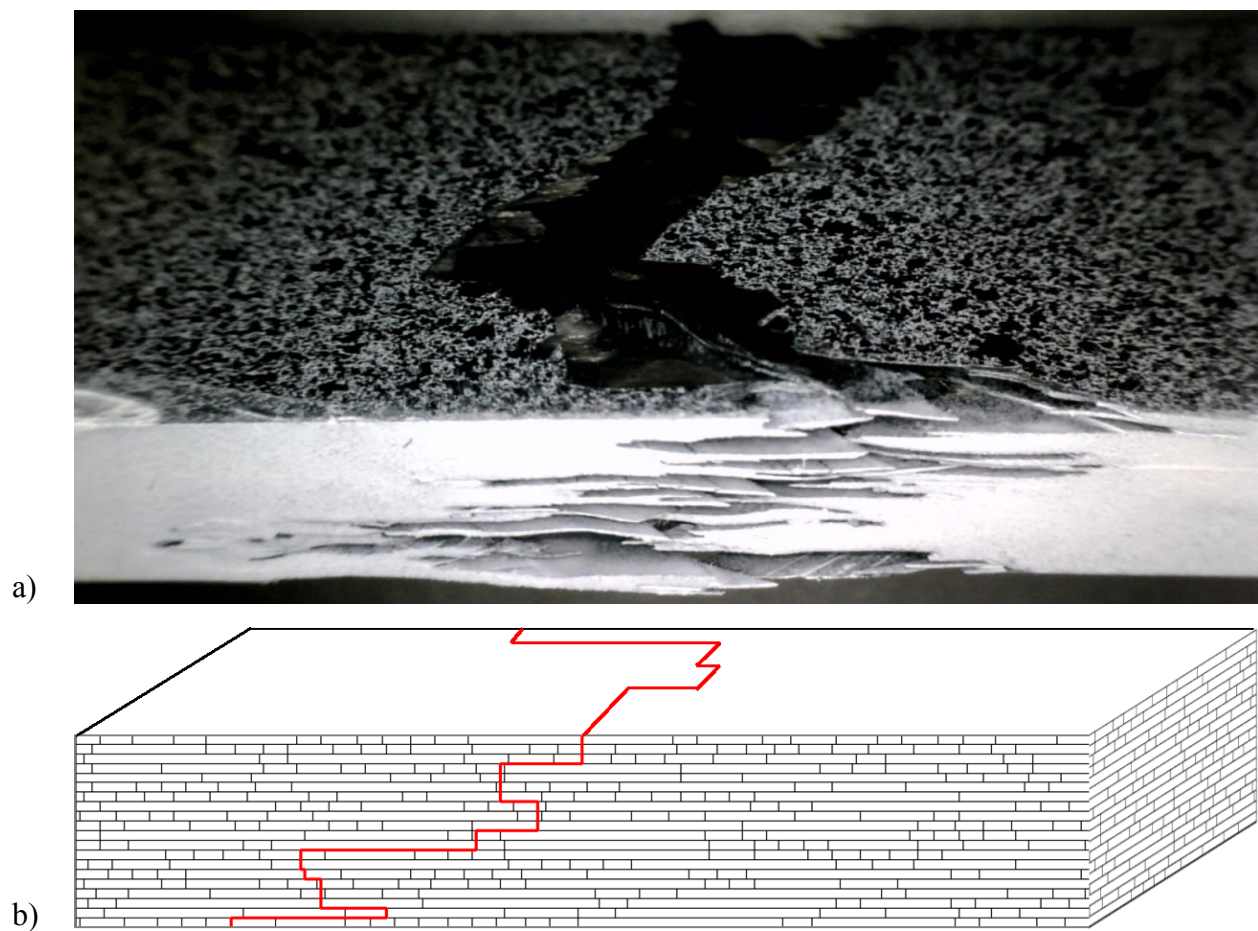


Figure 8-22 – 3D representation of the microstructure and failure path: a) actual and b) modelled

Chapter 9

Conclusions, recommendations and future work

The objectives of this thesis were to characterize, explain and model the mechanical properties of ROS composites. Extensive experimental work was performed to measure tensile, compressive and shear strength and modulus of ROS panels and to determine the sensitivity of these properties to strand sizes. Subsequently, two modelling schemes were proposed and evaluated. These techniques were based on 2D representation of either in-plane or through-the-thickness microstructure and took into account random strand distribution in the material. The following sections will highlight the main conclusions of this work, outline practical recommendations and propose topics for future work.

9.1 Conclusions: Investigation of mechanical properties

The different mechanical properties that were investigated can be summarized by the same conclusions as they all exhibited similar interrelated trends:

Strand length and heterogeneity. Mechanical properties and variability increase with increasing strand length. Strand length (or overlap length) plays a key role in the efficiency of the load transfer between the strands. Ideally, the maximum load that can be sustained by the

interface increases proportionally to the overlap length, eventually approaching properties of QI CF composites. However, due to the presence of stress concentration at strand ends, this ultimate strength is never attained. The use of longer strands augments spatial heterogeneity of the component leading to localized weak-spots that trigger premature damage initiation. Thus, the conclusions are twofold. One, strength of ROS composites is significantly lower than that of QI CF laminates because of the early onset of damaged caused by the presence of weak-spots in the material and stress concentrations at the strand ends. Two, a compromise between the average properties and the repeatability has to be reached when choosing the optimal strand size for a particular application.

Average properties. Interestingly, tensile, compressive and shear strength have a similar magnitude, which is not typically expected of composites. Additionally, tensile and compressive stiffness are also comparable, and in-plane shear stiffness can be calculated using the assumption of transverse isotropy and tensile properties. This observation enables preliminary designs to be done using only the tensile data, which is easier to obtain, before the complete set of design allowables becomes available. These results are explained by the fact that regardless of the direction of the applied in-plane load, load transfer mechanisms in the material are the same (i.e. interlaminar matrix shear and complex stress-state in the strands).

9.2 Conclusions: Modelling efforts

The following conclusions can be drawn regarding the overall model evaluation and the additional insights that models provided on ROS composites:

Model assessment. The two proposed models are simplified 2D representations of the significantly more complex 3D microstructure of ROS composites. Nonetheless, these models captured the heterogeneous nature of ROS composites, predicted the range of their tensile properties and demonstrated how their properties compare against those of QI CF laminates.

In order to account for strand size effects and to predict proper failure modes it is necessary to consider interlaminar (inter-strand) properties, as was done in the through-the-thickness model. Nonetheless, even the in-plane model, which completely ignored the effects of delamination, was

able to demonstrate the drastic reduction of properties from QI CF to ROS composites that was caused by the presence of localized weak-spots (i.e. matrix-dominated layups). Overall, the through-the-thickness model is more representative of the failure mechanics characteristic to ROS composites and is more propitious of the two.

Failure mechanics of ROS composites. Modelling results also showed that inherent material variability has a pronounced effect on the global properties. They also demonstrated that strength of ROS composites is strongly dependent on matrix shear strength and toughness, which effectively defines the transition point between strand failure (high global strength) and strand pull-out (low global strength). It can be concluded that better properties can be attained with ROS composites by improving their homogeneity (i.e. designing thicker parts or controlling strand placement) or increasing resin strength and toughness (i.e. choosing thermoplastic or other toughened resins over thermosets).

9.3 Practical recommendations

Two major practical recommendations can be made based on this thesis:

Size effects must be carefully considered. The discussion of size effects has been at the core of this thesis and has touched upon inherent material properties and experimental protocols. Experimental results indicate a clear increase of average properties with increasing strand length. The adverse outcome of using longer strands is high material heterogeneity which leads to lower design allowables and worse warpage. Material homogeneity improves with panel thickness and results in better mechanical properties and geometric tolerances. Hence, when selecting the optimal strand size for the application, average properties and standard deviation that are characteristic to a particular part thickness have to be examined. Manufacturing of thin components (< 2 mm) should be avoided. Furthermore, existing ASTM standards are not specifically designed for testing of ROS composites. Hence when characterizing ROS composites, the investigator needs to consider the feasibility of designing new test methods and fixtures to accommodate for larger gauge sections and/or to test more specimens than recommended by the standards to attain statistically viable results.

High interlaminar properties are critical for mechanical performance. Failure mechanisms that are prevalent to ROS composites are strand failure and strand pull-out. The latter is directly related to the interlaminar (i.e. matrix shear) strength and toughness. Experimental and modelling results indicated that tougher and stronger thermoplastic-based ROS composites perform better than their more brittle thermoset-based counterparts. Hence, the use of tough thermoplastics is more advisable over the use of thermosets.

9.4 Future work

Although notable contributions were made in this study, further work needs to be performed to advance the understanding of ROS composites and to develop modelling techniques that would simplify certification. The recommended areas for future work are summarized below:

Characterization of progressive failure. Thus far it is known that failure initiates at the weakest location and propagates in a stair-like or zig-zag manner. However, it is not clear what type of microstructural features serve as sites of crack initiation and how fast the crack actually propagates in the through-the-thickness and transverse directions. In-depth knowledge of damage development is required to further fine-tune the model and to classify certain microstructural features as defects. This experimental work can be done by running interrupted tensile tests and using a micro-CT scanner to detect and to monitor damage evolution with increasing load levels.

Quantifying edge effects. Strand size has a notable effect on properties, and cutting of the specimens reduces strand size along the edges, which potentially leads to premature damage initiation. On the other hand, actual ROS components are net-moulded and are not subject to cutting. At this stage it is difficult to comment on the improvement of properties between the net-shape and cut coupons, but this topic warrants further study.

Out-of-plane stresses. The models that were developed in the thesis dealt solely with in-plane loading. However, industrial ROS parts have 3D features, such as ribs, that would experience out-of-plane stresses and strains. It would be interesting to incorporate the effect of these stresses into the model and to visualize the corresponding nuances of damage propagation. An FE

microstructural model with proper contact definition between the strands would be required for this task.

Heterogeneity. Additional work needs to be done to address the issue of material heterogeneity both with respect to experimental work and modelling approaches. Supplementary recommendations regarding the number and size of test coupons (or model realizations) that are required for materials that are heterogeneous on the component level can potentially be drawn from other engineering fields. For instance, rigid foams and concrete also have a characteristic length scale of the microstructure (or heterogeneity) that is similar to the size of the component. Finally, the connection between the behaviour and variability of test specimens and the actual components needs to be made. This comparison will help to understand what specimen size and geometry are the most representative of the component properties.

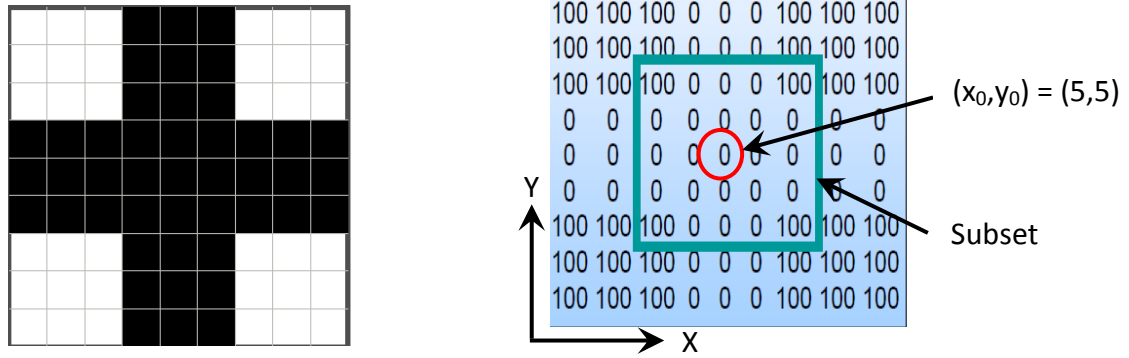
Warpage. It is essentially impossible to mould a thin flat ROS panel, due to the development of non-uniform residual thermal stresses. While this issue would not be as drastic for small complex industrial components, it might still pose a problem with achieving good geometric quality, precision and repeatability among moulded parts. Hence, it would be interesting to extend the in-plane model that was developed for stiffness to modelling of thermal stresses and potentially finding ways of mitigating them. This can be achieved by incorporating the COMPRO® subroutines into the ABAQUS script.

Appendix A

Digital image correlation

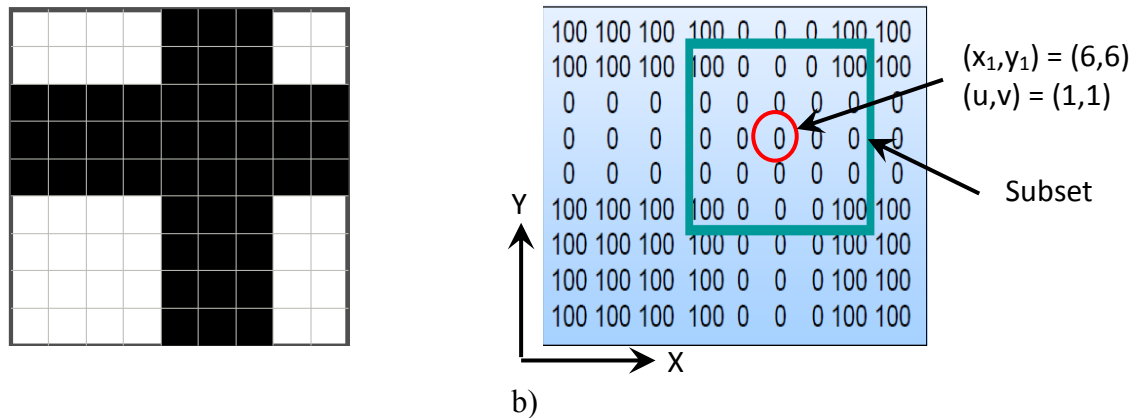
Digital image correlation (DIC) is an optical non-contact technique that is used to measure full-field displacement and strain of a deforming object. A short overview of this technique is presented in this section. For a more detailed explanation, the reader is referred to the book [100] and technical material [101] available from Correlated Solutions (the provider of VIC 2D). DIC is based on the concept of pattern recognition and works in the following way: 1) a random and unique greyscale pattern is applied on the surface of the specimen, 2) images of the speckle pattern are recorded during the tests with a digital camera, then 3) a correlation algorithm is used to compute the displacement vector of the pattern with respect to the reference image (unloaded state), finally 4) formulations similar to finite-difference methods is used to obtain a strain field from the displacement data.

To explain the workings of the DIC software, a simple example will be discussed. Figure A-1 shows a reference image (prior to loading) as it would appear on the screen and as it would be saved in the memory. The greyscale pattern is expressed by a matrix with values between 0 and 100, which represent the pixel light intensity.



a) b)
Figure A-1 – Reference image used for DIC as it appears a) on the screen and b) in the memory [101, 102]

Next, a deformed image shown in Figure A-2 is analysed to determine its displacement. It is impossible to track the motion of a single pixel since there are multiple pixels with the same intensity value (i.e. there are many black pixels). For this reason, a subset (or group) of pixels that represent a unique pattern (highlighted by a blue square in Figure A-1b and Figure A-2b) is considered. By locating the position of a particular subset in the deformed image, it is possible to calculate its displacement (u, v) by subtracting the before (x_0, y_0) and after (x_1, y_1) coordinates of its centroid (highlighted by a red circle in Figure A-1b and Figure A-2b).



a) b)
Figure A-2 - Deformed image used for DIC as it appears a) on the screen and b) in the memory [101, 102]

The excellent accuracy of this technique is attributed to its ability to deal with sub-pixel displacements by interpolating the image between the non-integer locations. In Figure A-3 the image is shifted to the right by 0.5 pixel. This technique is also robust enough to deal with subset deformation, since initially square subsets will typically become non-square during testing, refer to Figure A-4.

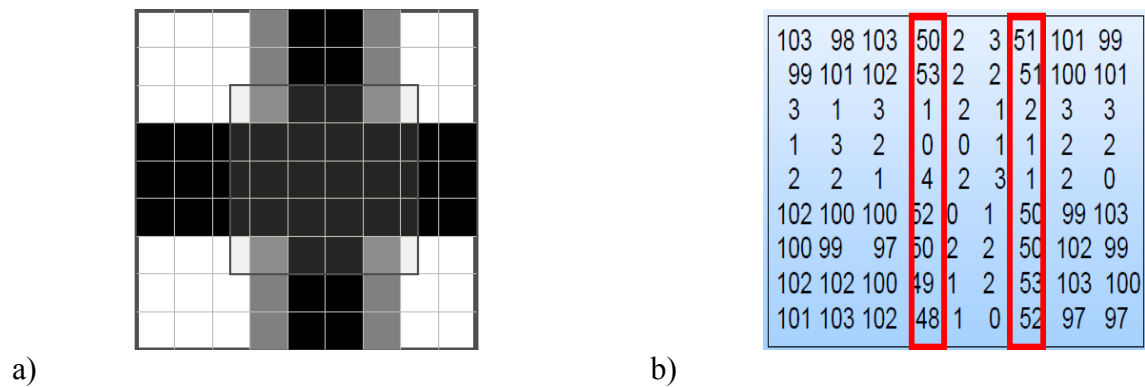
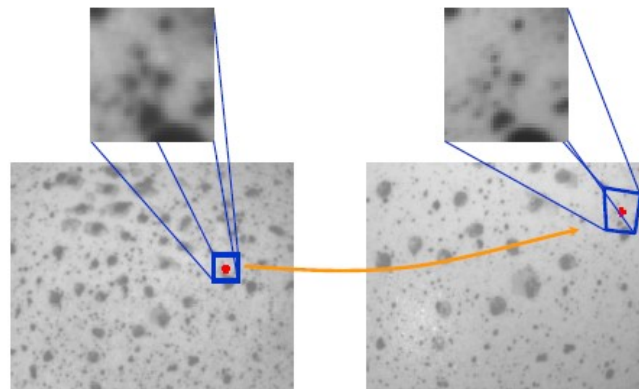


Figure A-3 - Deformed image used for DIC as it appears a) on the screen and b) in the memory. Sub-pixel displacement creates grey (50) areas in the image that was originally black (0) and white (100) [101, 102]



Time $t_0 \rightarrow$ Specimen deformation \rightarrow Time t_1

Figure A-4 – Reference and deformed image with non-square subset [101]

The reference image of an actual test specimen is discretized into numerous subsets as shown in Figure A-5, and the centroids of these subsets serve as grid points. Distance between the centroids is defined by the step size. Displacement values that correspond to each grid point are used to calculate the strain field by using finite-difference methods and low pass filtering.

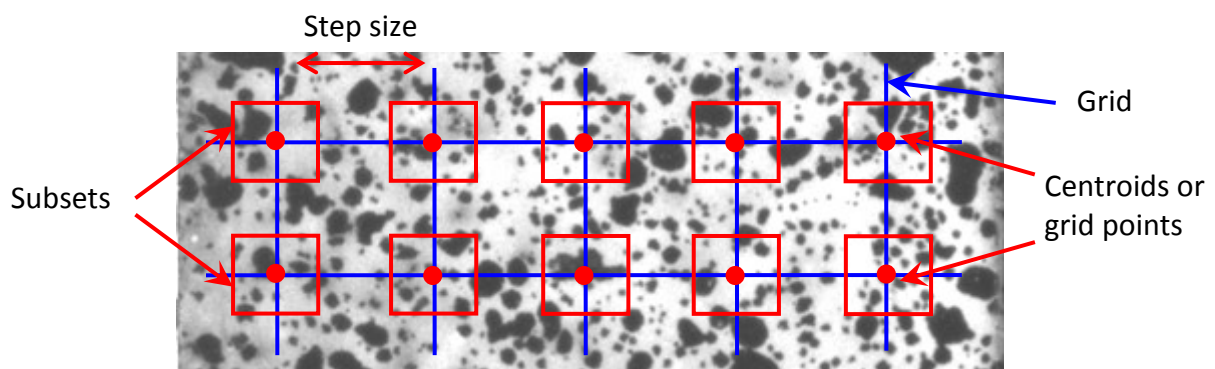


Figure A-5 – Speckle pattern discretized into subsets

DIC is a powerful technique for strain measurement, but it requires proper test setup (e.g. speckle pattern, good camera and lens) and choice of parameters for the analysis (e.g. subset and step size) to ensure accurate results. The speckle pattern must be non-repetitive and high-contrasting, and the recommended speckle size is 3-6 pixels in diameter. Speckles that are smaller than one pixel should be avoided, since their motion is difficult to track. Three speckle patterns are shown in Figure A-6, where the grid lines represent pixels and the red rectangles define subsets. Figure A-6a shows the optimal speckle pattern. In Figure A-6b, speckles are slightly larger than the optimal size, but would not cause a problem for the analysis. They should be reduced in size, however, if higher spatial resolution is required (i.e. detecting stress concentrations). On the other hand, when speckles are too small (Figure A-6c), their displacements cannot be accurately tracked, hence causing “noisy” data. To improve accuracy, the image must be zoomed in or a camera with higher resolution (i.e. more pixels) should be used.

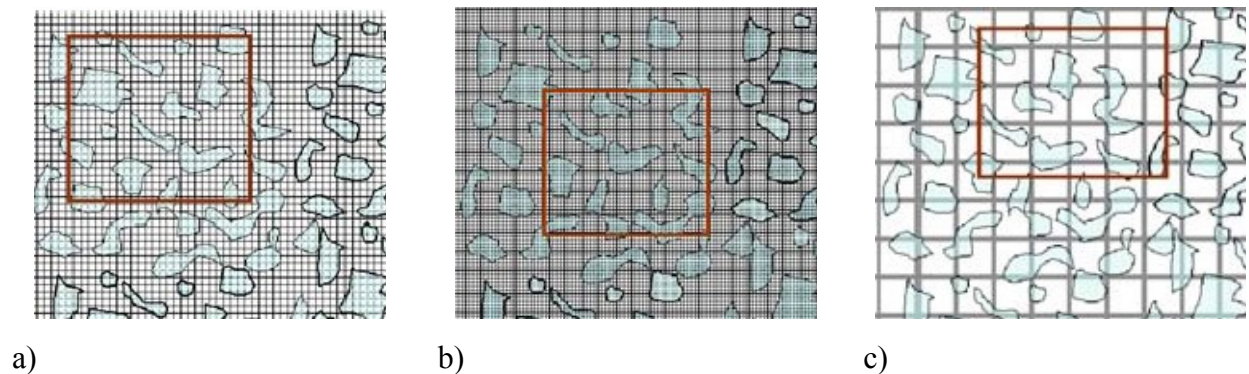


Figure A-6 – Different speckle patterns with speckles being a) the optimal size, b) slightly bigger and c) too small [100].

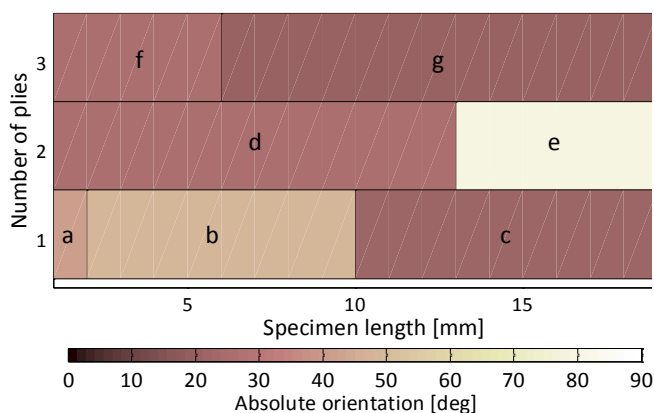
An optimal subset size would contain at least 3 x 3 speckles to ensure reasonable accuracy of the results. Overall, the larger the subset is, the more information it will contain and the more “unique” it will be, hence resulting in higher confidence associated with subset matching. On the other hand, smaller subsets are recommended for monitoring of regions with strain heterogeneities. For most applications, a step size that is $\frac{1}{4}$ of the subset size would give good results.

Overall, the settings discussed in this section serve as “rules of thumb” and should be adjusted to better suit a particular application.

Appendix B

Example of the through-the-thickness strength model

This section will demonstrate how the through-the-thickness model, which was detailed in Chapter 8, is applied to a small cross-section. This example is based on material properties for carbon/PEEK (Table 8-1). The first step is to generate a microstructure. For simplicity a small specimen that has 3 plies and is 18 mm long is modelled, Figure B-1a. In this figure, Latin letters (a, b...) define individual strands, and their orientations are summarized in Figure B-1b.



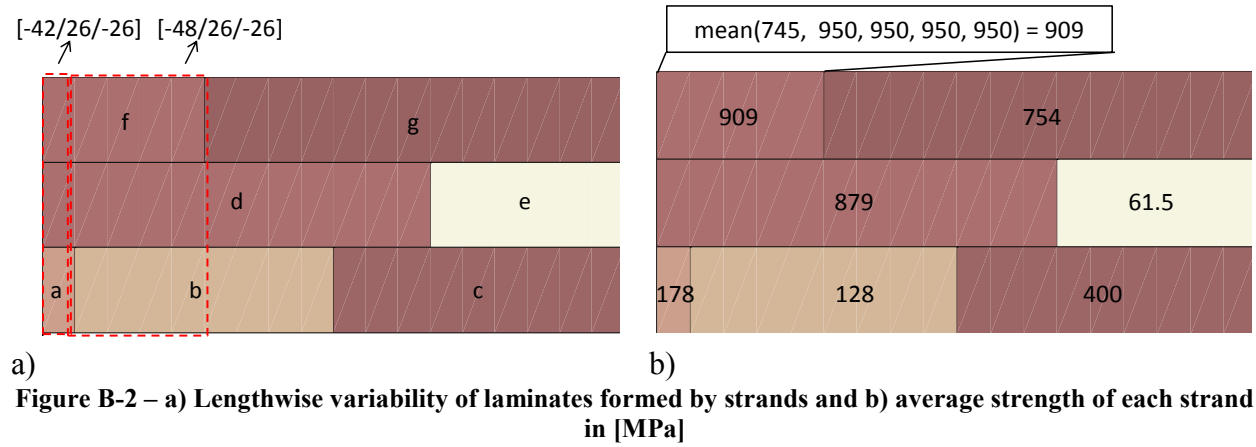
Strand	Orientation [°]
a	-42
b	-48
c	-22
d	26
e	80
f	-26
g	20

a)

b)

Figure B-1 – a) Modelled microstructure and b) summary of strand orientations

The next step is to assign a strength value to every strand and overlap, which will be used to create a network of all the possible failure paths. Strand strengths are calculated using the CLT and Hashin's failure criteria in 1 mm intervals. As a result of this discretization, each strand has multiple strength values associated with it. For instance, strand "f" is associated with two different layups (Figure B-2a), and hence will have a lengthwise strength variability associated with it (Figure B-2b). To simplify the subsequent calculations, an average strength value is assigned to each strand, as summarized in Figure B-2b.

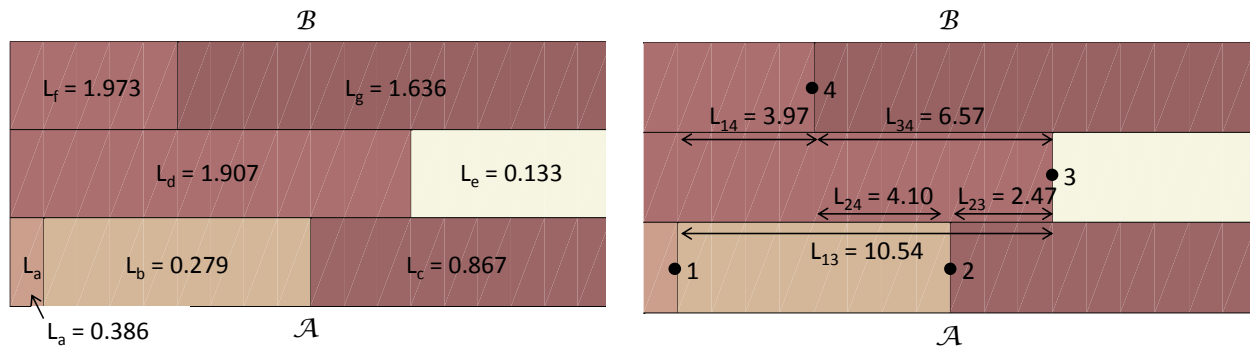


In order to combine strand and overlap strengths into the same network, consistent units must be used. In this model, the unit of length was chosen, and strand strength values are converted to the corresponding length values (L_a, L_b, \dots) using Eq. B-1. This step is summarized in Figure B-3a, where \mathcal{A} and \mathcal{B} denote the two sides of the laminate, which will be connected by the crack.

$$L = \frac{\sigma_s t_b}{\tau_i} = \frac{\sigma_s (0.139)}{64} = 0.00217 \sigma_x \quad \text{Eq. B-1}$$

Next step is to determine all the overlap lengths, which are shown in Figure B-3b, where nodes are defined by numerals (1, 2...). In order to account for the presence of the strength plateau, which is governed by the fracture toughness criteria, limit length (L_{lim}) is introduced. Based on Eq. B-2 - Eq. B-3, L_{lim} is 2.77 mm (for laminate thickness of 2.5 mm and interlaminar shear strength of 64 MPa). It is evident that in Figure B-3b, only L_{23} is shorter than L_{lim} and hence, the other overlap lengths will be set to L_{lim} .

Example of the through-the-thickness strength model



a) b)
Figure B-3 – a) Strand lengths (which are representative of their strengths) and b) overlap lengths in [mm]

$$\sigma_c = \sqrt{\frac{2E_{QI}G_{IIc,IL}}{t_b}} = \sqrt{\frac{2(51.9)1930}{0.139}} = 1200 \text{ MPa} \quad \text{Eq. B-2}$$

$$L_{\text{lim}|\tau=64} = \frac{\sigma_c n t_b}{(n-1)\tau_i} = \frac{1200 \cdot 2.5}{(18-1)64} = 2.77 \text{ mm} \quad \text{Eq. B-3}$$

Once the length values of all components are calculated, they can be assembled into a network of all the possible failure paths. Figure B-4a shows all the delamination paths, and Figure B-4b shows the superposition of the strand delamination and failure paths. A couple of connections are ignored in this example for the sake of clarity. The shortest or the weakest failure path is shown in by a red dashed line in Figure B-4b and is illustrated in Figure B-5 ($\mathcal{A} \rightarrow 4 \rightarrow \mathcal{B}$).

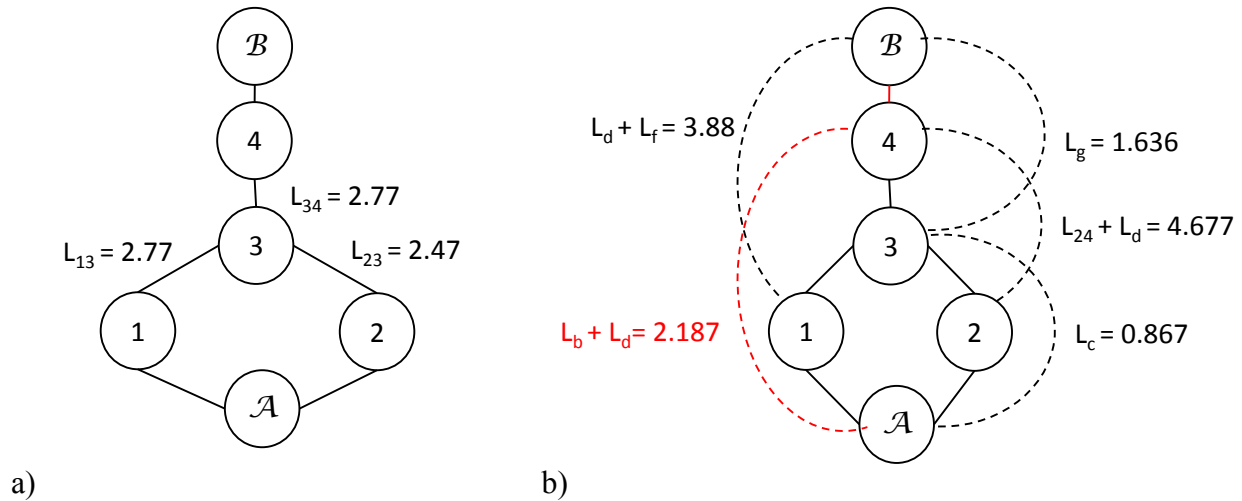


Figure B-4 – Graphical representation of the failure network: a) delamination paths and b) delamination and strand failure paths

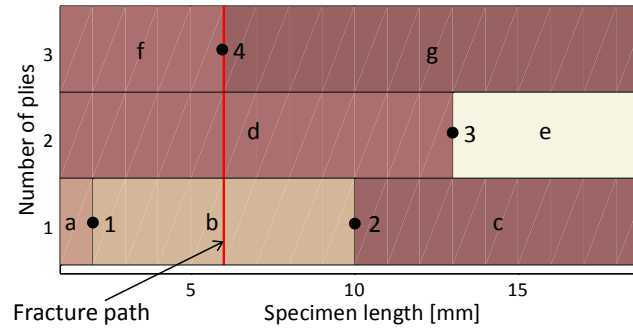


Figure B-5 – Failure path of the modelled microstructure

The final step is to calculate the specimen strength from the shortest failure path using Eq. B-4.

$$\sigma_{ROS} = \frac{L_{short} \tau_i}{n t_b} = \frac{2.187 (64)}{3(0.139)} = 336 \text{ MPa} \quad \text{Eq. B-4}$$

Visualization of different failure paths and their corresponding lengths (or strengths) are shown in Figure B-6.

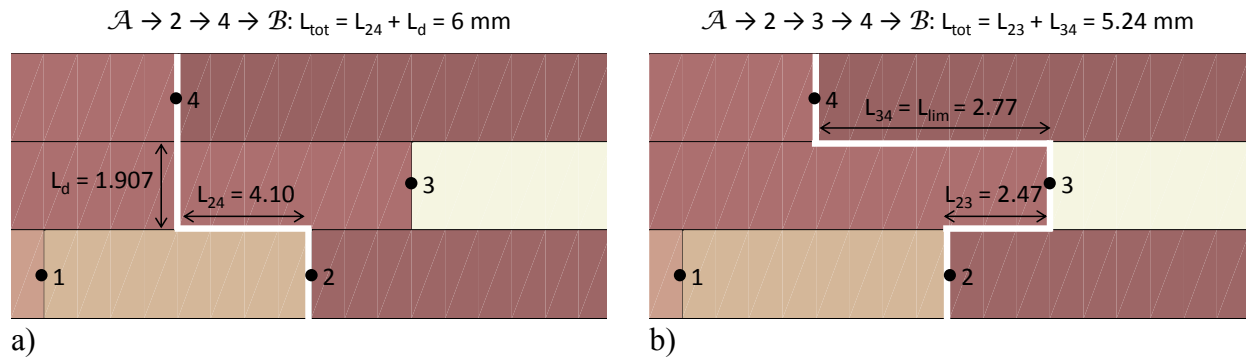


Figure B-6 – Visualization of different possible failure paths and their relative lengths (or strengths)

References

1. Hale, J., *Boeing 787 from the Ground Up*, in AERO 2006: Seattle, USA.
2. Muzzy, J.D., *Thermoplastics-properties*, in *Comprehensive Composite Materials*, K. Anthony and Z. Carl, Editors. 2000, Pergamon: Oxford. p. 57-76.
3. Offringa, A.R., *Industrial report. Thermoplastic composites - rapid processing applications*. Composites: Part A, 1996. 27A: p. 329-336.
4. Díaz, J. and L. Rubio, *Developments to manufacture structural aeronautical parts in carbon fibre reinforced thermoplastic materials*. Journal of Materials Processing Technology, 2003. 143-144: p. 342-346.
5. Angelos Miaris, K.E., Matthias von Hayek Boelingen. *A350 WXB: thousands of thermoplastic composite parts in an FRP aircraft. The breakthrough to a highly automated composite manufacturing*. in SAMPE Conference Proceedings. 2014. Seattle, WA.
6. Harper, L.T., *Discontinuous carbon fibre composites for automotive applications*. 2006, University of Nottingham: Nottingham.
7. Feraboli, P., et al. *Lamborghini "forged composites(R)" technology for the suspension arms of the Sesto Elemento* in The 26th American Society for Composites (ASC) Technical Conference 2011. Montreal, Canada.
8. Eguémann, N., et al. *Compression moulding of complex parts for the aerospace with discontinuous novel and recycled thermoplastic composite materials* in The 19th International Conference on Composite Materials. 2013. Montreal, Canada.
9. Jespersen, S., et al., *Rapid processing of net-shape thermoplastic planar-random composite preforms*. Applied Composite Materials, 2009. 16(1): p. 55-71.
10. Taketa, I., et al., *Enhancement of strength and uniformity in unidirectionally arrayed chopped strands with angled slits*. Composites Part A: Applied Science and Manufacturing, 2010. 41(11): p. 1639-1646.
11. Chang, I.Y. and J.F. Pratte, *LDF thermoplastic composite technology*. Journal of Thermoplastic Composite Materials, 1991. 4: p. 227-252.

12. Eguemann, N., et al. *Manufacturing and recycling of complex composite thermoplastic parts for aerospace applications*. in *SAMPE Europe 7th SETEC 12*. 2012. Lucerne, Switzerland.
13. LeBlanc, D., *Compression moulding of complex parts with randomly-oriented strand thermoplastic composites*, in *Department of Mechanical Engineering*. 2014, McGill University: Montreal.
14. Lessard, H., et al., *Influence of process parameters on the thermostamping of a [0/90]₁₂ carbon/polyether ether ketone laminate*. *Composites: Part A*, 2015. 70(1): p. 59-68.
15. Greene, Tweed XYCOMP® DLF high-performance thermoplastic composite 2014.
16. Howell, D.D. and S. Fukumote. *Compression molding of long chopped fiber thermoplastic composites*. in *The Composites and Advanced Materials Expo (CAMX)*. 2014. Orlando, USA.
17. Selezneva, M., et al. *Compression moulding of discontinuous-fibre carbon/PEEK composites: study of mechanical properties*. in *SAMPE*. 2012. Baltimore.
18. Selezneva, M., et al. *Mechanical properties of randomly oriented strands thermoplastic composites*. in *The 19th International Conference on Composite Materials* 2013. Montreal, Canada.
19. Picher-Martel, G.-P. and P. Hubert. *Squeeze flow behaviour of Carbon/PEEK Randomly-Oriented Strands under transverse compaction*. in *American Society for Composites 27th Annual Technical Conference/The 15th US-Japan Conference on Composite Materials*. 2012. Arlington, Texas, US.
20. Picher-Martel, G.-P., A. Levy, and P. Hubert. *Squeeze flow of randomly-oriented strands thermoplastic composites*. in *The 19th International Conference on Composite Materials*. 2013. Montreal, QC, Canada.
21. Landry, B. and P. Hubert. *Processing effect on the damage tolerance of randomly-oriented strands thermoplastic composites*. in *The 19th International Conference on Composite Materials*. 2013. Montreal, QC, Canada.
22. LeBlanc, D., et al. *Compression moulding of complex parts using randomly-oriented strands thermoplastic composites* in *SAMPE Conference Proceedings*. 2014. Seattle, USA.

23. LeBlanc, D., et al. *Study of processing conditions on the forming of ribbed features using randomly oriented strands thermoplastic composites*. in AHS 70th Annual Forum. 2014. Montréal, Canada.
24. Selezneva, M., et al. *Modelling of mechanical properties of randomly oriented strands thermoplastic composites*. in 16th European conference on composite materials. 2014. Seville, Spain.
25. Kilic, M.H. *Multi-scale modeling of discontinuous long-fibre composites* in SAMPE Conference Proceedings. 2014. Seattle, WA.
26. Thomas, G.P., *Compression Molded Composites: Processes, Benefits and Applications – An Interview With TenCate*, in AZoM.
27. Feraboli, P., et al., *Characterization of prepreg-based discontinuous carbon fiber/epoxy systems*. Journal of Reinforced Plastics and Composites, 2009. 28(10): p. 1191-1214.
28. Feraboli, P., et al., *Defect and damage analysis of advanced discontinuous carbon/epoxy composite materials*. Composites Part A: Applied Science and Manufacturing, 2010. 41(7): p. 888-901.
29. Feraboli, P., et al., *Modulus measurement for prepreg-based discontinuous carbon fiber/epoxy systems*. Journal of Composite Materials, 2009. 43(19): p. 1947-1965.
30. Feraboli, P., et al., *Notched behavior of prepreg-based discontinuous carbon fiber/epoxy systems*. Composites Part A: Applied Science and Manufacturing, 2009. 40(3): p. 289-299.
31. Feraboli, P., et al., *Stochastic laminate analogy for simulating the variability in modulus of discontinuous composite materials*. Composites Part A: Applied Science and Manufacturing, 2010. 41(4): p. 557-570.
32. Han, J.H., et al. *Effect of fabric reinforcement on failure response of discontinuous long fiber composite bolted joints*. in SAMPE 2011. Long Beach, CA.
33. TenCate Advanced Composites, *Datasheet: TenCate Cetex(R) MC1200 PEEK Thermoplastic BMC*. 2012.
34. Van Wijngaarden, M., A. Jongbloed, and J. De Vries. *Thermoplastic compound compression molding*. in SAMPE. 2010. Seattle, WA.
35. Eguémann, N., et al. *Processing of characterisation of carbon fibre reinforced PEEK with discontinuous architecture*. in ECCM16 - 16th European Conference on Composite Materials. 2014. Seville, Spain.

36. Johanson, K., et al., *Studying the heterogeneity of discontinuous fiber composites using a new full-field strain measurement system*, in *The 19th international conference on composite materials*. 2013: Montreal, Canada.
37. Qian, C., et al., *Notched behaviour of discontinuous carbon fibre composites: Comparison with quasi-isotropic non-crimp fabric*. *Composites: Part A*, 2011. 42: p. 293-302.
38. Sato, Y., et al., *Elastic modulus estimation of chopped carbon fiber taper reinforced thermoplastics using the monte carlo simulation*, in *The 19th international conference on composite materials*. 2013: Montreal, Canada.
39. Matsuo, T., et al. *Design and manufacturing of anisotropic hollow beam using thermoplastic composites*. in *The 19th international conference on composite materials*. 2013. Montreal, Canada.
40. Roux, M., et al., *Recycling of high performance thermoplastic composites with high voltage fragmentation*, in *The 19th international conference on composite materials*. 2013: Montreal, Canada.
41. Caba, A.C., *Characterization of carbon mat thermoplastic composites: flow and mechanical properties.*, in *Engineering Mechanics*. 2005, Virginia Polytechnic Institute and State University: Blacksburg.
42. Pan, Y., *Stiffness and progressive damage analysis on random chopped fibre composite using FEM*, in *Mechanical and Aerospace Engineering*. 2010, New Brunswick Rutgers, The State University of New Jersey: New Brunswick.
43. Tucker III, C.L. and E. Liang, *Stiffness predictions for unidirectional short-fiber composites: Review and evaluation*. *Composites Science and Technology*, 1999. 59(5): p. 655-671.
44. Eshelby, J.D., *The determination of the elastic field of an ellipsoidal inclusion, and related problems*. *Proceedings of the Royal Society of London. Series A, Mathematical and Physical Sciences*, 1957(241): p. 376-96.
45. e-Xtream Engineering, *Digimat 4.2.1 Manual*. 2012.
46. Mori, T. and K. Tanaka, *Average stress in matrix and average elastic energy of materials with misfitting inclusions*. *Acta Metallurgica*, 1973. 21(5): p. 571-574.
47. Benveniste, Y., *A new approach to the application of Mori-Tanaka's theory in composite materials*. *Mechanics of Materials*, 1987. 6: p. 147-157.

48. Ashrafi, B., *Theoretical and experimental investigations of the elastic properties of carbon nanotube-reinforced polymer thin films*, in *Department of Mechanical Engineering*. 2008, McGill University: Montreal.
49. Kelly, A. and W.R. Tyson, *Tensile properties of fibre-reinforced metals: copper/tungsten and copper/molybdenum*. *Journal of the Mechanics and Physics of Solids*, 1965. 13: p. 329-350.
50. Cox, H.L., *The elasticity and strength of paper and other fibrous materials*. *British Journal of Applied Physics* 1952. 3(3): p. 72-79.
51. Gibson, R.F., *Principles of Composite Material Mechanics*. 3rd ed. 2012, Boca Raton: CRC Press.
52. Abdul-Rasheed, M.I., et al., *Experimental characterisation of recycled (glass/TPU woven fabric) flake reinforced thermoplastic composites*, in *The 19th international conference on composite materials*. 2013: Montreal, Canada.
53. Fu, S.-Y. and B. Lauke, *Effects of fiber length and fiber orientation distributions on the tensile strength of short-fiber-reinforced polymers*. *Composite Science and Technology*, 1996. 56: p. 1179-1190.
54. Stanford, J.L., et al., *Experimental studies on the interfacial shear-transfer mechanism in discontinuous glass-fibre composites*. *Composites Science and Technology*, 2000. 60(3): p. 361-365.
55. O'Regan, M.D.F., Akay, and B. Meenan, *A comparison of Young's modulus predictions in fibre-reinforced-polyamide injection mouldings*. *Composites Science and Technology*, 1999. 59(3): p. 419-427.
56. Patcharaphun, S., *Characterization and simulation of material distribution and fiber orientation in sandwich injection molded parts*, in *Mechanical Engineering*. 2006, Chemnitz University of Technology.
57. Krenchel, H., *Fibre reinforcement*. 1964, Copenhagen: Akademisk Forlag.
58. Nielsen, L.E. and P.E. Chen, *Young's modulus of composites filled with randomly oriented fibers*. *Journal of Materials*, 1968. 3(2).
59. Baxter, W.J., *The strength of metal matrix composites reinforced with randomly oriented discontinuous fibers*. *Metallurgical Transactions A*, 1992. 23A: p. 3045-3053.

60. Hashimoto, M., et al., *Prediction of tensile strength of discontinuous carbon fiber/polypropylene composite with fiber orientation distribution*. Composites: Part A, 2012. 43: p. 1791-1799.
61. Halpin, J.C. and J.L. Kardos, *Strength of discontinuous reinforced composites: 1. fiber reinforced composites*. Polymer Engineering & Science, 1978. 18(6): p. 496-504.
62. Lielens, G., et al., *Prediction of thermo-mechanical properties for compression moulded composites*. Composites Part A: Applied Science and Manufacturing, 1998. 29(1-2): p. 63-70.
63. Advani, S.G. and C.L. Tucker, *The use of tensors to describe and predict fiber orientation in short fiber composites*. Journal of Rheology, 1987. 31(8): p. 751-784.
64. Pimenta, S. and P. Robinson, *An analytical shear-lag model for composites with 'brick-and-mortar' architecture considering non-linear matrix response and failure*. Composites Science and Technology, 2014. 104: p. 111-124.
65. Rexer, J. and E. Anderson, *Composites with planar reinforcements (flakes, ribbons) – A review*. Polymer Engineering & Science, 1979. 19(1): p. 1-11.
66. Wyser, Y., Y. Leterrier, and J.-A.E. Manson, *Analysis of failure mechanisms in platelet-reinforced composites*. Journal of Materials Science, 2001. 36.
67. *Structural behavior of joints*, in *Composite Materials Handbook*. 2002.
68. Volkersen, O., *Die nietkrafteerteilung in zubeanspruchten nietverbindungen mit konstanten loschonquerschnitten*. Luftfahrtforschung, 1938. 15: p. 41-47.
69. Hart-Smith, L.J. *Adhesive-bonded joints for composites phenomenological considerations*. in *Technology Conferences Associates Conference on Advanced Composites Technology*. 1978. El Segundo, California.
70. daSilva, L.F.M., *Design rules and methods to improve joint strength*, in *Handbook of Adhesion Technology*, R.D. Adams, Editor. 2011, Springer-Verlag: Berlin.
71. Czél, G., et al., *Demonstration of pseudo-ductility in unidirectional discontinuous carbon fibre/epoxy prepreg composites*. Composites Science and Technology, 2014.
72. Taketa, I., T. Okabe, and A. Kitano, *A new compression-molding approach using unidirectionally arrayed chopped strands*. Composites Part A: Applied Science and Manufacturing, 2008. 39(12): p. 1884-1890.

73. Yashiro, S. and K. Ogi, *Fracture behavior in CFRP cross-ply laminates with initially cut fibers*. Composites Part A: Applied Science and Manufacturing, 2009. 40(6-7): p. 938-947.
74. Li, H., W.-X. Wang, and T. Matsubara, *Multiscale analysis of damage progression in newly designed UACS laminates*. Composites: Part A, 2013.
75. Harper, L.T., et al., *Representative volume elements for discontinuous carbon fibre composites – Part 1: Boundary conditions*. Composites Science and Technology, 2012. 72(2): p. 225-234.
76. Harper, L.T., et al., *Representative volume elements for discontinuous carbon fibre composites – Part 2: Determining the critical size*. Composites Science and Technology, 2012. 72(2): p. 204-210.
77. Qian, C., et al. *Determination of the size of representative volume elements for discontinuous fibre composites*. in *18th International Conference on Composite Materials*. 2011. Jeju, Korea.
78. Bekah, S., R. Rabiei, and F. Barthelat, *The micromechanics of biological and biomimetic staggered composites*. Journal of Bionic Engineering, 2012. 9: p. 446-456.
79. Kilic, M.H. *A nonlinear 3D micromechanical and structural framework for analysis of discontinuous long-fiber thermoplastic composites*. in *CAMX – The Composites and Advanced Materials Expo*. 2014. Orlando, FL.
80. Unger, W.J. and J.S. Hansen, *The Effect of Cooling Rate and Annealing on Residual Stress Development in Graphite Fibre Reinforced PEEK Laminates*. Journal of Composite Materials, 1993. 27(2): p. 108-137.
81. Cytec fiberite, *Thermoplastic Composite Materials Handbook*. 1999.
82. Barthelat, F. and RezaRabiei, *Toughness amplification in natural composites*. Journal of the Mechanics and Physics of Solids, 2011. 59: p. 829-840.
83. TenCate Advanced Composites, *Datasheet: TenCate Cetex(R) TC1200 PEEK Resin System*. 2013.
84. Carlsson, L.A., J.W. Gillespie, and B.R. Trethewey, *Mode II interlaminar fracture of graphite/epoxy and graphite/PEEK*. Journal of Reinforced Plastics and Composites, 1986. 5: p. 170-187.
85. Han, J.H., W.B. Alexander, and A. Godwin. *Characterization of milled carbon fiber added random discontinuous long fiber composites*. in *SAMPE*. 2010. Baltimore. WA.

86. Eguémann, N., *Study on the mechanical behaviour of carbon fibre reinforced PEEK polymer with a layered discontinuous architecture*. 2013, L'U.F.R. des sciences et techniques de l'Université de Franche-Comté.
87. Eilers, O., *Shear characterization of AS4/3501-6 graphite/epoxy in static and fatigue*, in *Department of Mechanical Engineering*. 1995, McGill University: Montreal.
88. Adams, D., *The double-notch shear test specimen for composite materials*, in *High-Performance Composites*. 2013. p. 15-16.
89. Dai, C. and P.R. Steiner, *Spatial structure of wood composites in relation to processing and performance characteristics. Part 2. Modelling and simulation of randomly-formed flake layer network*. *Wood Science and Technology*, 1994. 28: p. 135-146.
90. Painter, G., H. Budman, and M. Pritzker, *Prediction of oriented strand board properties from mat formation and compression operating conditions. Part 1. Horizontal density distribution and vertical density profile*. *Wood Science and Technology*, 2005. 40(2): p. 139-158.
91. Lu, C., P.R. Steiner, and F. Lam, *Simulation study of wood-flake composite mat structures*. *Forest Products Journal*, 1998. 48(5): p. 89-93.
92. Naderi, M., *Stochastic analysis of inter- and intra-laminar damage in notched PEEK laminates*. *eXPRESS Polymer Letters*, 2013. 7(4): p. 383-395.
93. 21.3.2 *Damage initiation for fiber-reinforced composites*, in *Abaqus/Standard v. 6.10. Abaqus Analysis User's Manual*
94. 21.3.3 *Damage evolution and element removal for fiber-reinforced composites*, in *Abaqus/Standard v. 6.10. Abaqus Analysis User's Manual*
95. Lapczyk, I. and J.A. Hurtado, *Progressive damage modeling in fiber-reinforced materials*. *Composites Part A: Applied Science and Manufacturing*, 2007. 38(11): p. 2333-2341.
96. Rabiei, R., S. Bekah, and F. Barthelat, *Failure mode transition in nacre and bone-like materials*. *Acta Biomaterialia*, 2010. 6: p. 4081-4089.
97. Cervenka, A., *PEEK/Carbon fiber composites: experimental evaluation of unidirectional laminates and theoretical prediction of their properties*. *Polymer Composites*, 1988. 9(4).
98. *T700/2510 unidirectional tape*, in *Composite Materials Handbook*.

99. Deleo, F. and P. Feraboli. *Crashworthiness energy absorption of carbon fiber composites: experiment and simulation*. in *FAA Joint Advanced Materials and Structures (JAMS)*. 2010. Seattle, WA.
100. Sutton, M.A., J.-J. Ortu, and H.W. Schreier, *Image Correlation for Shape, Motion and Deformation Measurements: Basic Concepts, Theory and Applications*. 2009, New York: Springer.
101. Correlated Solutions. *Presentation on Digital Image Correlation: Overview of Principles and Software*. in *SEM 2009 Workshop*. 2009.
102. McNeill, S., *Presentation on Digital Image Correlation*.